5 RESEARCH ACTIVITIES

5.1 NUCLEAR PHYSICS

S. Muralithar, N. Madhavan and P. Sugathan

More than 20 Nuclear Physics experiments were performed using beams from Pelletron accelerator in 2018-2019, most of which were Ph.D. thesis related experiments. Of these, ten were in nuclear spectroscopy using INGA facility looking for high spin states in unstable nuclei and a few were lifetime measurements using Dopple-Shift Attenuation Method (DSAM) technique. The nuclear reaction experiments were carried out in HIRA (5), GPSC (4), HYRA (2) and NAND (1). As HYRA and NAND experiments usually require high energy, heavier projectiles from Pelletron + LINAC accelerator combination, the non-availability of LINAC beams during the year resulted in lesser number experiments in those two facilities.

Experiments in HIRA concentrated on sub- and near-barrier fusion reactions probing transfer and other channel coupling effects, effect of deformation and/or shell closure in colliding partners and quasi-elastic back-scattering measurements were also carried out in one case. Experiments in GPSC involved quasi-elastic back-scattering measurements and/or deciphering the effect of projectile break-up on elastic scattering and fusion cross-sections. HYRA experiments involved measurement of evaporation residue (ER) cross-sections just above the barrier in heavy systems with ^{16,18}O projectiles and ^{204,206,208}Pb targets. NAND was used to extract pre- and post-scission neutron multiplicities in ^{18}O + ^{186}W system by detecting neutrons using 50 liquid scintillation detectors in coincidence with either fission fragment.

Efforts are on to shift the GPSC facility beyond GDA structure (30 degree beam-line) from the existing 45 degree beam-line in beam hall I to make room for setting up of HCI beam transport components. There is a plan to upgrade to VME-based Data Acquisition System (DAS) using indigenous development from the existing CAMAC-based DAS in most of the nuclear physics facilities. A proposal has been submitted to SERB to realise a Charged Particle Detector Array for particle-gated gamma measurements using INGA facility at IUAC. Clover and ACS (BGO) detectors have been procured using IUAC grants to increase the efficiency of the array.

Based on results from earlier years' experiments, several articles have been published in reputed journals and a few research scholars have been awarded doctorate degrees.

A five-day school on "Modern techniques of γ-ray spectroscopy for nuclear structure studies" was organised in IUAC which was attended by more than thirty research scholars.

Ms. Gonika (Scientist Trainee) won one of three prizes for best presentation and Mr. Rohan Biswas (JRF) won a special prize, both in SERB School on Nuclear Astrophysics at SINP, Kolkata.

5.1.1 High spin spectroscopy of ^{153}Eu

K. Mandal[1,8], A. K. Mondal[1], A. Chakraborty[1], U. S. Ghosh[1], A. Dey[1], S. Rai[1,10], S. Biswas[1,9], K. Katre[2], Yasraj[2], Indu Bala[2], R. K. Gurjar[2], R. Kumar[2], R. P. Singh[2], S. Muralithar[2], A. Sharma[3], Saket Suman[4], S. K. Tandel[4], G. Mukherjee[5], B. Mukherjee[1], R. Raut[6], S. S. Ghugre[6] and A. K. Sinha[7]

[1]Department of Physics, Siksha Bhavana, Visva-Bharati, Santiniketan, West Bengal 731235, India
[2]Inter-University Accelerator Centre, Aruna Asaf Ali Marg, New Delhi 110067, India
[3]Department of Physics, Himachal Pradesh University, Shimla 171005, India
[4]UM-DAE Centre of Excellence in Basic Sciences, Mumbai 400098, India
[5]Variable Energy Cyclotron Centre, 1/AF, Bidhan Nagar, Kolkata 700064, India
[6]UGC-DAE-Consortium for Scientific Research, Kolkata 700098, India
[7]UGC-DAE Consortium for Scientific Research, Indore 452017, India
[8]Chandidas Mahavidyalaya, Khujutipara, Birbhum, West Bengal 731215, India
[9]Murshidabad College of Engineering and Technology, Berhampore, West Bengal 742102, India
[10]Department of Physics, Salesian College, Siliguri Campus, Siliguri 734001, India

The level structure of ^{153}Eu at high spin has been investigated. The purpose was to look for the missing parity doublet bands built on $[\pi d_{5/2}]3/2^+$ and $[\pi h_{11/2}]3/2^-$ orbitals [1] and to settle the debate related to reflection symmetric versus reflection asymmetric behavior for the ground state parity doublet band built on $[\pi d_{5/2}]5/2^+$ and $[\pi h_{11/2}]5/2^-$ orbitals [2,3].

The experiment was carried out using the fusion evaporation reaction ^{150}Nd(^{7}Li, 4n). The 38 MeV ^{7}Li beam was delivered by the 15UD Pelletron of IUAC. A thin foil made of enriched ^{150}Nd (thickness ~ 3mg/cm^2), with mylar backing, was used as the target. De-excited gamma rays were detected by the Indian National Gamma Array (INGA) comprising of sixteen Clover detectors and two LEPS. Six Clover detectors were placed at 90° relative to the beam axis. Arrangement of the other detectors was as follows: four at 148°, two at 123°, three at 32° and one at 57°. The two LEPS were at 119° and 61°. Detailed off-line analysis of the acquired data is in progress. A representative coincidence spectrum, with the gate on 151 keV ground state feeding transition of ^{153}Eu, is shown in Fig. 5.1.1.1.

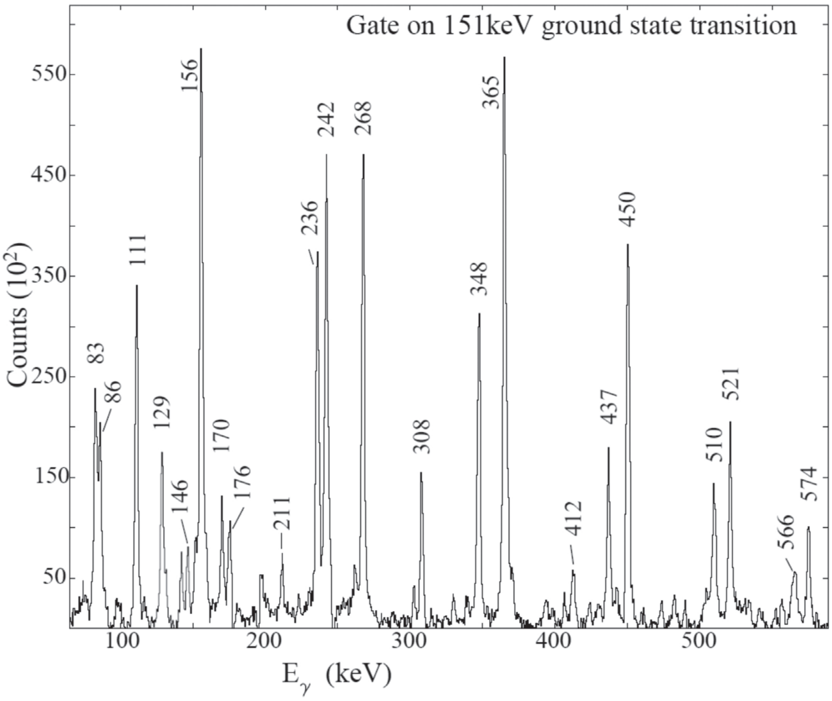

Fig. 5.1.1.1: A coincidence spectrum, gated with 151 keV ground state feeding transition of ^{153}Eu. The peaks labeled with their energies belong to ^{153}Eu.

REFERENCES:
[1] C. J. Pearson *et al.,* Phys. Rev. C **49**, R1239 (1994).
[2] D. Nosek *et al.,* Z. Phys. A **344**, 277 (1993).
[3] Somapriya Basu *et al.,* Phys. Rev. C **56**, 1756 (1997).

5.1.2 Quasi-elastic scattering measurements for ^{16}O,^{28}Si+^{144}Sm

Kavita Rani[1], B. R. Behera[1], A. Jhingan[4], G. Kaur[4], Saneesh N.[4], R. Mahajan[1], H. Arora[1], M. Kumar[4], D. Arora[2], S. Narang[1], D. Kaur[1], Kavita[2], Subodh[1], C. Sharma[1], Amit[1], A. Rani[3], K. Chakraborty[3], K. S. Golda[4], H. Singh[2] and P. Sugathan[4]

[1]Department of Physics, Panjab University, Chandigarh 160014, India
[2]Department of Physics, Kurukshetra University, Kurukshetra 136119, India
[3]Department of Physics and Astrophysics, University of Delhi, Delhi 110007, India
[4]Inter-University Accelerator Centre, Aruna Asaf Ali Marg, New Delhi 110067, India

The study of channel coupling in heavy-ion collisions has been a topic of interest for several years now. The enhancement in fusion reactions at sub-barrier energies is a result of this channel coupling which cannot be accounted by single potential model. The single potential barrier (V_b) splits into a distribution of barriers as a result of coupling of the relative motion between the colliding nuclei to their intrinsic motions as well as direct reaction channels. The barrier distribution (BD) formed due to this coupling acts as fingerprint for any reaction. Understanding the coupling schemes in any reaction is vital as it has a greater influence on the formation probability of compound nuclei [1-7]. The BD can be experimentally studied by the measurement of fusion excitation function $\sigma_{fus}(E)$ using the relation $D_{fus} = d2(E\sigma_{fus})/dE$ [2] and the quasi-elastic (QE) excitation function using $D_{qel} = -d\,(d\sigma_{qel} / d\sigma_R)/dE$ [4]. Theoretically, coupled-channel calculation scheme is used [6]. In the present work, we have performed an experiment for the QE-measurements for the systems ^{16}O, ^{28}Si+ ^{144}Sm. The aim is to extract information about the fusion barrier from experimental BD and study the role of nuclear structure as well as transfer channels in the reaction dynamics by comparing with the already existing results for ^{28}Si+ ^{154}Sm (having deformed target and positive neutron transfer reaction channels unlike in ^{28}Si+ ^{144}Sm) and ^{16}O+^{144}Sm.

The measurements have been performed in the General Purpose Scattering Chamber (GPSC) using the HYTAR [7] detection facility. Beam energy has been varied in steps of 5 MeV ranging from the barrier down to 25% below the barrier and in steps of 4 MeV ranging from the barrier up to 12% above the barrier for ^{28}Si. In case of ^{16}O, beam energy has been varied in steps of 3 MeV ranging from 20% below the barrier up to 10% above the barrier. Particle identification has been obtained with gas ionization chamber as ΔE detector and PIPS as E detector. Four telescope detectors, two in plane and two out of plane, each at an angle of 173° have been arranged in a symmetrical cone geometry. Nine telescopes, six at angles from +60° to +160° with angular separation of 20° and three at angles -30°, -42° and -54°, have been placed on rotatable arms of the GPSC. Two monitor detectors of thickness 300 μm have been placed at ±10° for normalization. Isotopic targets of samarium were prepared at the Target Development Laboratory of IUAC. Particle identification spectra obtained in the measurements have been shown in Fig. 5.1.2.1.

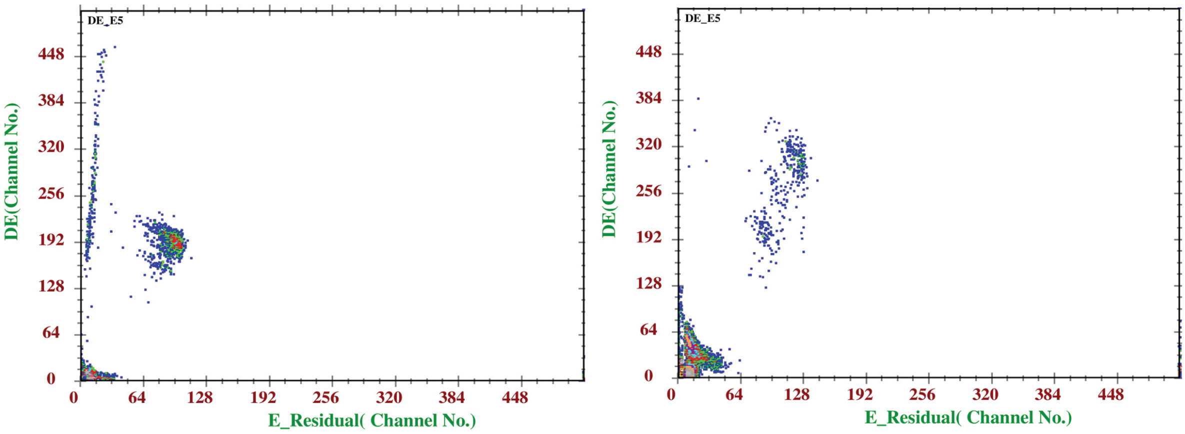

Fig. 5.1.2.1: Particle identification (E-ΔE) spectra for ^{28}Si+^{144}Sm at beam energy 132 MeV (left panel) and for ^{16}O+^{144}Sm at beam energy 76 MeV (right panel) at 140°, respectively.

The angular distributions of the QE events, for ^{28}Si+^{144}Sm (in the range 90 - 140 MeV) and for ^{16}O+^{144}Sm (in the range 60 - 82 MeV), have been measured. Fig. 5.1.2.2 shows the excitation functions extracted as a function of $E_{eff,}$ where $E_{eff} = 2E_{c.m.}/(1+\text{cosec}\,(\theta_{c.m.}/2))$ corrects for centrifugal effects. The measured QE events will be used to extract the experimental BD for both the systems.

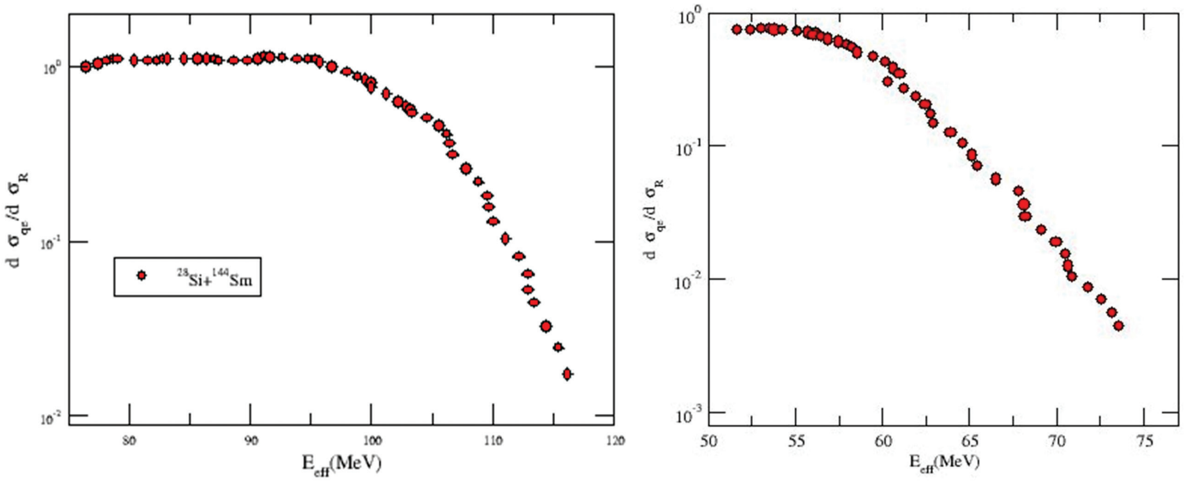

Fig. 5.1.2.2: Quasi-elastic excitation functions for ^{28}Si+^{144}Sm (left panel) and ^{16}O+^{144}Sm (right panel).

REFERENCES:

[1] G. Kaur et al., Phys. Rev. C **94**, 034613 (2016).
[2] Md. Moin Shaikh et al., Phys. Rev. C **91**, 034615 (2015).
[3] N. Rowley, G. R. Satchler, and P. H. Stelson, Phys. Lett. B **254**, 25 (1991).
[4] M. Dasgupta et al., Annu. Rev. Nucl. Part. Sci. **48**, 401 (1998).
[5] H. Timmers et al., Nucl. Phys. A **584**, 190 (1995).
[6] K. Hagino, N. Rowley, and A. T. Kruppa, Comput. Phys. Commun. **123**, 143 (1999).
[7] A. Jhingan et al., Nucl. Instrum. Methods A **903**, 326 (2018).

5.1.3 Role of positive transfer Q values in fusion evaporation residue cross-sections for $^{18}O+^{182,184,186}W$ reactions

P. Jisha[1], A. M. Vinodkumar[1], B. R. S Babu[1], S. Nath[2], N. Madhavan[2], J. Gehlot[2], S. Sanila[1], K. Arjun[1], A. Parihari[2], A. Vinayak[3] and Amit Raj[4]

[1]Department of Physics, Calicut University, Calicut 673635, India
[2]Inter-University Accelerator Centre, Aruna Asaf Ali Marg, New Delhi 110067, India
[3]Department of Physics, Karnataka University, Dharwad 580003, India
[4]Department of Physics, Panjab University, Chandigarh 160014, India

Study of fusion dynamics in the sub barrier energy region is interesting due to the well-established fact that fusion cross-sections are greatly enhanced when compared with predictions of 1D barrier penetration model (1D BPM) [1,2]. The coupling of the relative motion of colliding nuclei to the internal degrees of freedom plays an important role in describing sub-barrier fusion enhancement. The vibration of the nuclear surface and the rotation of deformed nuclei are used to explain many of the experimental results [3-6] for heavy nuclei. Also, Sargsyan et al. [7] suggested the role of transfer or transfer induced neutron rearrangement as reasons for fusion enhancement in the sub-barrier region. The change in the magnitude of the capture cross-section after the neutron transfer is suggested as an indirect effect of the quadrupole deformation. In order to study the effect of positive transfer Q-value, we performed an experiment to study the reactions $^{18}O+^{182,184,186}W$, which has positive 2n transfers Q values. One of the main objectives of this work was to compare the evaporation residue (ER) cross-section with nearby systems, namely $^{16}O+^{182,184,186}W$, with negative transfer Q values for 2n channels.

The experiment was performed using the Heavy Ion Reaction Analyzer (HIRA) at IUAC. HIRA was kept at 0^o with respect to the beam direction with 10 mSr entrance aperture. A pulsed beam of ^{18}O with 4 μs pulse separation was used to bombard the enriched $^{182,184,186}W$ targets of thickness ≈ 70 $\mu g/cm^2$, 200 $\mu g/cm^2$ and 100 $\mu g/cm^2$, respectively. ERs were measured from E_{lab} = 104 MeV to 68 MeV (35% above to 15% below the fusion barrier) in steps of 2- 4 MeV. A Multi-Wire Proportional Counter (MWPC) was placed at the focal plane of HIRA for the detection of the ERs. Two silicon surface barrier detectors (SSBD) were placed inside the target chamber at an angle of ±15° with respect to beam direction for normalization of cross-sections. A time of flight (TOF) was set up between anode signal of MWPC and RF signal to separate the beam-like particles from ERs. A two-dimensional spectrum between energy loss in MWPC and TOF is shown in Fig. 5.1.3.1. The preliminary results are shown in Fig. 5.1.3.2. A detailed analysis using a statistical model and CCFULL are in progress.

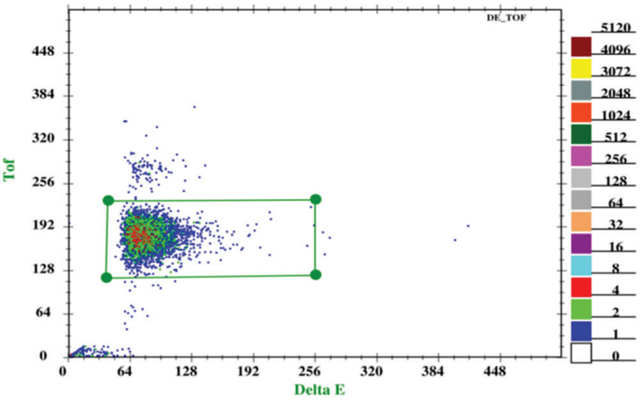

Fig. 5.1.3.1: Energy loss vs TOF spectrum for $^{18}O+^{182}W$ at E_{lab} = 84 MeV.

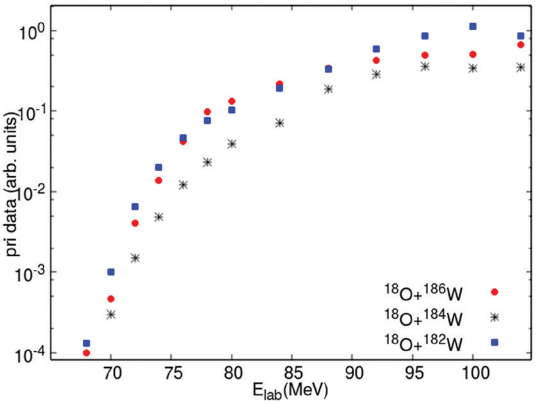

Fig. 5.1.3.2: Preliminary ER excitation functions for the reactions $^{18}O+^{182,184,186}W$.

REFERENCES:

[1] M. Beckerman, Phys. Rep. **129,** 145 (1985).
[2] M. Beckerman, Rep. Prog. Phys. **51,** 1047 (1988).
[3] J. X. Wei *et al.,* Phys. Rev. Lett. **67,** 3368 (1991).
[4] A. M. Stefanini *et al.,* Phys. Rev. Lett. **74,** 864 (1995).
[5] M. Trotta *et al.* Phys. Rev. C **65,** 011601 (2001).
[6] V. I. Zagrebaev *et al.* , Phys. Rev. C **64,** 034606 (2001).
[7] V. V. Sargsyan, Phys. Rev. C **85,** 024616 (2012).

5.1.4 Study of reaction dynamics involving weakly bound projectile and medium mass nuclei

Chhavi Joshi[1], N. L. Singh[1], H. Kumawat[2], R. K. Singh[1], S. D. Sharma[3], A. Parihari[4], K. Arora[5], J. Acharya[1], Ishtiaq Ahmed[4], P. K. Giri[6], Sushil Kumar[4], G. Kaur[4], K. S. Golda[4], Saneesh N.[4], Mohit Kumar[4], A. Jingan[4] and P. Sugathan[4]

[1]Department of Physics, The M. S. University of Baroda, Vadodara 390002, India
[2]Nuclear Physics Division, Bhabha Atomic Research Centre, Mumbai 400085, India
[3]Department of Physics, Aligarh Muslim University, Aligarh 202002, India
[4]Inter-University Accelerator Centre, Aruna Asaf Ali Marg, New Delhi 110067, India
[5]Department of Physics, Panjab University, Chandigarh 160014, India
[6]Centre for Applied Physics, Central University of Jharkhand, Ranchi 835205, Jharkhand, India

We performed an experiment to measure cross sections for elastic scattering, alpha production and fusion using the General Purpose Scattering Chamber (GPSC) at IUAC. The beams of weakly bounded projectiles were bombarded on two isotopes of molybdenum (^{92,100}Mo). Both the targets were prepared at the Target Development Laboratory of IUAC. Around 20 targets of ^{92}Mo and ^{100}Mo each, with thickness ~ 217 μg/cm^2 and 305 μg/cm^2 respectively, were prepared using the physical vapor deposition (PVD) technique [1]. In order to fabricate sustainable thin films of molybdenum, natural carbon was used as backing material.

In the experiment, ^{6,7}Li beams were used in the energy range 15 – 30 MeV. Both the beams are weakly bound and thus show interesting reaction dynamics around the barrier. The beam current was kept between 2 to 5 pnA. Silicon surface barrier detectors were mounted on rotatable arms inside the scattering chamber to cover wide range of angles. One High Purity Germanium (HPGe) detector was used to capture gamma-radiations produced in the experiment. Part of the analyzed data for elastic scattering angular distribution is presented in the Fig. 5.1.4.1.

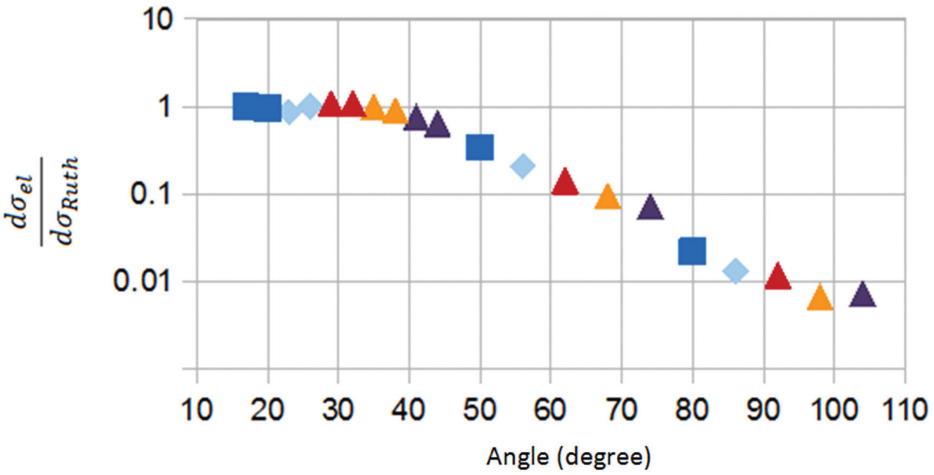

Fig 5.1.4.1: Angular distribution for the system ^{7}Li+^{100}Mo at E_{lab} = 30 MeV with inter detector normalization.

REFERENCE:
[1] C. Joshi *et al.,* Proc. DAE Symp. Nucl. Phys. **63**, 1210 (2018).

5.1.5 Lifetime of 6023 keV state in ^{104}Pd

C. Majumder[1], H. P. Sharma[1], S. Chakraborty[1], S. S. Tiwary[1], R. P. Singh[2], S. Muralithar[2], Indu Bala[2], S. S. Bhattacharjee[2], R. Garg[2], Neelam[3], S. Das[4], S. Samanta[4], S. S. Ghugre[4], A. Sharma[5], P. V. Madhusudhana Rao[6], R. Palit[7] and U. Garg[8]

[1]Department of Physics, Institute of Science, Banaras Hindu University, Varanasi 221005, India
[2]Nuclear Physics Group, Inter-University Accelerator Centre, Aruna Asaf Ali Marg, New Delhi 110067, India
[3]Department of Physics and Astrophysics, University of Delhi, Delhi 110007, India
[4]UGC-DAE Consortium for Scientific Research, Kolkata Centre, Kolkata 700098, India
[5]Department of Physics, Himachal Pradesh University, Shimla 171005, India

[6]Department of Physics, Andhra University, Visakhapatnam 530003, India
[7]Department of Nuclear and Atomic Physics, Tata Institute of Fundamental Research, Mumbai 400005, India
[8]Department of Physics, University of Notre Dame, Notre Dame, Indiana 46556, USA

Various structural effects were observed in the nuclei belonging to mass A ≈ 100 region, close to N = Z = 50 shell closures. In Pd isotopes, having four proton holes below Z = 50 shell gap and a number of neutron particles above N = 50 closed shell, a number of collective phenomena have been observed. The evolution of collectivity in these bands can be explained by the change of transition quadrupole moment. One of the ways to deduce the transition quadrupole moment (Qt) is measurement of lifetime of the states of a band. The lifetime of a number of states has been deduced by Doppler Shift Attenuation Method (DSAM). Lifetime of 6023 keV state, reported in Ref. [1], has been shown in this work.

High spin states of ^{104}Pd were populated via ^{94}Zr(^{13}C, 3n) fusion-evaporation reaction at a beam energy of 55 MeV at IUAC [2,3]. The target was ~1 mg/cm^2 thick with ~10 mg/cm^2 gold backing. The γ-rays were detected in the Indian National Gamma Array (INGA) [4] facility having eighteen Compton suppressed Clover detectors. To investigate the nucleus and deduce the lifetime of the states INGASort [5] and LINESHAPE [6] programs were used.

Table I: Summary of the experimental results, extracted from the present work.

E_γ(keV)	E_{ex} (keV)	I^π h	Q_t eb	τ (ps)	β_2	B(E2) e^2b^2	B(E2) W.u.
1059	6023	15	2.76 (7)	0.23 (1)	0.23	0.26 (.02)	90 (4)

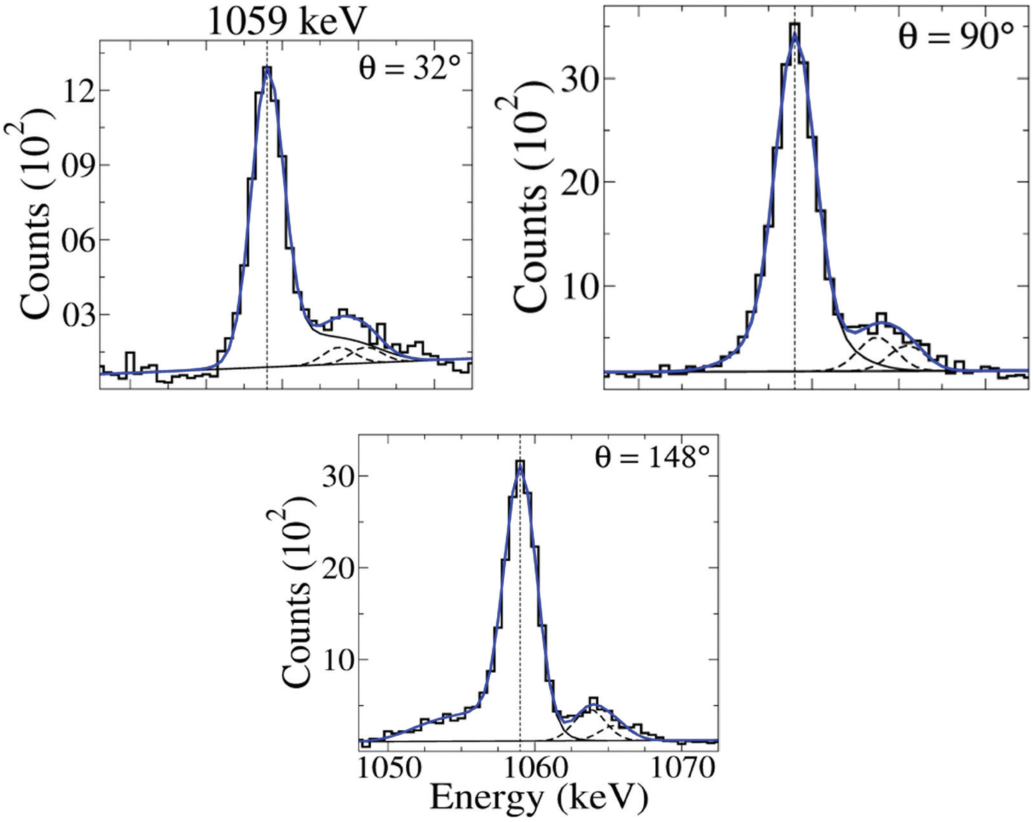

Fig. 5.1.5.1: Doppler shift attenuation spectra for the 1059 keV γ-ray at θ = 32°, 90° and 148°.

The quadrupole moment shows a moderate deformation of the state of the band. Lifetime of the other states is also measured and the work is underway.

REFERENCES:

[1] D. Sohler et al., Phys. Rev. C **85,** 044303 (2012).
[2] G. K. Mehta et al., Nucl. Instrum. Methods A **268,** 334 (1988).
[3] D. Kanjilal et al., Nucl. Instrum. Methods A **328,** 97 (1993).
[4] S. Muralithar et al., Nucl. Instrum. Methods A **622,** 281 (2010).
[5] R. K. Bhowmik, Proc. DAE Symp. Nucl. Phys. **44B,** 422 (2001).
[6] J. C. Wells et al., Tech. Rep. (1991).

5.1.6 Spectroscopy of ^{145}Gd

C. Majumder[1], H. P. Sharma[1], S. Chakraborty[1], S. S. Tiwary[1], S. Muralithar[2], R. P. Singh[2], Indu Bala[2], Yash Raj[2], K. Katre[2], B. Rohila[3], A. Kumar[3], Anuj[4], S. Kumar[4], R. Bhusan[4], S. K. Chamoli[4], A. Sharma[5] and T. Trivedi[6]

[1]Department of Physics, Banaras Hindu University, Varanasi 221005, India
[2]Inter-University Accelerator Centre, Aruna Asaf Ali Marg, New Delhi 110067, India
[3]Department of Physics, Panjab University, Chandigarh 160014, India
[4]Department of Physics and Astrophysics, University of Delhi, Delhi 110007, India
[5]Department of Physics, Himachal Pradesh University, Shimla 171005, India
[6]Department of Physics, Guru Ghasidas Vishwavidyalaya, Bilashpur 495009, India

^{145}Gd is a spherical nucleus, with Z = 64 sub-shell gap and one neutron hole below the N = 82 shell closure. A number of non-collective states have been reported at lower angular momentum [1,2]. The spin or parity of states is not firmly defined in the literature at higher angular momentum. The nucleus has been revisited and mostly all the de-excited gamma-rays, that are previously reported [1] have been seen in this investigation. A number of symmetric and asymmetric (angle dependent) matrices have been formed to study the γ-γ coincidence relationship and also to determine their multi-polarity. Some important energy-gated γ-spectra have been shown in Fig. 5.1.6.1. The value of correction factor $a(E_\gamma)$ of some of the detectors having three or four crystals are shown in Fig. 5.1.6.2. They are used for linear polarization measurements.

High spin levels of ^{145}Gd have been populated via ^{122}Sn(^{28}Si,5n) reaction at a beam energy 146 MeV at IUAC. ^{122}Sn target (99.3% enriched) has a thickness of ~1.9 mg/cm^2 with ~10.4 mg/cm^2 thick gold backing. The γ-rays have been detected in the Indian National Gamma Array (INGA) facility having sixteen Compton suppressed Clover detectors and two Low Energy Photon Spectrometers (LEPS). To investigate the nucleus, INGASort [3] program has been used.

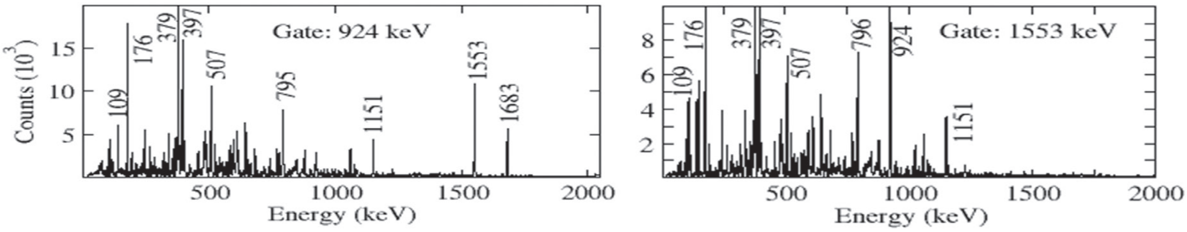

Fig. 5.1.6.1: Prompt γ-spectra gated with 924 keV (left panel) and 1553 keV (right panel) γ-line.

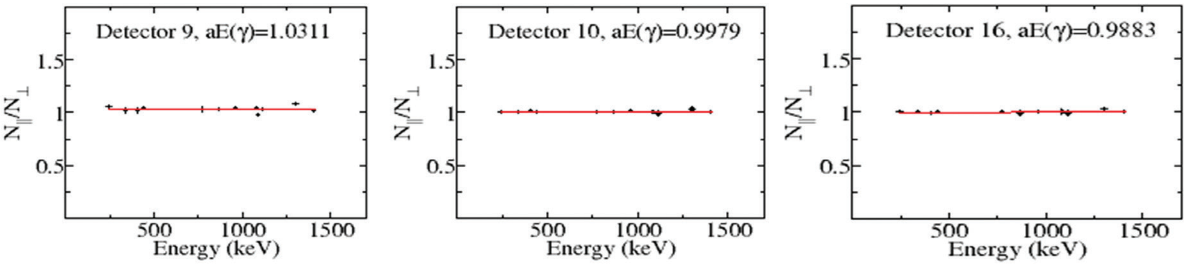

Fig. 5.1.6.2: The correction factor [$a(E_\gamma)$] for detectors 9, 10 and 16, as a function of energy.

REFERENCES:

[1] C. Schumacher, Z. Phys. A **354,** 123 (1996).
[2] A. Pakkanen, Nucl. Phys. **A373,** 237 (1982).
[3] R. K. Bhowmik, Proc. DAE Symp. Nucl. Phys., **44B,** 422 (2001).

5.1.7 Study of quasi-elastic scattering in ^{7}Li+^{116,118}Sn reactions

Arshiya Sood[1], Arzoo Sharma[1], Akashrup Banerjee[2], Pawan Kumar[1], Rudra N. Sahoo[1], Malika Kaushik[1], Pushpendra P. Singh[1], Kavita Rani[3], Abhishek Yadav[4], Gurpreet Kaur[5], Akhil Jhingan[5], N. Saneesh[5], Mohit Kumar[5], Manoj K. Sharma[6], K. S. Golda[5] and P. Sugathan[5]

[1]Department of Physics, Indian Institute of Technology Ropar, Punjab 140001, India
[2]Department of Physics and Astrophysics, University of Delhi, Delhi 110007, India
[3]Department of Physics, Panjab University, Chandigarh 160014, India
[4]Department of Physics, Jamia Millia Islamia , New Delhi 110025, India
[5]Inter-University Accelerator Centre, Aruna Asaf Ali Marg, New Delhi 110067, India
[6]Department of Physics, Shri Varshney College, Aligarh, Uttar Pradesh 202001, India

Heavy-ion (HI) induced reactions have inspired a great deal of efforts across the globe as they offer a radical rearrangement of nucleons in a many-body system, and have been prodigiously investigated to understand the underlying dynamics. An interesting strand of HI-reactions is the one involving weakly bound projectiles (^{6}Li, ^{7}Li, and ^{9}Be) at energies near- and below- the barrier as they offer widespread opportunities to explore different aspects of nuclear structure and reactions. There is a special interest in the field because fusion of weakly bound nuclei mimics unstable radioactive ion beams (RIBs) which have an ample relevance in astrophysical processes like nucleosynthesis and in producing new heavy and/or neutron rich isotopes [1,2]. Weakly bound nuclei are characterized by their cluster/halo structure and low breakup thresholds which makes breakup a dominant reaction process. The fusion cross-sections are sensitive to the internal structure of interacting nuclei as well as to the coupling to other reaction channels like inelastic excitations, breakup and direct nucleon transfer. This coupling essentially modifies the effective interaction potential, and leads to splitting of single, uncoupled fusion barrier into multiple barriers which results in the distribution of barriers. This distribution of barrier can be experimentally obtained by two complementary processes, *viz., fusion and large angle quasi-elastic (QEL) scattering [3,4].*

It has been observed that for strongly bound interacting partners, the distributions obtained from the foregoing two complementary approaches are similar at energies around the barrier [5,6]. However, for weakly bound projectiles, the distribution obtained from QEL has been found be to broader than that derived from fusion, and a relative shift in peak has also been observed between the two distributions indicating strong influence of breakup or breakup-like processes at energies near or below the barrier [7-9]. In this context, experiments have been performed to derive the barrier distributions from quasi-elastic back-angle scattering measurements for ^{7}Li+^{116,118}Sn systems.

The experiments have been performed in the General Purpose Scattering Chamber (GPSC) with beams of ^{7}Li in energy range 15-29 MeV (30% below- to above- the barrier) bombarded on self-supporting ^{116,118}Sn targets of thickness 430µg/cm^{2} . Targets were prepared in the Target Development Laboratory of IUAC. Beam energies have been varied in steps of 2 MeV below the barrier and 3 MeV above it. To detect and identify the charged particles produced in the reaction, HYTAR detector facility was used [10]. To measure the quasi-elastic backscattering events, four telescopes were arranged in symmetrical cone geometry, two in- and out- of plane each, at an angle of 173°. Additionally, six telescopes were placed at angles +60° to +160° and three telescopes were placed at angles -36° to -60° with an angular separation of 20° and 12°, respectively. Two monitor detectors were placed at ±10° with respect to the beam direction for normalization and beam monitoring. The experimental set-up is shown in the left panel of Fig. 5.1.7.1. A typical two-dimensional ΔE-Eres spectrum obtained from the telescope at +140° for ^{7}Li+^{118}Sn system is presented in the right panel of Fig. 5.1.7.1.

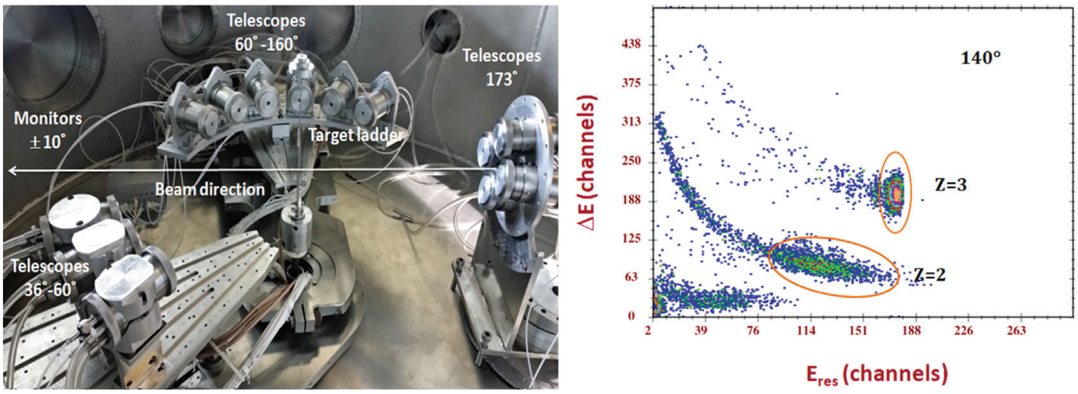

Fig. 5.1.7.1: (left) Experimental set-up for quasi-elastic scattering measurement and (right) ΔE-E_{res} spectrum at θ_{lab}= +140° for ^{7}Li+^{118}Sn at E_{lab} = 21 MeV.

The events corresponding to various elastic + inelastic scattering and breakup processes at E_{lab} = 21 MeV are marked in the right panel of Fig. 5.1.7.1 as Z = 3 and Z = 2, respectively. In Fig. 5.1.7.2, preliminary analysis of data for four angles *i.e.*, +120°, +140°, +160° and +173° is presented. The left panel of Fig. 5.1.7.2 shows the quasi-elastic excitation functions obtained at these angles and the right panel of the same figure shows the corresponding barrier distributions. The detailed analysis of data and its interpretation in the framework of theoretical models are underway.

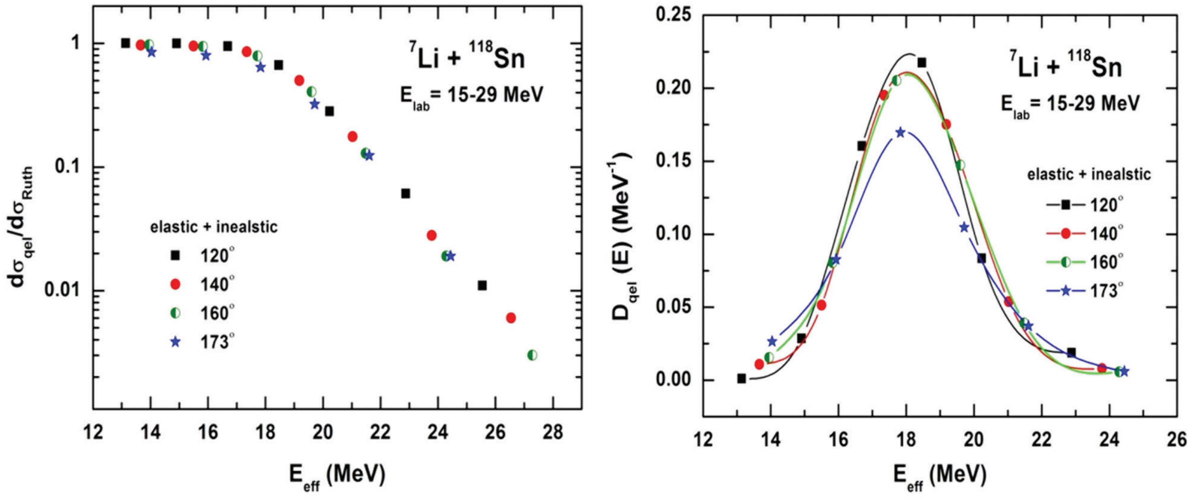

Fig. 5.1.7.2: (left) Quasi-elastic scattering excitation function and (right) corresponding barrier distribution obtained at θ_{lab}= +120° to +173° for ^{7}Li+^{118}Sn.

REFERENCES:

[1] L. F. Canto et al., Phys. Rep. **424**, 1 (2006), and references therein.
[2] V. Zagrebaev et al., Phys. Rev. C**78**, 034610 (2008).
[3] N. Rowley, G. R. Satchler and P. H. Stelson, Phys. Lett. B**254**, 25 (1991).
[4] H. Timmers et al., Nucl. Phys. A**584**, 190 (1995).
[5] M. Dasgupta et al., Annu. Rev. Nucl. Part. Sci. **48**, 401 (1998) and references therein.
[6] H. Timmers et al., Nucl. Phys. A**633**, 421 (1998).
[7] M. Zadro et al., Phys. Rev. C**87**, 054606 (2013), and references therein.
[8] C. S. Palshetkar et al., Phys. Rev. C**89**, 024607 (2014).
[9] Md. Moin Shaikh et al., Phys. Rev. C**91**, 034615 (2015).
10] A. Jhingan et al., Nucl. Instrum. Methods A **903**, 326 (2018).

5.1.8 Gamma-ray spectroscopy of ^{70}As

A. Biswas[1,2], U. S. Ghosh[1], B. Mukherjee[1], S. Rai[1,3], K. Mondal[1], A. Chakraborty[1], A. Sharma[4], S. Muralithar[5], R. P. Singh[5] and U. Dutta[6]

[1]Department of Physics, Siksha-Bhavana, Visva-Bharati, Santiniketan, Bolpur 731235, India
[2]Department of Physics, A. M. College, Jhalda, Purulia 723202, India
[3]Department of Physics, Salesian College, Siliguri Campus, Siliguri 734001, India
[4]Department of Physics, Himachal Pradesh University, Shimla 171005, India
[5]Inter-University Accelerator Centre, Aruna Asaf Ali Marg, New Delhi 110067, India
[6]Saha institute of Nuclear Physics, Kolkata 700064, India

The nuclei in A≈70 region exhibit various kinds of excitations, both single particle and collective, with different shapes, namely prolate, oblate and triaxial. Structures of the odd-odd nuclei in this region attract more attention. At low spins, properties of the nuclei are governed by $1f_{5/2}$, $2p_{3/2}$ and $2p_{1/2}$ spherical shell model orbitals. However, at higher spins and excitation energies, the particle-hole excitation from the $1f_{7/2}$ and $1g_{9/2}$ high-j intruder orbitals are important. In the odd-odd nucleus ^{70}As, the low lying states are similar to ^{72}As and were experimentally well investigated by Brink et al. [1] and Filevich *et al.* [2] using proton, alpha and light-ions as projectiles. The study of the high spin states of these nuclei, using heavy projectile was done by Badika *et al.* [3], using ^{16}O as the projectile. They could populate up to 11^+ and tentatively up to the 13^+ state at 4.076 MeV. The lifetime measurements of 11^+ and 13^+ levels, by Garcia Bermudez *et al.* [4] indicated an enhancement in B(E2) values of the 981 keV and 1343 keV. The work by Mukherjee *et al.* [5], using HIRA+GDA at IUAC extended the level scheme up to 8.9 MeV with tentative spin parity 19^+. Authors had reported three rotational bands, with two positive parity bands which were the signature partners of each other. However the signature partner of the negative parity band could not be established in this work. To get more information about the nuclear structure of ^{70}As, an experiment was performed using the INGA array at IUAC.

Excited states in ^{70}As were populated through in-beam γ-ray spectroscopic techniques using the ^{48}Cr(^{28}Si, αpn) fusion-evaporation reaction at a beam energy of 100 MeV. Emitted γ-rays of excited nuclei were detected in the γ-γ coincidence mode using 16 Compton suppressed Ge Clover detectors of the Indian National Gamma Array (INGA).

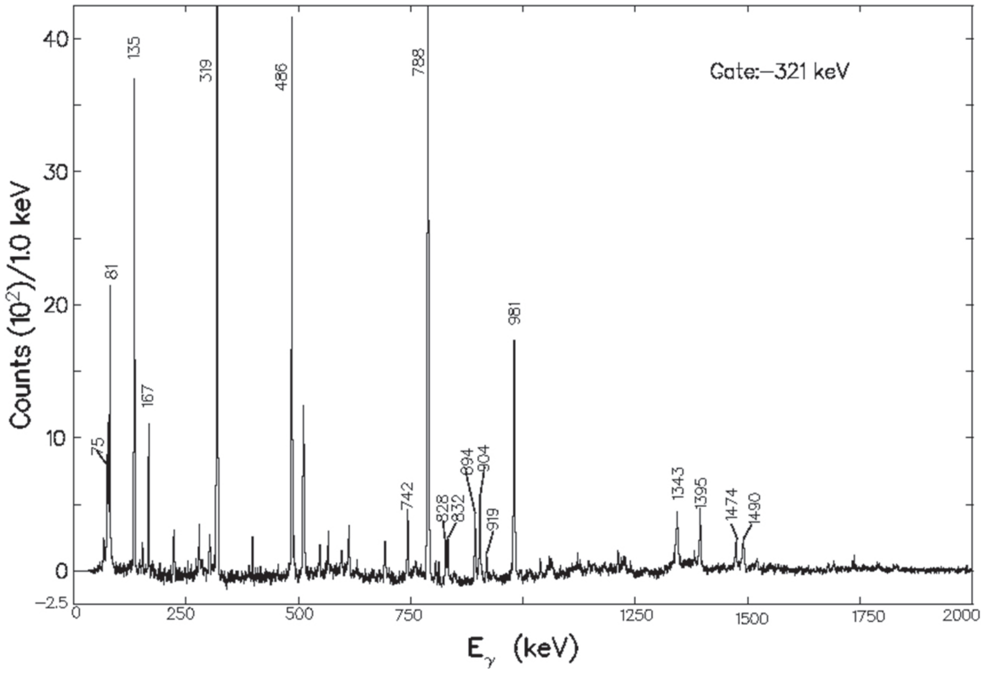

Fig. 5.1.8.1: Background subtracted γ-γ coincidence spectra for ^{70}As gated on 321 keV (7- → 5-) transition.

Data analysis is in progress. In Fig. 5.1.8.1 we have shown a 321 keV gated spectra of ^{70}As. Here, almost all the strong transitions are labelled. New results, in details, will be published as soon as the analysis is completed.

We acknowledge Abhilash S. R. for target preparation and the Pelletron staff of IUAC for providing excellent beam.

REFERENCES:

[1] B. O. Ten Brink, J. Akkermans and H. Verheul, Nucl. Phys. A**330**, 409 (1979).
[2] A. Filevich, M. Behar, G. Garcia Bermudez and M. A. J. Mariscotti, Nucl. Phys. A**309**, 285 (1978).
[3] T. Badika, V. Cojocaru, D. Pentelica, I. Popescu and N. Scintei, Nucl. Phys. A**535**, 425 (1991).
[4] G. Garcia Bermudez, J. Döring, G. D. Johns, R. A. Kaye, M. A. Riley, S. L. Tabor, C. J. Gross et al., Phys. Rev. C **56**, 2869 (1997).
[5] B. Mukherjee et al., Acta Phys. Hung. N. S. **11**, 305 (2000).

5.1.9 Study of high Spin States in A ~ 180 mass region

A. Sharma[1], Shashi. K. Dhiman[1], Pankaj Kumar[1], S. Muralithar[2], R. P. Singh[2], Yashraj[2], K. Katre[2], R. K. Gurjar[2], S. S. Tiwary[3], Neelam[4], Anuj[4], S. Kumar[4], S. Suman[5], S. K. Tandel[5], R. Raut [6], Sutanu Bhattacharya[7], Umakant Lamani[8] and Subodh[9]

[1]Department of Physics, Himachal Pradesh University, Shimla 171005, India
[2]Inter-University Accelerator Centre, Aruna Asaf Ali Marg, New Delhi 110067, India
[3]Department of Physics, Institute of Science, Banaras Hindu University, Varanasi 221005, India
[4]Department of Physics and Astrophysics, University of Delhi, Delhi 110007, India
[5]UM-DAE Centre for Excellence in Basic Sciences, Mumbai 400098, India
[6]UGC-DAE Consortium for Scientific Research, Kolkata Centre, Kolkata 700098, India
[7]Department of Pure and Applied Physics, Guru Ghasidas Viswavidyalaya, Koni, Bilaspur 495009, India
[8]Department of Physics, Indian Institute of Technology Bombay, Powai, Mumbai 400076, India
[9]Department of Physics, Panjab University, Chandigarh 160014, India

Investigation of the structure of atomic nuclei near Z = 82 shell closure is important due to co-existence of single particle and collective excitations. The high-j orbitals, *viz.* h$_{11/2}$ and h$_{9/2,}$ lie near proton Fermi surface along with low-j $_{s1/2,}$ d$_{5/2}$ and d$_{3/2}$ orbitals, resulting in number of K-isomers in this mass region. The Iridium nuclei lie between transitional and spherical nuclei. Nuclei in this region are soft to changes in deformation. In these transitional nuclei, a complex interplay between different competing degrees of freedom was observed, and in particular, consideration of the γ-degree of freedom plays a crucial role. Besides the collective excitations, a large number of different high-K multi-quasiparticle states of different shapes have been observed in these nuclei [1]. In this region, significantly larger deformation has been observed after back-bending in Ir isotopes [2]. The change in deformation would be caused by the polarization of the Osmium core by the odd proton [3]. The present study concentrates on ^{183}Ir and is part of a systematic study of nuclei in Os-Pt region. The information on ^{183}Ir is very scarce [4,5].

High spin states of ^{183}Ir were populated via ^{169}Tm(^{18}O, 4n) fusion evaporation reaction at beam energy 94 MeV, delivered by the 15 UD Pelletron at IUAC. The Indian National Gamma Array (INGA) [9] was used for detecting two and higher fold γ-γ coincident events. A self-supporting ^{169}Tm target of 6.5 mg/cm^2 thickness was used. Offline data analysis was carried out by CANDLE [6], INGASORT [7] and RADWARE [8] computer codes. In the present study, the high spin states of ^{183}Ir were investigated. The strongly populated $\pi h_{9/2}$ band has been observed up to ~ 6.1 MeV. In Fig. 5.1.9.1 total projection spectrum from γ-γ coincidence matrix for all the Clover detectors is shown. Fig. 5.1.9.2 shows a spectrum gated with 309 keV γ-line. Further data analysis is in progress.

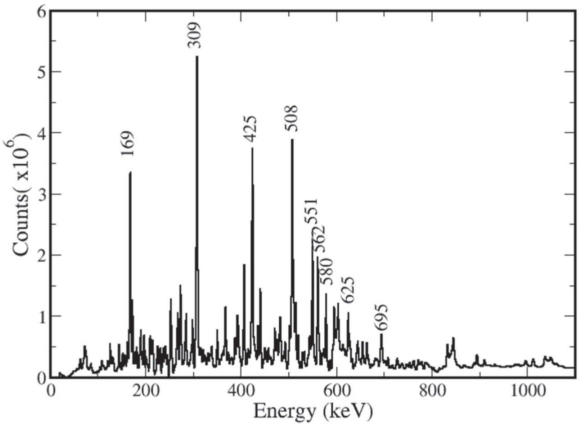

Fig. 5.1.9.1: γ-γ coincidence spectrum from the whole Clover array. Energy of the γ peaks is marked in keV.

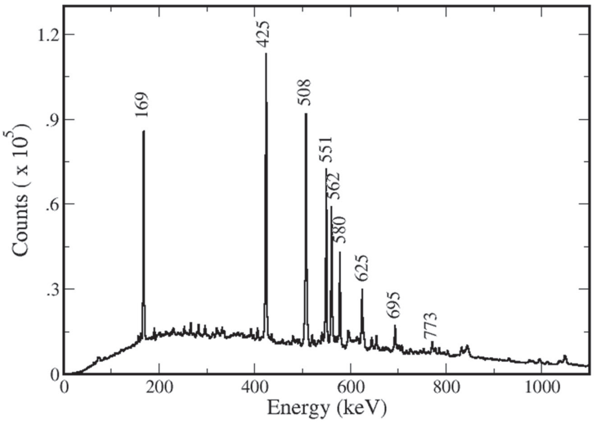

Fig. 5.1.9.2: Coincidence spectrum, gated with 309 keV γ-line of ^{183}Ir.

REFERENCES:

[1] V. Modamio *et al.,* Phys. Rev. C **81**, 054304 (2010).
[2] S. Andre *et al.,* Phys. Rev. Lett. **38**, 327 (1977).
[3] R. Kaczarowski *et al.,* Phys. Rev. C **41**, 2069 (1990).
[4] V. P. Janzen *et al.,* Phys. Rev. Lett. **61**, 2073 (1988).
[5] A. J. Kreiner *et al.,* Phys. Rev. C **42**, 878 (1990).
[6] Ajith Kumar B. P. *et al.,* Proc. DAE-BRNS Symp. Nucl. Phys. B**44**, 390 (2001).
[7] R. K. Bhowmik *et al.,* Proc. DAE-BRNS Symp. Nucl. Phys. B**44**, 422 (2001).
[8] D. C. Radford *et al.,* Nucl. Instrum. Methods A**361**, 267 (1995).
[9] S. Muralithar *et al.,* Nucl. Instrum. Methods A **622**, 281 (2010).

5.1.10 High spin states in ^{84}Sr

Naveen Kumar[1], Anuj[1], Suresh Kumar[1], Neelam[1], K. Rojeeta Devi[1], Neeraj Kumar[1], C.V. Ahmad[1], A. Banerjee[1], Aman Rohilla[1], C.K. Gupta[1], Anand Pandey[1], Ravi Bhusan[1], S. Verma[1], S. K. Chamoli[1], Unnati Gupta[1], S. K. Mandal[1], R. Garg[2], S. Bhatacharya[2], S. Muralithar[2], R. P. Singh[2], Indu Bala[2], Divya Arora[2], Vishnu Jyothi[3], Chandrani Majumder[4], H. P. Sharma[4], A. Sharma[5], S. K. Dhiman[5], Ajay Y. Deo[6] and P. C. Srivastava[6]

[1]Department of Physics and Astrophysics, University of Delhi, Delhi 110007, India
[2]Inter-University Accelerator Centre, Aruna Asaf Ali Marg, New Delhi 110067, India
[3]Department of Physics, Andhra University, Visakhapatnam 530003, India
[4]Department of Physics, Banaras Hindu University, Varanasi 221005, India
[5]Department of Physics, Himachal Pradesh University, Shimla 171005, India
[6]Department of Physics, IIT Roorkee, Roorkee 247667, India

Nuclei near the $Z \approx 40$ and $N < 47$ falls between the deformed and spherical region. The strontium (Sr) isotopes with $A \leq 88$ shows a gradual transition from the nearly doubly magic ^{88}Sr nucleus to the rotational like behaviour in ^{80}Sr nucleus. Investigation of these transitions is particularly interesting as the proton number (Z = 38 or 40) behaves like a magic one, at least when the neutron number is close to N = 50. Many collective bands have been seen in isotopes of Sr, Zr and Mo. The nucleus ^{84}Sr, which has four neutron holes in the $1g_{9/2}$, $2p_{1/2}$ and $1f_{5/2}$ subshells, displays both collective and single particle excitations. In the present experiment, the excited states of

^{84}Sr nucleus were studied to confirm the tentatively assigned spin to various previously known states. The aim also included searching for interesting high-spin phenomena like super deformation [1,2], loss of collectivity [3,4], band termination[5], chiral rotation[6] and shape-related effects [7,8].

The excited states of ^{84}Sr was populated through the reaction ^{76}Ge(^{12}C,4n)^{84}Sr, with a beam energy of 58 MeV which was provided by the 15UD Pelletron at IUAC. The gamma-rays were detected by the INGA spectrometer at IUAC [9] which consisted of 18 Compton- suppressed Clover detectors with four, four, six, two and two detectors placed at angles 148º, 123º, 90º, 57º and 32º, respectively, with respect to the beam direction. The distance between the target position and the detectors was 25 cm. The list mode data were collected in double and higher fold gamma-ray coincidence using a CAMAC based multi-parameter data-acquisition system along with the Collection and Analysis of Nuclear Data using Linux nEtwork (CANDLE) software. The symmetric and asymmetric matrices were generated by sorting the data with CANDLE and RADWARE [10]. The results of preliminarily analysis are shown in the Fig. 5.1.10.1 and 5.1.10.2. The analysis to obtain the RDCO and Polarization are in progress.

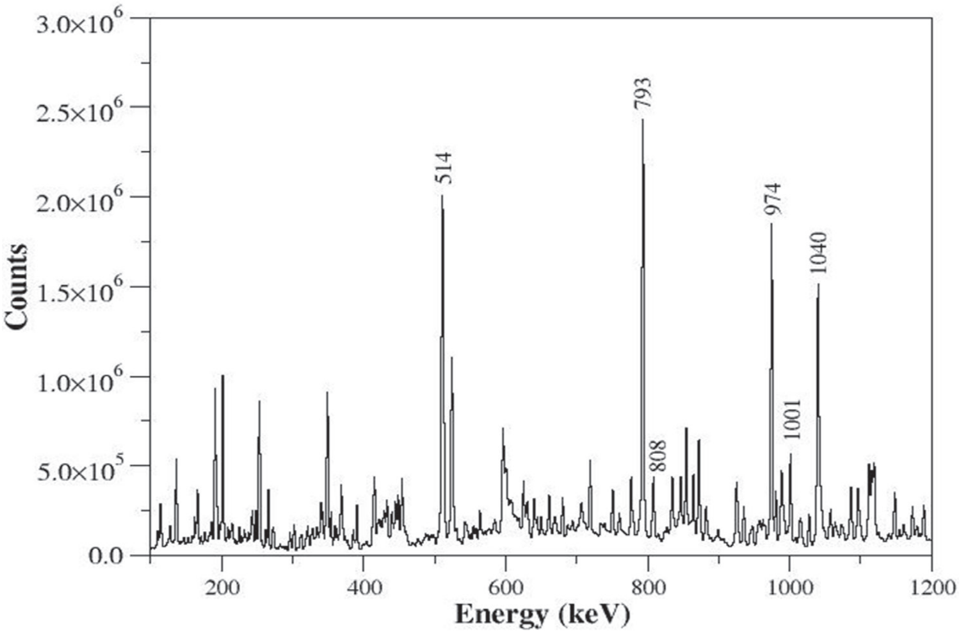

Fig. 5.1.10.1: Projection spectrum of coincidence data obtained at E_{lab} = 58 MeV. The gamma-rays belonging to the ^{84}Sr nucleus are labelled.

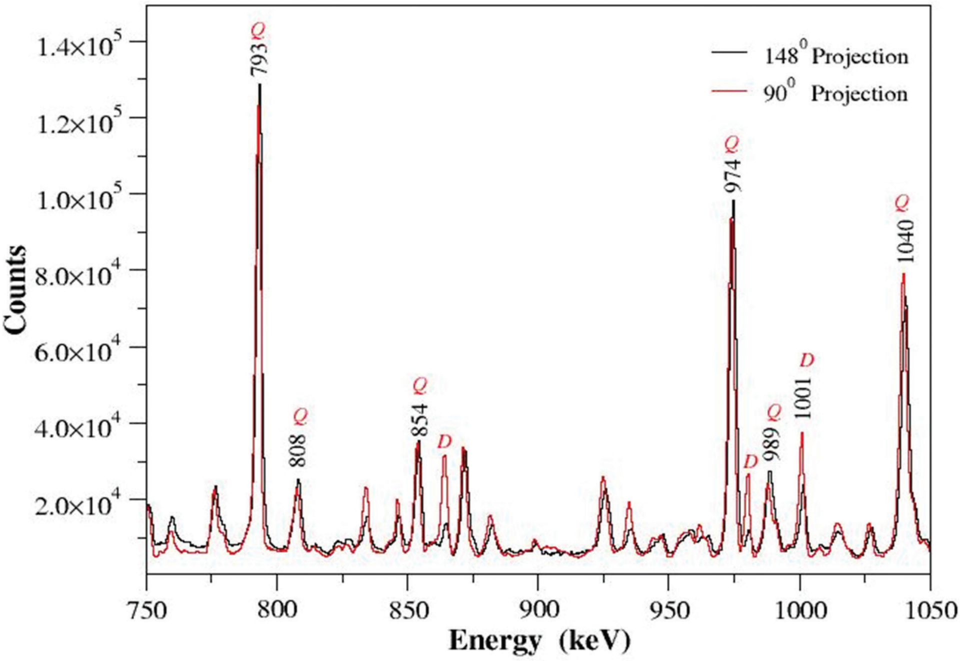

Fig. 5.1.10.2: The spectrum shows the projection of asymmetry matrix to obtain the DCO ratios – red line for 90º and black line for 148º. The quadrupole (Q) and dipole (D) nature of the gamma-ray transition is also marked along their energy in keV.

REFERENCES:

[1] B. Singh, R. Zywina and R. B. Firestone, Nucl. Data Sheets **97,** 241 (2002).
[2] D. R. LaFosse *et al.,* Phys. Lett. B **354,** 34 (1995).
[3] R. K. Sinha *et al.,* Eur. Phys. J. A **28,** 277 (2006); 29, 253 (2006).
[4] W. Nazarewicz, J. Dudek, R. Bengtsson, T. Bengtsson and I. Ragnarsson, Nucl. Phys. A**435,** 397 (1985).
[5] M. Wiedeking *et al.,* Phys. Rev. C **67,** 034320 (2003).
[6] S. Y. Wang *et al.,* Phys. Lett. B **703,** 40 (2011).
[7] A. Dhal *et al.,* Eur. Phys. J. A **27,** 33 (2006).
[8] Ch. Winter *et al.,* Nucl. Phys. A **535,** 137 (1991).
[9] S. Muralithar *et al.,* Nucl. Instrum. Methods A **622,** 281 (2010).
[10] D. C. Radford, Nucl. Instrum. Methods A **361,** 297 (1995).

5.1.11 Measurement of the pre and post-scission neutron multiplicity for the reactions ^{18}O+^{184,186}W

N. K. Rai[1], A. Gandhi[1], N. Saneesh[2], M. Kumar[2], G. Kaur[2], A. Parihari[2], D. Arora[2], N. K. Deb[3], A. Chakraborty[4], S. Biswas[4], T. K. Ghosh[5], Jhilam Sadhukhan[5], K. S. Golda[2], A. Jhingan[2], P. Sugathan[2], B. K. Nayak[6] and Ajay Kumar[1]

[1]Department of Physics, Banaras Hindu University, Varanasi 221005, India
[2]Inter-University Accelerator Centre, Aruna Asaf Ali Marg, New Delhi 110067, India
[3]Department of Physics, Gauhati University, Guwahati 781014, India
[4]Department of Physics, Siksha Bhawan, Visva-Bharti, Santiniketan, West Bengal 731235, India
[5]Variable Energy Cyclotron Centre, 1/AF Bidhan Nagar, Kolkata 700064, India
[6]Nuclear Physics Division, Bhabha Atomic Research Centre, Mumbai 400085, India

Heavy-ion induced fusion-fission reactions involve many complex processes, which are understood through experimental as well theoretical approach. It is well known that in a collision between two heavy nuclei there is a considerable contribution from quasi-fusion processes along with the fusion-fission processes. To investigate these processes, a number of attempts like mass distribution, mass-angle correlations, and mass-gated neutron multiplicity measurements have been done. In the recent years, nuclear dissipation has emerged as a topic of considerable interest involved in the fusion-fission process. Nuclear dissipation causes the delay in the fission process with respect to the statistical model of compound nucleus (CN) decay. The deep understanding of the nuclear dissipation is still a matter of detail study because of the complexities involved in the process. The measurement of neutron multiplicity has been done to investigate the details of the dynamical evolution of the nuclear system [1]. To understand the nuclear dissipation, evaporated neutrons are one of the preferred probes. Measurement of neutrons helps in measuring the time-scales of these processes and in understanding the mechanism of energy dissipation in heavy ion reactions. In the literature, some measurements have been reported to investigate the effect of entrance channel mass asymmetry, neutron shell closure, N/Z, etc. in the fission process [2-4]. In the present study, we have measured the neutron multiplicity for the reactions ^{18}O+^{184,186}W populating the compound nucleus ^{202}Pb and ^{204}Pb to understand the dissipative fission dynamics.

The experiment was performed using the National Array of Neutron Detectors (NAND) facility of IUAC. The pulsed beam of ^{18}O with a pulse separation of 250 ns, delivered from the 15UD Pelletron, was bombarded on ^{184}W and ^{186}W targets of thicknesses 770 μg/cm^2 and 637 μg/cm^2, respectively with carbon backing of 40 μg/cm^2. Neutron multiplicity measurements were performed at three energies, E_{lab} = 97, 102 and 107 MeV. The neutrons were detected in coincidence with the fission fragments using 50 organic liquid scintillators (BC 501) of 5”×5” dimensions, kept at a distance of 175 cm from the center of the target. Two Multi-Wire Proportional Counters (MWPCs) of active area 11×16 cm^2 were symmetrically placed at the folding angles, at a distance of 26 cm (35^o) and 21 cm (126^o) to detect the fission fragments. MWPCs were operated with the isobutene gas pressure of 4 mbar. Two Silicon Surface Barrier Detectors (SSBDs) were also placed inside the chamber at ±12.5^o with respect to the beam directions to monitor the beam. Event mode data were collected using the VME based data acquisition system coupled with Linux Advanced Multi-Parameter System (LAMPS) software. The fast time signals of the MWPCs were used to obtain the time of flight of the fission fragments. The acquisition was set according to the trigger logic generated by coincidence between RF of the beam pulse and the fission detectors.

Neutron detectors are sensitive to detect neutrons as well as gamma-rays. The discrimination between neutrons and gamma was done using the time of flight (TOF) technique as well as pulse shape discrimination (PSD) based on zero – cross over method. To identify the neutron and gamma event, a two-dimensional gate was applied to the neutron spectra. The neutron TOF spectra were converted into energy spectra by considering the gamma peak as a reference line. Neutron energy spectra were gated with TOF spectra of fission fragments to ensure that neutrons are only emitted from the fusion-fission process. Experimental values of the pre- and post-scission multiplicity are shown in Fig. 5.1.11.1 and Fig. 5.1.11.2.

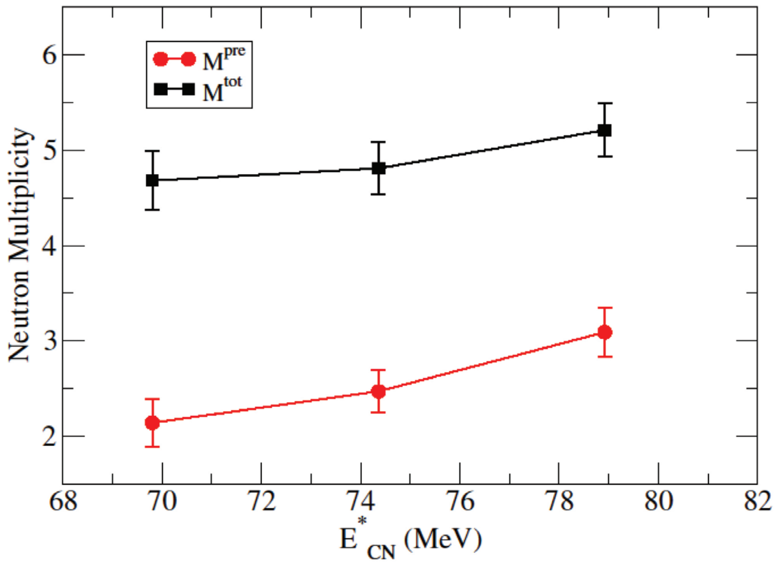

Fig. 5.1.11.1: Variation of the experimental values of pre-scission and total neutron multiplicity as a function of excitation energy for the reaction $^{18}O+^{186}W$.

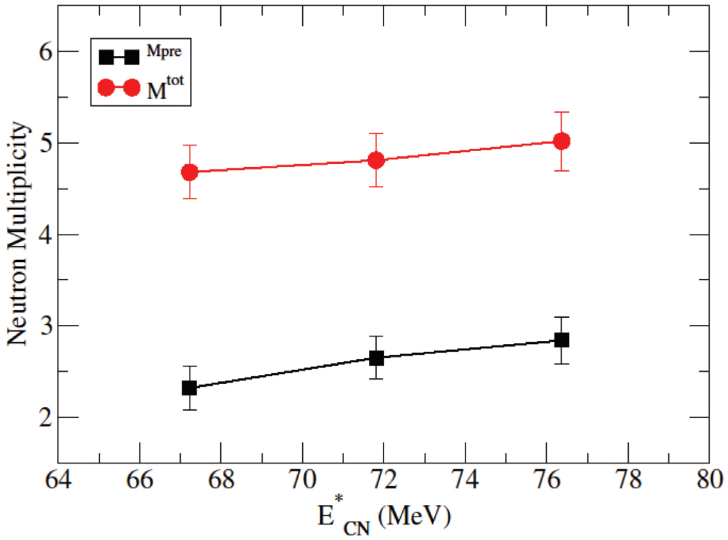

Fig. 5.1.11.2: Variation of the experimental values of pre-scission and total neutron multiplicity as a function of excitation energy for the reaction $^{18}O+^{184}W$.

REFERENCES:

[1] D. J. Hinde *et al.,* Phys. Rev. C **45,** 1229 (1992).
[2] Hardev Singh *et al.,* Phys. Rev. C **76,** 044610 (2007).
[3] V. Singh *et al.,* Phys. Rev. C **86,** 014609 (2012).
[4] Rohit Sandal *et al.,* Phys. Rev. C **87,** 014604 (2013).

5.1.12 Studying fusion in reactions forming medium heavy compound systems

A. C. Visakh[1], E. Prasad[1], S. Nath[2], N. Madhavan[2], J. Gehlot[2], Gonika[2], P. V. Laveen[1], M. Sharref[1], A. Shamlath[1], S. Sanila[3], Rohan Biswas[2], A. Parihari[2], A. M. Vinodkumar[3], B. R. S. Babu[3], K. M. Varrier[4] and S. Appannababu[5]

[1]Department of Physics, Central University of Kerala, Nileshwar 671314, India
[2]Inter-University Accelerator Centre, Aruna Asaf Ali Marg, New Delhi 110067, India
[3]Department of Physics, University of Calicut, Calicut 673635, India
[4]Department of Physics, University of Kerala, Thiruvananthapuram 695034, India
[5]Department of Nuclear Physics, Andhra University, Visakhapatnam 530003, India

Evaporation residue (ER) excitation function measurements for the reactions ^{16}O+^{142,150}Nd have been performed using the Heavy Ion Reaction Analyzer (HIRA) [1] at IUAC. The measurements were carried out in the beam energy range 54 - 104 MeV. Pulsed beam of ^{16}O with pulse separation of 4 μs was bombarded on isotopically enriched ^{142,150}Nd targets of thicknesses 140 μg/cm^2 and 162 μg/cm^2, respectively. The ERs were separated by the HIRA and were detected in the focal plane using a two-dimensional position-sensitive multi wire proportional counter (MWPC) with an active area of 150 mm × 50 mm. Two silicon surface barrier detectors were placed inside the target chamber to measure elastically scattered beam particles and to get absolute normalization of ER cross sections. A 30 μg/cm^2 thick carbon foil was placed 10 cm downstream from the target to reset the charge state of the ERs. The time interval between two successive pulses was slightly more than the time of flight (TOF) of ERs, from the reaction point to the focal plane of the HIRA. The ERs were selected from the two-dimensional spectrum of energy loss (ΔE) vs TOF.

The ER cross section was taken to be equal to the fusion cross section since the fission contribution in this energy region is negligible. The total ER cross section is given by

$$\sigma_{ER} = \frac{Y_{ER}}{Y_{mon}} \left(\frac{d\sigma}{d\Omega}\right)_{Ruth} \frac{\Omega_{mon}}{\epsilon_{HIRA}}$$

where, Y_{ER} and Y_{mon} are the yields of the ERs and Rutherford events respectively, $\left(\frac{d\sigma}{d\Omega}\right)_{Ruth}$ is the differential Rutherford scattering cross section in the laboratory frame, Ω_{mon} is the solid angle subtended by the monitor detector and ϵ_{HIRA} is the average transmission efficiency of the HIRA. ϵ_{HIRA} was calculated using the semi-microscopic Monte Carlo code, TERS [2, 3] for each xn-evaporation channel at all energies. The average ϵ_{HIRA} for all the ERs was obtained by taking the weighted average of the efficiency for different evaporation channels at each energy point. Relative abundance of different exit channels was estimated using the statistical model code PACE4 [4]. Preliminary ER excitation functions for the reactions studied are shown in Fig. 5.1.12.1 and Fig. 5.1.12.2. Detailed analysis is in progress.

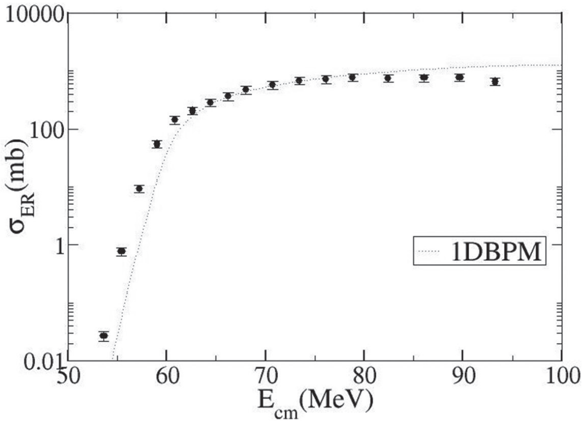

Fig. 5.1.12.1: Measured ER excitation function (preliminary) for ^{16}O+^{142}Nd.

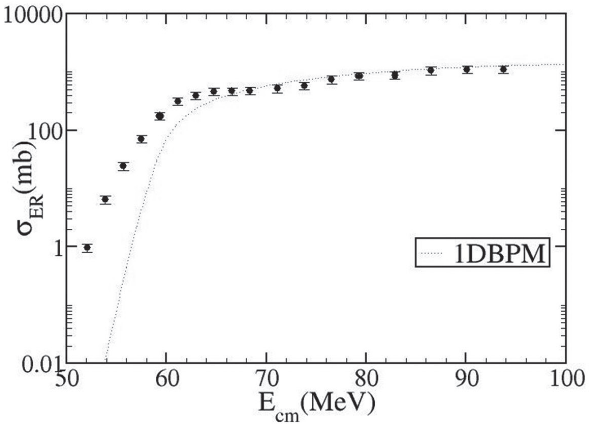

Fig. 5.1.12.2: Measured ER excitation function (preliminary) for ^{16}O+^{150}Nd.

REFERENCES:
[1] A. K. Sinha *et al.,* Nucl. Instrum. Methods A **339,** 543 (1994).
[2] S. Nath, Comput. Phys. Commun. **180,** 2392 (2009).
[3] S. Nath, Comput. Phys. Commun. **179,** 492 (2008).
[4] A. Gavron, Phys. Rev. C **21,** 230 (1980).

5.1.13 Revisiting the level structure of ^{103}Pd

A. Sharma[1], R. P. Singh[2], S. Muralithar[2], Indu Bala[2], S. S. Bhattacharjee[2], Ritika Garg[2], S. S. Tiwary[3], Neelam[4], S. Das[5], S. Samanta[5], S. S. Ghugre[5], Gurmeet Kumar[6], P. V. Madhusudhana Rao[7], R. Palit[8], S. K. Dhiman[1] and U. Garg[9]

[1]Department of Physics, Himachal Pradesh University, Shimla 171005, India
[2]Inter-University Accelerator Centre, Aruna Asaf Ali Marg, New Delhi 110067, India
[3]Department of Physics, Institute of Science, Banaras Hindu University, Varanasi 221005, India
[4]Department of Physics and Astrophysics, University of Delhi, New Delhi 110007, India
[5]UGC-DAE Consortium for Scientific Research, Kolkata Centre, Kolkata 700098, India
[6]J.C.D.A.V College Dasuya (PU), Punjab 144205, India
[7]Department of Nuclear Physics, Andhra University, Visakhapatnam 530003, India
[8]Department of Nuclear and Atomic Physics, Tata Institute of Fundamental Research, Mumbai 400005, India
[9]Department of Physics, University of Notre Dame, Notre Dame, Indiana 46556, USA

The level structure of A~100 nuclei reveals intriguing phenomena even at low and moderate spin regimes such as vibrations and rotations built upon prolate deformed states [1,2,3]. The underlying configurations present a favorable condition for the possible observation of wobbling, even at low spins [4]. The aforementioned features provided the necessary impetus for us to revisit the level structure of ^{103}Pd, especially at moderate angular momentum spins.

The ^{94}Zr(^{13}C, 4n) reaction at an incident energy ~55 MeV was employed to populate the high spin states in ^{103}Pd. The ^{94}Zr target was ~1 mg/cm^2 thick with ~10 mg/cm^2 gold backing. The de-exciting gamma transitions were detected using the Indian National Gamma Array (INGA) at IUAC. The detectors were placed at angles of 32°, 57°, 90°, 123° and 148° with respect to the beam direction. Data analysis was carried out using CANDLE, INGASORT and RADWARE. Different set of symmetric and angle dependent matrices were made to extract information of energy, intensity, parity and multi-polarity of coincident gamma transitions. Several new transitions were observed in coincidence with 477 keV gamma transition. These transitions have not been reported in previous work. The partial level scheme of ^{103}Pd developed from the present analysis is shown in Fig 5.1.13.1.

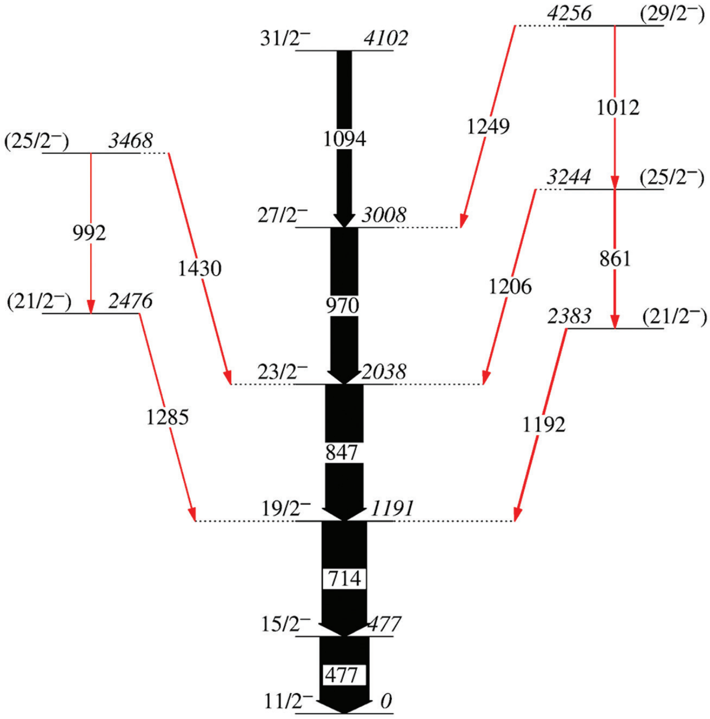

Fig. 5.1.13.1: Partial level scheme of ^{103}Pd.

REFERENCES:
[1] P. H. Regan *et al.,* J. Phys. G: Nucl. Part. Phys, **19**, L157 (1993).
[2] Dan Jerrestam *et al.,* Nucl. Phys. A**557,** 411c (1993).
[3] B. M. Nyako *et al.,* Phys. Rev. C **60,** 024307 (1999).
[4] J. T. Matta *et al.,* Phys. Rev. Lett. **114,** 082501 (2015).

5.1.14 γ-vibration in ^{124}Te

S. S. Tiwary[1], H. P. Sharma[1,*], S. Chakraborty[1], C. Majumder[1], S. Rai[2], Pragati[3], Mayank[4], S. S. Bhattacharjee[5], R. P. Singh[5], S. Muralithar[5], P. Banerjee[6], S. Ganguly[7], S. Kumar[8] and A. Kumar[9]

[1]Department of Physics, Institute of Science, Banaras Hindu University, Varanasi 221005, India
[2]Department of Physics, Visva-Bharati, Santiniketan 731235, India
[3]Department of Physics, Indian Institute of Technology Roorkee, Roorkee 247667, India
[4]Amity Institute of Nuclear Science and Technology, Amity University, Noida 201313, India
[5]Nuclear Physics Group, Inter-University Accelerator Centre, Aruna Asaf Ali Marg, New Delhi 110067, India
[6]Nuclear Physics Division, Saha Institute of Nuclear Physics, Kolkata 700064, India
[7]Department of Physics, Bethune College, Kolkata 700006, India

[8]Department of Physics and Astrophysics, University of Delhi, Delhi 110007, India
[9]Department of Physics, Panjab University, Chandigarh 160014, India

In A ~130 mass region, quasi–γ–bands were systematically reported in even-even Ba and Xe nuclei [1]. Previously, even-even Te-nuclei were considered as good examples of spherical vibrator [2], but recent studies on heavier Te-nuclei showed signatures of γ–soft behaviour [3-5]. Hence, the present work is dedicated to investigate the structural behavior of heavier Te-isotopes at low spin.

The in-beam study of ^{124}Te was carried out using ^{122}Sn(^{9}Be, α3n)^{124}Te fusion evaporation reaction at 48 MeV beam energy, obtained from the 15UD Pelletron [6,7] at IUAC. The INGA array [8] was used as the experimental setup for the present study. The array contained 14 Compton suppressed HPGe Clover detectors. The details of the experimental set-up and data analysis are discussed elsewhere [9].

Previously, the ground state band was reported up to $I = 16\hbar$ at 5481 keV excitation energy [10-12]. In the present work, levels up to 14ħ have been confirmed on the basis of γ-γ-coincidence relationship [Fig. 5.1.14.1]. The 2483, 3038, 3549 and 4240 keV levels have been newly established in the level scheme. On the basis of decay patterns and relative excitation energy with respect to corresponding ground state band these levels are predicted to be the members of one phonon quasi–γ–band. However, further investigations are underway.

The authors are thankful to the staff of the Target Development Laboratory and the Pelletron accelerator facility of IUAC. The authors acknowledge the INGA Collaboration supported by the University Grants Commission (UGC) and the Department of Science and Technology (DST) under INGA project (IR/S2/PF-03/2003-I). The first author is thankful to the UGC for financial support-vide contract no. 23/06/2013(I)EU-V.

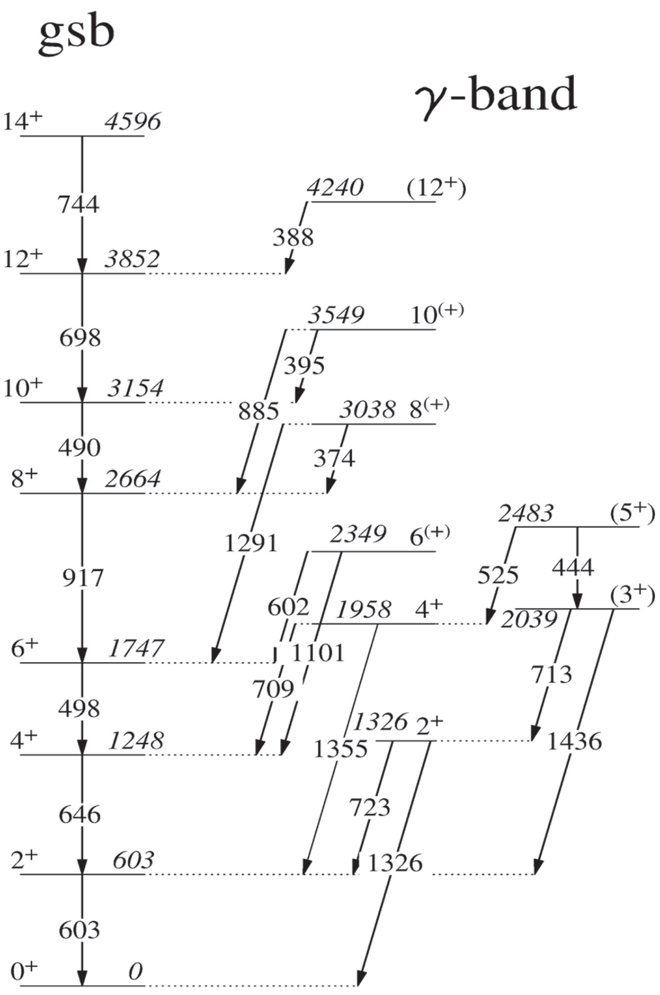

Fig. 5.1.14.1: Partial level scheme of ^{124}Te.

REFERENCES:
[1] H. Kusakari *et. al.,* Nucl. Phys. A**242,** 13 (1975).
[2] A. Kerek, Nucl. Phys. A**176,** 466 (1971).
[3] S. F. Hicks *et. al.,* Phys. Rev. C **95,** 034322 (2017).
[4] M. Saxena *et. al.,* Phys. Rev. C **90,** 024316 (2014).
[5] S. V. Jackson *et. al.,* Phys. Rev. C **15,** 1806 (1977).
[6] G. K. Mehta *et. al.,* Nucl. Instrum. Methods A **268,** 334 (1988).
[7] D. Kanjilal *et. al,* Nucl. Instrum. Methods A **328,** 97 (1993).
[8] S. Muralithar *et. al.,* Nucl. Instrum. Methods A **622,** 281 (2010).
[9] S. Chakraborty *et. al.,* Braz. J. Phys. **47,** 406 (2017).
[10] N. Warr *et. al.,* Nucl. Phys. A**636,** 379 (1998).
[11] N. Fotiades *et. al.,* Phys. Rev. C **89,** 017303 (2014).
[12] A. Astier *et. al.,* Eur. Phys. J. A **50,** 2 (2014).

5.1.15 Systematic study of low energy incomplete fusion reaction dynamics: Effect of target deformation

Suhail A. Tali[1], Harish Kumar[1], M. Afzal Ansari[1], Asif Ali[1], D. Singh[2], Rahbar Ali[3], Pankaj K. Giri[2], Sneha B. Linda[2], R. Kumar[4], Siddharth Parashari[1], R. P. Singh[4] and S. Muralithar[4]

[1]Department of Physics, Aligarh Muslim University, Aligarh 202002, India
[2]Centre for Applied Physics, Central University of Jharkhand, Ranchi 835205, India
[3]Department of Physics, G. F. (P. G.) College, Shahjhanpur 242001, India
[4]Inter-University Accelerator Centre, Aruna Asaf Ali Marg, New Delhi 110067, India

The study of heavy ion (HI) fusion reactions is of great interest for both theoretical and experimental nuclear physicists. In the energy region of ≈ 4-7 MeV/nucleon, the dominant reaction modes are complete fusion (CF) and incomplete fusion (ICF) reactions [1,2]. Many efforts are being made to comprehend the phenomenon of CF and ICF dynamics. The current interest is to understand the dependence of incomplete fusion on (a) incident projectile energy (b) projectile-target mass asymmetry (c) Coulomb effect (d) target deformation (e) projectile structure (Q_α-value) and to search some new entrance channel parameters on which ICF process may depend. Further the lack of proper theoretical model, which could reproduce the experimentally measured ICF reaction cross sections appropriately, is also a motivation for the present study [3,4]. Keeping the above points into consideration, the experiment was performed using ^{12}C (α-cluster) as the projectile and ^{165}Ho (deformed) as the target.

The experiment was performed at IUAC, New Delhi. The ^{165}Ho target foils and Al-catcher foils were prepared by using the rolling technique at the Target Development Laboratory of IUAC. The stacked foil activation technique was implemented, so as to cover a wide range of energy within limited beam time. Stacks consisting of target foils and backed by Al-foils were irradiated by the ^{12}C ion beam to cover energy above the Coulomb barrier and up to 87.4 MeV in the General Purpose Scattering Chamber (GPSC). After the irradiation, the target-catcher assembly was dismantled immediately from the GPSC and the γ-ray activities built-up in the foils were recorded by keeping them in front of a pre-calibrated High Purity Germanium (HPGe) detector. The HPGe detector was coupled to a PC through CAMAC based data acquisition system CANDLE.

When the incident projectile interacts with the target nucleus, the compound nucleus formed via CF and/or ICF process is in the highly excited state and de-excites via emission of light nuclear particles and their characteristic gamma rays. In the present work, the EFs of several ERs populated via xn, pxn, αxn, αpxn and 2αxn were measured. The experimentally measured cross sections were compared with the statistical model code PACE4, which gives only the CF cross sections. During the analysis, it was observed that the experimentally measured independent cross sections of the ERs populated via emission of xn and pxn channels were in good agreement with the PACE4 predictions with level density parameter a= $\frac{A}{10}$, MeV^{-1}, which shows that these ERs are populated via CF process. However, in case of αxn, αpxn and 2αxn emission channels, the experimentally measured independent cross sections show a significant enhancement from the PACE4 predictions with the same level density parameter a= $\frac{A}{10}$, which is attributed to the ICF process. The ICF fraction, which is defined as strength of ICF relative to total fusion i.e., FICF (%) = $\left(\frac{\sigma_{ICF}}{\sigma_{TF}}\right)\times 100$ (where $\sigma_{\rm TF} = \sigma_{\rm CF} + \sigma_{\rm ICF}$), was obtained from data. In order to understand the dependence of ICF on target deformation β_2, the FICF(%) deduced for the present system ^{12}C+^{165}Ho is plotted in Fig. 5.1.15.1 along with the earlier studied systems at constant relative velocity ($V_{\rm rel}$ = 0.053c) for various projectile-target combinations. It may be seen from Fig. 5.1.15.1, that $F_{\rm ICF}$(%) increases with increasing value of target deformation. But the increments are different for reactions induced by ^{12}C (α-clustered) and ^{13}C (non α-clustered) projectiles with the same target. However, a regular trend is not observed. An attempt has also been made to explore the dependence of ICF dynamics on the parameter $\mu Z_P Z_T$ (1-β_2) (a combination of entrance channel parameters), where μ is the mass asymmetry, $Z_P Z_T$ is the Coulomb effect and β_2 is the target deformation. $F_{\rm ICF}$(%) is plotted against μZ_P Z_T (1-β_2) in Fig. 5.1.15.2. It is important to mention that the systems and their symbols are the same as in Fig. 5.1.15.1. From this graph, it is clear that $F_{\rm ICF}$(%) increases almost linearly. But $F_{\rm ICF}$(%) is more for ^{12}C induced reactions compared to ^{13}C induced reactions with the same target. This difference may be explained on the basis of projectile Q_α value, which is simply defined as the amount of energy required to liberate an α-particle from the incident projectile. As the projectile Q_α value for ^{12}C (-7.37 MeV) is less compared to ^{13}C (-10.65 MeV), the reactions involving ^{12}C as the projectile shows more $F_{\rm ICF}$(%) compared to the reactions induced by ^{13}C. Moreover, the value of ICF fraction for both ^{12,13}C+^{159}Tb is less and is away from the linear trend, this is probably due to the less mass asymmetry of these systems compared to others.

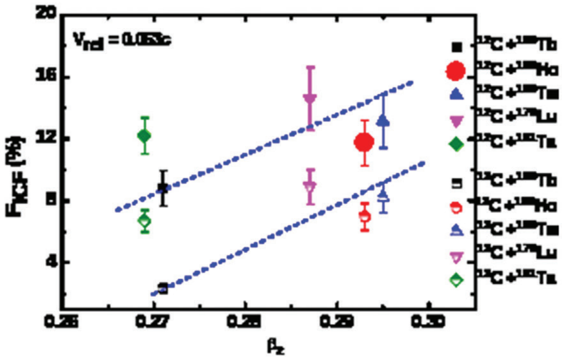

Fig. 5.1.15.1: The deduced ICF fraction F_{ICF}(%) as a function of target deformation (β2) at constant relative velocity (V_{rel} = 0.053c), for 12,13C projectile induced reactions with different targets. The dotted lines are just to guide the eyes.

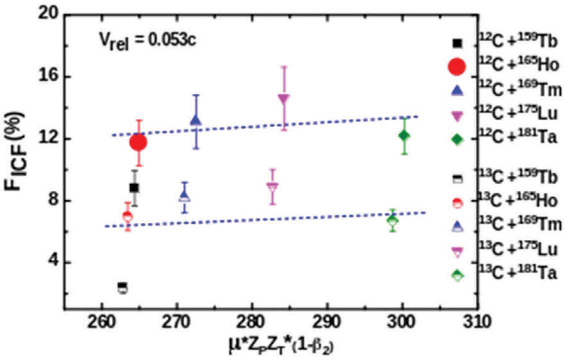

Fig. 5.1.15.2: The deduced ICF fraction FICF(%) as a function of $\mu_Z PZ_T$ $(1-\beta_2)$ at constant relative velocity (V_{rel} = 0.053c), for $^{12,13}C$ projectile induced reactions with different targets. The dotted lines are just to guide the eyes.

REFERENCES:

[1] Suhail A. Tali *et al.,* Nucl. Phys. A**970,** 208 (2018).
[2] Harish Kumar *et al.,* Phys. Rev. C **99,** 034610 (2019).
[3] Harish Kumar *et al.,* Nucl. Phys. A**960,** 53 (2017).
[4] A. Yadav *et al.,* Phys. Rev. C **96 ,** 044614 (2017).

5.1.16 Quasi-elastic scattering measurements in ^{28}Si + ^{142,150}Nd systems

S. Biswas[1,2], A. Chakraborty[1], P. Sugathan[3], A. Jhingan[3], D. Arora[3], B. R. Behera[4], R. Biswas[3], N. K. Deb[5], S. S. Ghugre[6], P. K. Giri[7], K. S. Golda[3], G. Kaur[3], A. Kumar[8], M. Kumar[3], B. Mukherjee[1], B. K. Nayak[9], A. Parihari[3], N. K. Rai[8], S. Rai[10], R. Raut[6], R. N. Sahu[11] and A. K. Sinha[12]

[1]Department of Physics, Siksha Bhavana, Visva-Bharati, Santiniketan 731235, India
[2]Department of Physics, Murshidabad College of Engineering and Technology, Berhampore 742102, India
[3]Inter-University Accelerator Centre, Aruna Asaf Ali Marg, New Delhi 110067, India
[4]Department of Physics, Panjab University, Chandigarh 160014, India
[5]Department of Physics, Gauhati University, Guwahati 781013, India
[6]UGC-DAE Consortium for Scientific Research, Kolkata Center, Sector III/LB-8, Bidhan Nagar, Kolkata 700098, India
[7]Department of Physics, Central University of Jharkhand, Ranchi 835205, India
[8]Department of Physics, Banaras Hindu University, Varanasi 221005, India
[9]Nuclear Physics Division, Bhabha Atomic Research Centre, Mumbai 400085, India
[10]Department of Physics, Salesian College, Siliguri 734001, India
[11]Department of Physics, Indian Institute of Technology Ropar, Punjab 140001, India
[12]UGC - DAE Consortium for Scientific Research, Indore 452017, India

An experiment was carried out for measurement of excitation functions and barrier distributions in ^{28}Si+^{142,150}Nd systems. The main motivation for this measurement was to study the effect of deformation of the target and projectile on the corresponding barrier distribution. The experiment was carried out in the General Purpose Scattering Chamber (GPSC) facility using ^{28}Si beam from the 15UD Pelletron at IUAC. The incident beam energy was varied from 84 to 136 MeV. The targets were ^{142}Nd and ^{150}Nd of thickness~150 μg/cm^2 with carbon capping and backing. The beam-like particles were detected at the back angles using an array of hybrid telescope detectors. A representative plot of the excitation function for ^{28}Si+^{150}Nd at 160° angle is shown in Fig. 5.1.16.1. Detailed analysis of the collected data is under progress.

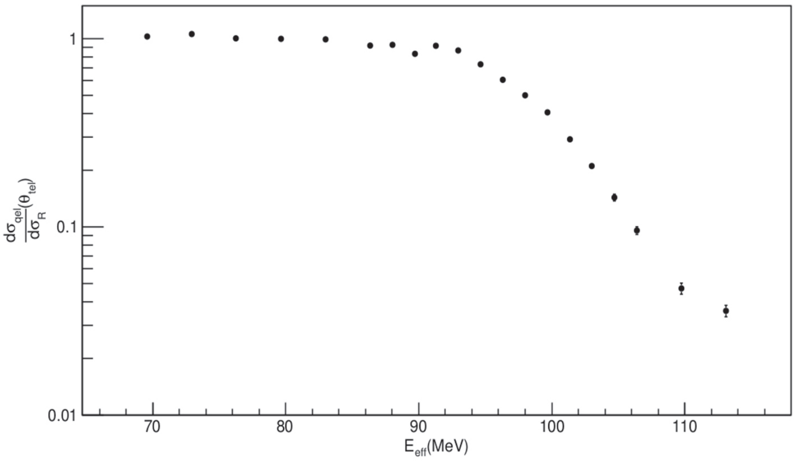

Fig. 5.1.16.1: Excitation function for ^{28}Si+^{150}Nd at 160°.

5.1.17 Nuclear structure study around doubly magic ^{56}Ni-core

Saradindu Samanta[1], Soumya Das[1], Suvronil Chatterjee[1], Sajad Ali[2], Sutanu Bhattacharya[3], Shashi Shekhar Tiwary[4], Kaushik Katre[5], Anupriya Sharma[6], Rajarshi Raut[1], Sandeep S. Ghugre[1], A. K. Sinha[7], R. P. Singh[5], S. Muralithar[5] and Umesh Garg[8]

[1]UGC-DAE Consortium for Scientific Research, Kolkata Centre, Kolkata 700098, India
[2]Saha Institute of Nuclear Physics, Sector 1, AF Block, Bidhannagar 700064, Kolkata, India
[3]Guru Ghasidas Viswavidyalaya, Bilaspur 495009, Chhattisgarh, India
[4]Department of Physics, Banaras Hindu University, Varanasi 221005, Uttar Pradesh, India
[5]Inter-University Accelerator Centre, Aruna Asaf Ali Marg, New Delhi 110067, India
[6]Department of Physics, Himachal Pradesh University, Shimla 171005, Himachal Pradesh, India
[7]UGC-DAE Consortium for scientific Research, University Campus, Khandwa Road, Indore 452017, India
[8]Department of Physics, University of Notre Dame, Notre Dame, Indiana 46556, USA

Nuclei around the doubly magic nucleus ^{56}Ni are excellent candidates for the study of competition between collective and single-particle excitations. At low spins, the properties of the A~60 nuclei are governed by the particle occupancy in the $1f_{5/2,}$ $2p_{3/2,}$ and $2p_{1/2}$ orbitals. At higher excitations the possibility of deformation, and consequent observation of rotational sequences, emerges due to the occupancy of deformation driving high-j $g_{9/2}$ orbital. This structural evolution from single particle nature in the lower excitation regime to band like structure at higher excited states makes these nuclei subjects of interest. At still higher energies there is precedence of observation of core-broken states from excitations of the ^{56}Ni-core. [1]

The Nuclear Physics Group at the Kolkata Centre has embarked on a systematic investigation of the structure of these nuclei in the vicinity of the Ni-core. One of the experiments under this programme was carried out previously at the Pelletron LINAC Facility in TIFR wherein nuclei such as ^{64}Cu (Z=29, N=35) [2] and ^{61}Ni (Z=28, N=33) [3] have been investigated following their population in ^{59}Co(^{7}Li, xnyp) reaction. These studies established excitations in the fpg model space for these nuclei. However no evidence of collectivity or core broken configurations could be observed therefrom. The quest for the same has recently been pursued with heavier projectile at IUAC. The nuclei of interest are slightly more massive ones, albeit in the same region around the Ni-core. These are ^{66}Zn (Z=30, N=36), ^{66,69}Ga (Z=31, N=35, 38), ^{69}Ge (Z=32, N=37) populated through ^{59}Co(^{13}C, xnypzα) reaction at E_{lab} = 45 - 50 MeV. The INGA, stationed at IUAC and consisting of 16 Compton suppressed clover detectors was used as the detection system. A 5.2 mg/cm^2 thick ^{59}Co (on a 4 mg/cm^2 Ta backing) foil was used as the target therein. Fig. 5.1.17.1 depicts the partial projection spectrum constructed from acquired data, which is indicative of the various nuclei populated in the present experiment. These have been observed up to excitations ~ 5 MeV and 10 ħ. Further analysis is currently in progress.

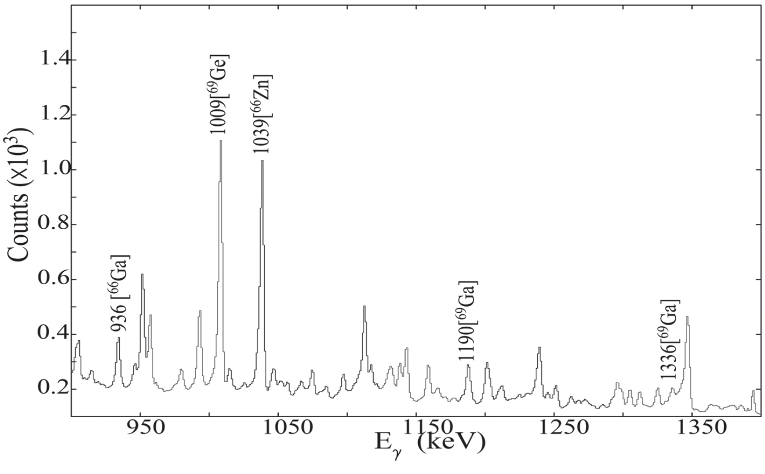

Fig. 5.1.17.1: Different nuclei populated in the present experiment.

REFERENCES:

[1] D. A. Torres *et. al.,* Phys. Rev. C **78,** 054318 (2008).
[2] S. Samanta *et. al.,* Phys. Rev. C **97,** 014319 (2018).
[3] S. Samanta *et. al.,* Phys. Rev. C **99,** 014315 (2019).

5.1.18 Level scheme of ^{127}Xe

S. Chakraborty[1], H. P. Sharma[1], S. S. Tiwary[1], C. Majumder[1], S. Rai[2], Pragati[3], Mayank[4], S. S. Bhattacharjee[5], R. P. Singh[5], S. Muralithar[5], P. Banerjee[6], S. Ganguly[7], S. Kumar[8], A. Kumar[9] and R. Palit[10]

[1]Department of Physics, Institute of Science, Banaras Hindu University, Varanasi 221005, India
[2]Department of Physics, Visva-Bharati, Santiniketan 731235, India
[3]Department of Physics, Indian Institute of Technology Roorkee, Roorkee 247667, India
[4]Amity Institute of Nuclear Science and Technology, Amity University, Noida 201313, India

[5]Nuclear Physics Group, Inter-University Accelerator Centre, Aruna Asaf Ali Marg, New Delhi 110067, India
[6]Nuclear Physics Division, Saha Institute of Nuclear Physics, Bidhannagar 700064, Kolkata, India
[7]Department of Physics, Bethune College, Kolkata 700006, India
[8]Department of Physics and Astrophysics, University of Delhi, Delhi 110007, India
[9]Department of Physics, Panjab University, Chandigarh 160014, India
[10]Department of Nuclear and Atomic Physics, Tata Institute of Fundamental Research, Mumbai 400005, India

The low lying structure of odd-A Xe nuclei in A~125 mainly consists of both positive and negative parity rotational bands based on $s_{1/2,}$ $d_{3/2,}$ $d_{5/2,}$ $g_{7/2}$ and $h_{11/2}$ neutron orbitals, lying near the Fermi surface [1,2]. Among these, the negative parity h11/2 band was reported with the highest intensity and angular momentum. In case of positive parity bands, the population of $g_{7/2}$ band was found significant than others. However, the experimental information on this band in ^{127}Xe is very scanty. In particular, the unfavoured signature partner of this band was reported tentatively up to I^π = ≤17/2$^+$ [1], whereas in lighter Xe nuclei, this band was reported up to ~25/2$^+$. This report presents a detail γ-ray spectroscopic study on $\nu g_{7/2}$ band in ^{127}Xe.

Energetic ^{9}Be beam of 48 MeV, obtained from the 15UD Pelletron accelerator of IUAC, was bombarded on a 8.4 mg/cm^2 thick 99.3% isotopically enriched ^{122}Sn foil to populate the high spin states of ^{127}Xe. 14 Compton suppressed Clover detectors of INGA were used to collect the coincident γ-rays. Offline data analysis was carried out using INGAsort and RadWare computer codes. Details of the experimental set up and data analysis are available in Refs. [3, 4].

From the present experiment, alignment of two $h_{11/2}$ neutrons was reported at higher spin in negative parity band [3]. Placement of previously reported two states at 2307 keV was revised [5, 6]. A rotational band above a three quasi-neutron high-K isomer was also established with a revised half-life of the isomer [4]. A positive parity band, based on I^π = 7/2$^+$ state at 342 keV ($\tau_{1/2}$=36 ns) was reported up to I^π = 19/2$^+$ [2]. In the present work, this band has been extended up to I^π = (23/2$^+$) by placing a 895 keV γ-transition, as shown in Fig. 5.1.18.1. The signature partner of this band, reported up to I^π = (17/2$^+$), has also been extended up to I^π = (25/2$^+$) state by placing two new γ-rays of 794 and 883 keV (Fig. 5.1.18.1). New placements are supported by the observation of the coincident γ-rays of this band in 773 and 733 energy gated spectra (Fig. 5.1.18.2). Spin and parity of several states have been assigned from present angular correlation and linear polarization measurements. Further study is underway.

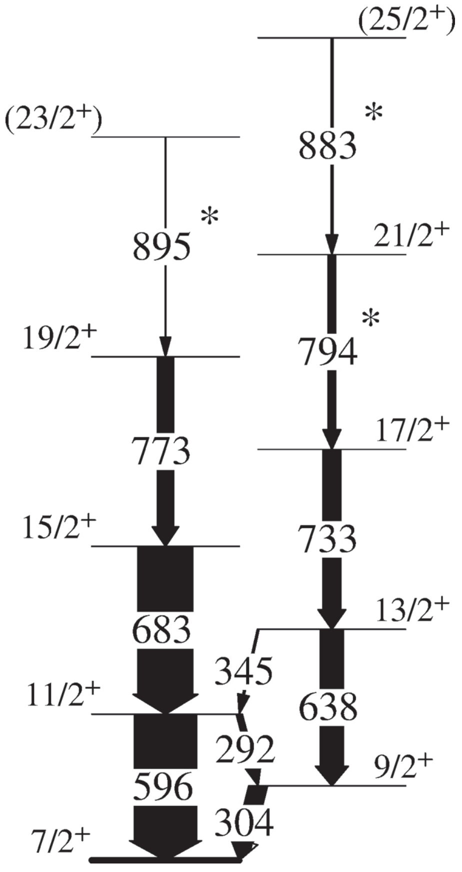

Fig. 5.1.18.1: Partial level scheme of ^{127}Xe.

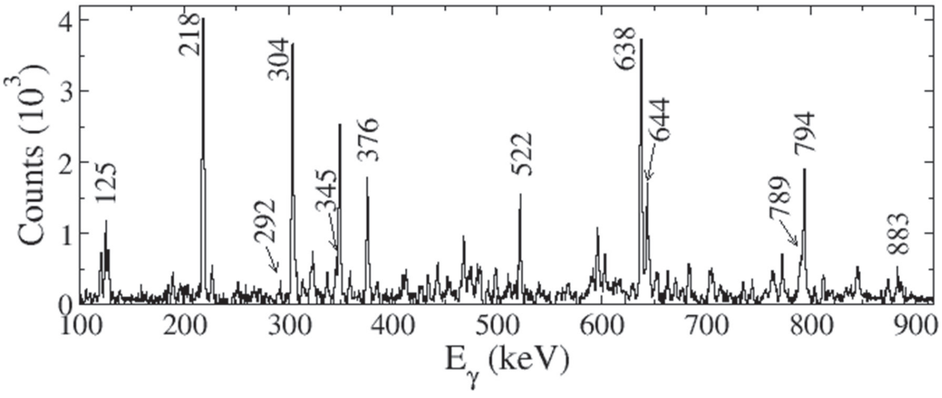

Fig.5.1.18.2: Coincidence energy gated spectrum of 733 keV.

The authors are thankful to the staff of the Target Development Laboratory and the Pelletron accelerator facility of IUAC. The INGA collaboration is duly acknowledged. The first author is also thankful to the CSIR for SRF, under file no. 9/13(662)/2017-EMR-I.

REFERENCES:
[1] W. Urban *et al.,* Z. Phys. A **320,** 327 (1985).
[2] S. Chakraborty *et al.,* Phys. Rev. C **97,** 054311 (2018).
[3] S. Chakraborty *et al.,* Braz. J. Phys. **47,** 406 (2017).
[4] S. Chakraborty *et al.,* Phys. Scr. **93,** 115302 (2018).
[5] S. Chakraborty *et al.,* Eur. Phys. Lett. **121,** 42001 (2018).
[6] I. Wiedenhöver *et al.,* Z. Phys. A **347,** 71 (1993).

5.1.19 Probing of incomplete fusion dynamics of ^{16}O interaction with ^{148}Nd

Pankaj K. Giri[1], Amritraj Mahato[1], D. Singh[1], Sneha B. Linda[1], Harish Kumar[2], Suhail A. Tali[2], Rahbar Ali[3], N. P. M. Sathik[4], M. Afzal Ansari[2], R. Kumar[5], S. Muralithar[5] and R. P. Singh[5]

[1]Department of Physics, Central University of Jharkhand, Ranchi 835205, India
[2]Department of Physics, Aligarh Muslim University, Aligarh 202002, India
[3]Department of Physics, G.F. (P.G.) College, Shahjahanpur 242001, India
[4]Department of Physics, Jamal Mohammed College, Tiruchirappalli 620020, India
[5]Inter-University Accelerator Centre, Aruna Asaf Ali Marg, New Delhi 110067, India

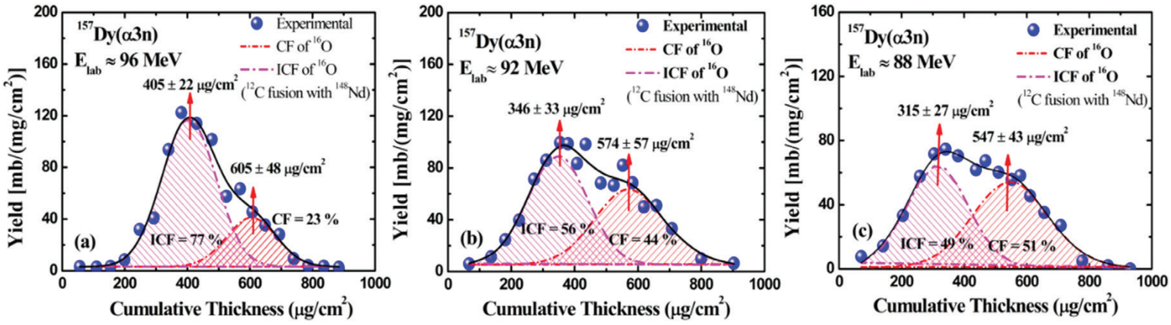

Fig. 5.1.19.1: Measured FRRDs of ER ^{157}Dy(α3n) populated in the interaction of ^{16}O with ^{148}Nd at energies ≈96, ≈92, and ≈ 88 MeV. Solid circles and dashed dotted curves represents, the measured data and Gaussian fit, respectively.

A series of offline gamma spectroscopy experiments were performed for the measurements of excitation functions (EFs) and forward recoil range distributions (FRRDs) of evaporation residues (ERs) using ^{16}O beam with ^{148}Nd target to explore the incomplete fusion (ICF) dynamics at Pelletron energy ≈ 3-7 MeV/A. Experiments were performed using the 15 UD Pelletron facility at IUAC. The enriched ^{148}Nd targets of thickness ≈ 200-700 μg/cm^2 were fabricated using high vacuum evaporation facility at the Target Development Laboratory of IUAC. The General Purpose Scattering Chamber (GPSC) was utilized for the irradiation of targets. The GPSC chamber has in vacuum target transfer facility. The irradiated stacks were taken out from the scattering chamber after buildup of sufficient activities. The ERs trapped in aluminum catcher foils were recorded by two pre-calibrated 100 cm^3 High Purity Germanium (HPGe) detectors coupled with PC through CAMAC based data acquisition system. The energy and efficiency calibration of HPGe detectors were done using standard ^{152}Eu source of known strength. The collection and analysis of data has been done by software CANDLE [1]. The detected ERs have been identified by their characteristics γ-rays and decay-curve analysis.

In the present work, FRRDs of ERs ^{159,158}Er(xn), ^{160,159}Ho(pxn), ^{157,155}Dy(αxn) and ^{155}Tb(αpxn) have been measured. The relative contributions of various ERs produced via complete fusion (CF) and/or ICF processes have been computed by fitting the measured FRRDs data using the software ORIGIN [2]. The theoretical recoil ranges have been computed using SRIM-2008 [3]. Measured FRRDs of ERs have been compared with their theoretical mean ranges. As a representative case, FRRDs of ER ^{157}Dy(α3n) at three different energies have been displayed in Fig. 5.1.19.1. From this figure, it can be seen clearly that the measured FRRDs of ER ^{157}Dy shows two peaks. The peak at larger cumulative thickness is associated with CF, while the second peak at shorter thickness can be referred to ICF of ^{16}O with ^{148}Nd. On the other hand, the peaks associated with CF and ICF channels shifted to higher cumulative thickness due to the larger momentum transfer at higher projectile energy. These FRRD results show that full and partial linear momentum transfer components are involved. It means that the ERs populated through α-emission channels are not only produced via CF, but also through ICF dynamics. The ICF fraction (F_{ICF}) has also been estimated from EFs and FRRDs and displayed in Fig. 5.1.19.2. It can be seen from this figure that the values of F_{ICF} for these measurements are in good agreement. Moreover, it can also be noticed from Fig. 5.1.19.2, that the ICF contribution increases with projectile energy. This increase in ICF contribution is due to the increase of breakup probability of projectile ^{16}O into ^{12}C and α with projectile energy.

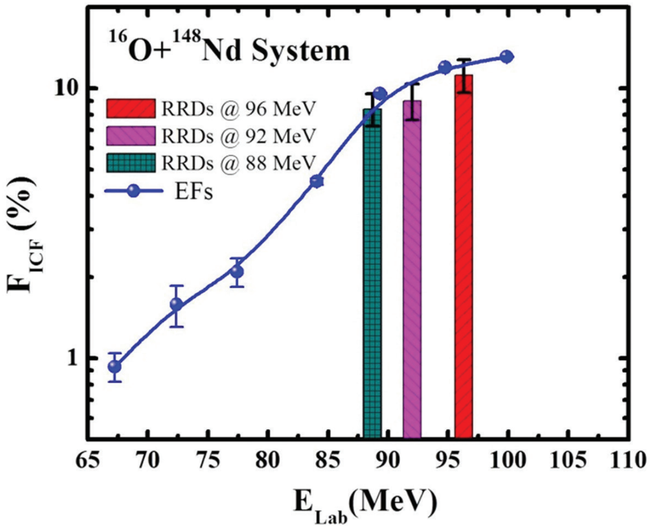

Fig. 5.1.19.2: The incomplete fusion fraction (F_{ICF}) as a function of projectile energy in the interaction of ^{16}O with ^{148}Nd.

REFERENCES:

[1] B. P. Ajith Kumar, E. T. Subramaniam, K. Singh and R. K. Bhowmik, DAE-BRNS Symp. Nucl. Phys., Kolkata, (2001); URL http://www.iuac.res.in/NIAS/.
[2] ORIGIN (OriginLab, Northampton, MA); URL http://www.originlab.com/.
[3] The Stopping and Range of Ions in Matter (SRIM-2008.04); URL: https://www.srim.org.

5.1.20 Study of transitional nuclei near N = 82 shell closure using in-beam gamma-ray spectroscopy

Neelam[1], Suresh Kumar[1], K. Rojeeta Devi[1], Anuj[1], Neeraj Kumar[1], Kajol Chakraborty[1], Anjali Rani[1], Unnati[1], S. Verma[1], S. K. Mandal[1], Madhu[2], Khamosh Yadav[2], Bharti Bhoy[2], Anil Kumar[2], Ajay Y. Deo[2], Praveen C. Srivastava[2], S. S. Tiwari[3], H. P. Sharma[3], A. Sharma[4], S. K. Dhiman[4], S. Bhatacharya[5], T. Trivedi[5], Kaushik Katre[6], Yashraj[6], Indu Bala[6], R. P. Singh[6] and S. Muralithar[6]

[1]Department of Physics and Astrophysics, University of Delhi, Delhi 110007, India
[2]Department of Physics, Indian Institute of Technology Roorkee, Roorkee 247667, India
[3]Department of Physics, Banaras Hindu University, Varanasi 221005 , India
[4]Department of Physics, Himachal Pradesh University, Shimla 171005 , India
[5]Department of Pure and Applied Physics, Guru Ghasidas University, Bilaspur 495009, India
[6]Inter-University Accelerator Center, Aruna Asaf Ali Marg, New Delhi 110067, India

The transitional nuclei in the A = 135 mass region lies near the N = 82 shell closure and are known to have γ-soft character. Many interesting high-spin phenomena such as magnetic rotation (MR), shape coexistence, chirality and bands based on the multi-quasiparticle excitations are reported in these nuclei [1-3]. In addition, the yrast 10+ isomeric states based on the $\nu[h_{11/2}]^{-2}$ configuration were also observed in the N =78 and 80 isotones [4, 5]. In the previous studies of the ^{136}Ba nucleus (N = 80) the yrast band has been studied up to spin $I^{\pi} = 10^{(+)}$ ħ and two isomeric states at spin $I^{\pi} = 10^{(+)}$ ħ and $7^{(-)}$ ħ were observed [6, 7]. Similar isomeric states were also observed in the ^{132}Xe nucleus (N = 78) at spin $I^{\pi} = (10^{+})$ ħ, $7^{(-)}$ ħ and $5^{(-)}$ ħ based on $\nu[h_{11/2}]^{-2}$, $\pi[h_{11/2}, d_{3/2}]$ and $\pi[h_{11/2}, s_{1/2}]$ configuration, respectively [8]. The structure of the ^{132}Xe nucleus has been studied up to $I^{\pi} = (16^{+})$ ħ [9].

In the present work, the excited states of ^{136}Ba and ^{132}Xe nuclei were populated using the ^{130}Te(^{9}Be, xn) reaction at 36 and 48 MeV beam energy, respectively. The ^{9}Be beam was provided by the 15UD Pelletron accelerator at IUAC. The ^{130}Te target had a thickness of 1.2 mg/cm^2 with 4.2 mg/cm^2 gold backing. The de-exciting gamma-ray transitions were detected using the Indian National Gamma Array (INGA) [10] consisting of 15 Clover detectors with 4, 2, 5, 1 and 3 detectors placed at 148º, 123º, 90º, 57º and 32º with respect to the beam direction, respectively. The list mode data was acquired using the CANDLE software. The offline data were sorted using the CANDLE and analysed using the RadWare software packages [11].

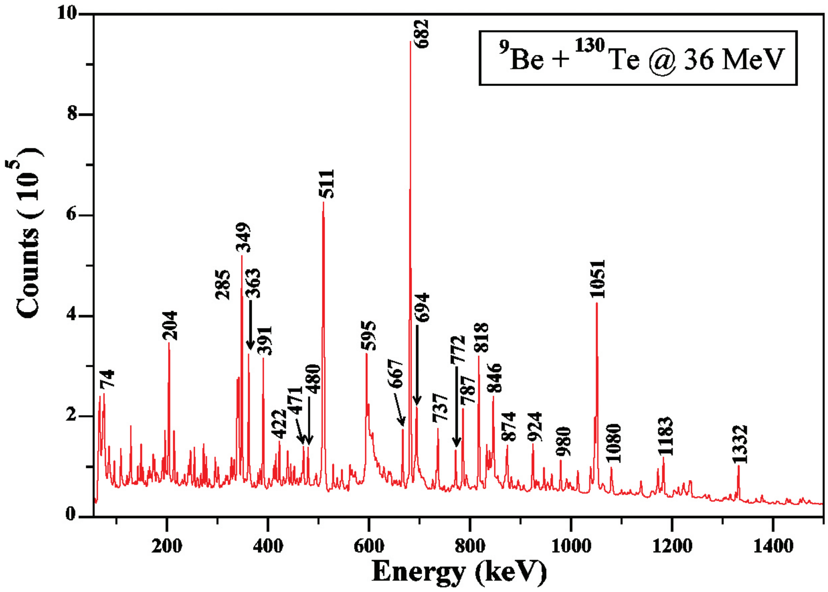

Fig. 5.1.20.1: The projection spectrum obtained in the ^{130}Te(^{9}Be, 3n) reaction at 36 MeV beam energy.

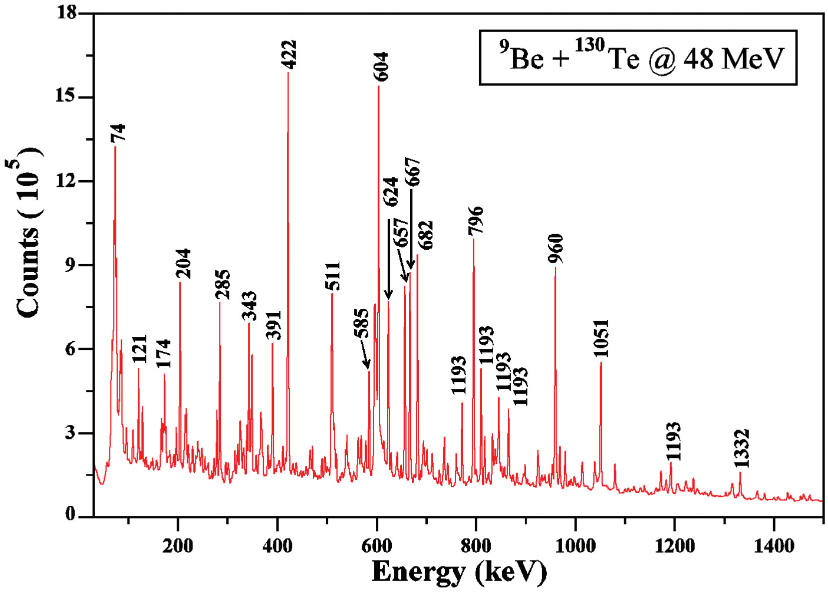

Fig. 5.1.20.2: The projection spectrum obtained in the ^{130}Te(^{9}Be, α3n) reaction at 48 MeV beam energy.

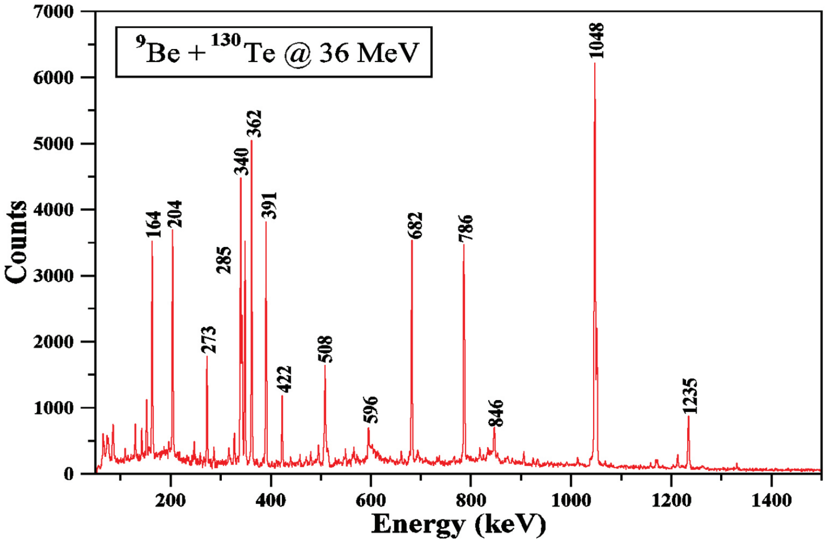

Fig. 5.1.20.3: The coincidence spectrum of the 818 keV gamma-ray transition of the ^{136}Ba nuclei obtained in the ^{130}Te(^{9}Be, 3n) reaction at 36 MeV reaction.

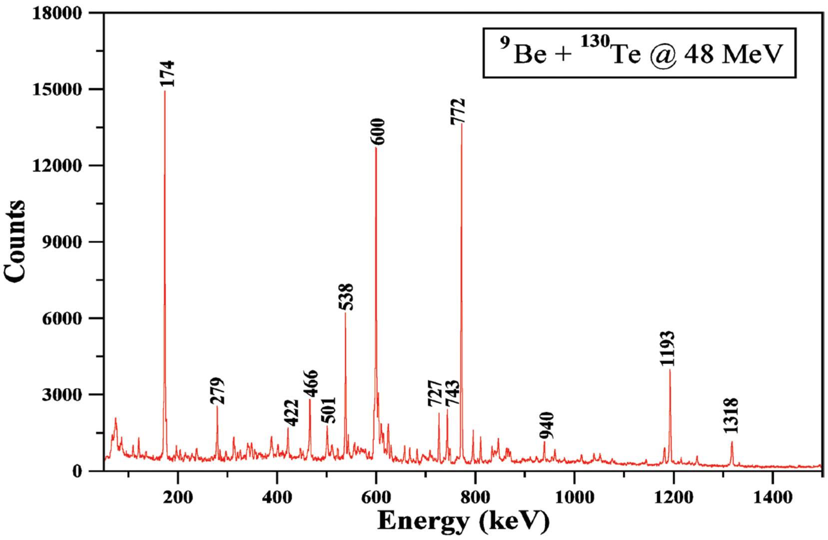

Fig. 5.1.20.4: The gated spectrum of 667 keV gamma-ray transition represents the gamma-ray transitions of the ^{132}Xe nucleus from the analysis of ^{130}Te(^{9}Be, α3n) reaction at 48 MeV beam energy.

After calibration and gain matching, the symmetric and anti-symmetric matrices were generated. The projection spectrum of the ^{130}Te(^{9}Be, xn) reaction obtained at 36 and 48 MeV beam energy are shown in Fig. 5.1.20.1 and 5.1.20.2, respectively. Fig. 5.1.20.3 and 5.1.20.4 represents the gamma-ray transitions of the ^{136}Ba and ^{132}Xe nuclei, in the gate of the 818 and 667 keV gamma-ray transitions, respectively. The previously observed gamma-ray transitions of the ^{136}Ba and ^{132}Xe nuclei were verified. The R_{DCO} and Polarization asymmetry measurements of the newly identified gamma-ray transitions are in progress.

One of the authors (Neelam), would like to acknowledge the financial assistance received from the University Grant Commission (UGC), New Delhi, via IUAC project (UFR – 51320, 62337). The financial support from the Department of Science and Technology (DST), India for the INGA project (No. IR/S2/PF-03/2003-I) is gratefully acknowledged. The supports provided by the Pelletron group, the Target Development Laboratory and the INGA group of IUAC are also gratefully acknowledged.

REFERENCES:

[1] E. S. Paul *et al.,* Phys. Rev. C **40,** 1255 (1989).
[2] S. Lakshmi *et al.,* Phys. Rev. C **69,** 014319 (2004).
[3] C. M. Petrache *et al.,* Phys. Rev. C **86,** 044321 (2012).
[4] T. Morek *et al.,* Z. Phys. A **298,** 267 (1980).
[5] J. C. Merdinger *et al.,* Nucl. Phys. A**346,** 281 (1980).
[6] J. J. Valiente-Dobón *et al.,* Phys. Rev. C **69,** 024316 (2004).
[7] T. Shizuma *et al.,* Eur. Phys. J. A **20,** 207 (2004).
[8] A. Kerek *et al.,* Nucl. Phys. A**172,** 603 (1971).
[9] A. Vogt *et al.,* Phys. Rev. C **96,** 024321 (2017).
[10] S. Muralithar *et al.,* Nucl. Instrum. Methods A **622,** 281 (2010).
[11] D. C. Radford, Nucl. Instrum. Methods. A **361,** 297 (1995).

5.1.21 Measurement of fusion excitation functions for ^{16,18}O+^{116}Sn,^{61,62}Ni

Nabendu K. Deb[1], K. Kalita[1], H. Rashid[1], S. Nath[2], N. Madhavan[2], J. Gehlot[2], Rohan Biswas[2], A. Jhingan[2], T. Varughese[2], Pankaj K. Giri[3], A. Mahato[3], R. N. Sahoo[4], N. K.Rai[5], A. Parihari[2], S. Biswas[6], B. J. Roy[7] and A. Rani[8]

[1]Department of Physics, Gauhati University, Guwahati 781014, Assam, India
[2]Nuclear Physics Group, Inter-University Accelerator Centre, Aruna Asaf Ali Marg, New Delhi 110067, India
[3]Department of Applied Physics, Central University of Jharkhand, Ranchi 835205, Jharkhand, India
[4]Department of Physics, Indian Institute of Technology Ropar, Ropar 140001, Punjab, India
[5]Department of Physics, Banaras Hindu University, Varanasi 221005, Uttar Pradesh, India
[6]Department of Physics, Visva-Bharati, Shantiniketan 731235, West Bengal, India
[7]Nuclear Physics Division, Bhabha Atomic Research Centre, Trombay 400085, Mumbai, India
[8]Department of Physics and Astrophysics, University of Delhi, Delhi 110007, India

Nuclear fusion cross section around the Coulomb barrier, reveals varieties of phenomena. One such phenomenon is the additional enhancement of the sub-barrier fusion cross sections as compared to the theoretical predictions of one dimensional barrier penetration model (1D-BPM) [1]. Such enhancement occurs due to the coupling of relative motion to internal degrees of freedom of the colliding nuclei such as deformation [2], vibration [3] and nuclear transfer channels [4] or neck formation [5]. It was observed that nuclear transfer with positive Q-values leads to fusion cross section enhancement [6]. However, the relationship between fusion enhancement in the sub-barrier region and positive Q-value neutron transfer (PQNT) is unclear [7]. Study of transfer reactions provides useful information on pairing correlation and its effect on fusion reaction mechanism. Therefore, in order to probe the PQNT effect on the sub barrier fusion cross section enhancement, experiments were performed with systems ^{18}O+^{61,62}Ni and ^{18}O+^{116}Sn, around the Coulomb barrier, using the Heavy Ion Reaction Analyzer (HIRA) at IUAC [8]. All these systems favour neutron transfer due to positive Q-values for two neutron stripping. Also ^{16}O+^{61}Ni system was studied to investigate the enhancement in the sub-barrier region with respect to the 1D-BPM.

The experiments were performed using Pelletron beams of IUAC. Pulsed beams of ^{16,18}O with a pulse separation of 4 μs was used in the experiment to bombard isotopically enriched ^{61}Ni, ^{62}Ni, and ^{116}Sn targets of thickness 110 μg/cm^2, 150 μg/cm^2 [9] and 150 μg/cm^2, respectively, on thin carbon backing of 30 μg/cm^2. The fusion excitation function measurements were performed at laboratory beam energies of 34 - 53 MeV at 1 MeV for the systems with Ni targets and 54 – 84 MeV at 1 MeV steps for the systems with Sn target. Two silicon surface barrier detectors were mounted inside the target chamber at ±15.5° with respect to beam direction to measure Rutherford-scattered beam-like particles and to get absolute normalization of Evaporation Residue (ER) cross sections. A 30 μg/cm^2 carbon foil was placed downstream of the target for re-equilibration of ER charge states. At the focal plane of the HIRA, a two-dimensional position-sensitive MWPC detector with an active area of 150 mm × 50 mm was used to detect ERs. Time of flight was defined for particles reaching the focal plane with respect to RF of beam to separate multiple-scattered beam-like particles and ERs. The solid angle of acceptance for HIRA was kept 10 mSr for the measurements. A raw spectrum of data taken for ^{18}O+^{116}Sn is shown in the left panel of Fig. 5.1.21.1, with the energy loss (ΔE) along x-axis and the corresponding time of flight (TOF) along y-axis. All other systems displayed the similar characteristics. From the spectrum, the beam-like particles are very well separated from the ERs. The ER cross section was taken to be equal to the total fusion cross section as the fission contribution in this energy region is negligible. The transmission efficiency of HIRA was calculated by using the semi-microscopic Monte Carlo code, TERS [10] for each xn-evaporation channel at all Elab. The relative abundance of different exit channels were estimated using the statistical model code PACE4 [11].

Preliminary result of the fusion excitation functions for ^{18}O+^{116}Sn system is plotted in the right panel of Fig. 5.1.21.1. It is compared with the similar work done by Tripathi et al. [3] for the system ^{16}O+^{116}Sn. The present system was found to exhibit more enhancements in the sub-barrier region which could be due to the PQNT effect. Further analysis is in progress for this system and even for the other systems. The coupled-channels calculations will be performed with a modified version of CCFULL [12] and FRESCO [13].

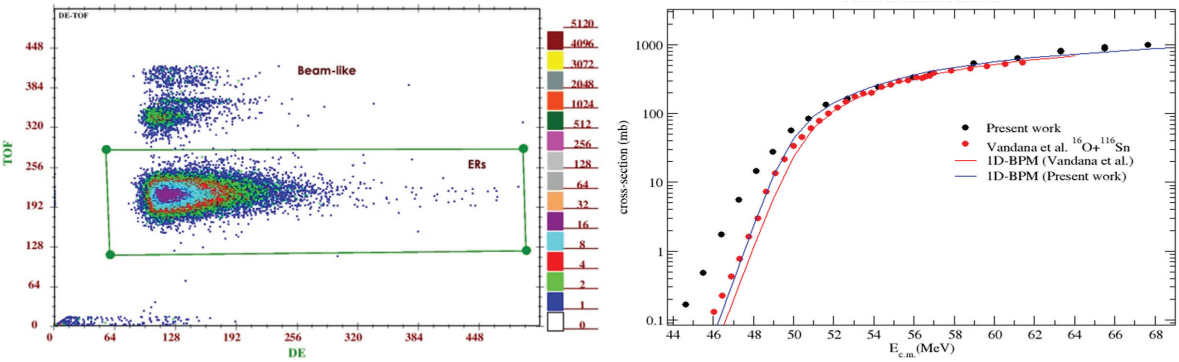

Fig. 5.1.21.1: (left) ΔE versus TOF spectrum at Elab = 66 MeV for ^{18}O+^{116}Sn and (right) the fusion excitation functions for ^{16,18}O+^{116}Sn.

REFERENCES:

[1] M. Dasgupta *et al.,* Ann. Rev. Nucl. Part. Sci. **48,** 401 (1998).
[2] J. R. Leigh *et al.,* Phys. Rev. C **52,** 3151 (1995).
[3] Vandana Tripathi *et al.,* Phys. Rev. C **65,** 014614 (2001).
[4] V. I. Zagrabaev, Phys. Rev. C **67,** 061601 (2003).
[5] C. E. Aguiar, L. F. Canto and R. Donangelo, Phys., Rev. C **31,** 1969 (1985).
[6] A. M. Stefanini *et al.,* Phys. Rev. C **73,** 034606 (2006).
[7] Z. Kohley *et al.,* Phys. Rev. Lett. **107,** 202701 (2011).
[8] A. K. Sinha *et al.,* Nucl. Instrum. Methods A **339,** 543 (1994).
[9] N. K. Deb *et al.,* Vacuum **163,** 148 (2019).
[10] S. Nath, Comput. Phys. Commun. **179,** 492 (2008); 180, 2392 (2009).
[11] A. Gavron, Phys. Rev. C **21,** 230 (1980).

[12] K. Hagino, N. Rowley and A. T. Kruppa, Comput. Phys. Commun. **123,** 143 (1999).
[13] I. J. Thompson, Comp. Phy. Rep. **7,** 167 (1988).

5.1.22 Study of fusion phenomena in ^{37}Cl+^{68}Zn reaction around and above barrier: A route for production of Pd radionuclides

A. Chauhan[1], R. Prajapat[1], R. Kumar[1], Malvika[1], G. Sarkar[1], M. Maiti[1], Gonika[2], J. Gehlot[2], N. Madhavan[2], S. Nath[2] and A. Parihari[2]

[1]Department of Physics, Indian Institute of Technology Roorkee, Roorkee 247667, India
[2]Inter-University Accelerator Centre, Aruna Asaf Ali Marg, New Delhi 110067, India

There is a great interest in understanding the heavy ion reaction dynamics around and above the barriers energies. The enhancement in fusion cross-sections has been observed compared to 1D-BPM in the sub-barrier region that could be understood based on the different internal degrees of freedom like different inelastic couplings and deformations, etc. [1-2]. However, the explanation for such observation in the sub-barrier region for more symmetric systems is multifarious. On the other hand, the product evaporation residues (ERs) may find different applications in the field of medicine. Considering the suitable physicochemical properties of palladium isotopes for such applications, many light-ion (p, d, ^{3,4}He) induced reactions have been reported to synthesize them [3-5]. However, heavy ion reaction data are scare. In this quest, fusion phenomena have been explored for the ^{37}Cl+^{68}Zn reaction over a wide energy range and the production cross-sections of ^{101}Pd, ^{101}Ag, ^{100}Pd, and ^{100}Ag radionuclides have been measured.

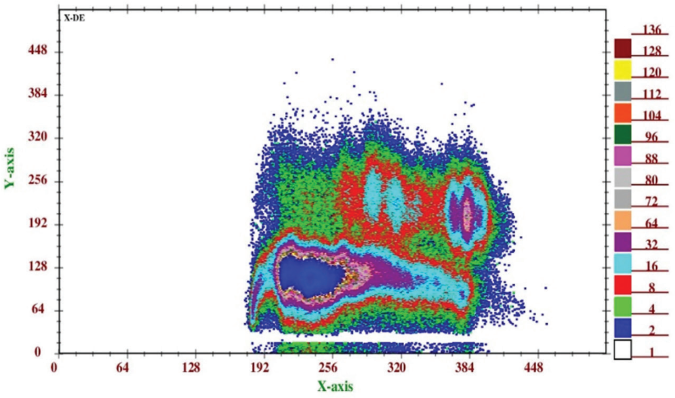

Fig. 5.1.22.1: A 2D spectrum of the energy loss (ΔE) of the product residues vs X-position at the MWPC at E_{lab} = 135 MeV. ERs with different m/q ratios and beam like particles are well separated from each other.

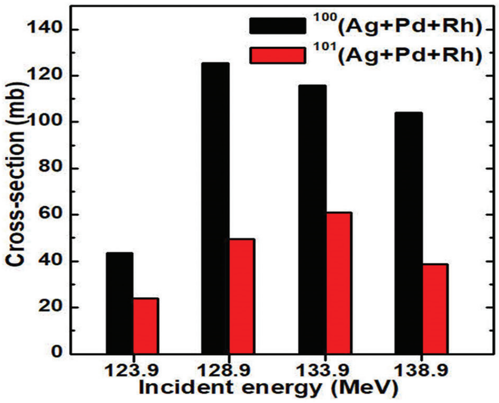

Fig. 5.1.22.2: Experimental cross-sections of ^{101,100}(Ag+Pd+Rh) at different values of $E_{lab.}$

The experiment was performed using the Heavy Ion Reaction Analyzer (HIRA) facility of IUAC. A pulsed ^{37}Cl beam was bombarded on ^{68}Zn in steps of 2 MeV in the range of E_{lab} = 96 - 100 MeV, and in steps of 5 MeV in the range of E_{lab} = 100 - 140 MeV. Evaporation residues were identified from the background events using a Multi-Wire Proportional Counter (MWPC) placed at the focal plane of HIRA. The ΔE vs TOF (time-of-flight) and X-ΔE spectra were recorded during the experiment. Fig. 5.1.22.1 shows an X-ΔE spectrum at E_{lab} = 135 MeV. The fusion cross-sections for ^{37}Cl+^{68}Zn were measured and compared with the CCFULL predictions. The fusion excitation function was found to be significantly higher than the predictions from the 1D-BPM below the barrier while the cross-sections were reproduced well in the above barrier region. The sub-barrier fusion enhancement was explained by the inclusion of inelastic couplings in the projectile as well as the target. We also measured the total cross-sections of mass 100 and 101 fractions populated through the ^{37}Cl+^{68}Zn reaction and found that the sum of all the residues is equal to the total fusion cross-section for a particular energy. In Fig. 5.1.22.2, the production cross-sections of ^{101,100}(Ag+Pd+Rh) are reported which shows that the ER cross-section is maximum around 128.9 MeV for mass-100, and 133.9 MeV for mass-101. This study would help to optimize the production parameters for palladium-100,101 radionuclides and to maximize the yield as short-lived ^{100,101}Ag decays to relatively long-lived ^{100,101}Pd.

REFERENCES:

[1] E. Martinez-Quiroz *et al.,* Phys. Rev. C **63,** 054611 (2001).
[2] S. Kalkal *et al.,* Phys. Rev. C **81,** 044610 (2010).
[3] A. Hermanne *et al.,* Nucl. Instrum. Methods B **170,** 281 (2000).
[4] S. Sudar *et al.,* Appl. Radiat. Isotopes **56,** 821 (2002).
[5] M. S. Uddin *et al,* Appl. Radiat. Isotopes **62,** 533 (2005).

5.1.23 Deciphering the low energy incomplete fusion reactions using the recoil range distribution technique

Mohd. Shuaib[1], Ishfaq Majeed[1], Manoj Kumar Sharma[2], Abhishek Yadav[3], Vijay R. Sharma[4], Arshiya Sood[5], Rudra N. Sahoo[5], Malika Kaushik[5], Pushpendra P. Singh[5], Unnati[6], Devendra P. Singh[7], S. Muralithar[8], R. P. Singh[8], R. Kumar[8], B. P. Singh[1], and R. Prasad[1]

[1]Nuclear Physics Laboratory, Department of Physics, Aligarh Muslim University, Aligarh 202002, India
[2]Physics Department, S. V. College, Aligarh 202001, India
[3]Department of Physics, Faculty of Natural Sciences, Jamia Millia Islamia, New Delhi 110025, India
[4]Departamento de Aceleradores, Instituto Nacional de Investigaciones Nucleares, Apartado postal 18-1027, C.P. 11801, Ciudad de Mexico, Mexico
[5]Department of Physics, Indian Institute of Technology Ropar, Ropar, Punjab 140001, India
[6]Department of Physics and Astrophysics, Delhi University, Delhi 110007, India
[7]Department of Physics, University of Petroleum and Energy Studies, Dehradun 248 007, India
[8]Nuclear Physics Group, Inter-University Accelerator Centre, Aruna Asaf Ali Marg, New Delhi 110067, India

In the present work, the relative contributions of complete fusion (CF) and incomplete fusion (ICF) reactions has been studied by measuring the forward recoil range distribution (FRRD) of reaction residues using the non α-cluster beam ^{19}F bombarded on ^{169}Tm target. It may be remarked that, most of the studies of ICF reactions have been carried out using the α-cluster beams like ^{12}C, ^{16}O, ^{20}Ne etc . However, the studies using the non α-cluster beams are still limited. Therefore, for better understanding of the effect of projectile structure on ICF, it is required to extend these investigations by including the non α-cluster beams on different targets covering the periodic table. The present work is in continuation of our recent investigation on ^{19}F+^{169}Tm system [1], where measured excitation functions (EFs) have been used to understand the break-up fusion processes. The experiments have been performed at IUAC. The recoil-catcher activation technique involving off-line γ-ray spectroscopy has been employed. The CF and ICF events have been tagged by full and partial linear momentum transfer components, respectively. In forward recoil range distributions (FRRDs), nine radio-nuclides viz., ^{184}Pt (4n), ^{185}Pt (5n), ^{184}Ir (p3n), ^{185}Ir (p4n), ^{183}Os (αn), ^{181}Os (α3n), ^{179}Os (α5n), ^{177}W (2α3n), and ^{175}Ta (2αp4n) have been measured at two distinct energies ≈ 96 and 106 MeV. In the case of xn/pxn channels, only a single peak in the recoil range distribution has been observed that corresponds to the entire linear momentum transfer from projectile to the target nucleus i.e., these channels are populated via CF process. However, for α-emitting channels, the RRDs are deconvoluted into more than one Gaussian peak. The peak at the higher cumulative depth indicates the contribution due to complete LMT (complete fusion) from projectile to the target nucleus. However, the peak at lower cumulative depth corresponds to the fusion of ^{15}N (if ^{19}F breaks up into ^{15}N+α and ^{15}N fuses) with ^{169}Tm target nucleus and strongly reveals the presence of partial linear momentum component associated with the ICF processes. The experimentally measured recoil ranges of xn/pxn and αxn/2αxn/2αpxn channels obtained from the RRD data are compared with those obtained from the SRIM [2] calculations and found to be in reasonably good agreement at both the energies. As a representative case the measured ranges of ^{177}W(2α3n) residues populated via CF/ICF processes (Fig. 5.1.23.1) are compared with SRIM calculations and found to agree well at both the energies. The analysis of presently measured RRDs clearly indicates the incomplete fusion of ^{19}F projectile at energies ≈ 4-6 MeV/nucleon. Hence, on the basis of results obtained from the analysis of RRD data, it may be concluded that, the non α-cluster beam (19F) also gives a significant contribution of ICF reactions at low energies.

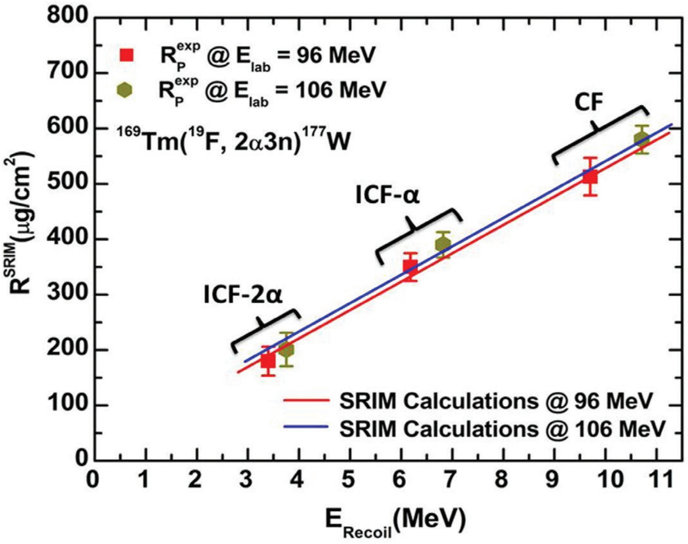

Fig. 5.1.23.1: A comparison of most probable mean ranges obtained from RRD of ^{177}W(2α3n) residues with SRIM calculations.

REFERENCES:

[1] Mohd. Shuiab, *et al.,* J. Phys. Rev. G: Nucl. Part. Phys. **44,** 105108 (2017).
[2] The Stopping and Range of Ions in Matter (SRIM-2008.04); http://www.srim.org/

5.2 MATERIALS SCIENCE

Ambuj Tripathi

The materials science facilities continue to support research programmes of a large number of users from different universities and institutions. This year there were a total of 63 user experiments spread over 202 shifts and were performed without any major beam time loss due to facility break down in materials sciences in beamhall I and II. These included 18 BTA runs spread over 53 shifts associated with students' Ph.D. programmes. Though the swift heavy ion (SHI) irradiation and related experiments mostly utilize irradiation chamber in the materials science beamlines in beamhall-I, 5 experiments of 23 shifts requiring low fluence irradiation were performed in GPSC beamline. Besides irradiation facilities, materials science group is also providing many materials synthesis and characterization facilities such as XRD, AFM, SEM, Raman, UV-Vis, I-V, Hall measurement etc and these are heavily utilized by users. Typically more than 2100 samples were characterized each year.

The materials science research programmes are being carried out in a wide range of energies varying from tens of keV to hundreds of MeV. This year there were many interesting results in the various areas of research including those on ion beams induced nanostructuring, synthesis of nanocomposites and applications, novel phase formations, etc.. Special emphasis is given to in-situ/ on-line measurements and many such experiments were performed this year. In-situ Investigation of 140 MeV Cu^{11+} and 160 MeV Br^{12+} ions induced damages in the NPN transistors showed that emitter-base (E-B) depletion region of the transistor can be effectively analyzed using Gummel characteristics. The intense energetic ions encountered in space can result in many transient and destructive single event effects (SEE) are studied with low ion fluence ($\sim 10^6$ cm^{-2}) test facility at GPSC beam line and three such runs took place this year to evaluate the radiation hardness of many microelectronic devices designed and fabricated at SCL. In-situ I-V and C-V characterization studies were carried out to determine the device quality of atomic layer deposited HfO_2/SiO_2/Si-based metal oxide semiconductor devices during 120 MeV Ag ion irradiation. An increase in the oxide layer thickness due to formation of an HfSiO interlayer was observed and attributed to swift heavy ion induced intermixing, and was confirmed by X-TEM and X-ray photoelectron spectroscopy measurements. In situ X-ray diffraction measurements showed an increase in the crystallinity of the Graphene Oxide film at low fluence after irradiation with 120 MeV Au ions at fluences ranging from 10^{10} to 10^{13} ions/cm^2. The irradiated samples showed an increase in the intensity of aromatic carbon bonds by Fourier transform infrared spectroscopy which indicated the maximization of graphitic regions for lower fluences up to 3×10^{11} ions/cm^2. In-situ current-voltage (I-V) studies on Cu-ZnO/P3OT hybrid heterostructures under 80 MeV O ion irradiations was also studied. The interaction of Graphene oxide with hydrogen gas at different pressures varying from 70 mbar to 900 mbar at room temperature using in-situ Xray diffraction technique was studied. Elastic recoil detection analysis (ERDA) technique was employed to determine the concentration of hydrogen in GO film which increased from $\sim 1.7\text{x}10^{22}$ atoms/cc (for pristine GO) to $\sim 9.5\text{x}10^{22}$ atoms/cc after exposing to 100% hydrogen environment at 900 mbar pressure, thus showing its applicability as hydrogen storage device. In situ current–voltage characteristics of Nb-doped TiO_2/p-Si-based heterojunction diode have been studied under dense electronic excitations of 84 MeV Si^{6+} ions. The diode parameters such as ideality factor, barrier height, reverse saturation current and series resistance were found to be a strong function of ion irradiation fluence. Such in situ studies on n-NTO/p-Si heterojunction diode under harsh radiation environment are very appropriate for the better understanding of heterojunction interface properties and make it suitable for use in aerospace industry and nuclear reactors. The defect induced photoluminescence studies on behavior of the Ga doped ZnO (GZO) thin films with varying doping (Ga) concentration and with energetic ion irradiation showed that violet emission might originate from zinc interstitial defects (Zni) and the concentration of Zni increases with increasing doping concentration. Electronic excitation induced modifications in the ferroelectric polarization of $BiFeO_3$ thin films have also been observed.

Apart from the studies on swift heavy ion irradiation, a large number users have published their work related to effects of low energy ion implantations and gamma irradiations in various physical properties of materials. The effect of Ni ion implantations in thermoelectric and electrical properties of $CoSb_3$ and the interface formation and magnetic properties due to 3d transition metal ion implantations have been studied. Enhancement of ferromagnetism due to ion implantations has been investigated in CeO_2, ZnO and FePt. Apart from these studies, work on solar energy, medical dosimetry, gas sensing and chemical sensing have been reported. Enhanced room temperature ferromagnetism and green photoluminescence with increase in doping in Cu doped ZnO thin film synthesised by neutral beam sputtering was observed. It was shown that synthesised Cu doped ZnO thin films can be used as spin LEDs and switchable spin-laser diodes. Investigations using gamma irradiation have demonstrated the enhancement of water oxidization catalytic performance in graphene oxide, multifunctionality in the same materials etc.

The International Conference on Ion Beams in materials Engineering and Characterization (IBMEC 2018) was organized by IUAC during October 9th to 12th, 2018. There were 21 invited talks (including 10 from foreigners), 15 oral presentations and 70 posters. The conference was preceded by a School on Characterization of Materials at IUAC during October 3-7, 2018 which included 5 lectures from foreigners. Another school on special topic of Ion Beams in Energy Materials was also organized by IUAC during July 12-18, 2018.

5.2.1 In situ Study of Radiation Stability and Associated Conduction Mechanisms of Nb-Doped TiO_2/p-Si Heterojunction Diode under Swift Heavy Ion Irradiation

Subodh K. Gautam[1], Jitendra Singh[1], R.G. Singh[2], Naina Gautam[3], Priyanka Trivedi[1], and Fouran Singh[1]

[1]Material Science Group, Inter University Accelerator Centre, New Delhi -110067, India
[2]Department of Physics, Bhagini Nivedita College, Delhi University, Delhi– 110043, India.
[3]Department of Electronic Science, University of Delhi South Campus, New Delhi-110023, India

The reliability of semiconductor devices in extreme environments, particularly in radiation-harsh conditions, is an important issue for applications in space, nuclear reactors, particle accelerators and military equipment [1, 2]. It is difficult to generalize whether irradiation environment causes degradation or improvement in the performance of the various types of devices. It depends on many parameters such as target material, projectile ion energy, and fluence, etc. This study reports the radiation stability and reliability of fabricated Nb-doped TiO_2 over p-Si based heterojunction diode along with the effect of secondary irradiation on various diode parameters and current conduction mechanisms. In situ current-voltage characteristics of Nb-doped TiO_2/p-Si heterojunction diode have been studied under dense electronic excitations of 84-MeV Si^{6+} ions using the 15UD Tandem Pelletron Accelerator at IUAC, New Delhi. Fig. (a) shows the schematic diagram of fabricated heterojunction diode operating under the exposure of 84-MeV Si^{6+} ion irradiation. The diode parameters such as ideality factor (η), barrier height (ϕ_B), reverse saturation current (J_s), and series resistance (R_s) are found to be a strong function of ion irradiation fluence. In Fig. (b), results show that important diode parameters such as ideality factor decrease with fluence, while barrier height shows an anomalous behaviour as first increases and then decreases as function of fluence. Similarly, J_s follows the inverse response of ϕ_B as first decreases and then increases as function of fluence. These observed unusual phenomena are understood mainly by an improvement in barrier inhomogeneity, irradiation induced-annealing of interface states. Generally, R_s plays an important current-limiting role in heterojunction based devices. It is found that R_s decreases with increasing irradiation fluence and follows a similar response as η with irradiation fluence. The improvements in η and R_s with irradiation is explained in terms of irradiation induced-structural ordering and creation of high density donor defects (oxygen vacancies (V_O) and Ti interstitials (Ti_i) and their defect complexes) induced enchantment in n-type conductivity of n-NTO later [3]. Furthermore, various current conduction mechanisms involved at different voltage ranges are discussed as a function of fluence with the help of constructed energy band diagram shown in Fig (c). It is found that trap-assisted space charge limited current conduction mechanism dominates at high voltage range and transforms to traps-free SCLC conduction at high irradiation fluence [4]. Thus, significant improvement in the diode parameters and high radiation stability makes it suitable for applications in the aerospace industry, nuclear reactors and accelerators. For details, see [Subodh K. Gautam et al. IEEE-Transactions on Electron Devices, 66 (2019) 1475].

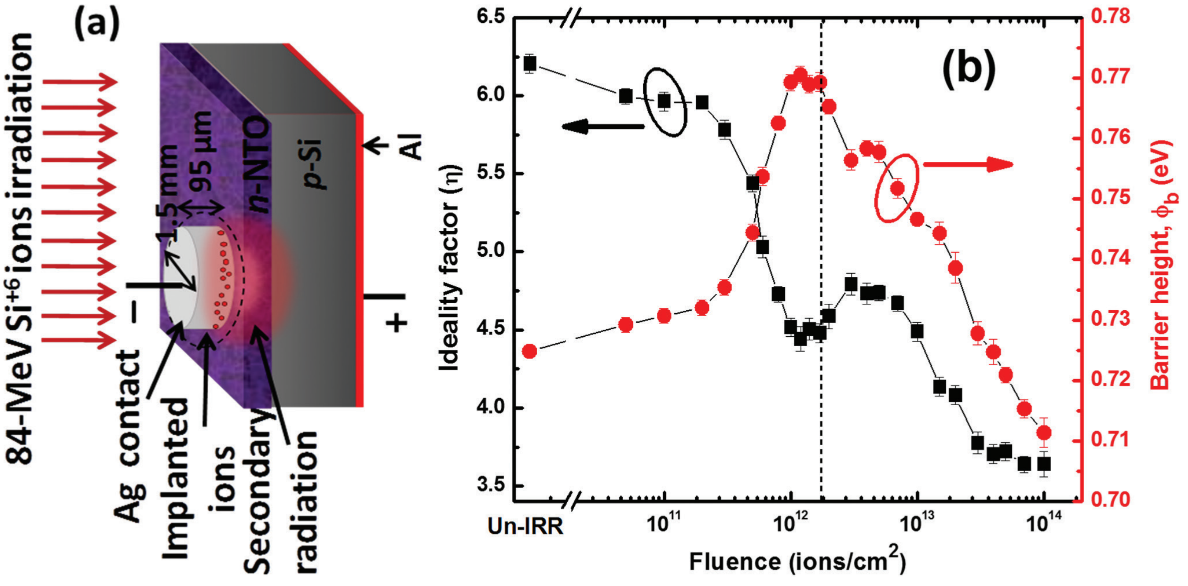

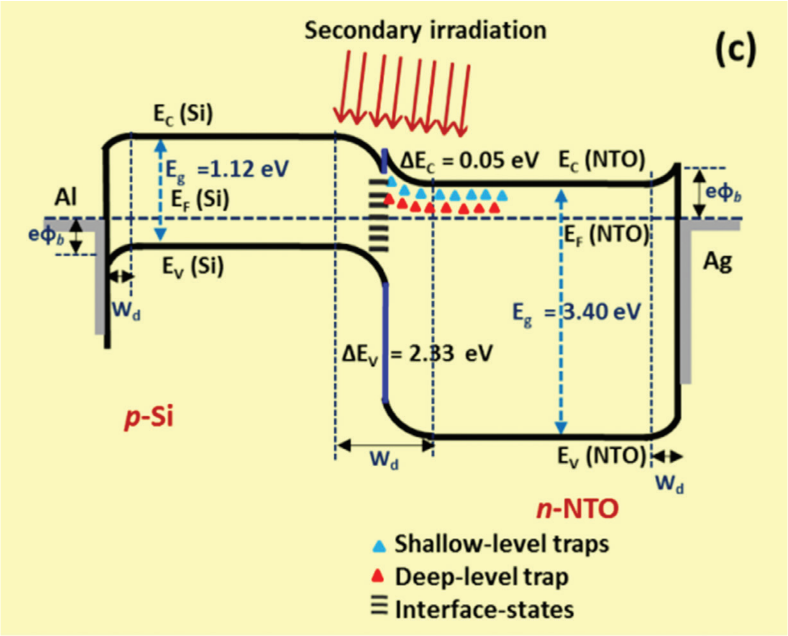

Figure: (a) Schematic diagram of fabricated heterojunction diode operating under the exposure of ion irradiation,
(b) *In situ* response of ideality factor and barrier height as a function of fluence, and
(c) energy-band diagram of irradiated n-NTO/p-Si heterojunction diode in equilibrium condition under the exposure of Si ions irradiation.

REFERENCES:
[1] C. Claeys *et al,* Radiation Effects in Advanced Semiconductor Materials and Devices, vol. **57,** Springer (2002)
[2] P. E. Dodd *et al.,* IEEE Trans. Nucl. Sci., **57** (2010) 1747
[3] Subodh K. Gautam *et al.* SSC **218** (2015) 20
[4] P. E. De Jongh *et al,* Phys. Rev. Lett., **77** (1996) 342

5.2.2 An In-situ Investigation of Bromine and Copper Ion Irradiation on NPN Transistors

T M Pradeep[1], N H Vinayakaprasanna[1], N Pushpa[2], Ambuj Tripathi[3] and A P Gnana Prakash[1*]

[1]Department of Studies in Physics, University of Mysore, Manasagangotri, Mysore-570 006, India.
[2]Department of PG Studies in Physics, JSS College, Ooty Road, Mysore-570 025, India.
[3]Inter University Accelerator Centre, Aruna Asaf Ali Marg, New Delhi-110 067, India.

The advancements in the semiconductor processing techniques have made it possible to use semiconductor devices in the instrumentations of deep space exploration spacecrafts and high energy physics experiments. However, devices operating in these applications are prone to radiation effects wherein a high density of high energy deterrent radiation exists. These radiations include energetic photons and charged particles that can cause severe degradation in the performance and operating life of the semiconductor devices [1-2]. Thus, it is very important to evaluate the radiation hardness of these devices for different radiations.

Experimental Details

The semiconductor devices investigated in the present work are silicon NPN rf power transistors (2N 3866) manufactured by Bharat Electronics Limited (BEL), India. The transistors were exposed to 160 MeV Bromine (Br^{12+}) and 140 MeV Copper (Cu^{11+}) ions using 15 UD 16 MV Pelletron Accelerator at Inter University Accelerator Centre (IUAC), New Delhi, India. The typical beam current was 0.25 p-nA and 0.5 p-nA for 160 MeV Br^{12+} and 140 MeV Cu^{11+} ions respectively. The different DC electrical characteristics such as the Gummel characteristics, excess base current (ΔI_B), dc current gain (h_{FE}), and output characteristics (I_C-V_{CE}) were studied before and after irradiation. The transistors were irradiated with different ions in the identical dose range of 1 Mrad to 100 Mrad. The ion irradiation results were compared with the ^{60}Co gamma irradiation results in the same dose range to quantify the influence of different ion irradiations on the various characteristics of transistors.

Results and Discussion

140 MeV Cu^{11+} and 160 MeV Br^{12+} ions induced damages in the emitter-base (E-B) depletion region of the transistor can be effectively analyzed using Gummel characteristics. The Gummel characteristics for 140 MeV Cu^{11+} ion irradiated transisters is shown in fig. 1 and it can be seen that IB increases with increase in the dose. The similar behavior was observed for the transistors irradiated with 160 MeV Br^{12+} ions. The increase in the IB is mainly due to the production of generation and recombination centers in the E-B depletion region. The fig. 2 shows the variation in normalized peak h_{FE} as a function of total dose for 160 MeV Br^{12+} and 140 MeV Cu^{11+} ions and ^{60}Co gamma irradiated transistors. After 100 Mrad(Si) of total dose, the peak h_{FE} is found to decreased by 99% for 160 MeV Br^{12+} and 140 MeV Cu^{11+} ions whereas 80% for ^{60}Co gamma irradiated transistors. From the fig. 2 it can be observed that the degradation in peak h_{FE} is more for 160 MeV Br^{12+} and 140 MeV Cu^{11+} when compared to ^{60}Co gamma radiation. Hence swift heavy ions (SHIs) induce more generation-recombination (G-R) trapped centers along with the point defects in the active region of the transistor when compared to ^{60}Co gamma radiation.

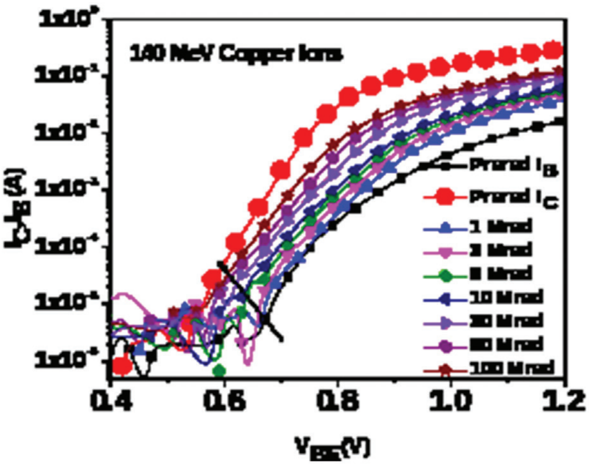

Figure 1. Gummel Characteristics of 140 MeV Copper ion irradiated transistor.

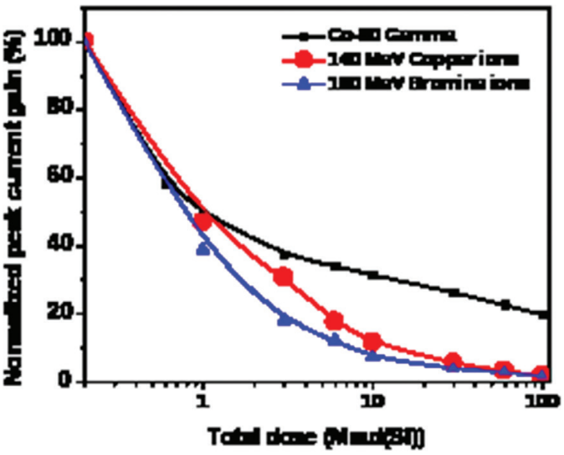

Figure 2. The variation in dc current gain after 140 MeV Copper, 160 MeV Bromine ion and ^{60}Co Gamma irradiation.

REFERENCES:

[1] A. P. Gnana Prakash, S. C. Ke and K. Siddappa, Semicond. Sci. Technol., (2004)19 1029-1039.

[2] C. Liu, X. Li, H. Geng, E. Rui, L. Guo, J.Yang, L. Xiao, Nucl. Instr. and Meth. A, (2012) 677 61-66.

5.2.3 Single Event Effects (SEE) Testing of Microelectronics for Space Applications

Kinshuk Gupta[1], Vinod Kumar[1], Raj Ramesh Babu[1], Sandhya V Kamat[1] and Saif Ahmad Khan[2]

[1]Components Management Group, U. R. Rao Satellite Centre, ISRO, Bengaluru-560017, India.
[2]Inter-University Accelerator Centre, New Delhi-110067, India.

A spacecraft encounters space radiation heavy ions of varying energies and fluxes during its lifetime in space. The heavy ions interact with spacecraft microelectronics which can lead to Single Event Effects (SEE). As the occurrence of SEE result in functional anomalies or catastrophic failures, they are a major spacecraft reliability concern for any space mission. With decreased feature size and critical charge for present day microelectronics, SEE have drawn large attention from the spacecraft radiation hardness assurance community. An assessment of the heavy ion irradiation response of susceptible spacecraft microelectronic components is indispensable and the Pelletron Facility at Inter University Accelerator Centre (IUAC) was used to test such components for assessing their usability in ISRO missions.

Experimental Details

The General Purpose Scattering Chamber (GPSC) of the Pelletron Facility at Inter University Accelerator Centre, New Delhi was used during (i)14-16 July, 2018 (ii)15-17 October, 2018 (iii)20-22 February, 2019 to obtain heavy ion beams for the SEE tests. The accelerator at this facility provided an ion current of typically 0.1 pnA (particle nano amperes). The beam was spread over an area such that the corresponding flux was about 6 x 10^8 ions/cm^2/s. However the ASTM F1192-00 (2006) standard requires the beam flux to be between $1x10^2$ to $1x10^5$ ions/cm^2/s. For the required low flux irradiation, the technique of scattering of direct beam was used.

There is a port at angle of 15 degree to the main port. The high energy direct ion beam is made incident on the 330 nm gold foil kept at the centre of GPSC. The flux of outgoing scattered beam in the 15 degree port is dependent on the thickness of the scatterer and the incoming ion flux, and was estimated using Surface Barrier Detector (SBD). Using this technique the required flux of 1x10^2 to 1x10^5 ions/cm^2/s was obtained for the SEE tests. The scattered ions are made incident on the Device Under Test (DUT) card mounted on the target ladder (Fig. 1) at the end of 15 degree port. The signals from the DUT card were terminated to the 50 pin hermetically sealed feed through connector. This was done to create a vacuum of the order of 10^{-6} mbar in the beam line so that the heavy ion beam is not attenuated by collision with air particles. The test and measurement equipment were kept near the low flux chamber.

Fig. 1: DUT card mounted on target ladder

Table 1 presents the ion beam parameters obtained at IUAC.

Table 1: Ion Beam Parameters

Heavy Ion Species	Energy (MeV)	LET (MeV-cm^2/mg)	Range (µm)	Flux (ions/cm^2/s)
Silicon	130	9.45	48.39	502
Titanium	140	22.9	29.08	582
Nickel	140	31.1	25.68	968
Silver	140	50.65	19.28	947

Results

Table 2 presents the results of SEE testing

Table 2: SEE Test Results

Microelectronic Device	Result
Application Specific Integrated Circuits	**Single Event Upsets observed**
Field Programmable Gate Array	**Single Event Functional Interrupt observed**
Hex Buffer	**No SEE observed**
16 bit Buffer	**No SEE observed**
16-Bit Transceiver	**No SEE observed**
Quad 2-Input NAND Gate-5V	**No SEE observed**
Quad 2-Input NAND Gate-3.3V	**No SEE observed**
Hex Schmit Trigger Inverter Inverter-5V	**No SEE observed**
Hex Schmit Trigger Inverter-3.3V	**No SEE observed**
Clock Drivers	**No SEE observed**

Conclusion

Microelectronic devices were tested at the Pelletron Facility, IUAC during (i) 14-16 July, 2018 (ii)15-17 October, 2018 (iii) 20-22 February, 2019. The test results indicate that some of the devices are susceptible to SEE while others are immune upto LET of 50.65 MeV-cm^2/mg. The immune devices are considered passed for on-board usage in geostationary, low earth orbit and interplanetary spacecraft missions of ISRO. Suitable mitigation techniques have been identified for the devices which have exhibited Single Event Effects.

5.2.4 Analysis of 140 MeV Copper and 160 MeV Bromine Ion Irradiation Effects on N-Channel MOSFETs

Arshiya Anjum[1], T M Pradeep[1], Vinayakprasanna N Hegde[1], N Pushpa[2], Ambuj Tripathi[3] and A P Gnana Prakash[1*]

[1]Department of Studies in Physics, University of Mysore, Manasagangotri, Mysore-570006.
[2]Department of PG Studies in Physics, JSS College, Ooty Road, Mysore-570 025, India.
[3]Inter-University Accelerator Centre, New Delhi-110067, India.

The N-channel metal oxide semiconductor field effect transistors (MOSFETs) are the key components in advanced integrated circuits and are used in space, military and other radiation harsh environments such as accelerators where high and low energy particles exist [1]. In order to use MOSFETs in radiation rich environments the devices need to withstand few krad to few Mrad of radiation [1]. Hence it is very essential to evaluate the radiation hardness of these devices from the application point of view.

Experimental Details

The MOSFETs (BEL 3N187) used in the present work were irradiated with 140 MeV Copper (Cu^{11+}) ions and 160 MeV Bromine (Br^{12+}) ions with dose ranging from 1 Mrad to 100 Mrad at Inter-University Accelerator Centre (IUAC), New Delhi using 15 UD Tandem Pelletron Accelerator. The typical beam current for 140 MeV Cu^{11+} ions and 160 MeV Br^{12+} ions is 0.5 pnA and 0.25 pnA respectively.

Results and Discussion

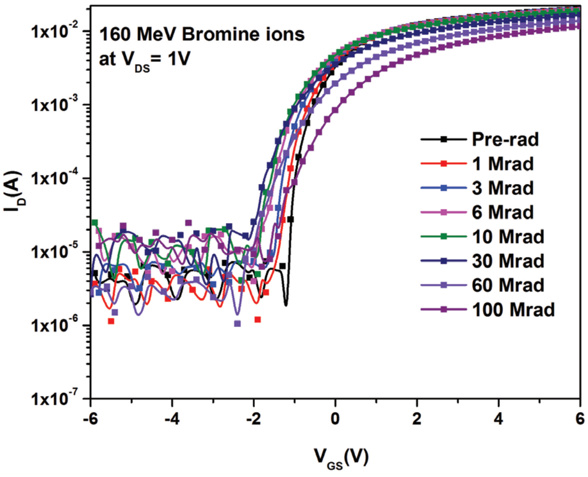

Figure 1. Transfer characteristics of 160 MeV Bromine ion irradiated MOSFET.

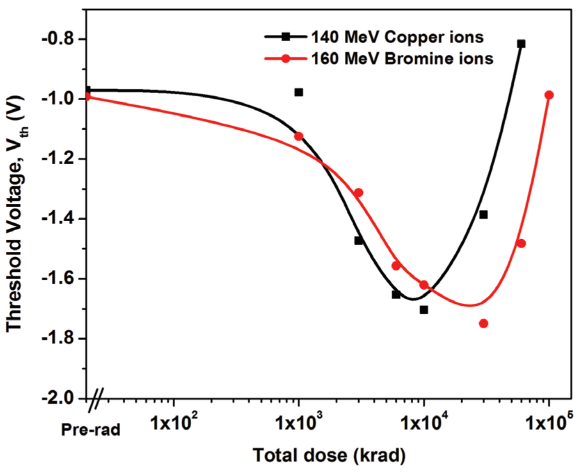

Figure 2. Variation in the V_{th} after 140 MeV Copper and 160 MeV Bromine ion irradiation.

The threshold voltage (V_{th}) is the primary degradation parameter in MOS devices and it can be determined using the subthreshold curve of MOSFETs. Fig. 1 shows the representative subthreshold curve for 160 MeV Br^{12+} ion irradiated MOSFETs. From the figure it can be seen that the subthreshold current curve shift towards negative gate voltages with slight variations in the shape of the curves as the dose increases. This is due to the fact that, the radiation induced degradation in the devices is dominated by the trapping of holes in the SiO_2 with the minimal interface states generation. The variation of V_{th} of MOSFETs with respect to dose after Cu^{11+} and Br^{12+} ion irradiations is shown in Fig. 2. It can be observed that Vth has decreased till 10 Mrad of total dose and above 10 Mrad, V_{th} was found to recover significantly which is due to the "rebound effect" or "superrecovery" [2]. It is also noticed that the degradation produced by both ion irradiations is almost identical.

REFERENCES:

[1] N. Pushpa, *et al.*, Nucl. Instr. Meth. A. **613** (2010) 280.
[2] T. P. Ma and Paul V. Dressendorfer, Ionizing Radiation Effects in MOS Devices and Circuits (1989).

5.2.5 In-situ current-voltage (I-V) studies on Cu-ZnO/P3OT hybrid heterostructures under swift heavy ion irradiations

Jitendra Singh[1], Himanshi Gupta[1], A. Kumar[1], R.G. Singh[2] and Fouran Singh[1]

[1]Materials Science Group, Inter University Accelerator Centre, Aruna Asaf Ali Marg, New Delhi-110067, India
[2]Department of Physics, Bhagini Nivedita College, Delhi University, New Delhi, 110043, India

Conducting polymer and metal-doped inorganic semiconductor based hybrid heterostructures have evoked an increasing interest to the researchers in the last few years due to their potential multifunctional applications for electronic and optoelectronic devices [1,2]. Therefore, a hybrid heterostructure (HH) (Ag/Cu-ZnO:P3OT/ITO) were prepared by depositing conducting poly (3-octylthiophene) (P3OT) polymer and Cu-doped zinc (Cu-ZnO) composites film on the indium-doped tin oxide (ITO) substrate by using sol-gel ultrasonication cast technique and the preparation details are reported in our previous study [3]. Further, the radiation stability and reliability of this HH has been tested for their possible application in the radiation harsh environments. Thusly, the in-situ current-voltage (I-V) measurements have been performed on such HH under swift heavy ion (SHI) irradiations using 80 MeV O^{6+} with increasing ion fluences from 1×10^{11} to 3×10^{13} ions/cm^2 at an applied bias voltage ± 2V as shown in Fig. 1. Interestingly, under irradiation with increasing ion fluences, the I-V characteristics of the HH reveal an insignificant changes in the forward and reverse currents which lead to the radiation hardness of HH. In this study primary incident ions effect were observed in the outer region of the HH's. However, the primary ions induced secondary charged particles radiations mostly secondary electrons effect were observed in the masked region *i.e.* near the periphery of Ag contact. Recently, a similar study has also been reported by our group to test the radiation stability and reliability of an inorganic Nb doped TiO_2/p-Si (NTO) heterojunction diode during *in-situ* I-V characteristics measurements under the influence of SHI irradiation induced secondary charged particles radiation. In that study, the I-V shows the improvements in the various diode parameters as function irradiations and reflecting the radiation hardness of NTO diode [4]. Interestingly, our study also emerges out to be very fascinating for an in-depth understanding of primary and secondary charged particles interaction process with HH. However, the detailed understanding of such phenomenon is still under progress. Thus, in-situ *I-V* studies on Ag/Cu-ZnO:P3OT/ITO HH under swift heavy ion irradiations will be very useful for the implementation of HH based devices in a variety of radiation harsh environments.

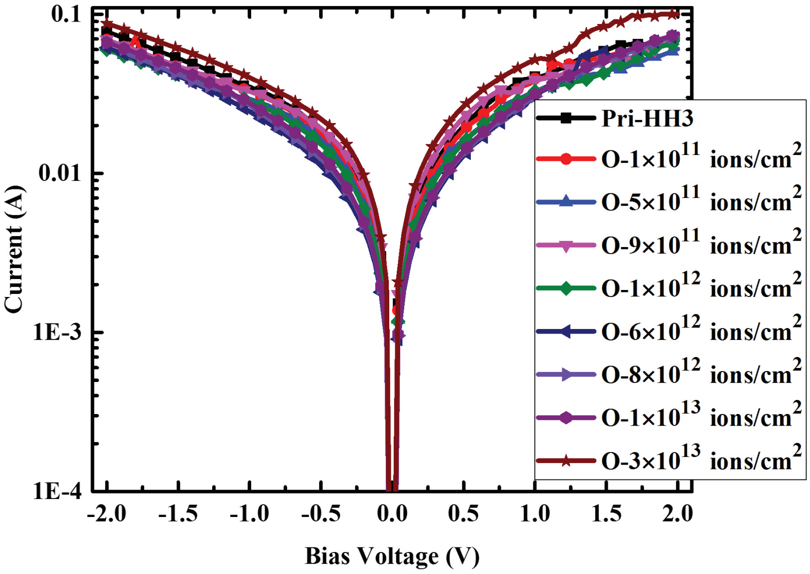

Figure 1: *In-situ* current–voltage *(I–V)* characteristics of hybrid heterostructures (HH3) under 80 MeV O^{6+} ions irradiation as function of ion fluences at an applied ± 2V bias voltage.

REFERENCES:
[1] J. Singh *et al.* J. Appl. Phys. **123** (2018) 174503.
[2] R G Singh *et al.* JRSE. **5** (2013) 033134
[3] J. Singh *et al.* Opt. Mater. (Amst). **94** (2019) 316–321.
[4] S.K. Gautam *et al.,* IEEE Trans. Electron Devices. PP (2019) 1–7.

5.2.6 Green synthesis of silver Nanoparticles and their size modulation by swift heavy ion irradiation.

Laden Sherpa[1] and Archana Tiwari[1]

[1]Department of Physics, Sikkim University, Gangtok 737102, India.

We have synthesized Ag nanoparticles (NPs) by green synthesis route. Bergenia cilliata leaves and roots are used for the synthesis. The plant extract thin films are irradiated with swift heavy ion irradiation using Ag^{15+} ions of energy 200 MeV at three different fluences, $5X10^{11}$ ions/cm^2, $1x10^{12}$ ions/cm^2 and $7x10^{12}$ ions/cm^2 . The irradiated and unirradiated plant extracts are used to synthesize the NPs and their morphologies are compared. The NPs synthesized using irradiated plant extracts are smaller in size as compared to those obtained using pristine extracts. In addition, self-assembly of NPs is also observed in some of the systems.

Experimental Details

The plants were freshly picked, washed and shade dried for a month. For the extraction, the dried plant parts were grinded in to powder. 1g of the each plant parts was taken in 10 mL of millipore water. The mixture was kept in water bath for 30 mins. The filtrate was utilized for the reduction of $AgNO_3$ and synthesis of Ag NPs. 2mL of the plant extract (drop-casted on the glass substrate for irradiation experiments) and 20ml of 1mM $AgNO_3$ were mixed and stirred for an hour using magnetic stirrer. Change in color of the solution to reddish brown was observed after about 5 mins of stirring in air and in the presence of sunlight.

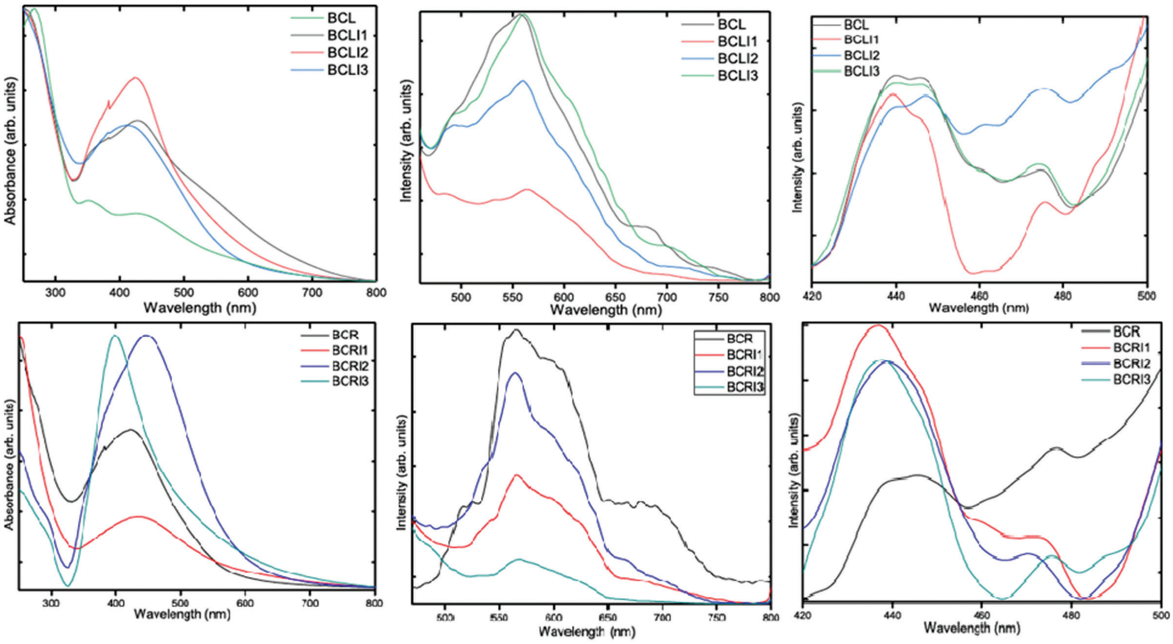

Figure 1: Absorbance spectra, Photoluminescence emission and excitation spectra of BCL and BCR Ag NPs.

Results

The synthesis of Ag NPs is confirmed by UV-vis absorption spectroscopy where the NPs synthesized using roots and leaves are labelled as BCR and BCL respectively. Signature absorption peaks centered between 400-500 nm corresponding to the surface plasmon resonance (SPR) of Ag NP are observed in all samples (Fig. 1) [1,2]. In BCR, deconvolution of luminescence spectrum (Fig. 1) shows peaks at 495 nm, 561 nm, 583 nm and 684 nm whereas in BCR the peaks are seen at 515 nm, 556 nm, 597 nm and 687 nm which are red shifted in comparison to BCL.

FTIR and XRD analysis suggest that the reduction of Ag ions and synthesis of Ag NPs are accompanied with their oxidation by hydroxyl and carbonyl groups. [3,5]. Owing to this, AgO NP crystal structure is observed at $2\theta = 29^o$ and 38^o in addition to FCC Ag NP. The effects of swift heavy ion irradiation on the sysnthesis of Ag NP is summerised in Table 1.

Table 1: Size, shape and lattice parameter data of the Ag NPs synthesized using all the plant extracts.

Reducing Agent	Irradiation (ions/cm^2)	Sample Label	Size (nm)	Shape	Lattice constant (A)
Bergenia Cilliata Leaves	Unirradiated	BCL	18.2±0.8	spherical, triangular, nanorods	4.092349
	5x10^{11}	BCLI1	18.0±0.7	spherical, oval, hexagonal	4.09121
	1x10^{12}	BCLI2	22.3±0.7	spherical, oval,	4.09525
	7x10^{12}	BCLI3	23.6±0.5	spherical, dendritic formation	4.073185
Bergenia Cilliata Roots	Unirradiated	BCR	12.0±0.5	spherical	4.049242
	5x10^{11}	BCRI1	8.3±0.1	spherical, dendritic formation	4.065
	1x10^{12}	BCRI2	19±1	spherical, hexagonal, oval, dendritic formation	4.074108
	7x10^{12}	BCRI3	11±1	spherical, dendritic formation	4.081

Dendrite like self assembly is observed upon irradiation in BCL and BCR NPs. Our research presents a simple fabrication technique for highly crystalline dendrite nanostructures of silver metals [4,6]. These dendrite structures may provide us a framework for the study of disordered systems as well as open up avenues for their applications in surface enhanced Raman spectroscopic sensors and catalysis.

REFERENCES:

[1] N. Vigneshwaran, R.P. Nachane, R.H. Balasubramanya, P.V. Varadarajan, A novel one pot 'green' synthesis of stable silver nanoparticles using soluble starch, Carbohydr. Res. 341 (2006).

[2] Kora, A., Beedu, S., & Jayaraman, A. Size-controlled green synthesis of silver nanoparticles mediated by gum ghatti (Anogeissus latifolia) and its biological activity. Organic and Medicinal Chemistry Letters, 2(1), (2012)..

[3] B. Sundararajan, G. Mahendran, R. Thamaraiselvi, B.D. Ranjitha Kumari, Biological activities of synthesized silver nanoparticles from Cardiospermum halicacabum L, Bull. Mater. Sci. 39 (2) (2016) 423–431.

[4] Partha P. Dutta, Manobjyoti Bordoloi, Kabita Gogoi, Sonali Roy, Bardwi Narzary, Dibya R. Bhattacharyya, Pradyumna K. Mohapatra, and Bhaskar Mazumder. Antimalarial silver and gold nanoparticles: Green synthesis, characterization and in vitro study. Biomed. Pharmacother., 91:567–580, 2017.

[5] Linlin Jing, Huiping Ma, Pengcheng Fan, Rongmin Gao, and Zhengping Jia. Antioxidant potential, total phenolic and total flavonoid contents of Rhododendron anthopogonoides and its protective effect on hypoxiainduced injury in PC12 cells. BMC Complement. Altern. Med., 15(1):1– 12, 2015

[6] Chen, Y., Wang, Z., He, Y., Yoon, Y. J., Jung, J., Zhang, G., & Lin, Z. Light-enabled reversible self-assembly and tunable optical properties of stable hairy nanoparticles. Proceedings of the National Academy of Sciences, 115(7), (2018).

5.2.7 Photo-absorption studies using ion-induced surface patterning of ITO thin films

G Poorani, GN Kumaraswamy

Organic Photovoltaics Laboratory, Department of Physics, Amrita Vishwa Vidyapeetham, Bengaluru-560035, India.

In organic solar cells, thin films of the transparent conducting indium tin oxide are commonly used as the top electrode. We can randomize the front surface of the cell and enhance the photo-absorption by increasing the optical path length by patterning the surface of indium tin oxide (ITO). The surface patterning of ITO was carried out using the Electron Cyclotron Resonance ion source (ECR) at the Low Energy Ion Beam Facility (LEIBF) at the Inter-University Accelerator Centre, New Delhi. Based on previous studies and its inert nature, Ar$^+$ ions were preferred for ion-induced surface patterning with a beam energy of 50 keV with doses varying from 10^{13} cm^{-2} to 10^{15} cm^{-2} (since the range of energy available at LEIBF is from 50 keV to 1.5 MeV for Ar ions). The ion beam angle was varied from grazing incidence to low angles (5º, 10º, 15º and 25º). The unpatterned ITO glass substrates from Ossila were used for the experiments.

Optical transmission studies of ITO samples post ion-induced patterning were done by performing UV-Vis Spectroscopy and surface studies using AFM. The ion-induced patterning of ITO increases the surface roughness of the thin films at grazing incidences, especially at 5º and 10º, sharp peaks are observed with increase in RMS roughness values. As the angle of irradiation is increased from grazing incidence to lower angles, there is a decrease in surface roughness and area of pattern formation which is confirmed by AFM images. Ripple pattern formation on thin films are well-studied and Bradley-Harper theory is widely used to study the same. According to the B-H theory there is always an interplay of smoothening versus roughening action influenced by surface diffusion, local surface curvature, sputter yield etc [2]. At 25°, the ITO surface is more exposed to the ion beam and with the highest does of irradiation, the surface roughness is observed to be less compared to other irradiated samples and the AFM image shows presence of more inhomogeneous patches (see Figure 1d) further established by the inability to measure the continuity of conductance in the thin film using multimeter. While the AFM images clearly depict the ion-induced pattern formation, the UV-Vis absorption spectroscopy performed on the samples indicate an increase in optical transmission with grazing incidence angles. As mentioned, ITO has high optical transmission in the visible range and is opaque in the UV, correspondingly its extinction coefficient in the visible range is zero, while in the UV range it is non-zero. The UV-Vis transmission spectrum of samples irradiated at 5° grazing angles with varied fluences is shown in Figure 1. It is evident that patterned ITO shows increased optical transmission over unpatterned ITO especially at lower fluences till $1x10^{14}cm^{-2}$. Above $1x10^{14}$ cm^{-2}, however there is no significant improvement in transmission compared to unpatterned ITO. Though there appeared a similar improvement for patterned ITO samples irradiated at an angle of 10°, it was not as considerable as it was for 5° and for lower doses, only a slight increase in transmission over a short range in the near UV region between 350 to 400 nm was observed. At 15°, patterning caused a decrease in transmission and was further degraded at 25°.

These results suggest low energy ion-induced pattern formation on ITO thin films might help increase the photo-absorption of solar cells, when such photovoltaic devices are fabricated over those patterned ITO substrates which exhibit a considerable improvement in optical transmission. Further studies involving the fabrication of solar cells over the patterned ITO surfaces are yet to be done, because the scaling issues involved with organic solar cell device fabrication require pixelated ITO surfaces, the patterned substrates cannot be used as is. Pixelating the ITO substrates in accordance with the desired device design involves etching of ITO, the effect of which on ion-induced patterned ITO substrates needs to be carefully examined before proceeding with device fabrication.

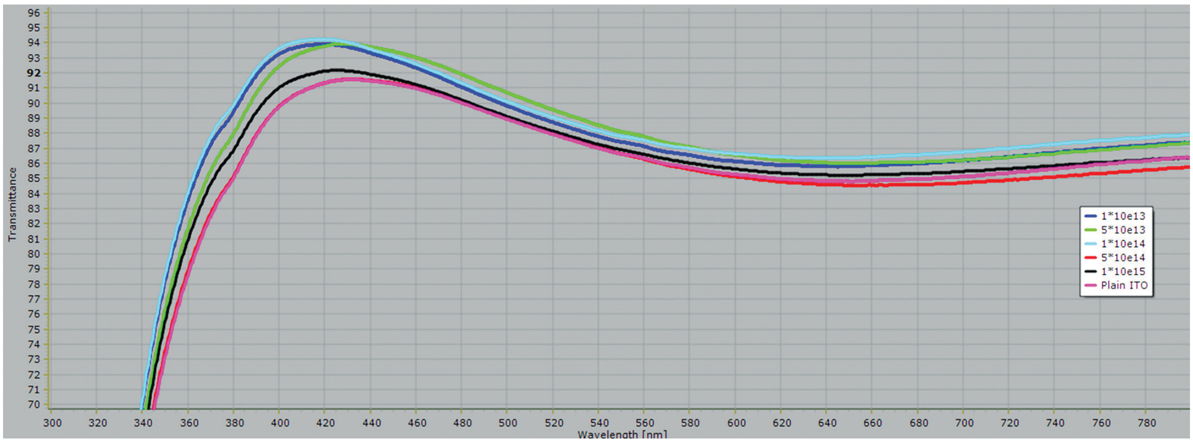

Figure 1. A comparison of UV-Vis transmission spectra of patterned ITO irradiated at a grazing angle of 5° at 5 different doses

REFERENCES:

[1] Hamberg, I., Granqvist, C. G., Berggren, K. F., Sernelius, B. E., & Engström, L, Physical Review B, 30(6) (1984): 3240.

[2] Škereň, T., Doornaert, D., Glorieux, C., Modarresi, H., Guan, T., Temst, K., Vandervorst, W. and Vantomme, A., Thin Solid Films, 589, pp.315-321 (2015)

5.2.8 Effect of patterned substrate morphology on the thin film magnetic properties

Safiul Alam Mollick[1,2], Dinakar Kanjilal[3] and Tapobrata Som[2*]

[1]Indian Association for the Cultivation of Science, Kolkata-700032, India.
[2]Institute of Physics, Bhubaneswar-751005, India.
[3]Inter-University Accelerator Centre, New Delhi-110067, India.

We have studied nanowire-like patterning by atomic manipulation using energetic Au ion beams for functional application as template for thin magnetic film. In general, highly ordered one-dimensional semiconductor nanostructures can be fabricated by self-organization methods using few tens of keV Au ions on Ge substrate. We have studied morphological and electrical properties of highly ordered nanowire-like patterned surface produced by 30 keV Au ion energy and $2x10^{13}$ ion cm^{-2} s^{-1} ion flux. These results shows good correlation with our earlier work in the ion energy range from 10 keV to 26 keV.

Experimental Details

Cleaned intrinsic Ge(100) wafer were placed in the processing chamber for ion irradiation. Ion irradiation was carried out at an oblique angle of 60° with respect to the surface normal by 30 keV Au− ions at room temperature (RT) using the negative ion implantation facility. For the present experiments, the ion flux was maintained at 2×10^{13} ions cm^{-2} s^{-1} and the fluence was 5×10^{17} ions cm^{-2}. The temporal evolution of Ge surface morphology was examined using atomic force microscopy (AFM) (Asylum Research, MFP3D), and scanning electron microscopy (SEM) (FEI, Quanta 200 FEG). The identification of phase and crystalline nature of Au-implanted samples was performed by x-ray diffraction (XRD) (Bruker, D8-Discover) under the Bragg–Brentano geometry and using the Cu-Kα radiation ($\lambda = 0.15418$ nm). Local probe-based electrical property measurements, KPFM was carried out as a non-contact local probe technique to map the work function using an Ir–Pt coated Si tip. Conductive atomic force microscopy (cAFM) measurement was employed for current mapping and I–V measurements using a conductive Pt-coated tip.

Nanowire-like Patterning on Ge

We have seen nanowire-like patterned surface fabrication doesn't depend on the incidence ion flux but only on the target projectile combination. Mollick et al [1,2] earlier reported fabrication of well ordered structure at an ion flux of 4×10^{14} ions cm^{-2} s^{-1}, here we have found similar patterning is possible at one order of lower ion flux of 2×10^{13} ions cm^{-2} s^{-1}. Figure 1(a)-(b) show AFM images of patterned substrate at two different fluences of 1×10^{17} and 5×10^{17} ions cm^{-2}. The wavelength of nanowire-like structures increases from 380 nm to 620 nm for increase of ion fluence from 1×10^{17} to 5×10^{17} ions cm^{-2}. The insets show the autocorrelation images from where the wavelength has been determined.

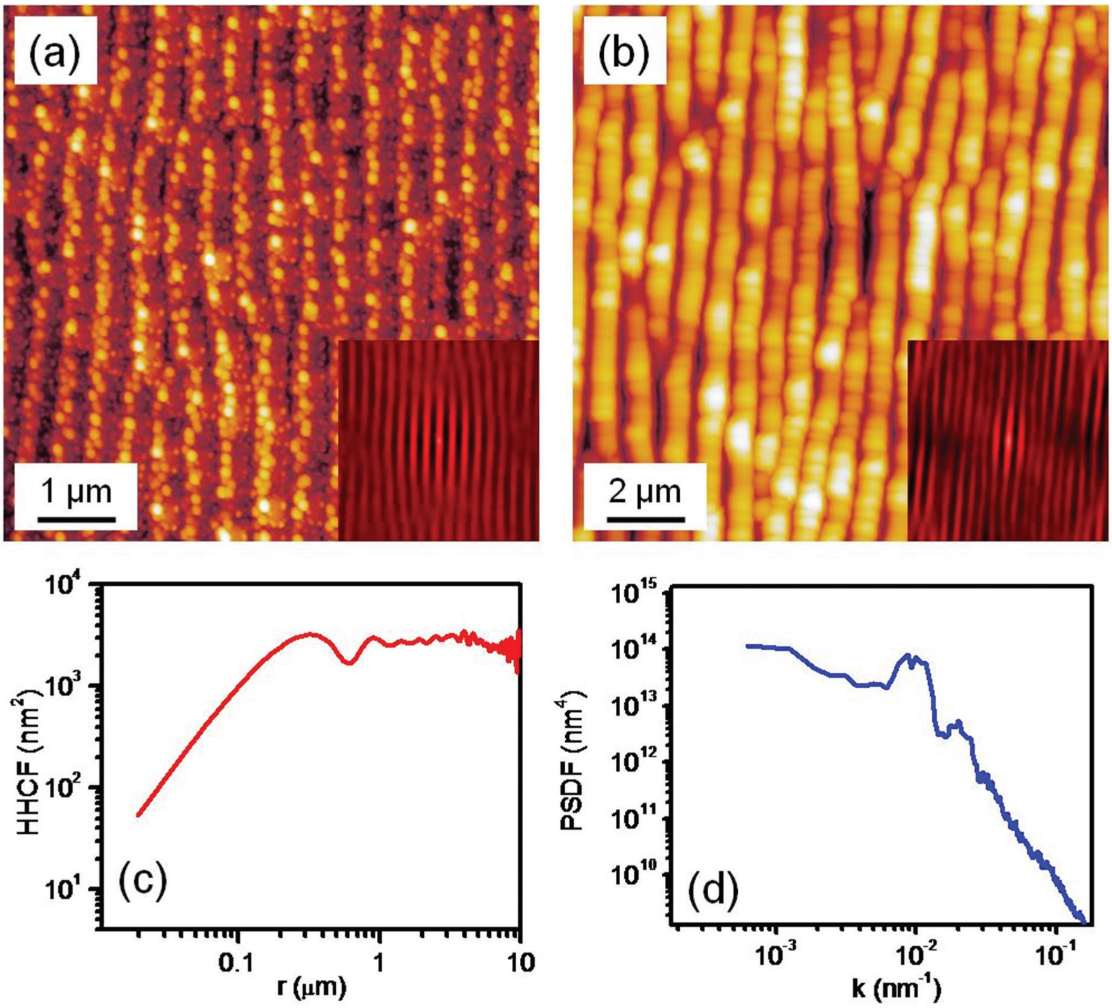

Figure 1. (a) and (b) shows AFM images for the fluences of 1×10^{17} and 5×10^{17} ions cm^{-2}.
(c) and (d) shows the 1D plot of HHCF and PSDF for the highest fluence.

The height-height correlation function (HHCF), g(r), which correlates two point heights of two different point on the surface as $g(R)=\langle[h(x.y) - h(x', y')]^2\rangle$ the pairs of points are laterally separated by $r=\sqrt{((x-x')^2-(y-y')^2}$ and $\langle\rangle$ denotes the ensemble average over all possible roughness configurations. The HHCF is shown in figure 1(c) from where the roughness exponent has been calculated. In our cases we found D_f varies in between 2.4 to 2.45. The scaling parameters obtained for two different fluences from HHCF is presented in Table –I

Table-I The Scaling parameters obtained from HHCF

Fluence (ions cm^{-2})	HHCF slope	Roughness exponent (α	Fractal Dimension (D=3 - α)
1×10^{17}	1.1	0.55	2.45
5×10^{17}	1.2	0.60	2.4

The statistical analysis of the surface morphology has also been performed from the scaling exponents calculated from the Power Spectral Density (PSD) gathered from the AFM topographical images using Gwyddion software, which is defined as: [3]

$$PSD(f_x, f_y) = \frac{1}{L^2}\left[\iint_0^L {}_e{}^{i2\pi fx}\, e^{i2\pi fy}\left[h(x,y)-h'\right]dxdy\right]^2$$

From PSD Spectrum also one can extract the roughness exponent α, correlation length ξ and fractal dimension D of the samples by fitting the power-law decay (in the linear region of the log-log plot) to

$$PSD\ (k > \xi^{-1}) = const/k^{\gamma}$$

Where γ is the slope in the linear region of the log-log plot and $\alpha=((\gamma-d')/2$, d' is dimension and in our case it is 1 for a line profile. The PSDF in Fig. 1(d) exhibit two distinct regions, (i) a plateau PSDF at low spatial frequencies and (ii) frequency-dependent decaying branch. The steeper portion of the latter is taken as the self affine range, while the high frequency range with a smaller slope is discarded since it is more affected by noise and aliasing. From the PSD obtained for the ZnPc thin film at asdeposited state and at different annealed temperature, the values of γ are obtained and fractal dimension D is also calculated from the eq.[4]

$$D= (8-\gamma))/2,$$

Table-II shows the scaling exponents obtained from the PSDF graph of the patterned samples. The fractal dimension D calculated from PSD study shows a similar trend to the one calculated from HHCF, which shows self affine characteristic of the patterned morphology.

Table-II The Scaling parameters obtained from PSDF

Fluence (ions cm^{-2})	PSDF slope (γ)	Roughness exponent (α	Fractal Dimension (D)
1×10^{17}	3.2	0.60	2.40
5×10^{17}	3.3	0.65	2.35

The functional application of these well studied surface will be done in future using the patterned substrate as template for thin film deposition.

REFERENCES:

[1] S.A. Mollick, M. Kumar, R. Singh, B. Satpati, D. Ghose, T. Som, Gold-decorated highly ordered self-organized grating-like nanostructures on Ge surface: Kelvin probe force microscopy and conductive atomic force microscopy studies, Nanotechnology. 27 (2016) 435302. doi:10.1088/0957-4484/27/43/435302.

[2] S.A. Mollick, D. Ghose, P.D. Shipman, R. Mark Bradley, Anomalous patterns and nearly defect-free ripples produced by bombarding silicon and germanium with a beam of gold ions, Appl. Phys. Lett. 104 (2014) 043103. doi:10.1063/1.4863342.

[3] F. Biscarini, P. Samorí, O. Greco, R. Zamboni, Scaling Behavior of Anisotropic Organic Thin Films Grown in High Vacuum, Phys. Rev. Lett. 78 (1997) 2389–2392. doi:10.1103/PhysRevLett.78.2389.

[4] D. Raoufi, Fractal analyses of ITO thin films: A study based on power spectral density, Phys. B Condens. Matter. 405 (2010) 451–455. doi:https://doi.org/10.1016/j.physb.2009.09.005.

5.2.9 Formation and isolation of organic nanowires via solid-state polymerization of small molecules by irradiation with swift heavy ions

Tsuneaki Sakurai[1], Kazuto Kayama[1], Koshi Kamiya[1], Shugo Sakaguchi[1], G.B.V.S. Lakshmi[2], Ambuj Tripathi[3], D.K. Avasthi[4] and Shu Seki[1*]

[1]Department of Molecular Engineering, Kyoto University, Nishikyo-ku, Kyoto 615-8510, Japan.
[2]Special Center for Nanoscience, Jawaharlal Nehru University, New Delhi 110067, India.
[3]Inter-University Accelerator Centre, New Delhi 110067, India.
[4]Amity Institute of Nanotechnology, Amity University, Noida 201313, India.

In this project, single particle-triggered linear polymerization (STLiP) method[1,2] was demonstrated, yielding wire-shaped nano-objects with controlled diameter and length by tuning the thickness of the target organic thin-films and fluence of the high-energy charged particles (ions). This is unique technique to obtain such uniform nanowires (< 10 nm in diameter) from organic materials, since "single" particle is the smallest unit as a tool to fabricate the materials. A series of π-conjugated small molecules, having particular functional groups such as ethynyl or halogen, were employed as targets. Thin films of the designed small molecular materials were fabricated on a silicon substrate by spin coating, drop casting, or vacuum deposition methods. Then, high-energy particles were irradiated at IUAC, where the fluence was set at $1 \times 10^9 \sim 1 \times 10^{11}$ cm^{-2} (~1 pnA, 1×1.5 cm^2 scan area). After the ion beam irradiation, the thin films were developed by organic solvents, and the obtained nano-objects were visualized by a series of microscopy techniques of atomic force microscopy (AFM) and scanning electron microscopy (SEM). The sublimation process instead of wet-development by solvents was tried in the present experiments, avoiding the irreversible adsorption of nanowires on the substrate. This allowed the isolation of vertically-aligned nanowires. Figure 1 shows a representative result by irradiation with 120 MeV ^{197}Au ions 1,6,7,12-tetrachloroperylene tetracarboxylic acid dianhydride (PTCAD-Cl_4). The depth of a valley observed in the AFM image Fig1(b) nearly corresponds to the initial thickness of the film (Figure 1c), which indicates the nanowires are vertically aligned, supporting the vertically aligned character of the nanowires after sublimation as visualized by a SEM image (Figure 1d).

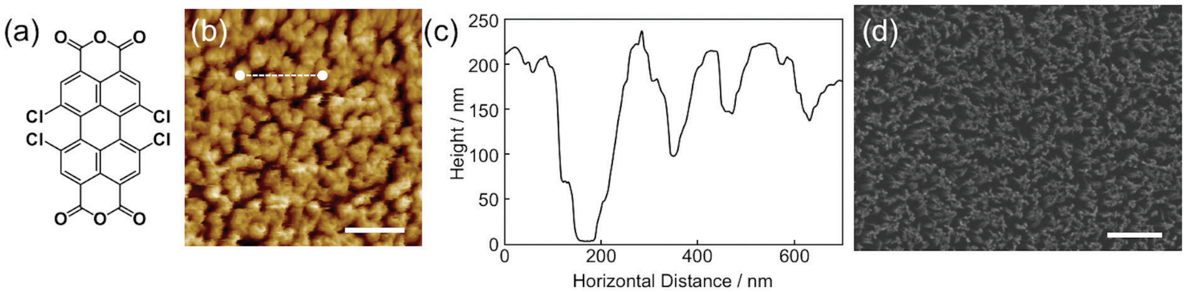

Figure 1. (a) Chemical structure of PTCAD-Cl_4, (b) AFM and (d) SEM images (top view) of nanowires from PTCAD-Cl_4 after irradiation with 120 MeV ^{197}Au at 1×10^{11} cm^{-2} and subsequent sublimation. (c) Height profile indicated as white line in (b). The thicknesses of the original film was 250 nm. Scale bars represent 500 nm.

REFERENCES:
[1] A. Horio, T. Sakurai, G.B.V.S. Lakshmi, D. K. Avasthi, M. Sugimoto, T. Yamaki, S. Seki, Nanoscale, 8 (2016) 14925.
[2] S. Sakaguchi, T. Sakurai, J. Ma, M. Sugimoto, T. Yamaki, A. Chiba, Y. Saito, S. Seki, J. Phys. Chem. B 122 (2018) 8614.

5.2.10 Electrical and optical properties of Zinc- and Strontium-Stannate thin films

Yogesh Kumar[1], Ravi Kumar[2], K Asokan[3] and A P Singh[1*]

[1]Department of Physics, Dr. B. R. Ambedkar National Institute of Technology, Jalandhar-144011, India.
[2]Centre for Material Science and Engineering, National Institute of Technology, Hamirpur -177 005, India.
[3]Inter-University Accelerator Centre, New Delhi-110067, India.

Perovskite-structured materials are one of the most technologically important materials due to their large range of physical properties varying from insulator to superconductor. In the present study, we are exploring the possibility of zinc-stannate (Zn-Sn-O) thin films thin films for transparent conducting applications. Swift heavy ion (SHI) irradiation is a very useful technique to modify the properties of materials. Zinc-stannate (Zn-Sn-O) thin films were irradiated with 120 MeV Ag^{9+} ions to study the effect of irradiation on the structural, electrical and optical properties of the thin films. The temperature dependent resistivity for pristine and irradiated thin films were studied in the range from 100 K to 400 K. The Rutherford Backscattering (RBS) Spectrometry was used to characterize the thin films thickness.

Experimental Details

Zinc-stannate (Zn-Sn-O) thin films, deposited using pulsed laser deposition (PLD) technique, were irradiated with 120 MeV Ag^{9+} ions at the fluence of 2×10^{12} ions/cm^2 using 15UD tandem pelletron accelerator, according to the beam time that had been scheduled as per letter no. IUAC/XIII.4A/63210, dated Nov. 29, 2018 on Dec. 12, 2018 at IUAC, New Delhi. Three shifts were used for the irradiation. SRIM was used to calculate the range, electronic energy loss, and nuclear energy loss of 120 MeV Ag ions. As the electronic energy loss (1.316×10^3 eV/Å) is much higher than the nuclear energy loss (6.385 eV/Å) at this energy, the modification in the film is mainly due to electronic energy loss.

Rutherford backscattering (RBS) spectrometry was used to calculate thin film thickness using 5SDH–1.7 MV Tandem accelerator at Pelletron Accelerator for RBS–AMS System (PARAS) at IUAC, Delhi. During the experiment, a pressure of the order of 10^{-6} Torr was maintained in the chamber. The intensity of helium ion beam of 2 MeV was kept constant at 10 nA and 5 μC charge was collected per spot. The RBS data was simulated and analyzed using RUMP code [1].

Results and Discussions

GIXRD patterns of the pristine and the irradiated zinc-stannate thin films is represented in fig.1. The film was found to have SnO_2 (JCPDS No. 78-1063) and Zn_2SnO_4 (JCPDS No. 74-2184) phases, as indicated in fig. 1(a). The results obtained in this work are in accordance with the observed results by Minami et. al.[2]. The crystalline to amorphous phase transformation in zinc-stannate thin film has been observed with irradiation (fig. 1(b)).

The measured RBS spectra for the pristine and the irradiated thin films are shown in black in fig. 2 (a) and (b), respectively. The calculated thicknesses are 568 nm and 534 nm for pristine and irradiated thin films, respectively.

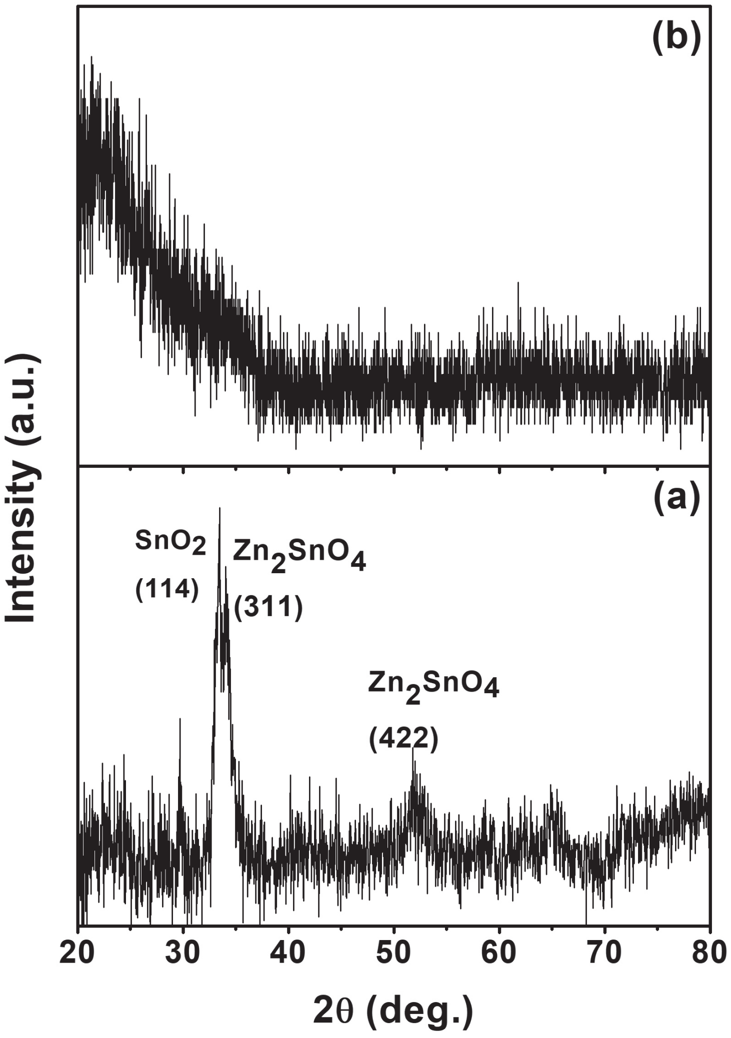

Figure 1. XRD patterns in the left are of (a) as deposited Zn-Sn-O thin films and (b) irradiated Zn-Sn-O thin films.

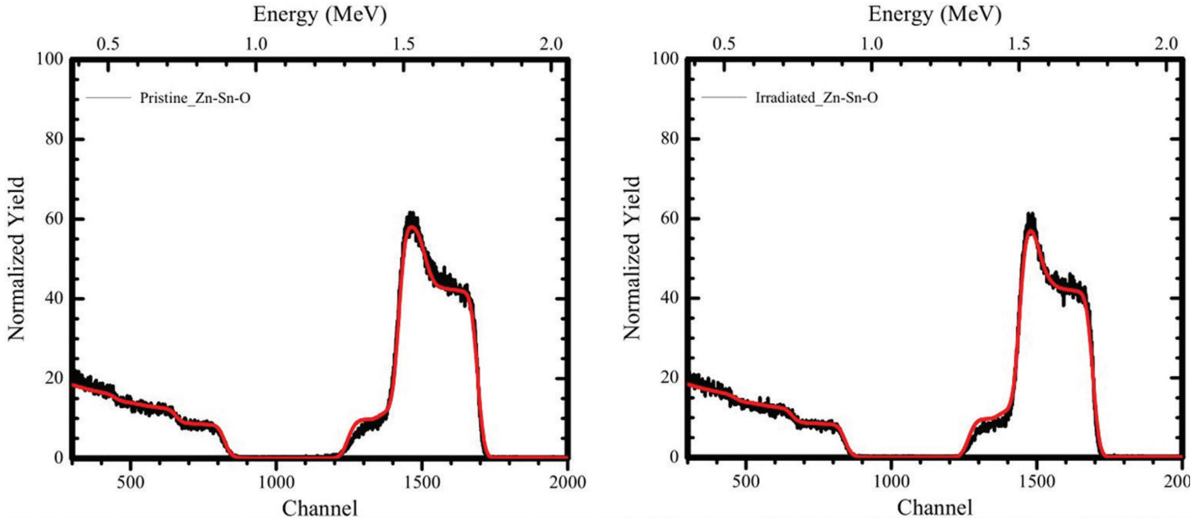

Figure 2. Representation of RBS spectrum (black color) and simulation of RBS data (red color) of (a) pristine and (b) irradiated zinc stannate thin films.

REFERENCES:

[1] Lawrence R. Doolittle. Nuclear Instruments and Methods in Physics Research Section B: Beam Interactions with Materials and Atoms, 9(3):344 – 351, 1985.

[2] T. Minami, H. Sonohara, S. Takata, and H Sato. Japanese Journal of Applied Physics, 33(Part 2, No. 12A): L1693–L1696, 1994.

5.2.11 Dielectric behavior of SHI irradiated Ba-Hexaferrite/LSMO bilayer films

Sushant Zinzuvadiya[1], Nirav C. Pandya[1], Poornima Sengunthar[1], S.A. Khan[2], A. Tripathi[2] and U.S. Joshi[1]

[1]Department of Physics, University School of Sciences, Gujarat University, Ahmedabad-380009, India

[2]Inter University Accelerator Centre, Aruna Asaf Ali Marg, New Delhi-110067

To study the defect assisted modifications in different nanostructured dielectric materials, we have irradiated different magneto dielectric materials deposited on platinized silica substrates. For the study of the effect of irradiation at heterojunction of ferroelectric and ferromagnetic thin films we chose Barium Hexaferrite(BAM)/La-Sr-Mn-O (LSMO) thin film. Frequency dependent dielectric properties and possible magneto-electric coupling are under investigations for the films irradiated with 120 MeV Au and 80 MeV Ni beams.

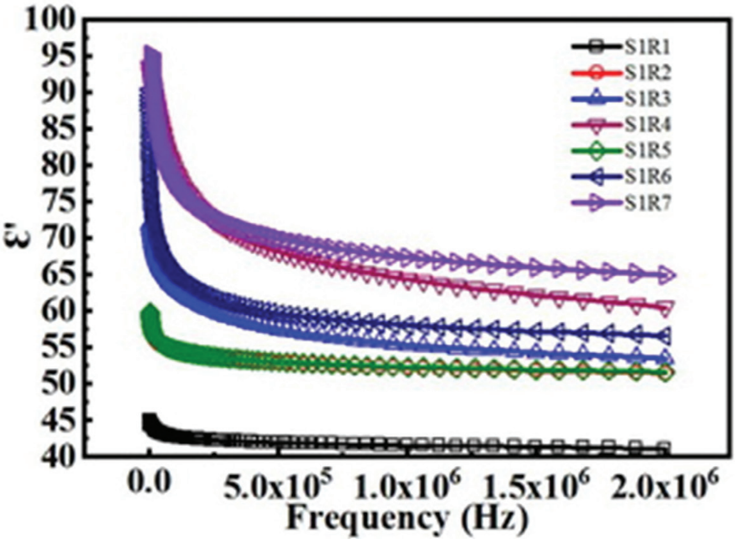

Figure. 1. Frequency dependent dielectric properties of BAM/LSMO/Pt/Si (S1R1-Pristine sample, S1R2-4- Samples irradiated with 120 MeV Au^{+9} ion, S1R5-6- Samples irradiated with 80 MeV Ni^{+5} ion)

Experimental Details

With the intention of studying the effect of irradiation caused by the SHI ion with high and medium energy respectively, Au^{+9}(120 MeV) and Ni^{+5}(80MeV) were chosen as a source of ion beam. Heterostructures of high k dielectric materials i.e. barium hexaferrite and conducting ferromagnetic material i.e. LSMO grown by PLD were irradiated for the study of the modification at the heterojunction and the variation in its electric and magnetoelectric properties.

As shown in Fig. 1, the dielectric behavior of BAM/LSMO junctions do not degrade at least upto 2 MHz frequency even after SHI irradiation using Au and Ni at different fluence values. A systematic increase in the permittivity values upon SHI irradiation is encouraging for such a system. We are investigating magneo-dielectric behavior and structural issues of the system under test.

5.2.12 100 MeV O^{7+} swift heavy ions modified molybdenum disulfide-reduced graphene oxide/ polypyrrole nanotubes ternary nanocomposite for hybrid supercapacitor electrode

Devalina Sarmah[1], P.K. Kulriya[2], Fouran Singh[2] and Ashok Kumara*

[1]Material Research Laboratory, Department of Physics, Tezpur University, Tezpur 784028, Assam, India
[2]Inter University Accelerator Centre (IUAC), Aruna Asaf Ali Marg, New Delhi 110067, India

Molybdenum disulfide, reduced graphene oxide and polypyrrole nanotubes (MoS_2-rGO/PPyNTs) based ternary nanocomposites have been synthesized by incorporating pre-synthesized PPyNTs in the MoS_2-GO hetero-structures followed by hydrothermal reduction of rGO without using any reducing agent. The MoS2-rGO heterostructures have been synthesized by layer-by-layer self-assembly between negatively charged GO with positively charged MoS_2 followed by hydrothermal reduction [1]. The ternary nanocomposite has been irradiated with 100 MeV O^{7+} swift heavy ions at the fluence of $3.3x10^{11}$, $1x10^{12}$, $3.3x10^{12}$ and $1x10^{13}$ ions cm^{-2}. FESEM images indicated the structural defects like folding and incision appeared in the electrode at a fluence of $3.3x10^{12}$ ions cm^{-2}. XRD spectra revealed that the polymer's crystallinity increased up to the fluence of $3.3x10^{12}$ ions cm^{-2} due to cross-linking in the polymer chain and degraded at the highest fluence $1x10^{13}$ ions cm^{-2}. MoS_2 also got crystallized at the fluence of $3.3x10^{12}$ ions cm^{-2} due to the simultaneous effects of polymer crystallinity, hammering effects from swift heavy ions and formation of periodic tracks. FTIR spectra suggest that different vibrational bands have different sensitivity towards SHI irradiation. Raman spectra revealed the increasing number of defects density in MoS2 due to the appearance of LA peak. In RAMAN spectra of rGO, the disorder parameter first decreased due to annealing and then continuously increased up to the highest fluence, indicating the increased defects or disorder in the nanocomposite. (D+D/) band was also appeared in the RAMAN spectra of the nanocomposite due to the activation of various defect states. Contact angle analysis suggests that the surface energy is mainly dominated by the vdW elements (MoS_2 and rGO) by the formation of temporary dipoles and increases with increasing SHI fluence. The GCD curve of pristine MoS_2-rGO/PPyNTs/ITO electrode showed longer discharge duration and possessed very high value of specific capacitance of 1505 F g^{-1} at 1 fold current density. The irradiated electrodes were also found to possess higher discharge period with enhanced specific capacitance for supercapacitor energy storage. The GCD curve of the electrode irradiated with fluence $3.3x10^{11}$ and $1x10^{12}$ ions cm^{-2} was found to be more linear in both charging and discharging processes (Fig. i). This might be due to the fact that, SHI irradiation widen up the pores of the electrode as observed from FESEM images. Moreover, PPyNTs got aligned and becomes crystalline as well. Therefore, the electrolyte ions can directly penetrate to the MoS_2 and rGO nanosheets and as result EDLC contribution increases after irradiation. Highest gravimetric discharge duration was observed for the electrode irradiated with $3.3x10^{12}$ ions cm^{-2} with enhanced specific capacitance. The GCD measurements for the electrode irradiated with fluence of $3.3x10^{12}$ ions cm^{-2} are performed at 1, 3, 5, 7, 9 and 11 A g^{-1} current densities and are displayed in fig. (ii). The electrode exhibits specific capacitance of 1875 F g^{-1}, 1868.5 F g^{-1}, 1678.6 F g^{-1}, 1462.5 F g^{-1}, 1099.75 F g^{-1} and 769.25 F g^{-1} at 1, 3, 5, 7, 9 and 11 A g^{-1} current densities, respectively. The pristine electrodes and the electrodes irradiated with fluence of $3.3x10^{11}$, 10^{12}, $3.3x10^{12}$ and 10^{13} ions cm^{-2} show rate capability of 46.3%, 47%, 49%, 58.6% and 46%, respectively at 9-fold of current density (Fig. iii). The pristine MoS_2-rGO/PPyNTs/ITO electrode possesses power density of 800.05 W kg^{-1} and energy density of 535.15 Wh kg^{-1} while the electrode modified with ion dose of $3.3x10^{12}$ ions cm^{-2} possesses impressive energy density of 666.72 Wh kg^{-1} maintaining almost the same power density at 1-fold current density (Fig. iv). The ternary MoS_2-rGO/PPyNTs/ITO electrode irradiated with SHI fluence of $3.3x10^{12}$ ions cm^{-2} shows power density of 8800.78 W kg^{-1} and energy density of 273.53 Wh kg^{-1} at 11-fold of current density, while the pristine electrode possesses power density of 8801.56 W kg^{-1} with energy density of 159.87 Wh kg^{-1} at of current density of 11 A g^{-1}.

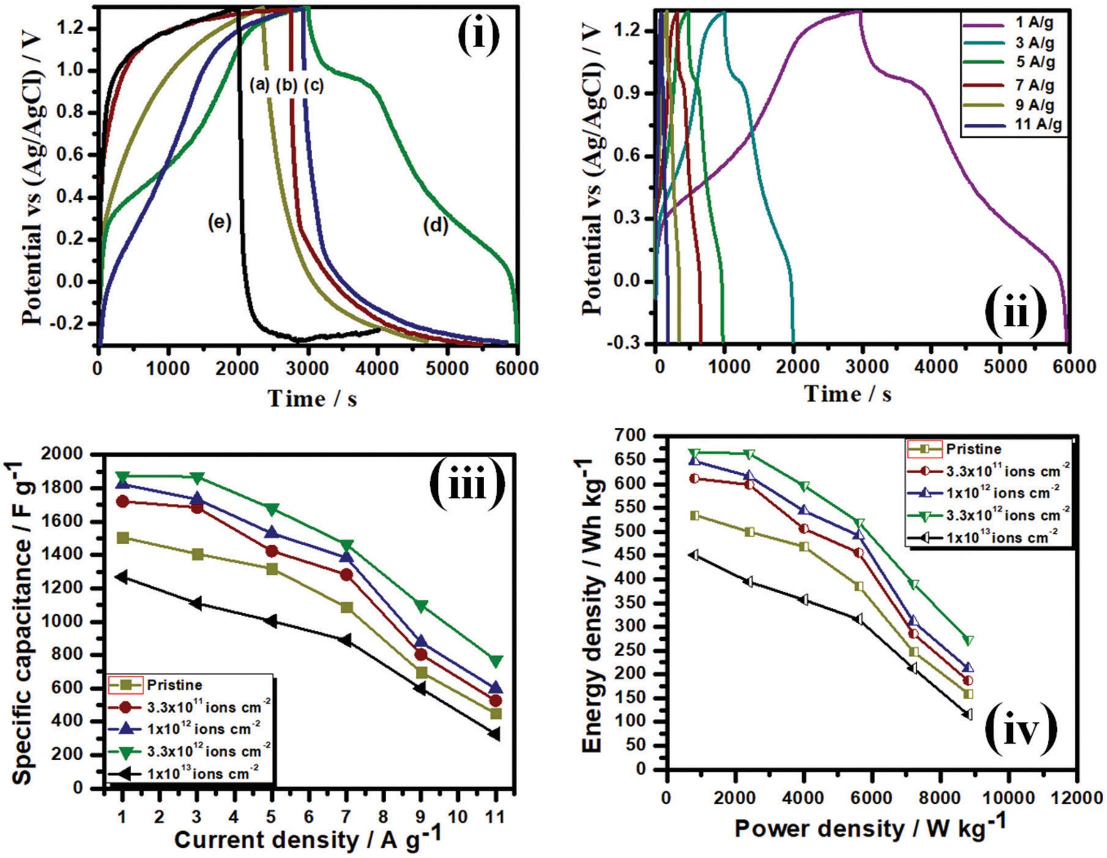

Fig.: Galvanostatic charge-discharge (GCD) measurements of (i) ternary MoS_2-rGO/PPyNTs, (a) pristine and irradiated with fluences (b) 3.3×10^{11}, (c) 1×10^{12}, (d) 3.3×10^{12}, (e) 1×10^{13} ions cm^{-2} in 1M KCl solution in 1 A g^{-1} current density; (ii) GCD curves of 3.3×10^{12} ions cm^{-2} irradiated electrode at current densities of 1, 3, 5, 7, 9, 11 A g^{-1} in 1M KCl solution, (iii) rate capability of pristine and irradiated ternary MoS_2-rGO/PPyNTs electrodes and (iv) Ragone plot of pristine and irradiated ternary MoS_2-rGO/PPyNTs electrodes.

REFERENCES:

[1] Q. Li, C. Lu, C. Chen, L. Xie, Y. Liu, Y. Li, Q. Kong, H. Wang, Energy Storage Materials, 8 (2017) 59-67.

5.2.13 Defects induced photoluminescence from gallium doped zinc oxide thin films: Influence of doping and energetic ion irradiation

Himanshi Gupta[1], Jitendra Singh[1], R. N. Dutt[1], Sunil Ojha[1], Soumen Kar[1], Ravi Kumar[2], V. R. Reddy[3] and Fouran Singh[1]

[1]Department Inter University Accelerator Centre, New Delhi -110067, India.
[2]Centre of Materials Science and Engineering, National Institute of Technology, Hamirpur (H.P.) – 177005, India.
[3]UGC DAE Consortium for scientific research, Khandwa Road Indore 452017, India.

Research in ZnO remains a matter of interest due to its interesting and unique properties. Zinc oxide is an n-type semiconductor having a stable hexagonal wurtzite structure at ambient conditions. ZnO has a direct wide band gap of 3.37 eV and large exciton binding energy of 60 meV at room temperature (RT). Due to these properties, ZnO has potential applications in optoelectronics devices from LED to solar cell. [1]. So there is a great eagerness to understand the optical properties of ZnO. Moreover, ZnO exhibit a strong UV emission with a broadly visible emission [2]. The origin of the UV emission band in ZnO is well established and assigned to the exciton recombination or band to band transition. In the present report, the defect induced photoluminescence behavior of the Ga doped ZnO (GZO) thin films with varying doping (Ga) concentration and with energetic ion irradiation has been investigated. The XRD spectra reveal that all films are polycrystalline in nature with the wurtzite crystal structure. The transmittance spectra show that all of the films have high transmittance in the visible region more than 75 %. The micro-photoluminescence (μ-PL) measurements were carried out to investigate the defect-related emission with the variation of doping concentration and ion irradiation. PL spectra reveal that all films showed near band edge (NBE) emission along with a broad visible emission band consists of violet, blue, green, and yellow emission bands. The intensity of these emission bands is found to be strongly dependent on the Ga doping concentration and ion irradiation. Interestingly, a pronounced violet emission band around 2.99 eV (415 nm) observed for highly Ga doped ZnO thin film, while an irradiated film with high ion fluence exhibit a strong green emission around 2.39 eV (519 nm). The origins of all the emission bands in the visible region are identified. Comparing experimentally observed emission energy and theoretically calculated defects level energy we propose that defects responsible for violet emission, blue emission, green emission, and yellow emission are Zn_i (+2/+1), extended state of Zn_i (+1/0), singly ionized V_O (+1/0), and transition between Zn_i (+2/+1) level and singly ionized VO (+1/0) respectively. As the concentration of Zn_i increases with increasing doping concentration and the concentration of VO defects increases with increasing ion fluence. For details, see the published article **[Himanshi Gupta *et al.* Phys. Chem. Chem. Phys. 2019, DOI: 10.1039/ C9CP02148E].**

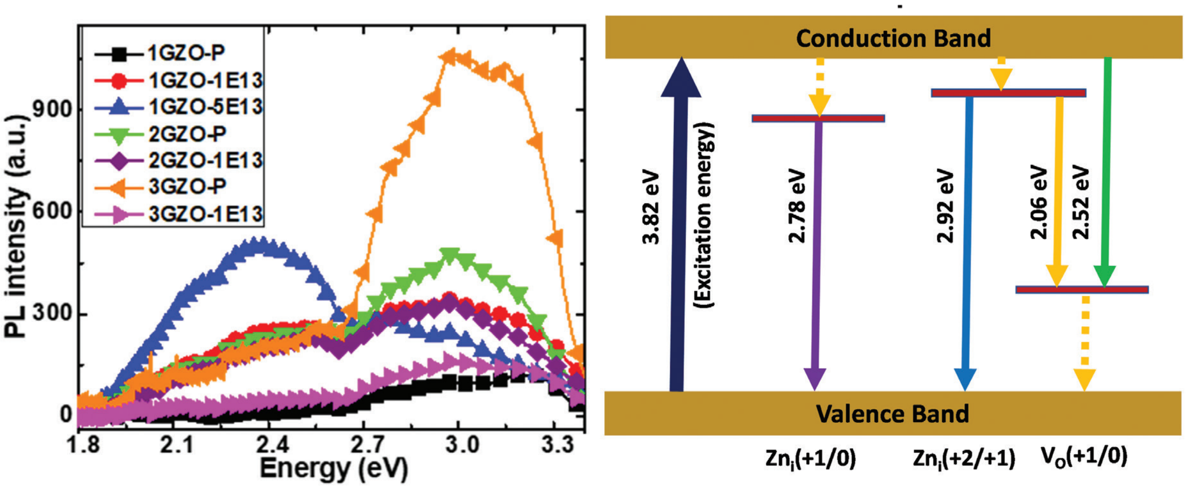

Figure: (Left) PL spectra of Ga doped ZnO thin films with varying Ga concentration and ion irradiation, (right) Schematic of defects energy levels responsible for visible emission.

REFERENCES:

[1] Ü. Ö. Hadis Morkoç, Zinc Oxide:Fundamentals,Materials and Device Technology (n.d.).

[2] W. Z. Xu *et al.,* Appl. Phys. Lett. **88,** 173506 (2006).

5.2.14 Evolution of symmetry forbidden and silent Raman modes of cadmium doped zinc oxide films activated by swift heavy ion irradiation

Naina Gautam[1], Himanshi Gupta[2], A. Kapoor[1] and Fouran Singh[2]

[1]Department of Electronic Science, University of Delhi South Campus, New Delhi-110023, India
[2]Material Science Group, Inter University Accelerator Centre, New Delhi -110067, India

In recent years wide band gap semiconductors have gained much research interest due to their potential applications in electronic and optoelectronic devices. Among which ZnO has been investigated widely for a long time. ZnO has a high band gap of 3.37 eV and high exciton energy of 60 meV at ambient conditions. Due to which it is used in a large number of applications from LED to solar cells [1]. In general optoelectronic devices gets effected by the behavior of long range longitudinal phonon modes (LO) of a material. Although there are a huge number of Raman study on ZnO yet detailed study of Raman spectra of ZnO thin films with ion irradiation is limited. Previously, effect of ion irradiation on nano-crystalline ZnO thin films were reported by our group [2]. In the present study, origin of the evolution of Raman modes from cadmium doped zinc oxide thin films are reported under swift heavy ion irradiation by performing the systematic micro-Raman investigations at various ion fluences and energy deposited into the lattices. Films were also well characterized for their structural and morphological properties. It is reported that Raman spectra of silver irradiated films show that the E_2(high) peak intensity reduces with peak broadening upon an increase in ion fluences, but not completely disappeared like in the case of undoped zinc oxide films. Evolution of intense A_1(LO) peak was also observed along with significant softening and understood by phonon localization due to a high density of defects induced by irradiation. On the other hand, irradiation by oxygen ions induces relatively strong A_1(TO) and B1(low) modes including the non-appearance of A_1(LO) mode, which were supposed to be symmetry forbidden in back-scattering and silent modes, respectively. Thus, the present study provides better experimental insights about the Raman modes for their possible implications in optoelectronic devices. For details, see the published article **[Naina Gautam *et al.* Physica B 570 (2019) 13] [3].**

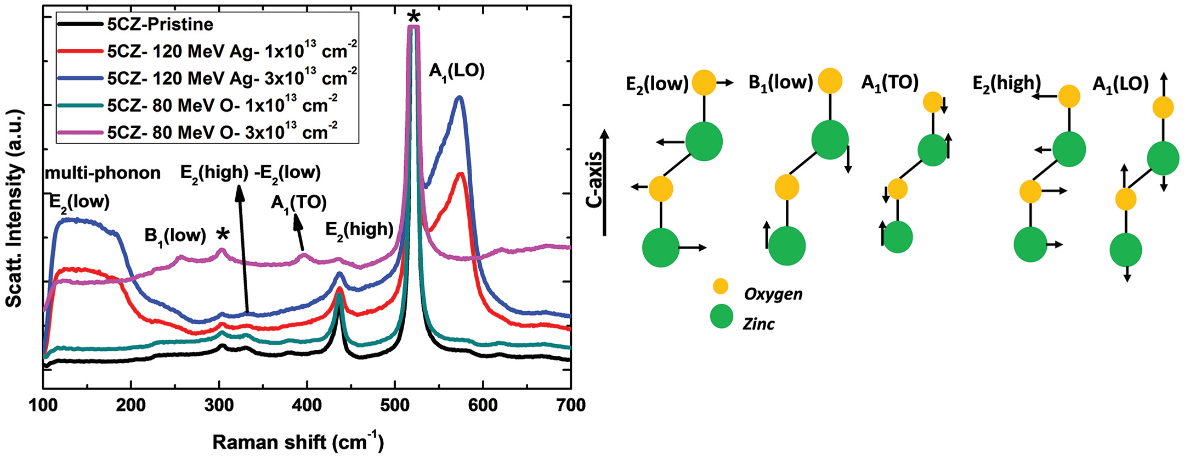

Figure: (Left) Raman spectra of pristine and irradiated thin films with 120 MeV Ag^{9+} ions and 80 MeV O^{6+} ions at varying of 1×10^{13} ions/cm^2 and 3×10^{13} ions/cm^2, (right) Schematics of the symmetry of various phonon modes of ZnO.

REFERENCES:

[1] Ü. Ö. Hadis Morkoç, Zinc Oxide:Fundamentals,Materials and Device Technology (n.d.).

[2] F. Singh, R. G. Singh, V. Kumar, S. A. Khan, and J. C. Pivin, J. Appl. Phys. **110,** 083520 (2011).

[3] N. Gautam, H. Gupta, A. Kapoor, and F. Singh, Phys. B Condens. Matter **570,** 13 (2019).

5.2.15 Tailoring dielectric properties and multiferroic behavior of nanocrystalline $BiFeO_3$ via Ni doping

Nadeem M.[1], Khan Wasi[2], Khan Shakeel[1], Husain Shahid[2] and Ansari Azizurrahaman[3]

[1]Department of Applied Physics, Z.H. College of Engineering & Technology, Aligarh Muslim University, Aligarh-202002, India.
[2]Department of Physics, Aligarh Muslim University, Aligarh-202002, India.
[3]Department of Materials Science Programme, Indian Institute of Technology Kanpur, Kanpur-208016, India.

In order to tailor the multiferroic as well as dielectric properties, we have synthesized bismuth ferrite, BiFeO3 (BFO) and Ni-doped BFO nanoparticles of composition $BiFe_{1-x}Ni_xO_3$ ($0 \leq x \leq 0.07$) via sol-gel method. [*for details, see Mater. Res. Express 5 (2018) 065506*]. The influence of Ni-doping at Fe site of $BiFeO_3$ on the structural, dielectric and multiferroic properties was investigated via various characterization techniques such as Raman spectroscopy, Vibrating sample magnetometer, polarization-electric field (P-E) loop tracer and LCR meter. The Raman spectra reveal the rhombohedral distorted perovskite structure of the samples in the R3c space group. The frequency dependent dielectric measurements at room temperature show that the dielectric constant for the pristine sample is an order of magnitude lower than the 1% Ni-doped BFO sample. It is also evident that the ac conductivity increases with the increase in frequency as well as Ni content. Further, the universal dielectric response (UDR) phenomenon is responsible for the dielectric behavior of all the samples in whole frequency range except for $BiFeO_3$ and $BiFe_{0.97}Ni_{0.03}O_3$ samples. These samples exhibit deviation from UDR phenomenon at higher frequencies. The room temperature hysteresis (M-H) loops exhibit the saturation in magnetization at higher magnetic fields. The result demonstrates a significant influence on the saturation magnetization with the Ni doing in BFO, prompting the ferromagnetic nature of the samples. The saturation magnetization of 7% Ni-doped sample is approximately six times higher than the pristine one. The saturated P-E hysteresis loops establish the ferroelectric nature of the synthesized samples that are enhanced significantly on Ni doping. Thus, the doping of Ni in $BiFeO_3$ improves the multiferroic properties of the matrix. *[for details, see J. Appl. Phys. 124 (2018) 164105].*

In order to investigate the effects of the swift heavy ion (SHI) irradiation on the structural, optical, electrical and magnetic properties of $BiFeO_3$ and Ni-doped $BiFeO_3$ thin films, we have deposited the pristine and, 1%, 3% and 5% Ni-doped $BiFeO_3$ thin films on Si (100) wafer using pulsed laser deposition (PLD) technique at UGC-DAE CSR, Indore. The distance between the target and substrate was adjusted at 5 cm and the laser energy during the deposition was 250 mJ with repetition rate of the target as 10 Hz. These films have been deposited at two different oxygen partial pressure i.e. 100 mTorr and 300 mTorr. During the deposition substrate temperature was maintained at 700 ºC and all the films were deposited for 30 minutes. After phase analysis the films were irradiated using 15 UD Pelletron tandem accelerator at Inter University Accelerator Centre (IUAC), New Delhi with 120 MeV Ag^{9+} ions at three different ion fluences i. e. 1×10^{13} ions/cm^2, 5×10^{13} ions/cm^2 and 1×10^{14} ions/cm^2.with current of 1pnA (particle nanoampere). All the films were fixed to the target ladder placed inside the high vacuum (~10^{-6} torr) chamber during irradiation. Irradiation was performed in the direction perpendicular to the sample surface. The ion beam was focused to a spot of 10 mm diameter and then scanned over an area of 1×1 cm^2 using magnetic scanner to cover the complete sample surface for uniform irradiation. To investigate the structural changes because of the irradiation, we have carried out the XRD measurements of the irradiated thin films at room temperature at IIT Kanpur. To study the effects on optical, electrical and magnetic properties of the irradiation the other measurements and analysis are under process.

References:
[1] M. Nadeem, Wasi Khan, Shakeel Khan, Mohd Shoeb, Shahid Husain and Mohammad Mobin, Mater. Res. Express 5 (2018) 065506.
[2] M. Nadeem, Wasi Khan, Shakeel Khan, Shahid Husain and Azizurrahaman Ansari, J. Appl. Phys. 124 (2018) 164105.

5.2.16 Swift Heavy Ion Irradiation Induced Modifications in Graphitic Nanocomposites

Pankaj Singh Rawat[1], R. C. Srivastava[1], Gagan Dixit[1], G. C. Joshi[1] and K. Asokan[2].

[1]Dept. of Physics, CBS&H, G.B. Pant Univ. of Ag. & Tech. Pantnagar
[2]Inter-University Accelerator Centre, New Delhi-110067, India.

Nanocomposites derived from graphene oxide (GO), reduced grapheme oxide (rGO) and magnetic nanoparticles (ferrites) are of larger interest due to variety of possible applications such as in fabricating functional nanocomposites, waste water treatment and electromagnetic wave absorbers etc. Ferrites play useful role in many technological applications due to their high electrical resistivity and sufficiently low dielectric losses over a wide range of frequency [1-2]. The present research work is focused on synthesis and investigation of graphene oxide based nickel ferrite (GO/$NiFe_2O_4$) nanocoposites before and after SHI irradiation. X-ray diffraction (XRD), energy dispersive X-ray spectroscopy (EDX), Raman spectroscopic measurements and temperature dependent dielectric measurements of pristine samples were carried out at IUAC, New Delhi. Materials science beam-line, 15 UD Pelletron-Accelerator facility of Inter-University Accelerator Centre (IUAC), New Delhi was used to irradiated the samples by 100 MeV Au ions.

Experimental Details

XRD pattern of samples confirmed the pure phase of GO, $NiFe_2O_4$, $MnFe_2O_4$ and GO/$NiFe_2O_4$ composites. Room temperature Raman spectroscopic measurements showed the characteristic D-band at 1357 cm^{-1} attributed to the sp^3 defects in the sp^2 graphitic lattice and G-band at 1614 cm^{-1} from sp^2 carbon atoms in GO samples. EDX study confirmed the proper stoichiometry for all the samples (Ni:Fe, Mn:Fe – 1:2, C:O – 1.04 in GO and C:O – 8.09 in rGO). An increased C/O (at. wt. %) ratio (from 1.04(GO) to 8.09(RGO)) confirmed the reduction process in GO. Significantly high dielectric loss was observed in GO due to its conductivity. The dielectric constant showed a decrease when the composite is sintered at higher temperature. The dielectric constant values at 1MHz were 313, 103, 101, 68 and 39 for $NiFe_2O_4$, GO, GO/$NiFe_2O_4$, GO/$NiFe_2O_4$ (500ºC), GO/$NiFe_2O_4$ (800ºC) samples respectively [Fig.1 (a, b)]. The high dielectric loss observed in GO is due to its partially conducting nature, whereas the addition of $NiFe_2O_4$ nanoparticles lead to the reduction in electronic conductivity. The order of resistance of GO/$NiFe_2O_4$ composite (~10^3 Ohm) was found to be less than that of GO and $NiFe_2O_4$ (~10^6 Ohm) samples due to the partial reduction of GO into rGO while forming GO/$NiFe_2O_4$ composite. The partial reduction of GO into rGO in GO/$NiFe_2O_4$ composite was also confirmed in X-ray absorption spectroscopic (XAS) characterization (C-k edge, 280-315 eV and O-k edge, 520-555 eV) of the samples.

The selected samples of graphene oxide and composite were irradiated with 100 MeV Au - ions at fluences of ~ 5E11, 5E12 and 1E13 ion/cm^2. The beam current was kept constant at 1 pnA (particle-nano ampere). The energy loss, ion beam energy and projected range of ions in material were obtained using SRIM (2013) software before SHI irradiation. The optical band gap of pristine and samples irradiated at fluences of 5E11, 5E12 and 1E13 ion/cm2 was estimated from DRS spectrum using Kubelka-Munk function. A decrease in band gap from 1.64 eV for pristine $NiFe_2O_4$ to ~ 1.59 eV for irradiated $NiFe_2O_4$ samples [Fig.2 (a, b)] and from 1.67 eV for pristine GO/$NiFe_2O_4$ composite to ~1.64 eV for irradiated composite samples [Fig.3 (a, b)] was observed with an increase in fluence. This can be attributed to the introduction of defect levels by ion irradiation causing increase in charge flow in irradiated samples. Further characterization of pristine and irradiated samples and analysis of data is in underway.

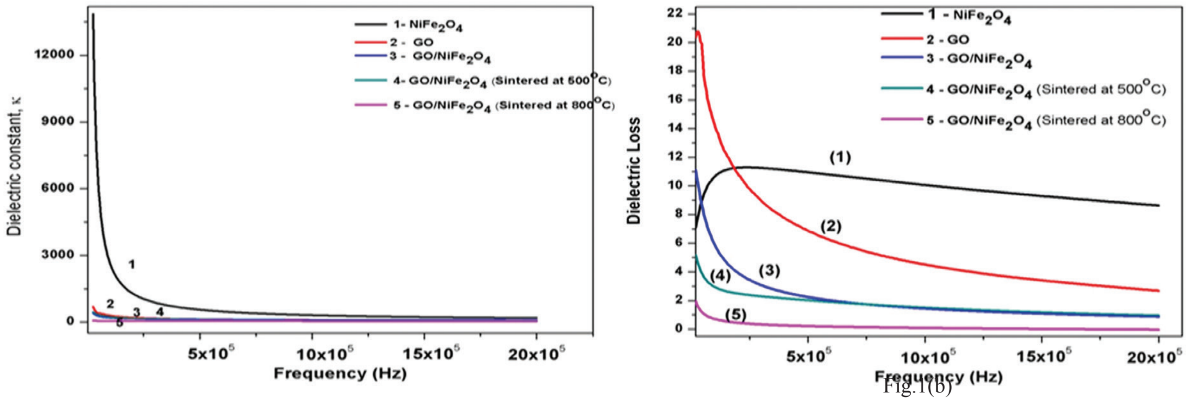

Fig.1(a)

Fig.1(b)

Figure 1. (a) Dielectric constant vs Frequency (b) Dielectric loss vs Frequency of pristine samples.

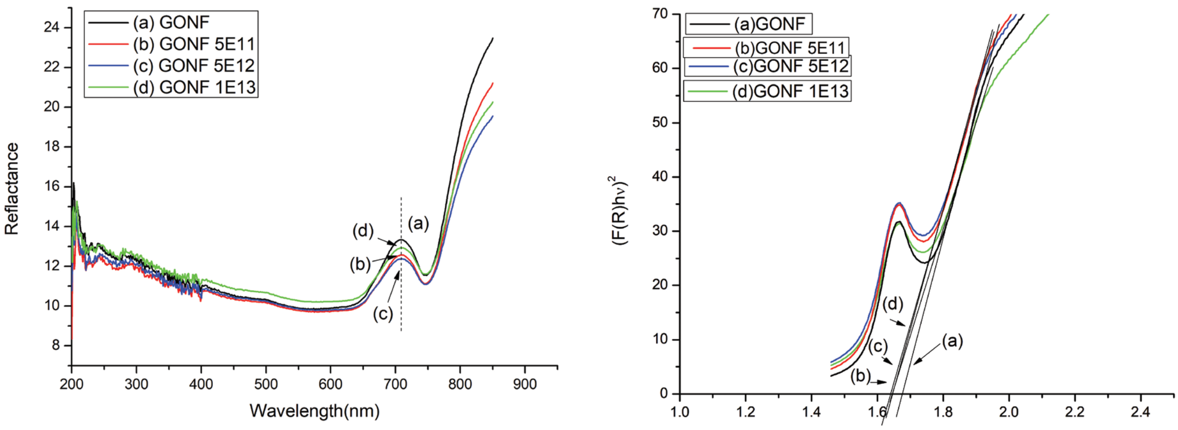

Fig.2(a)

Fig.2(b)

Figure 2. (a) DRS spectrum and (b) Tauc plot of pristine and irradiated $NiFe_2O_4$ samples.

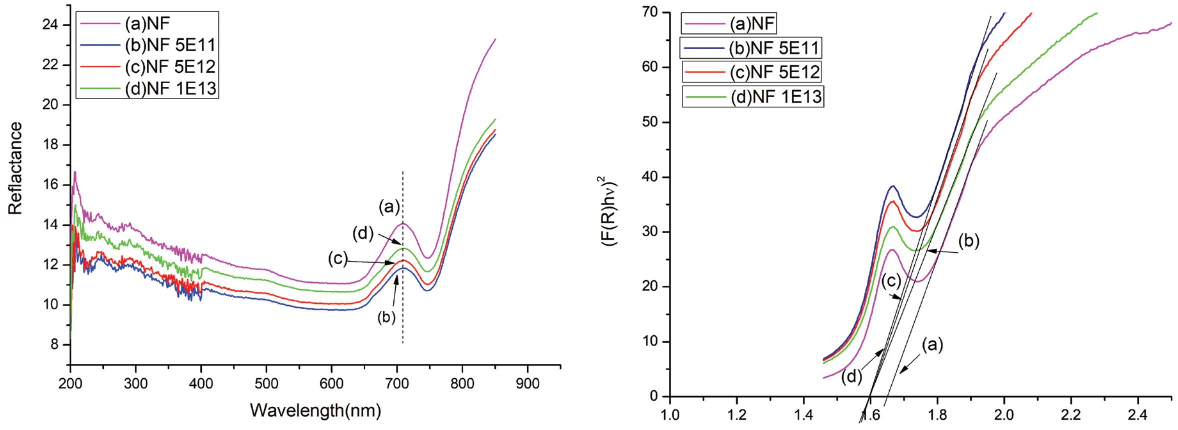

Fig.3(a)

Fig.3(b)

Figure 3. (a) DRS spectrum and (b) Tauc plot of pristine and irradiated $GO/NiFe_2O_4$ samples.

REFERENCES:

[1] S. Chen *et al.,* ACS Nano. 4,2822 (2010)
[2] Y. Song *et al.,* Electrochim. Acta. 71, 58 (2012)
[3] U. Dembereldorj *et al.,* Photochem. Photobiol. 90, 659(2014)

5.2.17 Effect of Si ion irradiation on structural and optical properties of pure and Ag doped $Ge_2Sb_2Te_5$ (GST) thin films

Neetu Kanda[1], Anup Thakur[2], Fouran Singh[3], A.P. Singh[1*]

[1] Department of Physics, Dr. B. R. Ambedkar National Institute of Technology, Jalandhar-144011, India.
[2] Department of Physics, Punjabi University, Patiala, Punjab 147002, India
[3] Inter-University Accelerator Centre, New Delhi, Delhi – 110067

The most promising materials for rewritable storage are chalcogenide alloys. These materials act as active media for phase change memory devices. In our study, we study phase change materials for optical storage devices. PCM material with most favourable properties is $Ge_2Sb_2Te_5$ (GST), which is the focus of the present study. GST thin films are irradiated with Silicon ions at high energy. These high energy ions introduce defects in these films, which will ultimately change their optical and structural properties. Slight crystallization is observed for highest irradiation dose which is also indicated by the decrease in bandgap with irradiation.

Experimental Details

Bulk alloy of GST were prepared by melt quenching technique. Thin films of these samples were deposited on glass substrate by thermal evaporation technique with the help of Hind HIVAC system (Model: BC-300), at deposition rate 2-3 Å /s under the base pressure of 2.4×10^{-6} mbar. The film thickness was measured using digital thickness monitor during thermal deposition. These films were irradiated with Si^{6+} ions at different fluences at 120 MeV energy. These films are characterized using XRD, FESEM and UV-Vis-NIR spectroscopy to study the changes introduced due to ion irradiation.

Results

$Ge_2Sb_2Te_5$ is a chalcogenide alloy which is used in many phase change applications like electrical and optical non-volatile memory and photonic devices etc. [1,2,3]. This material shows drastic contrast in their optical and electrical properties while changing phase from amorphous to crystalline. These properties can be modified by swift heavy ion irradiation. In the present work, thin films of pure GST are irradiated with Si^{6+} ions with 120 MeV energy at 5×10^{11}, 1×10^{12}, 5×10^{12}, and 1×10^{13} ions/cm^2 fluences and these samples are named as G0, G5e11, G1e12, G5e12 and G1e13 respectively. The xrd spectra of G1e13 is shown in fig1. The highly irradiated film show one peak at 29.26˚ which shows the fcc phase of these films after ion irradiation. However other films do not show any phase transformation. FESEM images of G0, G5e11, G5e12 and G1e13 films are shown in fig2. It is clearly visible from fig2 that with the increase in irradiation fluence, there is generation of crystal nuclei, which ultimately leads to phase change for higher irradiation dose. Moreover, the bandgap is obtained from transmission spectra using tauc plot. Table1 shows the different values of bandgap with different fluence of irradiation. This shows that with irradiation bandgap decreases, which ensures the generation of crystal nuclei and hence crystallization with highest fluence.

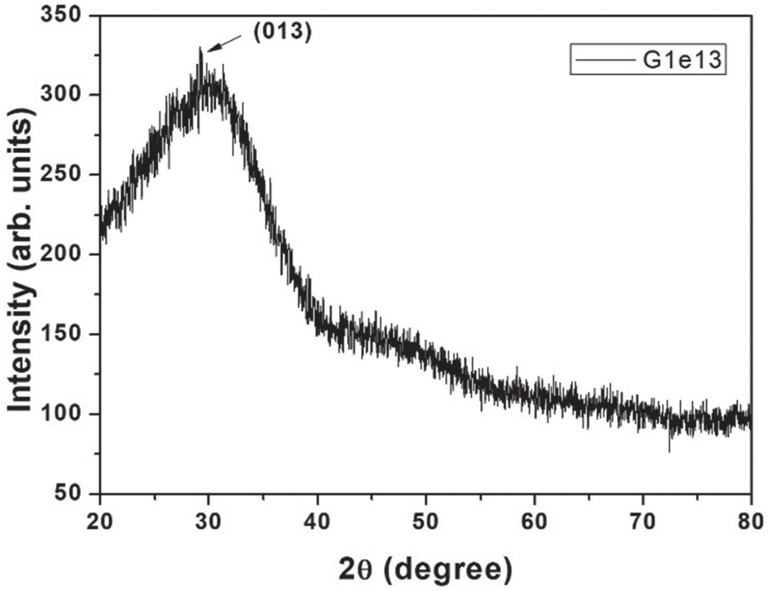

Fig1. XRD spectra of G1e13.

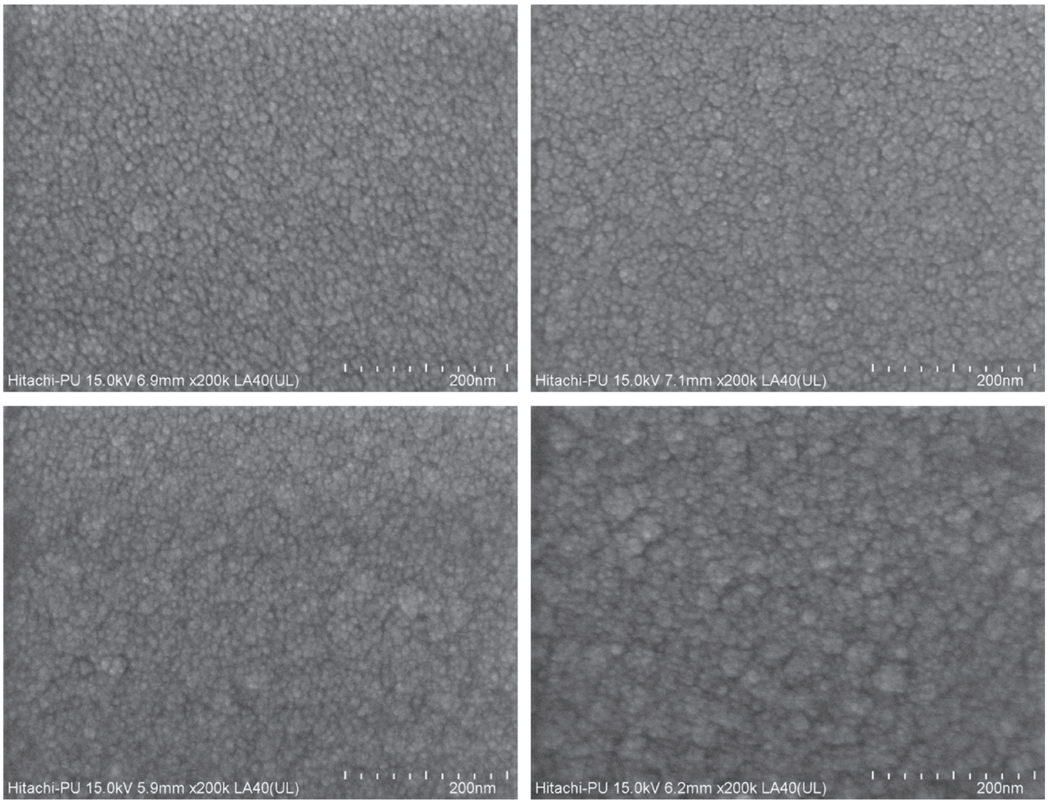

Fig2. FESEM images of G0, G5e11, G5e12 and G1e13.

Table1: bandgap of pure and irradiated thin films.

Sample	G0	G5e11	G1e12	G5e12	G1e13
Bandgap (eV)	0.65	0.64	0.64	0.58	0.55

REFERECNES

[1] G. Atwood. Phase-Change Materials for Electronic Memories. Science, 321:210, 2008.

[2] H. Lv, P. Zhou, Y. Lin, T. Tang, B. Qiao, Y. Lai, J. Feng, B. Cai, and B. Chen. Electronic properties of GST for non-volatile memory. Microelectronics Journal, 37:982, 2006.

[3] P. Singh, A. P. Singh, N. Kanda, M. Mishra, G. Gupta, and A. Thakur. High transmittance contrast in amorphous to hexagonal phase of Ge2Sb2Te5: Reversible NIR-window. Applied Physics Letters, 111:261102, 2017.

5.2.18 Enhanced thermoelectric properties of SHI irradiated metal chalcogenide thin films

P. Matheswaran[1], B. Gokul[1], R. Sathyamoorthy[1], K. Asokan[2] and D. Kanjilal[2]

[1]Department of Physics, Kongunadu Arts and Science College, Coimbatore - 641029, India
[2]Inter University Accelerator Centre, New Delhi - 110067, India

Experimental Details

The as grown $In_2(Te_{1-x}S_{ex})_3$ films were subjected to SHI irradiation ($In_2(Te_{1-x}S_{ex})_3$: 120 MeV Au, 120 MeV Ni and 120 MeV Ag) for different ion fluences (0.5 pnA) in the range 10^{12}-10^{13} ions/cm^2. The energy loss and projected range of the ions in the target was calculated with the help of SRIM-2008 simulation program.

Results and discussion

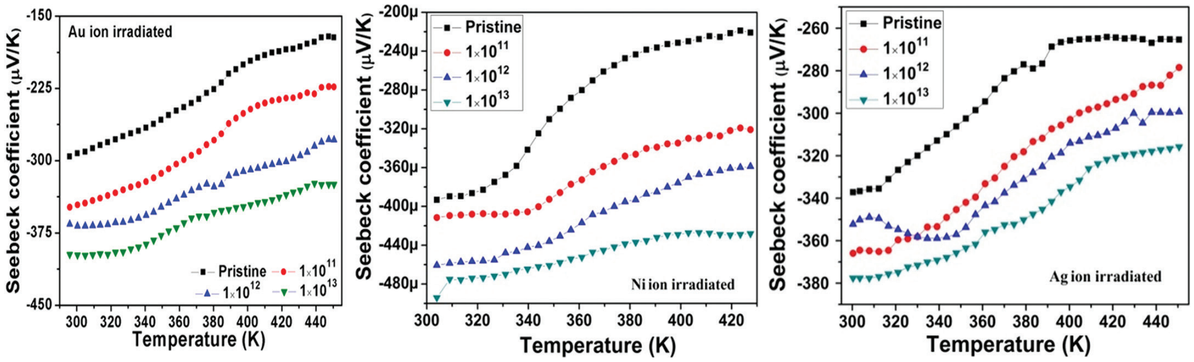

Figure.1 Seebeck coefficient (S) of all pristine and irradiated $In_2(Te_{1-x}S_{ex})_3$ thin film

XRD patterns of all the pristine and irradiated $In_2(Te_{1-x}S_{ex})_3$ thin films confirms formation of ternary In_2(Te.Se)3 phase, binary In_2Se_3 and In_2Te_3 phase (not shown here).

The FESEM image shows the uniform fragmentation of grains throughout the surface of the sample after irradiation. The negative value of Seebeck coefficient confirms the nature of n-type conductivity in the pristine and Ni ion irradiated $In_2(Te_{1-x}S_{ex})_3$ (x=0.06) samples. The Seebeck coefficient value for pristine sample is found to about ~196 μVK^{-1} and it is enhanced to ~347 μVK^{-1} at the higher fluence of 1×10^{13} ions/cm^2 at 420 K. The power factor value is about ~3.80 $\mu W/K^2m$ corresponds to sample irradiated at the fluence of 1×10^{13} ions/cm^2, shows 3 times greater as compared to pristine sample value of ~1.28 $\mu W/K^2m$ [1].

The maximum Seebeck coefficient value for the pristine $In_2(Te_{1-x}S_{ex})_3$ (x=0.02) sample is about ~221 μVK-1. At higher fluence (Au) of $1\times10_{13}$ ions/cm$_2$, the Seebeck coefficient value is found to ~427 μVK^{-1} at 400 K, shows almost 50% greater than the pristine sample value. The maximum power factor is found to ~1.23 $\mu W/K^2m$ and 4.91 $\mu W/K^2m$ are corresponding to the pristine and 1×10^{13} ions/cm^2 irradiated films. It shows irradiated sample value is 3 times greater as compared to pristine sample and hence, the enhancement to the Ni ion irradiated films. So that, charge scattering due to the grain boundary lead to significant improvement in thermoelectric properties of the irradiated films [2]. These results may find great interest in thermoelectric device applications.

Additionally, we have selected Ag^{7+} ion to enhance the thermoelectric properties of $In_2(Te_{1-x}S_{ex})_3$ (x=0.15) films. The maximum Seebeck coefficient value for the pristine sample is about ~265 μVK^{-1}. At higher fluence of 1×10^{13} ions/cm^2, the Seebeck coefficient value is found to ~335 μVK-1 at 400 K, shows almost 30% greater than the pristine sample value. All the Seebeck coefficient values are in negative shows the nature of n-type conductivity in the films. Further, the maximum power factor is found to ~1.98 $\mu W/K^2m$ and 3.48 $\mu W/K^2m$ are corresponding to the pristine and 1×10^{13} ions/cm^2 irradiated films. It shows irradiated sample value is enhanced as compared to pristine sample. Moreover, the improved thermoelectric properties of Ag ion irradiated $In_2(Te_{1-x}S_{ex})_3$

Summary

Thermoelectric performance of As grown and SHI ion (Au, Ni and Ag) irradiated $In_2(Te_{1-x}Sex)_3$ (x=0.06, 0.02 and 0.15) thin films was measured using Bridge method. The effects of SHI irradiation on structural, morphological and electrical transport properties were studied. The Seebeck coefficient and power factor values are enhanced with SHI irradiation in comparison to the as grown samples. In particular, Ni ion irradiated samples shows better thermoelectric performance and this could be due to the irradiation induced defects in the samples.

REFERENCES:

[1] J. Martin, L. Wang, L. Chen, G. S. Nolas, Phys. Rev. B - Condens. Matter Mater. Phys.79 (2009) 115311.
[2] A. Popescu, L.M. Woods, J. Martin, G.S. Nolas, Phys. Rev. B. 79 (2009) 205302.

5.2.19 Study of gas sensing behavior of 2D MoS_2 after irradiation by Au and Li ions

Rahul Kumar[1], Neeraj Goel[1], Pawan Kulriya[2] and Mahesh Kumar[1*]

[1]Department of Electrical Engineering, Indian Institute of Technology, Jodhpur-342037, India.
[2]Inter-University Accelerator Centre, New Delhi-110067, India.

We want to study of gas sensing behavior of 2D MoS_2 after irradiation by the Gold (Au) and Lithium (Li) ions. The gas sensing behavior will be investigated of the irradiated MoS_2 film by measuring the change in resistance value of the device before and after exposure the gas. The selectivity, stability aspects of the fabricated sensor from irradiated MoS_2 would also be examined. Here, we synthesized horizontally and vertically aligned MoS_2 by the conventional chemical vapor deposition process using MoO_3 and sulfur solid precursor and also fabricated the wafer scale MoS_2 through sulfurization in CVD to RF sputtering deposited Mo film on SiO_2 substrate. After irradiation the MoS_2 films of different structures, we performed the Raman and SEM experiments at room temperature. Active Raman peaks of MoS_2 show changes in its position, intensity and fwhm because of increased defects with enhanced fluence of the ions. It was also noted that surface morphology of horizontally aligned MoS_2 was also changed with high fluence. The gas sensing experiments to examine the gas sensing behavior of ion irradiated MoS_2 are in progress.

Experimental Details

2D MoS_2 flakes were synthesized using two solid precursor molybdenum trioxide (MoO_3) and sulfur (S) by three zone chemical vapor deposition (CVD) technique through kinetically controlled rapid growth processes. The substrate was put vertically away from MoO_3 in same alumina boat in the centre zone and annealed MoO_3 at 1000 ºC for 60 min at atmospheric pressure and high heating rate 50 ºC per min was used to increase the temperature. Sulfur was put in upstream heated at 180 ºC and Ar gas flow was 160 sccm through all reaction time. Finally, the furnace was turned off and the tube was cooled naturally back to room temperature. Additionaly, the MoS_2 film was also grown using a two-step process: deposition of a ~4 nm DC sputtered Mo film followed by sulfurization. During the deposition of the Mo film, the chamber pressure, DC power and Ar gas flow were maintained at 6.5×10^{-3} mbar, 40 W and 40 sccm, respectively. The sulfurization of the deposited Mo film was done using the CVD technique.

To observe the effect of SHI irradiation on gas sensing behavior of MoS_2 depsoited film, we irradiated these thin films with 100 MeV Au ions at three fluences (1×10^{11}, 1×10^{12}, and 1×10^{13} ions/cm^2) using the Pelletron accelerator at IUAC, New Delhi. Few CVD grown MoS^2 samples were also irradiated using 50 MeV Li ions at fluences of 1×10^{11}, 1×10^{12}, and 1×10^{13} ions/cm^2. The effects of ion irradiation on structural properties of MoS_2 are investigated through Raman spectroscopy. The formation of peripheral fragmentation was observed after ion irradiation, which influences the gas sensing mechanism at the surface.

5.2.20 Swift Heavy Ion (SHI) Irradiation Effects on Multiferroic BFO Thin Films

Venkatapathy Ramasamy[1], Asokan Kandasami[2], Indra Sulania[2], Devarani Devi Kshetrimayum[3] and Ramesh Kumar Gubendiran[1*]

[1]Department of Physics / UCE Arni, Anna University, Tamil Nadu -632326, India.
[2]Materials Science Division, Inter-University Accelerator Centre, New Delhi 110067, India.
[3]Pelletron and Negative Ion Implanter laboratory, IUAC, New Delhi 110067, India.
[*]E-mail: rameshvandhai@gmail.com

Thin films of Bismuth ferrite [$BiFeO_3$ - BFO] were irradiated using Ti^{7+} at various ion fluences. Upon irradiation, the multiferroic BFO thin films have been characterized using Grazing Incidence angle X-Ray Diffraction (GIXRD), UV-Vis NIR Spectroscopy, Field emission scanning electron microscopy (FESEM) and I-V measurements. Irradiation induced modifications on the structural, optical and Leakage Current properties have been studied in detail.

Results

The crystalline structure of deposited thin films of pristine and ion irradiated BFO was characterized by Grazing incidence angle x-ray diffraction (GIXRD). The GIXRD patterns of the thin films were indexed for a rhombohedral structure, and the BFO thin films grown on ITO substrate exhibited single phase perovskite with secondary phases.

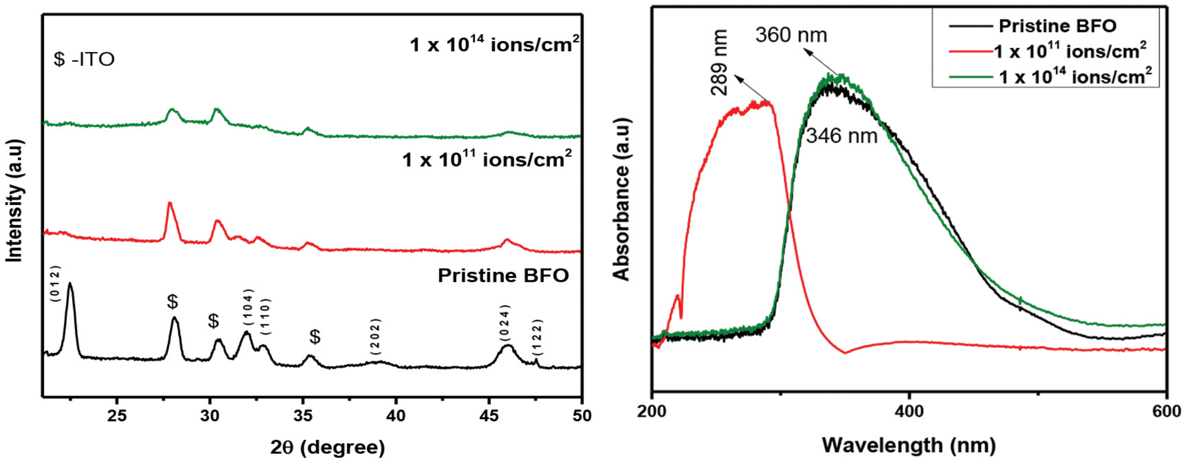

(a) GIXRD (b) UV-Vis NIR Spectroscopy

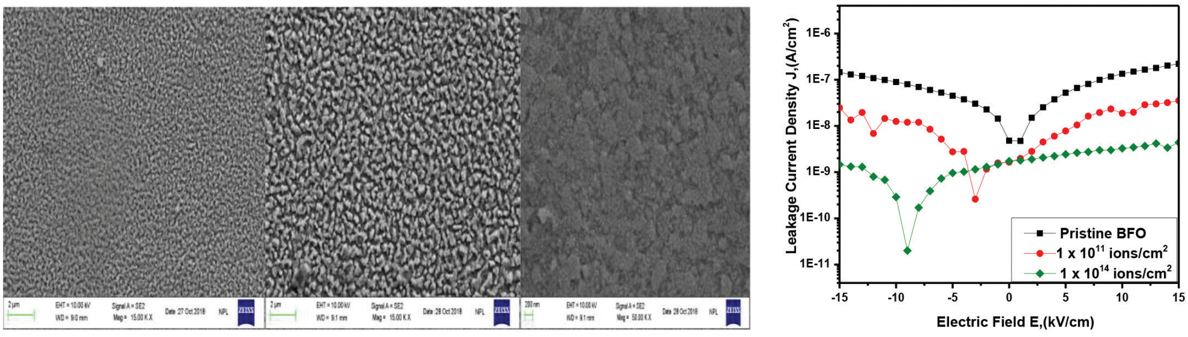

(c) FESEM (d) I-V measurements

REFERENCES:

[1] Q.H. Jiang, C.W. Nan, journal of Amer.cera.soci. 89 (2006) 2123-2127.

[2] Dash B N, Mallick P, Dash P, Biswal R, Jai prakash, TripathI A, Kanjilal D, Mishra N C, Bull.Mate. Scie. 36 (2013) 813–818.

[3] Linlin Zhang, Jian Yu, Jour. of mater. Scie.27 (2016) 8725-8733.

5.2.21 Effect of 120 MeV Ni^{10+} and Ag^{7+} swift heavy ion irradiation on CdSe and CdS nanocrystalline thin films

Pijush Ch. Dey[1], Simi Debnath[1], Debojyoti Nath[1], Fouran Singh[2] and Ratan Das[1*]

[1]Department of Physics, Tripura University, Suryamaninagar-799022, India.
[2]Inter-University Accelerator Centre, New Delhi-110067, India.

We have prepared CdSe and CdS nanoparticles using a wet-chemical method and then deposited on silicon substrate to study the effect of swift heavy ion irradiation. The prepared CdSe and CdS nanocrystalline thin films have been irradiated with 120 MeV swift Ni^{10+} and Ag^{7+} ions having fluences of 1×10^{12} and 3×10^{13} ions/cm^2. Structural analysis of the nanocrystalline thin films has been studied before and after the irradiation, through X-Ray diffraction and Raman Study, whereas the morphological properties have been studied using SEM and TEM. Further, optical properties has been studied through UV-Vis spectrometer and Photoluminescence.

From the study of the Raman spectra of CdSe and CdS, it has been found that longitudinal optical (LO) phonons mode dominates, which may be attributed to the lattice vibration of the nanocrystals and a weaker mode arises due to second order Longitudinal optical (2LO) phonon. It has been observed that for low fluence irradiation, an increment in LO peak occurs, whereas, a drastic decrease in LO peak has been observed at maximum fluence. This variation of the intensity of LO peak may be attributed to the accumulation of defects during irradiation, as well as the associated bond distortions and tensile stress. Further, X-Ray study reveals a cubic to hexagonal phase transition for both the materials, with a different fraction of hexagonal phase depending on the electronic energy loss of the incident ion. Variation in the elastic properties of the pristine and the ion irradiated materials have been studied using Williamson-Hall, Warren-Averbach and Variance method based on the broadening of the XRD peak. It has been observed that the value of microstrain and the dislocation density also get increased after the irradiation, due to the change in the lattice structure after the irradiation. SEM and TEM analysis confirms the increase in the average particle size. Further to study the variation of the optical properties, UV-Vis and Photoluminescence analysis has been employed, which reveals an increase in PL intensity with increase in fluence with decease in the energy band. This may be attributed to the defect state formation due to SHI irradiation.

REFERENCES:

[1] Vishnu Chauhan, T. Gupta, Paramjit Singh, P.D. Sahare, N. Koratkar, Rajesh Kumar1, Physics Letters A 383 (2019) 898-907.

[2] V.V. Ison, A. Ranga Rao, V. Dutta, P.K. Kulriya, D.K. Avasthi, S. K. Tripathi J. Appl. Phys. 106, (2009) 023508

[3] S. Negi, M. P. S. Rana, F. Singh, R. C. Ramola J Sol-Gel Sci Technol (2015) 76:608–613

[4] A.Benyagoub, L.Thome, Phys.Rev.B 38 (1988) 10205.

5.2.22 Effect of 120 MeV Ag ion irradiation on gallium oxide thin films

Saurabh Yadav[1], Subhra Das[2], A. K. Patra[2], R. Singh[3] and Y. S. Katharria[1]

[1]PDPM Indian Institute of Information Technology, Design and Manufacturing, Jabalpur-482005, Madhya Pradesh
[2]Department of Physics, Central University of Rajasthan, Bandarsindri-305817, Rajasthan
[3]Department of Physics, Indian Institute of Technology Delhi, New Delhi-110016, Delhi

Gallium oxide (β-Ga_2O_3) is a wide bandgap semiconductor (E_g ~ 4.9 eV) which is stable both chemically and thermally, and is, thereby, suitable for operations under harsh chemical environment as well as at high temperatures [1]. It has found diverse applications in optoelectronic devices such as gas sensors, deep UV solar blind photodetectors [2], etc. The radiation hardness of β-Ga_2O_3 devices may be useful for space and military applications where issues of radiation tolerance are critical. Therefore, understanding the changes in the structural and optical properties of β-Ga_2O_3 caused by the ion irradiation effects is of critical importance. In this work, we have studied the irradiation effect of 120 MeV Ag^{9+} ions on β-Ga_2O_3 thin films.

Thin films of β-Ga_2O_3 were grown on silicon (100) and quartz substrates at room temperature using e-beam evaporation method. After deposition, the films were annealed at 900 °C for 30 min under oxygen environment to obtain stoichiometric, crystalline phase. Thereafter, swift heavy ion irradiation was carried out using 120 MeV Ag^{9+} ions with ion fluences (ϕ) of 1×10^{11}, 3×10^{11}, 5×10^{11}, 1×10^{12} and 5×10^{12} ions-cm^{-2}. X-ray diffraction (XRD) measurements were performed using a PANalytical-Empyrean system using CuK_α radiation with a wavelength of 1.5404 Å. UV-visible absorption measurements were carried out using a Hitachi U3300 dual beam spectrophotometer.

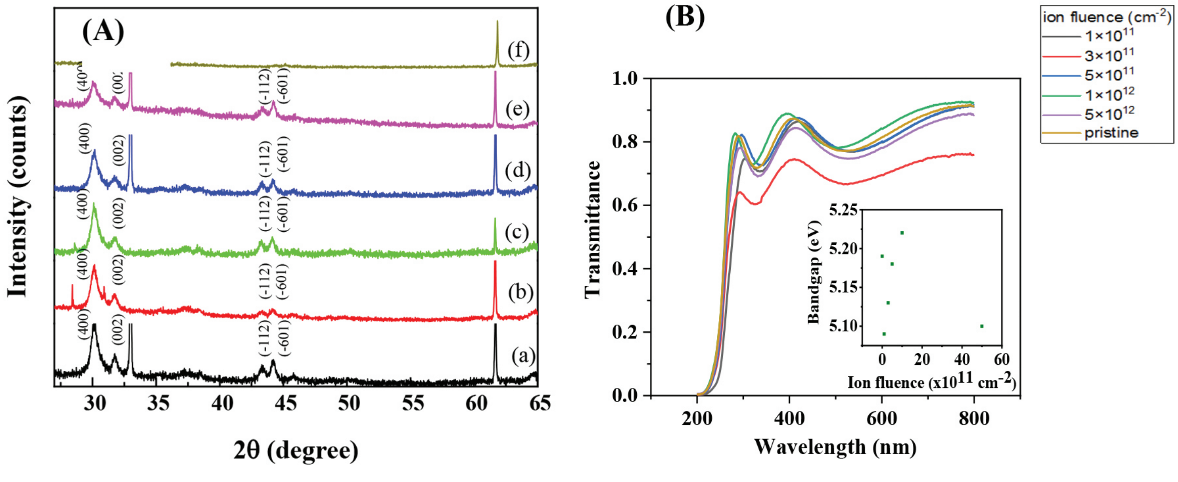

Fig.1. (A) XRD patterns; and (B) transmittance spectra of samples annealed at 900ºC, with ion fluences (ϕ), (a) $\phi = 0$, (b) $\phi = 1\times10^{11}$, (c) $\phi = 3\times10^{11}$, (d) $\phi = 5\times10^{11}$, (e) $\phi = 1\times10^{12}$, (f) $\phi = 5\times10^{12}$ ions-cm^{-2}. The inset of fig.1 (b) shows the variation of bandgap with ion fluence.

Fig.1 (A) shows XRD patterns of 120 MeV Ag^{9+} irradiated β-Ga_2O_3 thin films with ϕ varying from 1×10^{11} cm^{-2} to 5×10^{12} cm^{-2}. An increasing disorder and decrease in the crystalline size of β-Ga_2O_3 with increasing ϕ is obvious from the increasing FWHM and decreasing intensity of the peaks. Average crystallite size was ~ 13.6 nm for unirradiated thin film, and decreases to ~ 8 nm for the thin films irradiated at $\phi = 5\times10^{12}$ ions-cm^{-2}. Such a decrease in crystalline fraction under ion irradiation was also reported by Tracy et al. [3]. Fig.1 (B) shows the UV-visible absorption spectra of ion irradiated β-Ga_2O_3 thin films. For all wavelengths above 275 nm, transmittance of the films was more than 80%. The as-grown film has a sharp absorption edge at wavelength around 240 nm. This corresponds to a bandgap of ~5.19 eV. The bandgap remained almost constant within the range of 5.10 - 5.21 eV under ion irradiation suggesting the robust nature of the Ga_2O_3 against ion-irradiation and its suitability for space applications.

REFERENCES:

[1] M.A. Mastro and S.J. Pearton, ECS J. Solid State Sci. Technol. 6, P356 (2017).
[2] A. Pratiyush, S. Krishnamoorthy, and D. N. Nath, Appl. Phys. Lett. 110, 221107 (2017).
[3] C. L. Tracy, M. Lang, D. Severin, M. Bender, C. Trautmann, and R. C. Ewing, Nucl. Instrum. Meth. B 374, 40 (2016).

5.2.23 Electrocatalytic activity of ion implanted rGO/PEDOT:PSS hybrid nanocomposites towards methanol electro-oxidation

Bhagyalakhi Baruah[1], Ashok Kumar [1*], G.R. Umapathy[2] and Sunil Ojha[2]

[1]Material Research Laboratory, Department of Physics, Tezpur University, Tezpur 784028, Assam, India
[2]Inter University Accelerator Centre (IUAC), Aruna Asaf Ali Marg, New Delhi 110067, India

Nanocomposites of Reduced graphene oxide (rGO) and Poly (3,4-ethylenedioxythiophene): Polystyrene sulfonate (PEDOT:PSS) nanocomposites have been synthesized via *in situ* polymerization technique. The synthesized nanocomposite films have been implanted with Xe^+ ions at different fluences of 3.3×10^{14}, 3.3×10^{15} and 3.3×10^{16} ions cm^{-2}. FESEM images show the growth of carbon rich clusters in floral pattern at the fluence 3.3×10^{16} ions cm^{-2}. Raman spectra reveal the annealing of the nanocomposite at lower fluence of 3.3×10^{14} ions cm^{-2} and then increase in disorder parameter with further increase in ion fluence. The rGO/PEDOT:PSS hybrid nanocomposite implanted with 3.3×10^{16} ions cm^{-2} Xe^+ ions exhibits slightly different CV pattern with increase in fluence and at the fluence of 3.3×10^{16} ions cm^{-2}, drastic change in CV pattern is observed with lower oxidation potential (0.54 V) and higher anodic current density (48 mA cm^{-2}). The gradual change in CV pattern with fluence can be attributed to the gradual structural changes due to: (i) degassing, where the functional groups present in the nanocomposites transform to 'pre-carbon' structures, (ii) growth of carbon-rich clusters and formation of C=C bond network, (iii) the carbon clusters aggregate to form quasi-continuous carbonaceous layer and (iv) at the highest fluence i.e. 3.3×10^{16} ions cm^{-2}, the carbonaceous layer transforms to graphite like material [1]. 3.3×10^{16} ions cm^{-2} ion irradiated nanocomposite electrode exhibits enhanced cyclic stability of 93% as compared to the pristine one at 800th cycles.

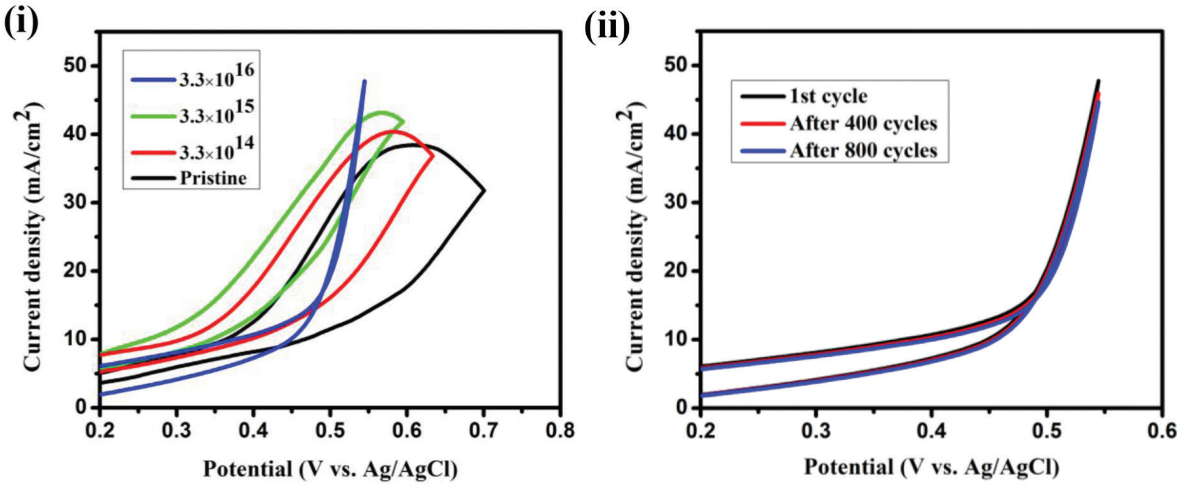

Figure: Cyclic voltammograms of pristine and irradiated rGO/PEDOT:PSS/ITO electrodes with different ion fluences in (i) presence of 0.5 M methanol containing 0.5 M NaOH solution at scan rate 50 mVs^{-1}.
(ii) cyclic stability of rGO/PEDOT:PSS/ITO electrode irradiated with 3.3×10^{16} ions cm^{-2} at a scan rate of 50 mVs^{-1}.

REFERENCES:

[1] V.N. Popok Rev. Adv. Mater. Sci 30 (2012) 1.

5.2.24 Ion irradiation study of Au-C_{60} nanocomposite thin film

Singhal Rahul*, Sharma Kshipra and Vishnoi Ritu

[1]Department of Physics, Malaviya National Institute of Technology-302017, India.

The interaction of light with metal nanoparticles is pointed out by Gustav Mie in 1908, this interaction results in oscillations of collective charge density confined to metallic nanostructures in resonance with the light field and this phenomena is known as surface plasmons resonance (SPR). Tuning of SPR is an interesting study and can be used in solar cells, sensors etc.

Here, we developed Au-C_{60} nanocomposite thin films using thermal co-evaporation method. Then ion irradiation was performed on the developed nanocomposite thin films at different fluences. After irradiating the films, we investigated the modifications occurred in the optical and structural properties of the films at different fluences.

The developed nanocomposite thin films were irradiated with swift heavy Au ions carrying energy of 120 MeV at various fluences using Pelletron accelerator at IUAC, New Delhi. The nanocomposite thin films were exposed to irradiation for an estimated time for each fluence. The films were irradiated at following fluences; 1e12, 3e12, 6e12, 1e13 and 3e13. The electronic (Se) and nuclear energy loss (Sn) for 120 MeV Au ions in Au-C_{60} nanocomposite film were estimated by SRIM 2013 program. After irradiating the films, we studied the modifications taken place in the optical, structural and electrical properties. In order to investigate the optical property, structural property, chemical property and electrical property, we used UV-visible spectroscopy, raman spectroscopy, XPS and I-V measurements and we obtained blue shift of ~117 nm in SPR wavelength. In this study, we got very interesting results which can be further used in the applications of sensors and solar cells.

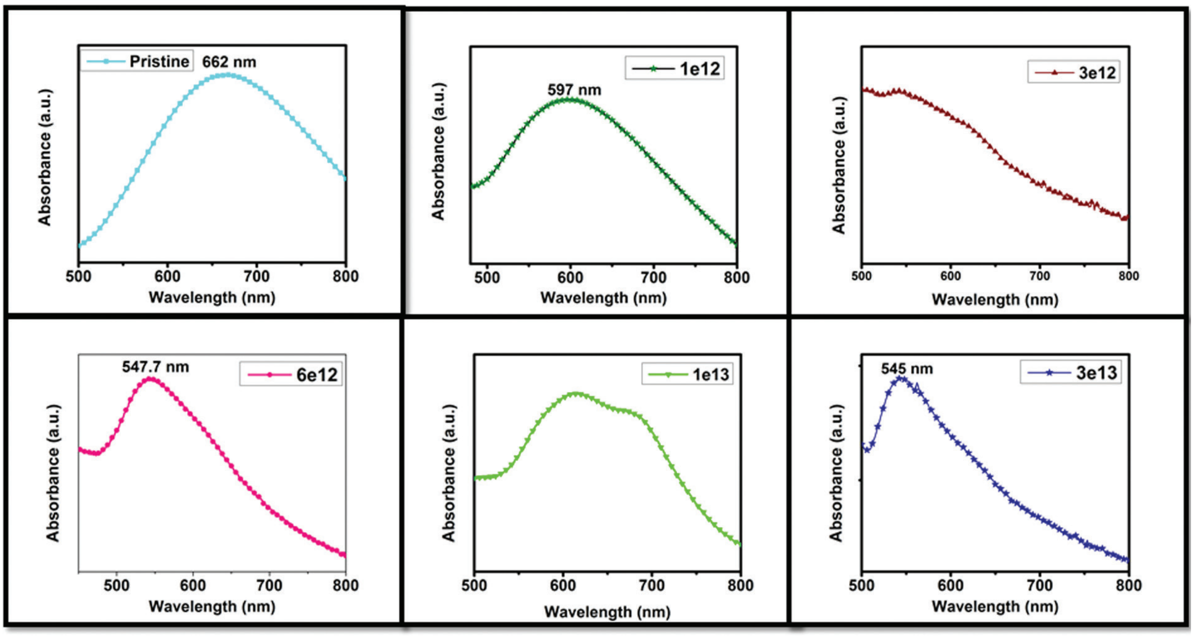

Fig.1. UV-visible absorption spectra of Au-C_{60} nanocomposite thin films at different fluences

5.2.25 Thermoelectric Properties of Fe Ion Implanted $CoSb_3$ Thin Films

Anha Masarrat[1,2], Anuradha Bhogra[1], Ramcharan Meena[1], Manju Bala[3], Ranveer Singh[4], Vineet Barwal[5], Chung-Li Dong[6], Chi- Liang Chen[7], T. Som[4], Ashish Kumar[1], A. Niazi[2] and K. Asokan[1*]

[1]Inter University Accelerator Centre, Aruna Asaf Ali Marg, New Delhi-110067, India
[2]Department of Physics, Jamia Millia Islamia University, New Delhi-110025, India
[3]Department of Physics, Delhi University, New Delhi-110007, India
[4]Institute of Physics, Bhubaneswar - 751005, India
[5]Department of Physics, Indian Institute of Technology Delhi, New Delhi-110016, India
[6]Research Center for X-ray Science, Department of Physics, Tamkang University, Tamsui, Taiwan 251
[7]National Synchrotron Radiation Research Centre, Hsinchu, Taiwan

In the present study, thin films of $CoSb_3$ phase were deposited on Si (100) substrates by pulsed laser deposition (PLD) using a polycrystalline target of $CoSb_3$. These films were implanted by 120 keV Fe-ions with three different fluences: 1×10^{15}, 2.5×10^{15} and 5×10^{15} ions/cm^2. All these films were well characterized for structural, electrical properties including Seebeck Coefficient, S, and electronic structures.

Figure. 1 shows the S for the Fe ion implanted $CoSb_3$ thin films. Inset shows the XRD pattern of the samples before and after annealing.

The S is found to vary with the fluences for a temperature range of 300 K to 420 K and found to be highest, i.e., 254 μV/K at 420 K for the film implanted with 1×10^{15} ions/cm^2. There is change of sign of S from negative for pristine film to positive for Fe implanted samples. X-ray absorption measurements confirm that Fe ions occupy the Co site in the cubic frame of the skutterudite and exist in 3+ oxidation state in this structure [1-3]. Our study shows that the Fe ion is implanted in $CoSb_3$ in Fe^{3+} state and Co ions are in divalent state. It is also found that the S of Fe ion implanted sample is around three times higher than that of Fe doped bulk sample.

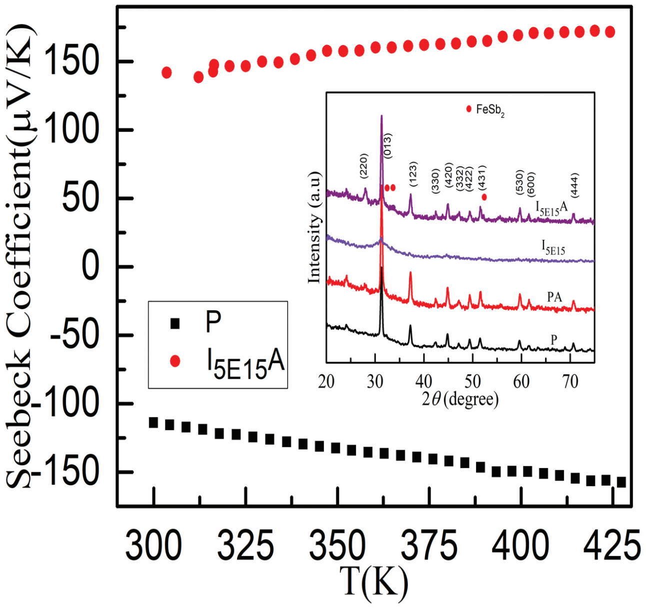

FIGURE 1. XRD pattern of pristine and post-irradiated TiO2/STO bilayer

REFERENCES:

[1] Yang, J., Meisner, G. P., Morelli, D. T. & Uher, C. Iron valence in skutterudites : Transport and magnetic properties of Co 1-x Fe x Sb 3. Phys. Rev. B 63, 1–11 (2000).

[2] Caillat, T., Borshchevsky, A. & Fleurial, J. -P. Properties of single crystalline semiconducting $CoSb_3$. J. Appl. Phys. 80, 4442–4449 (1996).

[3] Bala, M. et al. Evolution of nanostructured single-phase $CoSb_3$ thin films by low-energy ion beam induced mixing and their thermoelectric performance Manju. Phys. Chem. Chem. Phys. 19, 24886–24895 (2017).

5.2.26 Enhancement of thermoelectric properties of $TiO_2/SrTiO_3$ bilayer after Ar ion irradiation

Anuradha Bhogra[1*], Anha Masarrat[1], Ramcharan Meena[1], Dilruba Hasina[2], T. Som[2] and K.Asokan[1]

[1]Inter-University Accelerator Centre, ArunaAsaf Ali Marg, New Delhi-110067, INDIA
[2]Institute of Physics, Bhubaneswar - 751005, INDIA

TiO_2/STO bilayer was deposited on silicon substrate by PLD. The film was grown by ablation of STO bulk ceramic target at energy density of 4.2 J/cm^2 and target was rotated to ensure uniform deposition. The substrate temperature was kept at 700 °C and Ar gas was introduced at a pressure of 20 mTorr using mass flow controller. The thickness of each layer was kept 50 nm. Further, this film was irradiated by using 1 MeV Ar ion beam at a fluence of 1×10^{16} ion/cm^2 using Low Energy Ion Beam Facility (LEIBF) at Inter University Accelerator Centre (IUAC), New Delhi.

Figure 1 shows the XRD spectra of bilayer before irradiation and after irradiation. The pristine bilayer showed the mixed phases of TiO_2 and STO. The peaks in XRD spectra could be assigned to brookite and anatase TiO_2 and cubic STO. After irradiation, poor crystallinity was observed. Figure 1(b) shows the vacancies produced due to Ar irradiation calculated from TRIM simulations.

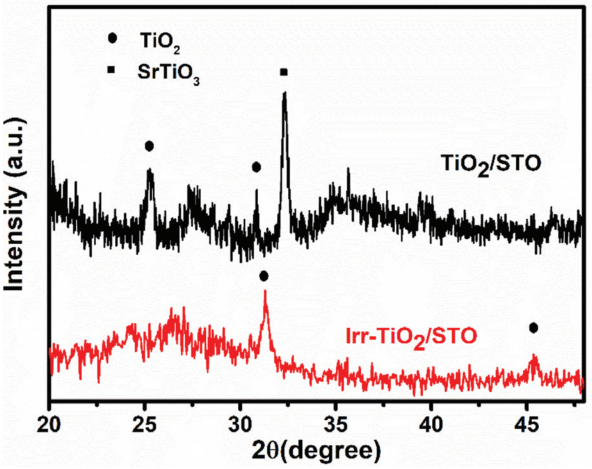

FIGURE 1. XRD pattern of pristine and post-irradiated TiO_2/STO bilayer

Figure 2 shows the variation of resistivity with temperature in the range of 300 to 420 K. Before irradiation, the sample was very much insulating (~$10^{12}\Omega$) to measure with the two probe measurements. After irradiation, resistivity drastically reduced to $1.5\times10^{-4}\Omega$-m and show semiconducting behavior with temperature. This change in resistivity can be attributed to the Ar irradiation induced oxygen vacancies in TiO_2/STO bilayer. For a comparison, the resistivity measurements have been tried for the 1 MeV Ar irradiated STO films deposited on silicon but resistance was very high to measure. This indicates that interface between TiO_2 and STO layer plays a role in enhancing the conductivity of the sample. It is expected that oxygen deficient TiO_2 film after irradiation may take out oxide ions from the STO layer and electrons get confined within interface layer.

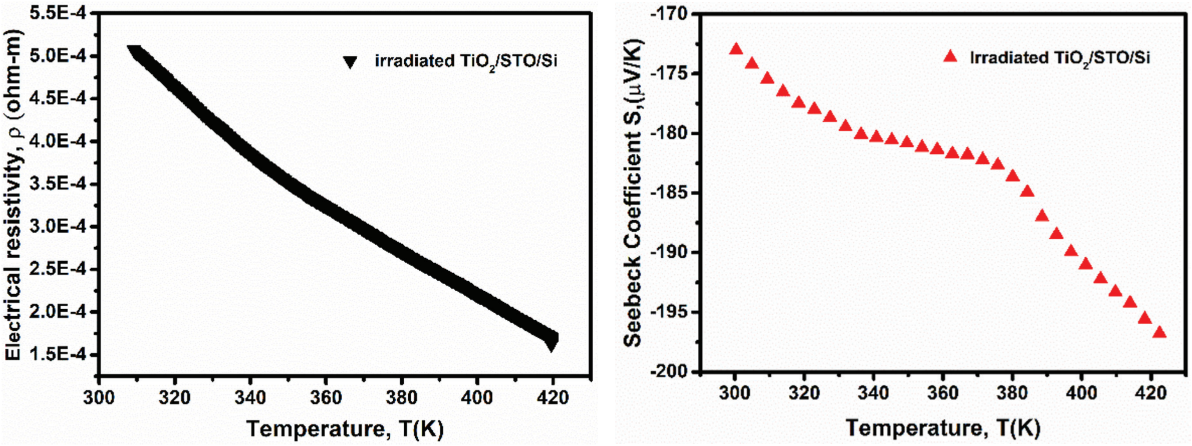

FIGURE 1. XRD pattern of pristine and post-irradiated TiO_2/STO bilayer

The temperature dependence of Seebeck coefficient is shown in figure. The magnitude increases with the temperature and shows semiconducting behavior. At 300 K the Seebeck coefficient reached 173 μV/K which is ~2.8 times larger than the bulk $SrTi_{0.98}Nb_{0.2}O_3$ (61 μV/K).

The TiO_2/STO bilayer was successfully deposited on silicon substrate by PLD. Further, this bilayer was irradiated by 1 MeV Ar ion beam. The XRD spectra recorded reveal the mixed phases of TiO_2 and STO before irradiation and decreased crystallinity after irradiation. The XAS measurements demonstrated the shifting of absorption spectrum to lower energy indicating the presence of oxygen vacancies. This is further observed in thermoelectric measurements where resistivity is dramatically reduced and Seebeck coefficient enhanced after Ar irradiation.

REFERENCES

[1] K. Szot, W. Speier, G. Bihlmayer and R.Waser, Nat Mater**5**, 312-320 (2006).
[2] H. Wang and C.Wang, Journal of Materiomics**2**, 225-236 (2016).
[3] S. A. Hayward and E. K. H. Salje, Phase Transitions **68**, 501-522 (1999).
[4] H. Ohta and K. Koumoto,Nature Materials**6**, 129-134 (2004).
[5] C. H. Chen and M.Hong, Applied Physics Letters**52**, 841-843 (1988).
[6] V. S. Lusavardi and A. Teplyakov, Surface Science **397**, 237-250 (1998).
[7] T. Teranishi and Y. Inada, Journal of American Ceramic Society **96**, 2852-2856 (2013).

5.2.27 Studies to understand the influence of morphology on semiconductor/electrolyte interface in photoelectrochemical splitting of water

Asha Kumari[1], Saif Khan[2], Vibha Rani Satsangi[3], Rohit Shrivastav[1], Rama Kant[4] and Sahab Dass[1*]

[1]Department of Chemistry, Faculty of Science, Dayalbagh Educational Institute, Dayalbagh, Agra,282005, India
[2]Inter-University Accelerator Center, New Delhi, Delhi -110067
[3]Department of Physics & Computer Science, Faculty of Science, Dayalbagh Educational Institute, Dayalbagh, Agra 282005, India
[4]Department of Chemistry, University of Delhi, Delhi, 110007, India

Nanostructured thin films of ZnO prepared by RF sputtering technique were successfully irradiated by low energy (100 KeV) Ar^+ ion beam at an incidence angle of 0°, 40° and 60°. Morphological modifications induced in the films due to ion beam irradiation were quantitatively characterized by Power Spectral Density analysis. Therefore, value of surface microscopic features viz. fractal dimension (D_H), lower (l) and upper cut off length scale (L) were calculated for the pristine and the irradiated samples. The samples were further studied for their photoelectrochemical (PEC) performance for water splitting. A correlation in the PEC performance and morphological surface features was established. It was found that the sample irradiated at 40° angle at the fluence of 5 x 10^{16} ions/cm^2 was found to possess maximum fractal dimension of 2.72, lower and upper cut off length scale of 3.16 nm and 63.00 nm respectively. This sample exhibited maximum photocurrent density of 3.19 mA/cm^2 at 1.23 V/RHE.

Experimental Details

Nanostructured thin films of ZnO were prepared by RF sputtering technique. These films were then subjected to low energy (100 KeV) ion beam irradiation conducted at LEIBF Facility, Inter University Accelerator Centre (IUAC), New Delhi. Irradiation of the films was performed at three different angles viz. 0° i.e. the normal angle of incidence, 40° and 60°, each irradiated at three different fluences 1 x 10^{16} ions/cm^2, 5 x 10^{16} ions/cm^2 and 1 x 10^{17} ions/cm^2. All the pristine and the irradiated films were characterized for thickness measurement (Surface profilometer), surface morphology (Field Emission Scanning Electron Microscopy, FE-SEM) and roughness measurement (Atomic Force Microscopy, AFM). Electrodes of the thin films were prepared and were subjected to electrochemical and photoelectrochemical treatment using a 300W Xenon arc lamp (Newport, RI, USA) with an intensity of 300 mW/cm^2.

Surface morphology analysis

Field-Emission Scanning Electron Microscope (FE-SEM) images of all the samples before and after irradiation is shown in Figure 1. FE-SEM image of Pristine ZnO film shows (Figure 1(A)) that preparation of the samples using RF sputtering technique resulted in the formation of nanopyramidal particles. A homogeneous and uniform deposition can be seen with densely packed particles. It could be concluded that lower fluences in all the angles of incidence caused sharpening or changing of morphology from nanopyramids to nanopspheres while highest fluence of 1x10^{17}ions/cm^2 resulted in complete distortion of the nanoparticles.

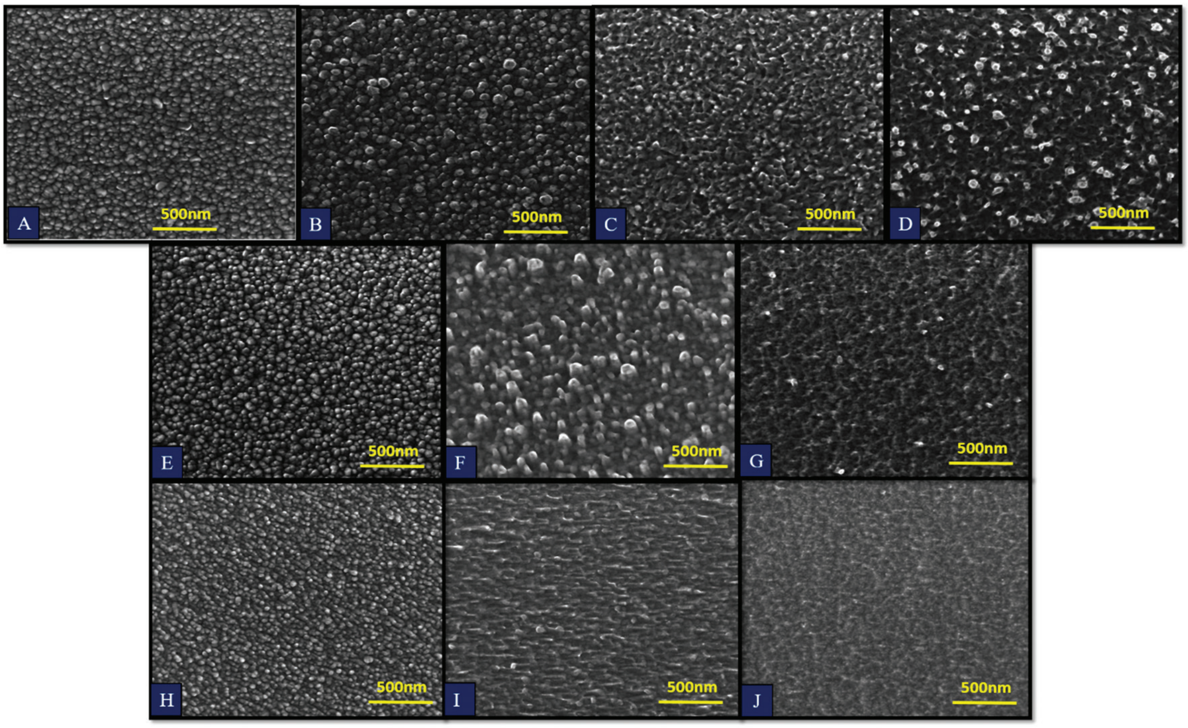

Figure 1. FE-SEM images of (A) Pristine ZnO, samples irradiated at (B) 0°, 1x10^{16} ions/cm^2, (C) 0°, 5x10^{16} ions/cm^2, (D) 0°, 1x10^{17} ions/cm^2, (E) 40°, 1x10^{16} ions/cm^2, (F) 40°, 5x10^{16} ions/cm^2, (G) 40°, 1x10^{17} ions/cm^2, (H) 60°, 1x10^{16} ions/cm^2, (I) 60°, 5x10^{16} ions/cm^2, (J) 60°, 1x10^{17} ions/cm^2

Atomic force microscopy analysis

AFM images of thin films were recorded to investigate their surface topography. As evident from the AFM images, a uniform and dense deposition of nanoparticles can be seen. All the images and structural pattern matches closely with the corresponding FE-SEM images of pristine and irradiated samples. ZnO films irradiated with angle of 40° appear rougher than the films irradiated at 0° and 60° This could be due to decrease in the cystallinity and deterioration of nanopyramids as revealed from XRD and FESEM results. It could be concluded that ZnO thin films irradiated with low energy ion beams (100 KeV) incidented at an angle of 40° enhances the nanoparticles morphology and surface topography.

Power Spectral Density (PSD) analysis

Power Spectral Density analysis was carried out for all the films before and after low energy ion beam irradiation treatment to determine the values of morphological parameters viz. l_c, L and D_H [1,2] as shown in Fig2.

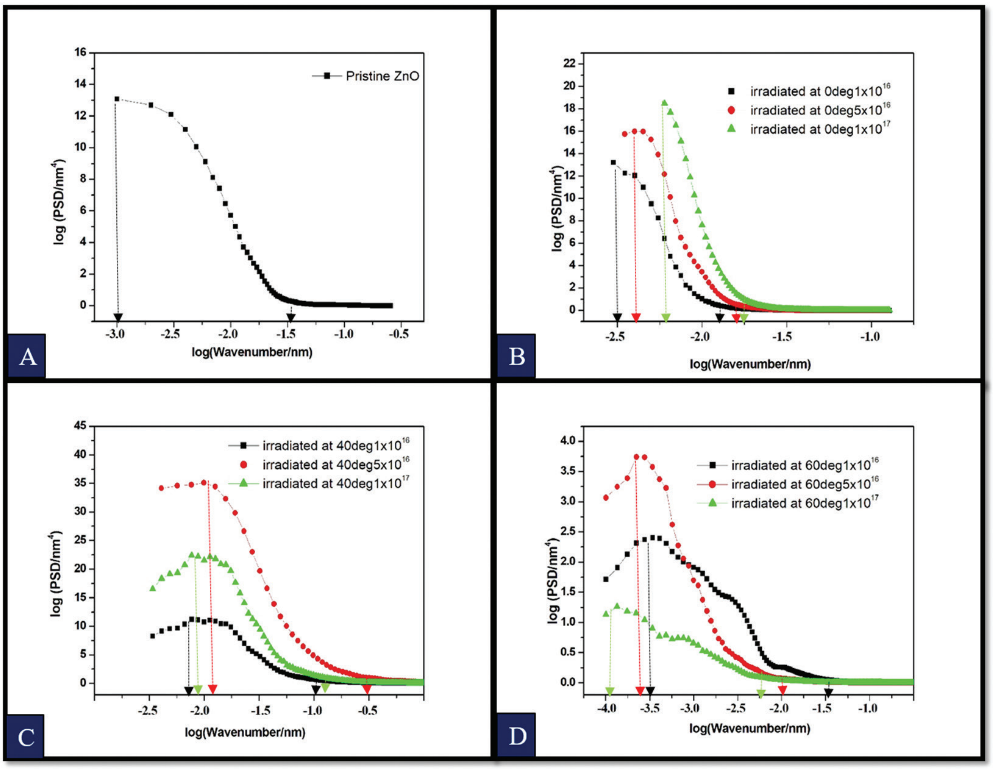

Figure 2. Power spectrum of (A) Pristine ZnO, samples irradiated at (B) 0°, (C) 40°and (D) 60°

Photoelectrochemical Studies

Photoelectrochemical density plots are shown in Figure 3. It is clearly evident from the figure that photocurrent density increases with the increase in the angle of irradiation and fluence up to 40°. Highest photocurrent density of 3.19 mA/cm^2 was obtained in case of the sample irradiated at the fluence of 5 x 10^{16} ions/cm^2.

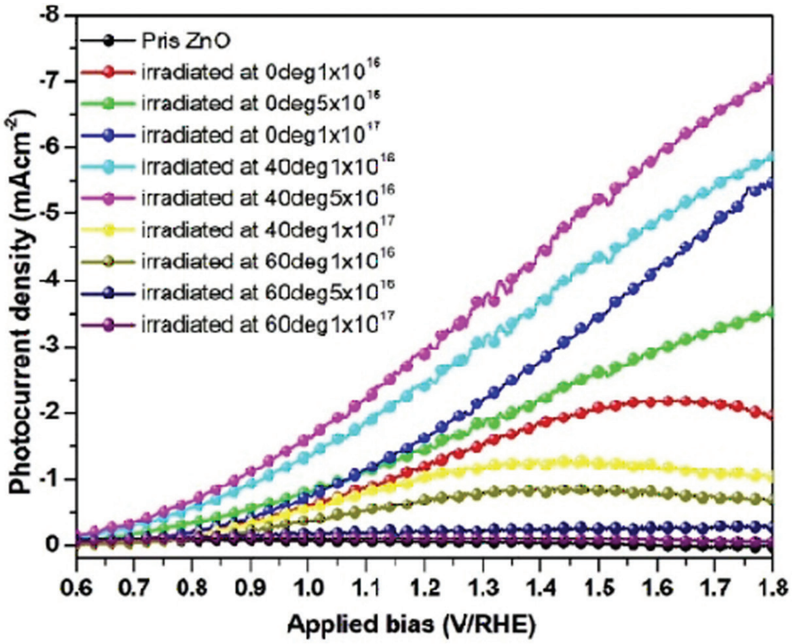

Figure 3. Photocurrent density curves under constant illumination for all ZnO samples in 0.1 M NaOH electrolyte

REFERENCES

[1] S. Dhillon, and R. Kant, Appl. Surf. Sci. 282 (2013), 105
[2] K. Asha et al, J. Power Sources, 432 (2019), 38

5.2.28 Ion implantation induced tunable resistive switching property of HfO_2 thin films

Dilruba Hasina[1], Sudheer[1], Rupam Mandal[1,2] and Tapobrata Som[1]

[1]SUNAG Laboratory, Institute of Physics, Bhubaneswar, Odisha-751005, India.
[2]Homi Bhabha National Institute, Training School Complex, Anushakti Nagar, Mumbai 400085, India

Towards developing next generation scalable HfO_2-based resistive switching (RS) memory devices, the efficacy of 30 keV Au--ion implantation to achieve tunable resistive switcging property at a threshold fluence of 1×10^{16} ions cm^{-2} and at ambient temperature is presented. The RS behaviour of as-grown and ion implantation films are confirmed by conductive atomic force microscopy (cAFM) technique. The different fluence of Au ions is used to tune the number density of defects per unit volume which becomes useful in the tuning of resistive switching properties. X-ray diffraction shows that both as-grown and implanted HfO_2 films are amorphous in nature, whereas atomic force microscopic studies show that all films are granular in nature and RMS roughness increases with increasing ion fluence. To investigate the variation in work function of ion implanted HfO_2 thin films at different fluences, Kelvin probe force microscopic studies are underway.

Experimental Details

As-grown HfO_2 films were implanted by 30 keV Au- ions at room temperature at incident angles of 0˚ and 45˚ with series of ion fluences in the range of $0.05\text{-}1\times10^{16}$ ions cm^{-2}. The Au-ions were obtained from low energy ion beam facility (LEIBF) at IUAC, New Delhi. The Faraday cup was used to monitor the beam current (up to 2.4 μA). We maintained a working pressure of the scattering chamber is at 5×10^{-6} mbar for all fluences. The projected range and the atomic concentration ratio of Hf and O at the HfO_2 surface as a function of the fluence were simulated by the TRIDYN simulation code. X-ray diffraction studies were carries out to identify the crystalline nature of HfO_2 films, whereas atomic force microscopy-based studies were performed to study the morphology, roughness, and nanoscale transport property of HfO_2 films before and after Au-ion implantation. To investigate the variation in work function of ion implanted HfO_2 thin films at different fluences, Kelvin probe force microscopic studies are underway. Further to this, x-ray photoelectron spectroscopic measurements were performed to study the composition and nature of chemical bonds in the films.

Results and Discussion

HfO_2 films were grown by RF magnetron sputtering technique by applying 100 W power and a commercially available target (99.99% purity) and Si substrates coated with different back contacts. It is known that the crystallinity plays an important role in determining the electrical properties of a thin film. Thus, the XRD measurements of all HfO_2 films are carried out under similar conditions (eg., scan speed, scan rate, slit width) and presented in Figure 1. XRD data reveal that as-grown HfO_2 films are amorphous and remain so even after ion implantation.

For investigation on the resistive switching (RS) behavior of HfO_2 films before and after implantation, detailed I-V measurements have been carried out by cAFM using standard two-terminal devices (Ti/HfO_2/Pt). The local I-V characteristics of the Rs device fabricated under the fluence of 1×10^{16} ions cm^{-2} (ion immpalatation angle: 45˚) is depicted in Figure 2(a). However, no RS behavior is observed for the as-grown (current map not shown) and ion irradiated samples up to a fluence of 5×10^{15} ions cm^{-2} even after applying a sweeping voltage of ±10V. However, a distinct local RS behavior has been observed within an applied bias of ±2V for a fluence of 1×10^{16} ions cm^{-2} with SET and RESET voltages are 1.92 V and 0.76 V, respectively. Figure 2(b) shows the cAFM image of the top HfO2 layer having a fluence of 1×10^{16} ions cm^{-2} using +2 V tip bias.

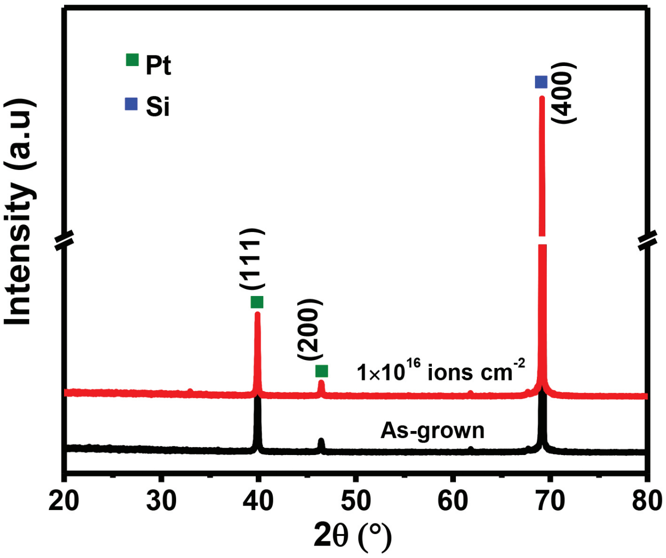

Figure 1. XRD spectra of as-grown and implanted HfO_2 films.

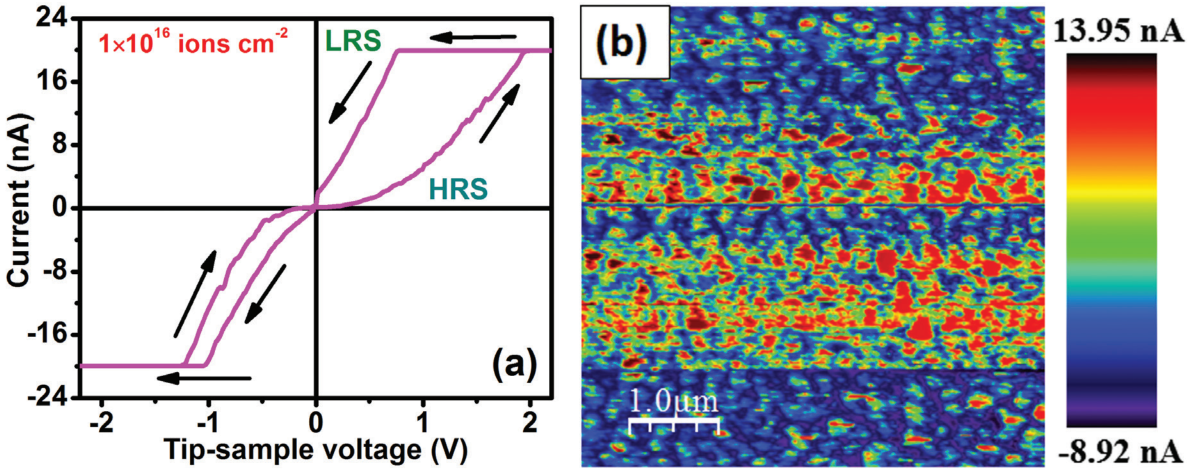

Figure 3. Power spectrum of (A) Pristine ZnO, samples irradiated at (B) 0°, (C) 40°and (D) 60°

X-ray photoelectron spectroscopic measurements show increasing degree of oxygen vacancies in the films with fluence. KPFM measurements are underway to probe implantation-mediated change in the work function of the films to correlate with the observed RS behavior of the films.

5.2.29 Study on the room temperature photoluminescence property of Al implanted ZnO nano rods

Amaresh Das[1], Debdulal Kabiraj[2] and Durga Basak[1]

[1]School of Physical Sciences, Indian Association for the Cultivation of Science, Kolkata-700032, India
[2]Inter-University Accelerator Centre Aruna Asaf Ali Marg, New Delhi-110067, India

We present a detailed study on the effect of Al ion implantation in the room temperature (RT) photoluminescence (PL) properties of ZnO nanorods (NRs). Irrespective of growth technique, Pl spectrum of ZnO shows two peaks, one in the ultraviolet region due to near band edge emission (NBE) and one broad peak in the visible region due to defect levels (DL) within the band gap. When ZnO NRs array film is implanted with Al ions, an by 1.4 times in the ratio of INBE / IDL has been observed for the ZnO NRs implanted with a 5×10^{13} ions/cm^2 fluencies of Al ions. Beyond 5×10^{13} ions/cm^2 , the ratio is decreased with an increase in the Al dose, though it is always higher than that of the pristine sample up to a Al dose of 1×10^{15} ions/cm^2. Finally, a 0.87 times drop in the ratio is observed for the highest dose (1×10^{16} ions/cm^2) Al implanted sample.

Experimental details:

ZnO NRs were grown on glass substrates by aqueous chemical growth (ACG) method.[1] The cleaned glass substrates were spin coated by 0.1 M solution of zinc acetate ($Zn(CH_3COOH)_2$) to obtain seed layer of ZnO and then immersed into a mixed aqueous solution of $(CH_3COO)_2Zn\cdot2H_2O$ and hexamethylenetetramine ($((CH_2)_6N_4)$) in a beaker. The beaker containing the precursor and the substrate was kept at 80 °C for growing ZnO NRs and after growth, the substrates were removed from the solution, rinsed in de-ionized water and dried. The as grown ZnO NRs were implanted with 100 keV Al ions having various doses ranging from 1 x 10^{13} to 1 x 10^{16} ions/cm^2 at IUAC, New Delhi using the LEIBF facility. After Al implantation, the implanted ZnO NRs were annealed in Ar ambient at 450 °C for 60 min. The nomenclature of the Al implanted samples according to the dose are as follows: Al/ZnO113 (1 x 10^{13} ions/cm^2), Al/ZnO513 (5 x 10^{13} ions/cm^2), Al/ZnO114 (1 x 10^{14} ions/cm^2), Al/ZnO115 (1 x 10^{15} ions/cm^2), Al/ZnO116 (1 x 10^{16} ions/cm^2. The implanted NRs were characterized using Xray diffractometry (XRD), field emission scanning electron microscopy (FESEM), transmission electron microscopy (TEM), high resolution transmission electron microscopy (HRTEM), RT PL, X-ray photoelectron spectroscopy (XPS), techniques.

Results and discussion:

The XRD patterns of the pristine and ZnO NRs implanted with different doses of Al and Ar show the presence of (100), (002), (101), (102), (103) and (110) peaks of hexagonal wurtzite ZnO (JCPDS card No. 36-1451). The (002) diffraction peak is the strongest among all peaks, implying the growth of NRs along <002> direction. It has been observed that the (002) peak position of the Al implanted ZnO NRs shifts towards the lower 2θ value as compared to the pristine ZnO NRs indicating an existence of the tensile stress.[2] The values of the lattice parameter (c) and full with at half maxima (FWHM) of (002) peak have been observed to be increased as doses of Al is increased.

To understand the microstructure of the Al implanted ZnO NRs at various doses, the SEM, measurement was performed. As seen in top view FESEM images, the hexagonal ZnO NRs have been grown vertically on the seeded glass substrate, which is at par with the XRD results. After implantation with Al, the rod-like structure of ZnO NRs has been maintained. However, for higher dose Al implanted NRs (Al/ZnO116) tips of the NRs have been modified slightly. The morphological changes due to Al implantation have been again examined by HRTEM analysis. The lattice fringes are clearly observed in the HRTEM image for pristine sample, which indicates that the pristine ZnO NRs are free of extended defects such as dislocations, stacking faults, defect clusters etc.[3] The HRTEM image of lower Al implanted NRs is similar to that of pristine, indicating to the complete recovery of implantation induced structural damages due to annealing at 450 ºC. At higher dose of Al, the stacking fault arises due to the distorted lattice arrangement of (0002) planes.

Figure 2a shows the RT PL spectra of pristine and some representative Al implanted samples. All the samples show the strong NBE emission in UV region and a broad emission in the visible. As implanted samples show emission intensities lower than the pristine sample. For implanted and post-implantation annealed samples, the PL properties are highly improved.

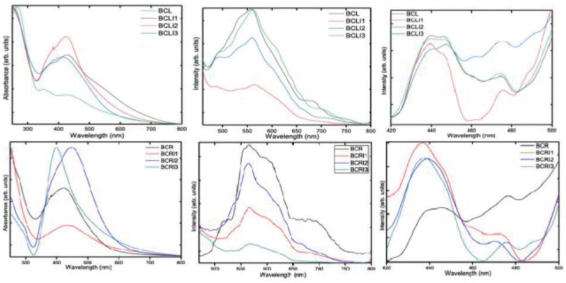

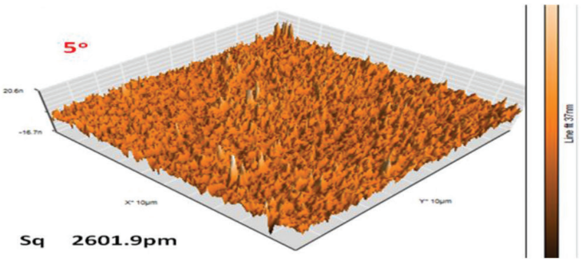

Figure 2a shows that I_{NBE} is maximum for 1 x 10^{13} ions/cm^2 Al implanted NRs. The highly enhanced I_{NBE} for lower dose can be assigned to a recovery of the lattice damages by the annealing treatment, which is supported by our HRTEM results. With increase in the Al dose, extended defects appear,[3] which act as non-radiative recombination centers results reducing PL emission at higher Al dose. However, a blue shift of is found in the NBE peak position for the higher dose (1x 10^{16} ions/cm^2) of Al implanted NRs. Similar to I_{NBE}, the intensity of DL emission is also increased at lower dose and then is gradually decreased for higher dose (The inset of Figure 2a). The DL emission center is seen to be shifted towards higher energy side (~2.4 eV) as compared to the pristine one, which means the visible emission shifts from yellow-orange to green one. V_{Zn} type of defects have been well accepted to be responsible for the green emissios.[4-5] As dose increases, the net effect of V_{Zn} in green emission is expected to be decreased. The creation of radiative recombination path is also a factor for reduction in the PL emissions. The ratio of INBE / IDL has been calculated as summarized by the bar diagram in Figure 2b. It is observed that the value for the pristine sample is 54, while the value is highly enhanced for a lower doses of 1x 10^{13} ions/cm^2 Al implantations to 73. As the dose increases, the INBE /IDL decreases gradually and for 1 x10^{16} ions/cm^2 it becomes 47.

Further study of excitation power dependence of PL spectra confirms that the Al related donor bound excitons are responsible for the radiative recombinations and enhancement in the I_{NBE} / I_{DE} ratio at lower Al dose. At higher Al dose, the extended defects forms act as the non radiative recombination centers, and as a result, the INBE is reduced.

To confirm the presence of Al inside ZnO, XPS measurements were also carried out for Al/ZnO1^{16} sample. The observed peak with a binding energy around 74.37 eV confirms the successful substitution of Zn^{2+} ions by Al^{3+} ions in the ZnO lattice of Al/ZnO116 sampless.[6-7] Detailed analyses of the O 1s peak provide support of the formation surface defects.

Conclusions:

In, summary, we demonstrate the effect of Al ion implantation on the RT PL properties of ZnO NRs. The formation of neutral Al donor bound excitonic recombination centers is responsible for PL enhancement for the lower dose Al implanted samples. This Work has been communicated and is under review at Applied Surface Science, 2019.

REFERENCES:

[1] M. Mahanti, T. Ghosh and D. Basak, Nanoscale, 2011, 3, 4427-4433.
[2] F. Mouzaia, D. Djouadi, A. Chelouche and L. Hammiche, Cham, 2018.

[3] L. D. Yao, D. Weissenberger, M. Durrschnabel, D. Gerthsen, I. Tischer, M. Wiedenmann, M. Feneberg, A. Reiser and K. Thonke, J. Appl. Phys., 2009, 105.

[4] F. Fabbri, M. Villani, A. Catellani, A. Calzolari, G. Cicero, D. Calestani, G. Calestani, A. Zappettini, B. Dierre, T. Sekiguchi and G. Salviati, Sci Rep, 2014, 4.

[5] D. C. Reynolds, D. C. Look and B. Jogai, J. Appl. Phys., 2001, 89, 6189-6191.

[6] T. N. Sky, K. M. Johansen, V. Venkatachalapathy, B. G. Svensson, and L. Vines, Physical Review B, 2018, 98, 245204.

[7] H. Lee, K. Sivashanmugan, C. Y. Kao and J. D. Liao, Jpn. J. Appl. Phys., 2017, 56.

5.2.30 Tuning of PMA in trilayer films by ion irradiation technique

A. K. Sahoo[1], A. Talapatra[1,2], J. A. Chelvane[3], and J. Mohanty[1]

[1]Nanomagnetism and Microscopy Laboratory, Department of Physics, Indian Institute of Technology Hyderabad, Kandi, Sangareddy, 502285, Telangana, India
[2]Department of Electrical and Computer Engineering, National University of Singapore, 117576 Singapore
[3]Advanced Magnetics Laboratory, Defence Metallurgical Research Laboratory, Kanchanbagh, Hyderabad 500058, India

Tuning of perpendicular magnetic anisotropy (PMA) of the material systems is a keen interest of scientific communities as well as industries. Trilayer magnetic films are irradiated by Ar$^+$ ions with two different energies viz. 50 and 100 KeV at 300K. It is observed that as energy in- creases, PMA abruptly decreases. Magnetic domains, which was observed in as-deposited film, became deteriorated at 50 and 100 KeV. Roughness and defects of the irradiated samples are progressively increased as energy is increased.

Experimental Details

Trilayer film [TbFe(100nm)/ GdFe(50nm)/ TbFe(100nm)] was prepared on the Si <100> wafer by e-beam evaporation technique. Ar$^+$ ions were used for irradiations in this case. Film was irradiated with two different energies, 50 and 100 KeV, at constant ion fluence of 10^{14} ions/cm^2. Samples are kept perpendicular to ion fluxes.

Magnetic films exhibiting PMA, have a great importance towards data storage device and read/write heads because of its thermal stability, high coercivity, and large data storage capacity (nearly 1 Tb/in^2). PMA can be tuned by varying film compositions, growth conditions (variation in deposition pressure, and substrate temperature), and external treatments (like thermal annealing, ion implantations, and ion irradiations etc.). Ion irradiations can induce changes in structural, magnetic, and morphological properties of films [1]. TbFe(100nm)/ GdFe(50nm)/ TbFe(100nm) film was irradiated in order to observe the modification in magnetic domains and PMA.

Atomic force microscopy (AFM) [Fig. 1(a)] and corresponding magnetic force microscopy (MFM) [fig. 1(b)] images of the as de- posited and irradiated films are shown in Fig. 1. It is observed that irradiated films show slightly higher roughness as compared to the as-deposited film. As-deposited film has roughness of around 1 nm whereas, irradiated films have roughness around 1.5 nm. Fig. 1(b) (left) represents MFM image of The as-deposited film. This image contains two distinct contrasts, red and yellow colors. Yellow color represents up-magnetization, whereas red color represents down-magnetization for the out-of-plane magnetized domains. One can clearly observe the patch-kind of domains are present in the as-deposited film. These magnetic domains form in order to minimize the magnetostatic energy of the system. As the film is irradiated with 50 KeV and 100 KeV energies, magnetic domains became deteriorated severely. Middle and right images of Fig. 1(b) represent MFM images of 50 and 100 KeV, respectively. The magnetic phase contrast of irradiated MFM images (0.4degree) are weaker compared to as deposited MFM image (1deg). Further in-depth characterization followed by micromagnetic modeling can provide more details on tuning of PMA of the films as a result of ion irradiation.

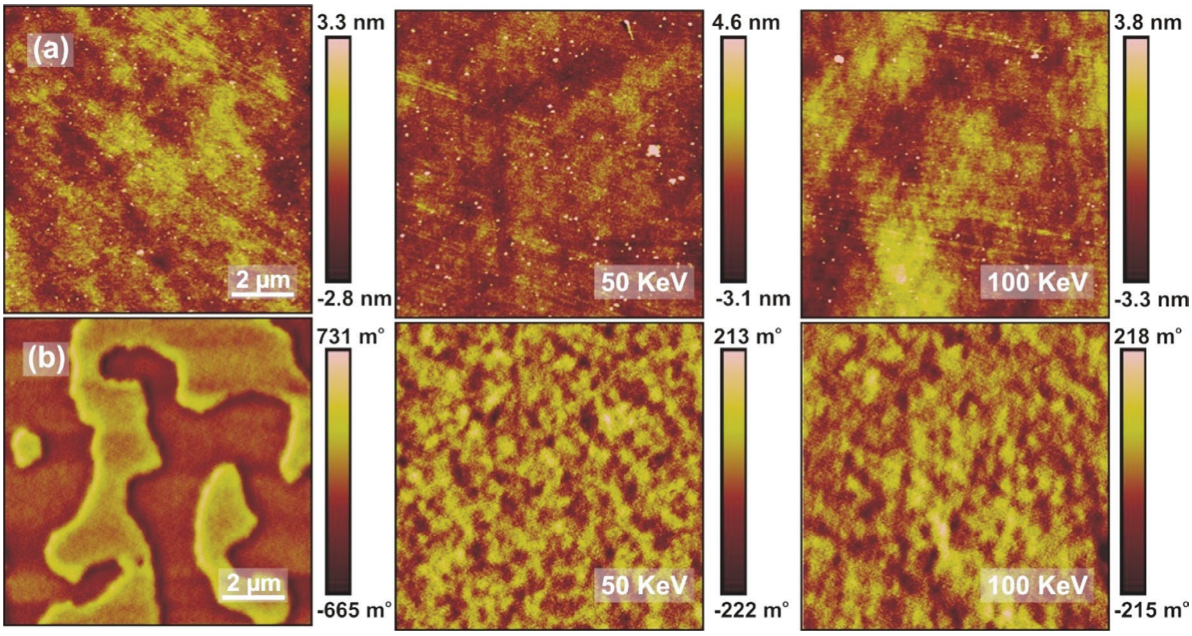

Figure 1: (a) Topography images of as-deposited TbFe(100nm)/ GdFe(50nm)/ TbFe(100nm) film (left), at 50 KeV (middle), and at 100 KeV (right) (b) Corresponding MFM images of the film. MFM images are free from topographic influences.

REFERENCE:

[1] Pawanpreet Kaur, K.K. Sharma, Rabia Pandit, R.J.Choudhary, and Ravi Kumar, Journal of Magnetism and Magnetic Materials, 398 (2016) 220-22.

5.2.31 Enhancement of exchange bias in Ni-NiO bilayer films implanted with Cu ions

Lisha Raghavan[1], Sunil Ojha[1] and D Kanjilal[1]

[1]Inter University Accelerator Centre, New Delhi.

Exchange bias refers to the shift in hysteresis loop of a ferromagnet (FM) in contact with an antiferromagnet (AFM) on cooling below the Neel temperature of the AFM. These kinds of exchange coupled systems are an integral part of magnetic tunnel junctions and spin valves [1]. Exchange bias has been observed in bilayer films, core shell structure, nanotubes, nanoparticulates and so on [2-4]. Exchange bias depends on various factors like FM-AFM thickness, interface, crystallinity etc. and can be tuned by various methods. Defect creation and doping the layers with non magnetic ions has been proven as a suitable way to tune exchange bias [5]. Doping the layers can be done effectively using ion implantation as the energy can be chosen judiciously to dope at the required depths.

In the present work Ni films were prepared by thermal evaporation and annealed at 400ºC for 1 hour to form the NiO layer. The film thickness was measured by Rutherford Backscattering Spectrometry (RBS) and found to be 100 nm thick NiO and 40 nm thick Ni layer. 100 keV Cu ions were implanted in the films and their range in NiO was 42 nm. That is 100 keV Cu ions get implanted in NiO layer. The films were implanted with various fluences ranging from 5e14 to 5e16 ions/cm^2. Hysteresis loop were measured after cooling the system from 300K to 10 K in the presence of 1.5 T magnetic fields. It was observed

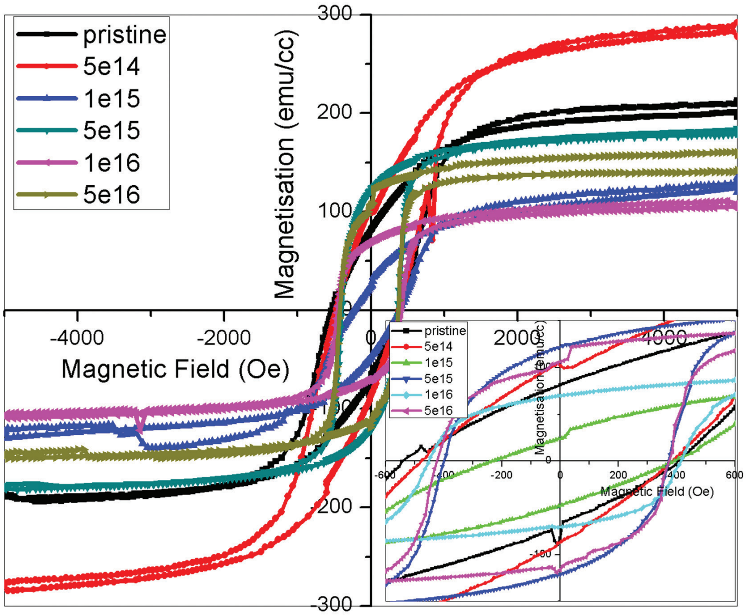

Figure1. Hysteresis loop of Ni-NiO films at 10 K

that the pristine film exhibited an exchange field of -72 Oe. On irradiation the exchange field increased and at a fluence of 1e15 maximum value of +72 Oe was obtained. The exchange bias shifted to positive value on ion implantation. On further increase of ion fluence exchange field decreased and again shifts to negative values.

The exchange bias was tuned effectively by Cu ion implantation.

REFERENCES:

[1] J. Nogués, J. Sort, V. Langlais, V. Skumryev, S. Suriñach, J.S. Muñoz, and M.D. Baró, Phys. Rep. 422 (2005) 65.

[2] A. Roy, J.A. De Toro, V.S. Amaral, P. Muniz, J.M. Riveiro, J.M.F. Ferreira, J. Appl. Phys. 115 (2015) 073901

[3] H.L. Chaghouri, F. Tuna, P.N. Santhosh, and P.J. Thomas, Solid State Comm. 230, (2016) 11

[4] T. Yu, Z.W. Zhang, Y.H. Xu, Y. Liu, W.J. Li, Y. Nie, X. Zhang, and G. Xiang, J. Magn. Magn. Mater. 429 (2017) 74

[5] P. Miltényi, M. Gierlings, M. Bamming, U. May, G. Güntherodt, J. Nogués, M. Gruyters, C. Leighton, and I.K. Schuller, Appl. Phys. Lett. 75, (1999) 2304

[6] A.Mougin, T. Mewes, M. Jung, D. Engel, A. Ehresmann, H. Schmoranzer, J. Fassbender, and B. Hillebrands, Phys. Rev. B 63 (2001) 060409-1.

5.2.32 Effect of alpha irradiation on transition metals free and transition metals-containing high-level nuclear waste base glasses

Prince Rautiyal[1*], Pawan K. Kulriya[3], Ruth Edge[2], Laura Leay[2], Alan H. Jones[1] and Paul A. Bingham[1]

[1]Materials and Engineering Research Institute, Sheffield Hallam University, Sheffield, UK,
[2]Dalton Cumbrian Facility, University of Manchester, Cumbria, UK,
[3]Inter-University Accelerator Centre, New Delhi, India.

Performance assessment of high-level radioactive waste (HLW) glasses against radiation damage is of crucial importance to ensure safe and economic disposal over geological disposal periods (tens of thousands to a million years) [1]. This work aims to study alpha irradiation effects in simple glasses using mainly EPR spectroscopy (electron paramagnetic resonance), UV-Vis IR optical absorption spectroscopy and Raman spectroscopy. Alpha irradiation induced defects in two international glasses with and without transition metals namely UK-MW lithium-sodium borosilicate and Indian sodium-barium borosilicate which are being used as immobilization glass matrices for HLW by the UK and India, will be reported. This report presents methodologies and the work underway to achieve the aims of the study.

Experimental Details

Sample prep: All the glasses were prepared using melt-quenched method and annealed below glass transition temperature. Glasses were then cut into small thin samples of thickness ~1mm using a diamond precision cutter. They were then polished using SiC sheets up to grit size of 1000 (approximate size of 8.4 micron).

Irradiations at IUAC: Glasses were irradiated at Inter university accelerator center, Delhi, India using low energy ion beam facility (LEIBF) with a He^{2+} of 650 KeV to simulate the damage from alpha particles. Indian and UK-MW base glasses with and without dopants were irradiated with four different doses; $1x\ 10^{15}$, $1x\ 10^{16}$, $5\ x\ 10^{16}$ and $1\ x\ 10^{17}$ ions per square cm.

Raman spectroscopy: Raman spectra on pristine and irradiated samples were acquired using a depolarized 532nm excitation laser wavelength on a Thermo Scientific DXR2 Raman imaging microscope.

Optical absorption spectroscopy: UV-Vis IR optical spectroscopic measurements were done on the pristine and irradiated samples to observe the irradiation-induced absorption bands.

EPR spectroscopy: First derivative continuous wave powdered EPR spectra will be recorded for all the pristine and irradiated glasses at room temperature using an X-band, frequency of 9.6 GHz, EPR Bruker spectrometer [2].

REFERENCES:

[1] R. Ewing, W. Weber and F. Clinard, "Radiation effects in nuclear waste forms for high-level radioactive waste", Progress in Nuclear Energy, vol. 29, no. 2, pp. 63-127, 1995.

[2] M. Mohapatra, R. Kadam, R. Mishra, C. Kaushik, B. Tomar and S. Godbole, "Gamma Radiation-Induced Changes in Trombay Nuclear Waste Glass Containing Iron", International Journal of Applied Glass Science, vol. 4, no. 1, pp. 53-60, 2012.

5.2.33 Mimicking neutron irradiation impact on insulating materials by SHI and low energy ion beam

Sejal Shah

ITER-India, Institute for Plasma Research, Bhat, Gandhinagar, 382428, India

Collaborators:

1. Sunil Kumar, A. Chakraborty. ITER-India, Inst. for Plasma Research, Bhat, Gandhinagar
2. I. Sulania, F. Singh. IUAC, New Delhi
3. V. Sathe, V. Reddy. IUC, Indore

The present study is undertaken to investigate low energy ion beam effect on Al_2O_3. Due to limitation of neutron sources for long operational period and limited fluxes, ion beam is used as surrogate techniques for neutron irradiation. Damage calculations at different fluences for ion beam are carried out using TRIM. 300 keV Ar^{6+} ion beam is used for present study for the fluence ranging from 5×10^{11} ions/cm^2 to 1×10^{16} ions/cm^2. Impact of radiation on structural material properties is studied using different characterization techniques such as Raman, PL, XRD and AFM. Raman analysis shows defect density increase after irradiation at lower fluences where defect annealing at higher fluence. GIXRD data shows the defect creation at lower fluence up to 1×10^{14} ions/cm^2 whereas at higher fluence re-crystallization starts. Re-crystallization/annealing are explained by beam current heating of material. XRD study confirms no sign of amorphization even at highest fluence 1×10^{16} ions/cm^2 used for the irradiation. The results are further validated by Raman and PL study. Overall results confirm the structural integrity of the material for the applied radiation level.

Reference:

1. “Structural investigation of low energy ion irradiated Al_2O_3” Sunil Kumar, Sejal Shah, I. Sulania, F. Singh, A. Chakraborty, J. of Ceramic International.
2. “Radiation Impact on Ceramic materials Intended for Nuclear Reactor Applications” Sejal Shah, Sunil Kumar, S. Vala, R. Kumar, M. Abhangi, I. Sulania, F. Singh and A. Chakraborty.. Presently under review at Publication committee of ITER-India and soon will be submitted to IEEE Transaction on Plasma Science.

5.2.34 Oxide heterostructures on ion-implanted $SrTiO_3$

Ojha Shashank[1], Patel Ranjan[1], Kumar Siddharth[1], Mandal Prithwijit[1], Ojha Sunil[2], Devrani[2], K. Asokan[2] and Middey Srimanta[1]

[1]Department of Physics, Indian Institute of Science, Bangalore-560012, India.
[2]Inter-University Accelerator Centre, New Delhi-110067, India.

Utilizing the spin degrees of freedom is the basic idea for spin-based electronics, where, it is not the electron’s charge but the electron’s spin that carries information and offers opportunities for a new generation of devices with new functionalities[1]. Discovery of two-dimensional electron gas (2-DEG) at oxide interfaces has attracted huge attention in the recent years and is believed to play a pivotal role in realization of next generation oxide-based electronics[2]. In spite of various attempts to realize magnetic 2-DEG at oxide interfaces, creating and manipulating spin polarized 2-DEG at complex oxide interfaces has remained an experimental challenge so far. In the past, much of the attention has been paid to the interface between $LaAlO_3$ and $SrTiO_3$ (LAO/STO). Emergent magnetism at LAO/STO interface is very weak and the microscopic origin of ferromagnetism[3] at LAO/STO is highly debated. Alternatively, ferromagnetic layers have been used to induce the spin-polarization in 2DEGs but room temperature ferromagnetic 2-DEG remains elusive so far.

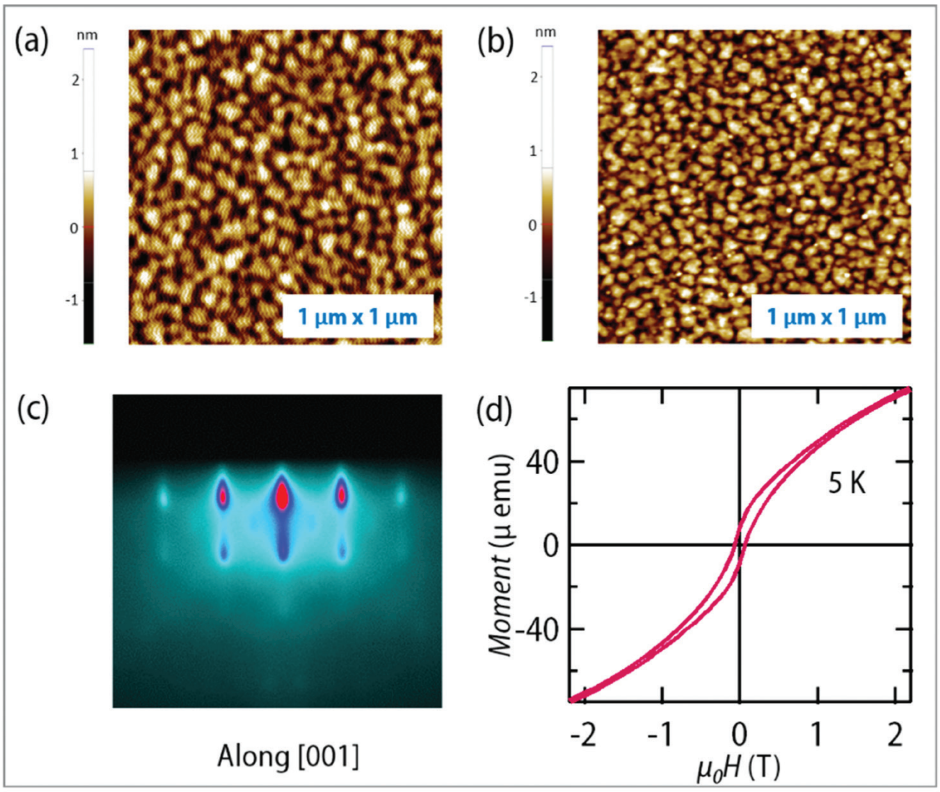

Figure 1: (a) AFM image of implanted substrate after annealing. (b) AFM image, (c) RHEED image along [001] direction (d) M vs magnetic field for 5 u.c. γ-Al_2O_3 film on 5% Co:STO (001).

In order to realize magnetic 2-DEG, we are combining two very different techniques: ion implantation and thin film growth. To introduce magnetic moment, various doses of Co ions have been introduced in single crystalline STO substrates by negative ion beam implantation technique in low energy negative ion beam facility of IUAC. These implanted substrates were post annealed in N_2 gas to restore the crystallinity of the substrate. Fig. 1(a) shows the AFM image of the substrate after annealing. The single crystallinity was confirmed by reflection high energy electron diffraction (RHEED). 4 nm of Al_2O_3 was grown on such Co-implanted STO substrates by pulsed laser deposition in Indian Institute of Science. The AFM image (Fig. 1(b)) and RHEED pattern (Fig. 1(c)) testify the success of the epitaxial growth. Magnetization vs field measurement reveals that this film is indeed ferromagnetic (Fig. 1(d)). However, the film does not exhibit metallic behavior. Optimization of growth conditions to achieve 2-DEG on these implanted substrates is under progress.

REFERENCES:

[1] I. Zutic et al., Rev. Mod. Phys. **76,** 2 (2004).
[2] E. Lesne et al., Nat. Mater. **15,** 1261 (2016).
[3] A. Brinkman et al., Nat. Mater. **6,** 493 (2007).

5.2.35 Low Ion Beam Induced Joining of Strontium Manganate ($SrMno_3$) Nanowires and their Surface Modification in Various Nanodevices Application

Manoj K Rajbhar and Shyamal Chatterjee*

School of Basic Sciences, IIT Bhubaneswar, Odisha-752050, India.

The focal point of our work is to comprehend the effect of ion irradiation treatment on $SrMno_3$ nanowires in network form, especially on their surface properties and in addition the potential outcomes and constraints to tune these properties. We have studied the joining/welding of mesh of nanowires with increase ion source energy at 50 keV, and 80 keV and the dynamics of controlling the wetting properties of fluids on nanostructured surfaces by varying the ion fluences of 5×10^{15}, 8×10^{15}, 1×10^{16}, 2×10^{16}, and 3×10^{16} ions/cm^{-2} respectively, which covered the whole conceivable range of entire wetting (from the superhydrophilic to superhydrophobic). This type of unique control on wettability is achieved by varying the ion energy and fluence. The change in wetting behaviour has vast application in different areas of interest, particularly in microfluidics, as a Laban-a-chip in making nanodevices, chemical micro reactors, microelectronics to control the thermal property, communication based on optical property, drag deliveries, self-cleaning mechanism etc as well as many modern well developed other areas [1]. We will mainly concentrate on the most recent advances in the synthesis of metal nanowires, specifically of $SrMnO_3$ (a perovskite) nanowires, and in addition their properties and a few applications[2]. These nanowires are basically intriguing from the perspective of their wetting properties, which emphatically rely upon the nanowires size and shape. The wetting properties are established relation between the surface property interaction of nanomaterials with incident ion irradiation at different ion energy (varying from 3 keV to 100 keV) and various fluences. Here we also discuss the bending and welding (joining) of Strontium Manganite ($SrMnO_3$) nanowires at the large scale, induced by N^+ ion irradiation at different ion energies and various ion fluences [3]. Transmission electron microscopy (TEM) and field emission scanning electron microscopy (FESEM) studies pointed out interesting structural modifications and joining of the randomly orientated nanowires induced by ion irradiation. The Ion energy above 50 keV having different ion fluences clearly show the joining between two adjacent nanowire in a very large scale, this large scale random bending and joining of the nanowires, at higher energy and higher fluences shows different type of shape of the junction [4].

Thin/ Thick film of $SrMnO_3$ sample are prepared by spin coating and drop casting the liquid sample which is well stirred ultra-sonicated mixture of few milligram $SrMnO_3$ n powder in highly pure 10 ml ethanol bought from Sigma Aldrich, on preheated (~50°C) highly conducting n-type (100 oriented) silicon substrate. The ion irradiation experiments for low ion beam energy were done at energies 50 keV, 80 keV, and 100 Kev for argon (Ar^+) are performed in the Low Energy Ion Beam Radiation Facility at Inter University Accelerator Centre (IUAC, New Delhi), for various ion fluence of 5×10^{15}, 8×10^{15}, 1×10^{16}, 2×10^{16}, and 3×10^{16} ions.cm^{-2}. Sessile contact angles measurements of water droplet (deionized (DI) water (18 M-cm, Millipore)) on both pristine and irradiated $SrMnO_3$ samples were done at ambient temperature (Room temperature) with drop volume of 08 µL using a contact angle measurement unit (Model No. OCA15EC).

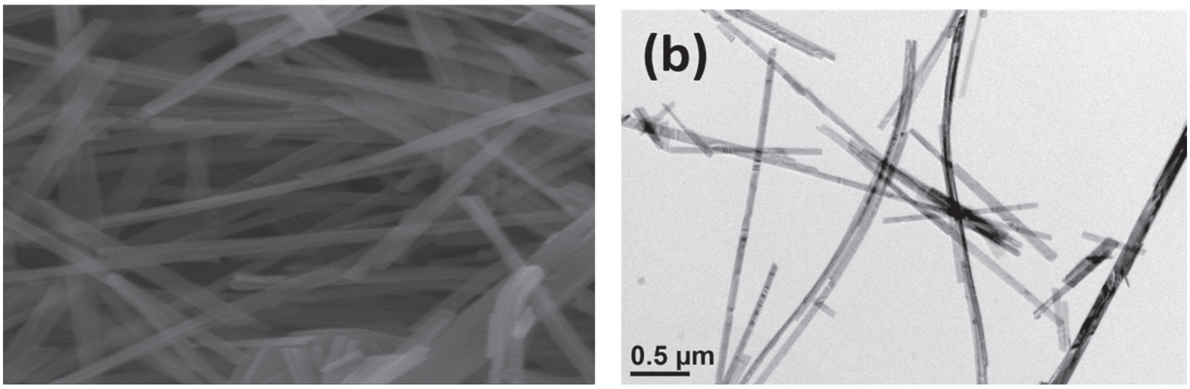

Figure 1. (a) FESEM image, (b) HRTEM image of pristine $SrMnO_3$ nanowires.

The as-synthesized nanowires are usually straight and well separated and uniformly spread on silicon substrate. Figure 1. (a) shows the plan view FESEM image and (b) the HRTEM image of the pristine $SrMnO_3$ nanowires, which shows diameters close to 60 nm as estimated by the histogram plot of pristine sample. The high magnification HRTEM image shows that nanowires are completely straight in length and uniform in diameter along the growth direction (012) which is confirmed by the selected area electron diffraction (SAED) pattern (not shown here).

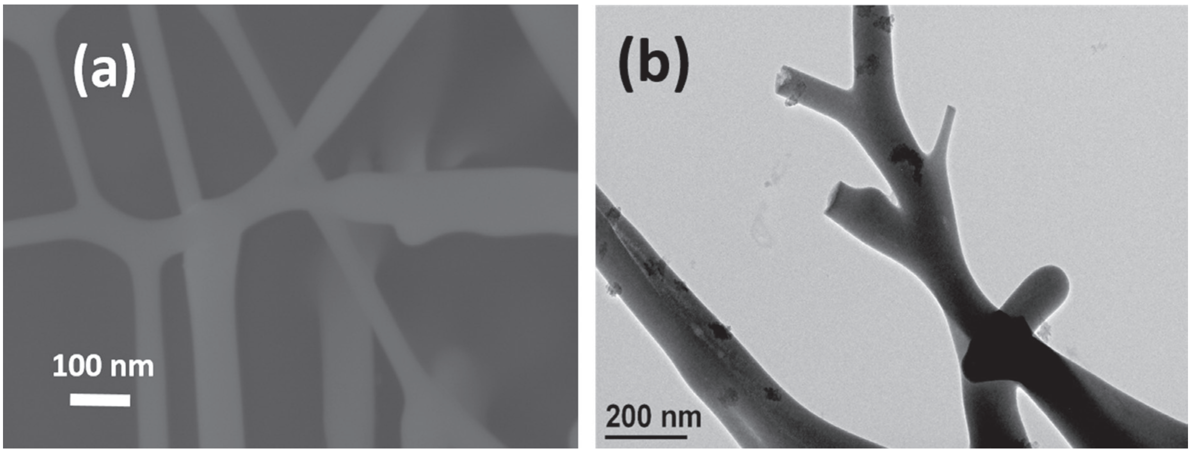

Figure 2. (a) Plan view FESEM image, (b) HRTEM image of joined $SrMnO_3$ nanowires by irradiating it at ion energy 50 keV and at a fluence of 3×10^{16} ions.cm^{-2}.

When we increase the ion energy from initial 3 keV for N^+ ions to 50 keV, 80 keV and 100 keV N^+ ions large scale joining and welding of the nanowires observed which lead to the various type of shape formation of junction such as 'X', 'T','V', 'Y' etc. (Fig 2).The wetting nature of ion modified nanowire assembly is under progress.

REFERENCES:

[1] T. N. Krupenkin, J. A. Taylor, T. M. Schneider, and S. Yang, "From rolling ball to complete wetting: the dynamic tuning of liquids on nanostructured surfaces," Langmuir, vol. 20, no. 10, pp. 3824–3827, 2004.

[2] M. Yoshimura, W. L. Suchanek, T. Watanabe, and B. Sakurai, "In situ fabrication of SrTiO3–BaTiO3 layered thin films by hydrothermal-electrochemical technique," J. Eur. Ceram. Soc., vol. 19, no. 6–7, pp. 1353–1359, 1999.

[3] S. Dhal, S. Chatterjee, S. Sarkar, L. C. Tribedi, R. Bapat, and P. Ayyub, "Nano-welding and junction formation in hydrogen titanate nanowires by low-energy nitrogen ion irradiation," Nanotechnology, vol. 26, no. 23, p. 235601, 2015.

[4] M. K. Rajbhar et al., "Joining of two different ceramic nanomaterials for bottom-up fabrication of heterojunction devices," Appl. Surf. Sci., 2019.

5.2.36 Effect of Low energy N^+ ion implantation in brownmillerite $Ca_2Fe_2O_5$

Durga Sankar Vavilapalli[1], Shubra Singh[1] and K. Asokan[2]

[1]Crystal Growth Centre, Anna University, Chennai-600025,India
[2]Inter-University Accelerator Centre, New Delhi-110067, India. Email: shubra6@gmail.com

It is a well-established fact that material properties can be successfully tailored by using ion implantation technique. Low energy ion bombardment on the metal oxides result in controlled ion - doping or implantation which alter the structural, optical, electrical and magnetic properties. Multifunctional brownmillerite $Ca_2Fe_2O_5$ (CFO) is promising material for energy and environmentalapplications such as fuel cells, batteries, H_2 production and CO_2 capturing etc. owing to their oxygen deficiency, catalytic and mixed ionic electronic conduction (MIEC) properties [1-5]. Brownmillerite structured CFO consists of alternate layers of FeO_6 and FeO_4polyhedra as shown in Figure1. The oxygen vacancies in these compounds are distributed orderly in the two-dimensional FeO_4 tetrahedral layer. Nitrogen (N) substitution in FeO_{4-x} may lead to changes in optical properties by narrowing its bandgap, owing to the lower electronegativity of N than O. Nitrogen substitution can also affect the electrical and magnetic properties of CFO. Keeping in mind, the above mentioned aspects and possibilities, by Nitrogen substitution, we attempted N- ion implantation on CFO bulk films for the first time. Structural and optical properties as implanted films were analyzed.

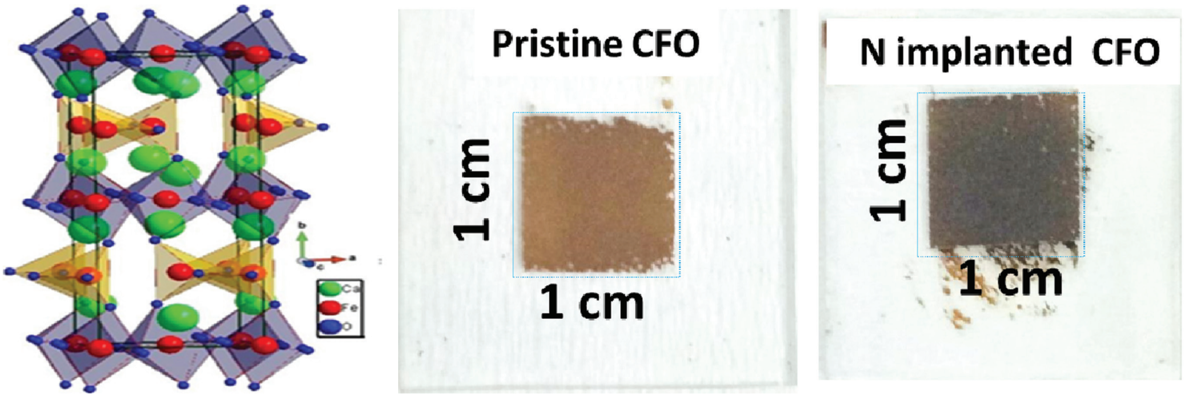

Figure 1 (left) Crystal structure of $Ca_2Fe_2O_5$ with alternate tetrahedra and octahedra layers (right) images of pristine and implanted films

Experimental Details :

Polycrystalline single phase $Ca_2Fe_2O_5$ was prepared by chemical route method [5] and then CFO bulk films were fabricated using Doctor blade method on glass substrate. As coated films annealed in furnace at 300 ºC for 3 hr.These CFO films were then implanted with 1 MeV of N^+ ion beam with a beam current of 1 μA using low energy ion beam facility (LEIBF). The implantation was performed at three ion fluences 10^{14}, 10^{15} and 10^{16} ions per cm^2.

Results and discussion :

X-ray diffraction (XRD) measurements were performed to investigate the effect of N ion implantation on the crystal structureand the nature of crystallinity of CFO films. No additional diffraction peaks corresponding to other phases are detected. This is attributed to the fact that N ionsare incorporated completely into the host lattice site instead ofoccupying some interstitial positions.Figure 1 also shows the image of pristine and N implanted CFO films, the N implanted CFO colour changed due to incorporation of N ions. Nitrogen (N) doping/ substitution in CFO is expected to change the optical properties by narrowing its bandgap due to the lower electronegativity of N as compared to Oxygen.

Conclusion :

CFO films were fabricated using a conventional doctor blade method. The N ions were successful implanted on CFO films with various fluencies successfully. The effect of N ion implantation on CFO films has been examined. The implantation of N ions into CFO significantly decreases the band gap.

REFERENCES:

[1] Baijnath, P. Tiwari, S. Basu, Cobalt and molybdenum co-doped Ca2Fe2O5 cathode for solid oxide fuel cell, International Journal of Hydrogen Energy, 44 (2019) 10059-10070.

[2] S. Dhankhar, P. Tiwari, K. Baskar, S. Basu, S. Singh, Effect of low Cobalt doping on morphology and properties of calcium ferrite and its application as cathode in Solid Oxide Fuel Cell, Current Applied Physics, 17 (2017) 467-473.

[3] S. Dhankhar, S.S. Menon, B. Gupta, K. Baskar, S. Singh, Electrochemical performance of brownmillerite calcium ferrite for application as supercapacitor, AIP Conference Proceedings, 1832 (2017) 080050.

[4] M. Ismail, W. Liu, M.S.C. Chan, M.T. Dunstan, S.A. Scott, Synthesis, Application, and Carbonation Behavior of Ca2Fe2O5 for Chemical Looping H2 Production, Energy & Fuels, 30 (2016) 6220-6232.

[5] K. Gupta, S. Singh, M.S. Ramachandra Rao, Fast, reversible CO2 capture in nanostructured Brownmillerite CaFeO2.5, Nano Energy, 11 (2015) 146-153.

5.2.37 X-Ray Diffraction study of metal ion implanted $BiVO_4$ thin films

P. Sundara Venkatesh[1], M. Ganeshbabu[1], G. Paulraj[2], K. Jeganathan [2] and K. Asokan [3]

[1]Department of Physics, Sri S. Ramasamy Naidu Memorial College, Sattur - 626203, Tamilnadu, India
[2]Centre for Nanoscience and Nanotechnology, Department of Physics, Bharathidasan University, Tiruchirappalli-620024, Tamilnadu, India.
[3]Inter-University Accelerator Centre, New Delhi-110067, India.

Herein, we report the dislocation density and peak shift of the ion implanted Bismuth Vanadate ($BiVO_4$) thin films. $BiVO_4$ thin films were prepared by a simple spin coating technique. After that, the low energy Copper, Nickel and Cobalt ions were implanted on the $BiVO_4$ films with optimum fluency rate. The implanted samples were characterized by X-Ray diffraction (XRD) analysis.

Introduction:

Doping of impurity atoms into a semiconductor material is a traditional way to enhance the physical, chemical and electrical properties [1]. Making composite and heterojunction formation is often used to tailor structural and optical behaviors of the nanomaterials and thin films. But, the distribution of dopant in the host material by chemical process is still not satisfactory. Ion implantation is a promising physical approach to achieve uniform distribution of doping material with great extend.

In this context, we report the structural properties of the BiVO4 thin films with different metal ion implantations at optimum fluency range. $BiVO_4$ is identified as a n-type semiconductor material having ~2.4 eV band gap. Due its narrow band gap nature, it is extensively investigated in the field of visible light photocatalysis and Photoelectrochemical (PEC) systems. The major problem arises when it is used alone are poor charge transportation, high charge recombination and slow hole kinetics of oxygen evolution [2]. In order to overcome this problem we have planned to introduce some metal ions on $BiVO_4$ thin films by ion implantation method.

Simple and cost effective spin coating technique was used to fabricate BiVO4 thin films. Cu and Co ions of 60 keV and Ni ions of 120 keV were implanted on BiVO4 thin films with 5 X 10^{15} ions/cm^2 fluency rate at Inter University Accelerator Centre (IUAC), New Delhi, India.

Results and Discussion:

X-ray Diffraction patterns of the ion implanted $BiVO_4$ thin films were depicted in the given below figure. XRD patterns of the all samples closely matched with JCPDS Cord no: 00-014-0688. This represents the monoclinic phase of $BiVO_4$. As compared to the bare $BiVO_4$ thin films, the dominant (121) peak was shifted to the higher angle side. This may be attributed to the incorporation of ions on the host matrix. The average grain size and dislocation density calibrated from William's and Hall plot. The result obtained from W-H plot is given in the following table.

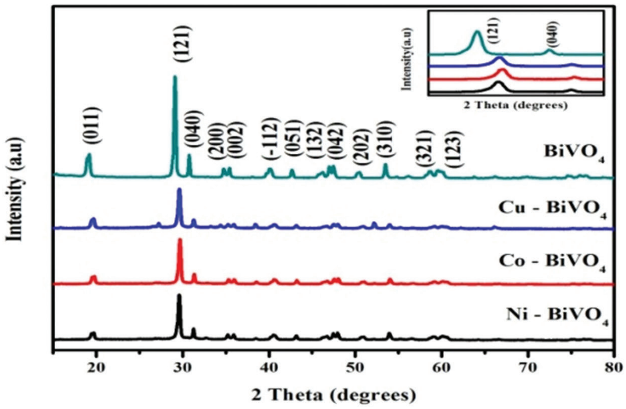

Fig-1 : X-ray Diffraction spectra of pristine and metal ion implanted films

Table-1 :

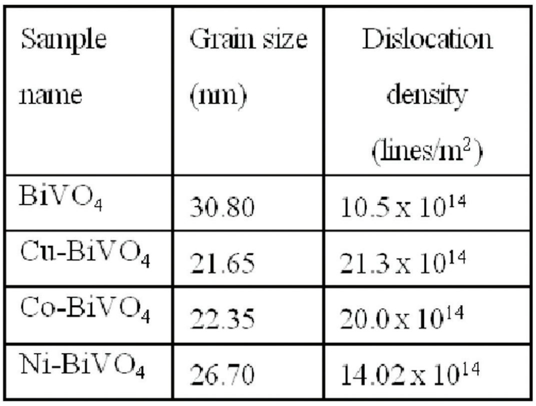

Sample name	Grain size (nm)	Dislocation density (lines/m^2)
BiVO$_4$	30.80	10.5 x 10^{14}
Cu-BiVO$_4$	21.65	21.3 x 10^{14}
Co-BiVO$_4$	22.35	20.0 x 10^{14}
Ni-BiVO$_4$	26.70	14.02 x 10^{14}

Crystallite size and dislocation density of the pristine and metal ion implanted films

Conclusion:

XRD patterns of the bare and implanted samples showed that the monoclinic structure of BiVO$_4$. The right angle peak shifts in XRD pattern and dislocation density confirms the defects in the irradiated samples.

REFERENCES:

[1] J. Wallentin & M.T. Borgstrom, Journal of Materials Research, 26 (2011) 2142-2156.

[2] G. Park, H. Kim, H. Kim et al., Nanoscale Adv., 3 (2019) 799-806.

[3] B. Paul, J. S. Sagu, et al., Chem. Vap. Deposition 20(2014), 1–5.

5.2.38 Raman investigation of N implanted ZnO: Defects, disorder and recovery

A Mondal[1], S Pal[2], A Sarkar[3], T. S Bhattacharya[4], S Pal[5], A Singha[4], S. K Ray[6], P Kumar[7], D Kanjilal[7] and D Jana[1,*]

[1]Department of Physics, University of Calcutta, 92 , Acharya Prafulla Chandra Road, Kolkata 700009, India.
[2]Department of Physics, School of Natural Sciences,Shiv Nadar University, NH 91, Tehsil Dadri, Gautam Buddha Nagar, Uttar Pradesh – 201314.
[3]Department of Physics, Bangabasi Morning College, 19 Rajkumar Chakraborty Sarani, Kolkata 700009, India.
[4]Department of Physics, Bose Institute, 93/1, Acharya Prafulla Chandra Road, Kolkata 700009, India.
[5]Department of Physics, Indian Institute of Technology, Kharagpur 721302, India.
[6]S. N. Bose National Centre for Basic Sciences, JD Block, Sector-III, Salt Lake City, Kolkata - 700 106, India.
[7]Inter University Accelerator Centre, Post Box 10502, Aruna Asaf Ali Marg, New Delhi 110067, India.
*Email: djphy@caluniv.ac.in

Understanding defects, disorder and doping due to N implantation in ZnO is one of the most debated issues for the last few years. In the present work, a comprehensive investigation has been carried out using Raman, photoluminescence (PL) spectroscopy and grazing-incidence X-ray diffraction on 50 keV N ions implanted granular ZnO with different fluence (~ up to 6.5% atomic concentration) along with post-implantation annealing. Raman investigation suggests that 275, 510, 643, 857 cm^{-1} modes are directly related to nitrogen. Additionally, VZn may have some role in stabilizing 275 cm^{-1} mode. The broadening (or tailing) of E_2^{low} mode is related to vibration of distorted Zn sublattice, may be a product of ion implantation generated defect cluster like VZn-VO. The distortion starts to reduce with annealing at elevated temperatures. Direct correlation between 555 cm^{-1} Raman mode and the tailing of E_2^{low} mode have been found. More defect clustering is vivid from the reduced PL of the ZnO samples with increasing implantation fluence. So, tailing of E_2^{low} Raman mode, increasing intensity of 555 cm^{-1} mode and non radiative defect centers are of common origin. Both the ratios E_1(2LO)/E_1(LO) and E_2^{high} /E_1(LO) both can be used as parameters to measure the defective nature of ZnO after ion implantation/ irradiation. Low temperature PL (selected samples) suggests absence of shallow acceptor states, although negative thermal quenching above 250 K has been observed (implantation fluence 1×10^{16} ions/ cm^2 and annealed at 500 ºC) which can be a signature of deep acceptors.

Experimental Details

Polycrystalline ZnO (99.99% pure, Sigma-Aldrich, Germany) powder in pellet forms has been annealed in a Muffle furnace at 500 ºC for four hours to make samples unwanted organic and H2O free. Annealed samples have been implanted by 50 keV nitrogen ion beam at LEIBF facility in IUAC, New Delhi, India with fluences varying from 10^{12} to 10^{17} ions/cm^2. Furthermore, samples implanted with 10^{16} ions/cm^2 nitrogen ion beam have been further annealed with different temperature (200, 250, 300, 400, 500 and 600 ºC) for 4 hour at ambient air to study the recovery of defects with annealing temperatures.

Raman spectra (RS) have been measured by Lab RAM HR Jovin Yvon Raman set-up equipped with Peltier cold CCD detector having 488 nm Argon laser as an excitation source. Both room and low temperature PL properties of all samples have been recorded using 325 nm laser source with output power 45mW and a TRIAX 320 monochromator was fitted with a cooled Hamamatsu R928 photomultiplier detector. Grazing-incidence X-ray diffraction (GIXRD) measurements has been performed (model: Bruker, D8 Discover) to understand the structural evolution of the implanted layers. Here, the X-ray incidence angle has been kept at 1º to ensure the probe region of the X-ray to be confined within the implanted region.

Results and Discussion:

Figure 1 (a) and (b) depicts the Raman spectra of implanted and post-implanted annealed samples. In the following section, we intend to discuss few key features of Raman spectra in disordered ZnO. From the comparative study of two Raman spectra whose 580 cm^{-1} peak area or height is more or less same it is unambiguous that 275 510, 643, 857 cm^{-1} are related to nitrogen. This is not true for 555 cm^{-1} Raman mode. Rather this Raman mode scales with the disorder which is responsible for the broad tailing of E_2^{high}. Figure 1 (c) depicts that the variation is almost linear. Hence, 555 cm^{-1} Raman mode is indeed related to disorder. Zeng et. al have proposed [1] that typical defects like IZn residing at the interface of Zn/ZnO interface are responsible for 555 cm^{-1} Raman mode. Such kind of defects can be generated due to grain fragmentation during ion irradiation. In our opinion, the distorted Zn sub-lattice vibration gives rise to such tailing of E_2^{low}. The same distortion exists at the fragmented grain interface and/thus distortion generated IZns are also likely to be present there. It is generally understood that 580 cm^{-1} peak intensity scales with the concentration of VOs in ZnO, if we assign the 2.42 eV room temperature PL (RTPL) emission with the VO in ZnO, a correlation is expected which, however, is not found (not shown). Further, it is well known that the intensity ratio of E_1(2LO) and E_1(LO) is an important parameter in ZnO [2] and other semiconductors [3,4] which indicates the spatial extent (average) of coherently scattering regions (CSR) as probed by Raman spectroscopy. So, the ratio of E_1(2LO)/E_1(LO) is closely related with the disorder present in the material. In the same graph (Figure 1 (d)) both intensity ratio of E_1(2LO)/E_1(LO) and E_2^{high} /E_1(LO) have been plotted. If this ratio with fluence is plotted in a log-log scale, almost a linear variation is observed in the whole fluence regime studied here. The uncanny similarity can be understood from the exponential decay fitting (not shown) of of E_1(2LO)/E_1(LO) and area under E_2^{high}. The thermal activation energy of E_1(2LO)/E_1(LO) and area under E_2^{high} turn out to be nearly same. Low activation energy of disorder recovery is representative of the increase of length scale of CSR, mostly found in nanocrystalline materials [5,6]. Similarity in activation energies manifests the fact they share common origin and both the parameters (i.e. E_1(2LO)/E_1(LO) and E_2^{high} /E_1(LO)) can be used to assess the extent of damage due to implantation/irradiation. As the implantation fluence increases the ratio decreases gradually while the ratio increases with annealing temperature.

In conjunction to RTPL findings (not shown), it is evident that defects responsible for the tailing of E_2^{low} mode are mostly non-radiative in nature. The recovery of band edge emission starts above 250 ºC annealing temperature. As manifested by Raman findings, the implanted ZnO gradually recovers with increasing annealing temperature with full recovery at 600 ºC. It is clear that RTPL from ZnO is sensitive to particular type of defects whereas Raman signal probes overall disorder in the sample.

Low temperature PL (LTPL) spectra of un-implanted, implanted samples (with fluences 1E16, 1E17) and post-implanted annealed samples (annealed at 500 ºC and 600 ºC) at near band emission (NBE) mainly dominated by 3.313 eV emission are mostly assigned as free electron transition to localized acceptor states (not shown). Compared to un-implanted sample, the DBX emission is suppressed in all the measured PL spectra of other samples. It can be understood that N implantation inhibits the emission from shallow donors which is indeed interesting. However, no identifiable signature of shallow acceptor bound emission has been noticed in the LTPL spectra of any of the samples. In cases of post-implanted 500 ºC annealed sample, temperature dependent PL spectra exhibits negative thermal quenching (NTQ) above 250 K which can be a signature of deep acceptors. This responsible defect is generated as a combined effect of N implantation and subsequent annealing. Thus, transforming such deep acceptors to shallower one in ZnO is still as a challenge.

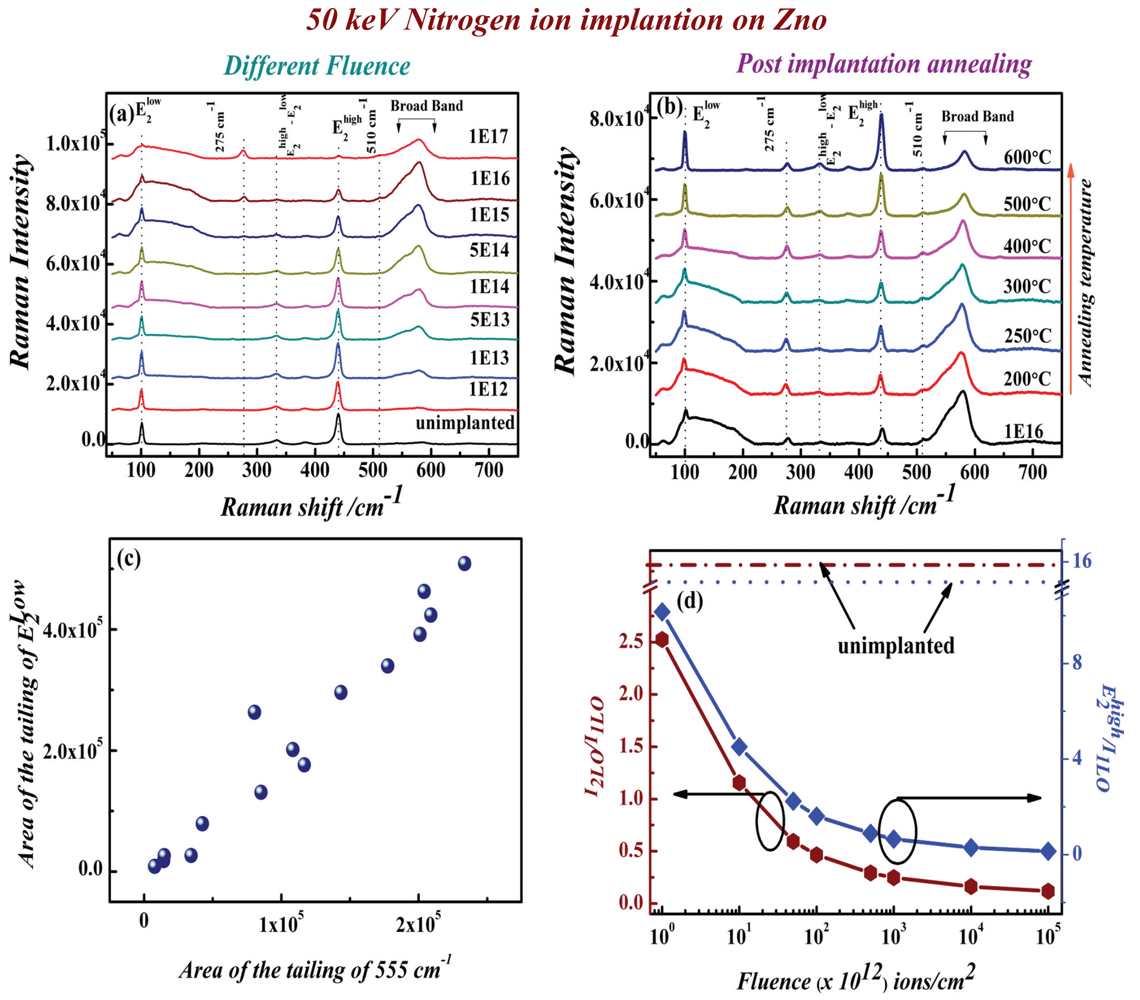

Figure 1: (a) Room temperature Raman spectra of (a) N- implanted at different fluences (b) post-annealed N-implanted (c) variation of area of the tailing of E_2^{low} (100 cm^{-1}) with area under 555 cm^{-1} mode (d) variation of E_1(2LO)/E1(LO) and E2high/E1(LO) with fluences.

REFERENCES:

[1] H. Zeng, X. Ningab and X. Liab, Phys. Chem. Chem. Phys.17 (2015) 19637.

[2] H. M. Cheng, K. F. Lin, H. C. Hsu and W. F. Hsieh, Appl. Phys. Lett. 88 (2006) 261909.

[3] J. Li, J. Ye, F. Ren, D. Tang, Y. Yang, K. Tang, S. Gu, R. Zhang and Y. Zheng, Sci. Rep. 7 (2017) 44399.

[4] D. Paramanik and S. Varma, J. Appl. Phys. 101 (2007) 023528.

[5] X. H. Huang, C. Zhang, C. B. Tay, T. Venkatesan, S. J. Chua, Appl. Phys. Lett. 102 (2013) 111106.

[6] S. Shukla, S. Seal, R. Vij, S. Bandyopadhyay, Nano Lett. 3 (2003) 397.

5.2.39 Development of Ion Beam Modified Self- Cleaning Zno Thin Films for Improved Antimicrobial Efficacy Against Multidrug Resistant Bacteria

Subhavna Juneja[1], Prof. Prasenjit Sen[2] and Dr. Jaydeep Bhattacharya[1]

[1]School of Biotechnology, Jawaharlal Nehru University, New Delhi-110067
[2]School of Physical Science, Jawaharlal Nehru University, New Delhi-110067

Metal oxides are excellent antimicrobial agents with restricted applicability. Limited optical responsiveness, poor adhesion and mechanical strength are its major drawbacks. Plasmonic nanocomposites address these issues to a certain extent however, they have adverse effects in probability of self-recombination, complex surface passivation protocols and controlled functionalization. Thus, manipulating metal oxide matrix at atomic level through implant technology offers to be a good alternative as it is controlled and forms no self-recombination centres.

Experimental Details

In this work, we irradiated previously synthesized zinc oxide nanocomposites with different metallic and gaseous sources for their application as an improved antimicrobial agent. The sources used were Au, Ar and N (Low energy beams).

Results:

Preliminary results obtained from antimicrobial assay indicate similar activity as to control. No significant change in killing efficiency of irradiated and non-irradiated samples was observed. The killing efficiency estimated is approx. ~ 97% in 2 hours. However, these results have been performed only once thereby drawing a firm conclusion is difficult and requires some more experiment to affirm its statistical significance. We'll repeat the implant in the next phase and shall continue to perform the biological measurements. The work has been done in collaboration and discussion with Dr. Asokan.

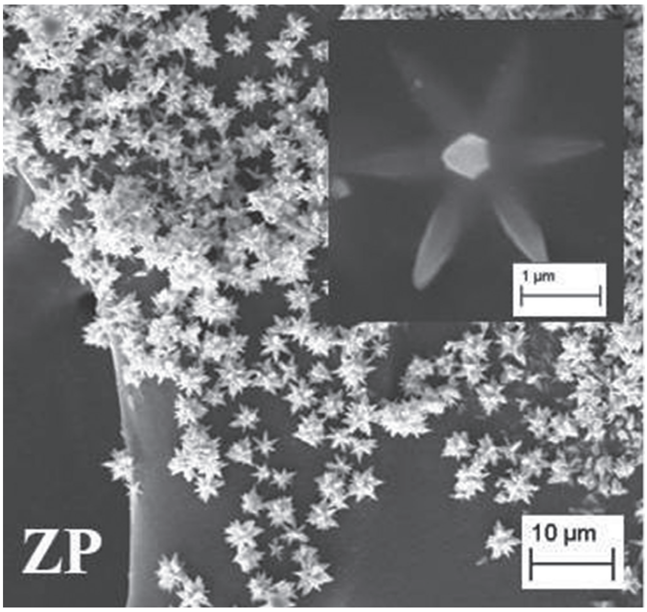

Figure 1: SEM micrograph of the chemically synthesized zinc oxide nanostructures implanted with different ions.

5.2.40 Impact of Space Radiation on stability of medicines flown to spacecraft

Dhara Bhayani[1], Saif Khan[2] and Priti Mehta[1*]

[1]Institute of Pharmacy, Nirma University, Ahmedabad, Gujarat-382481, India.
[2]Inter-University Accelerator Centre, Aruna Asaf Ali Marg, New Delhi 110067, India.

The drugs are inevitable part of healthcare system. Stability of medicines assures its safety and efficacy. The changes in drug product stability can risk a patient safety by formation of toxic degradation product or deliver a lower dose than expected. Exposure of the drugs to space radiations during space missions can lead to alteration in stability of the medicines. Among various space radiations, one of the component – Heavy ion radiation causes damaging effects on the exposed material. So, evaluation of their effects on the drug stability is essential.

We have exposed drugs and their tablet formulations to ^{56}Fe irradiation (^{56}Fe, 100 MeV with 50 cGy, 1 Gy, 10 Gy and 50 Gy doses at RT). Their stability was evaluated post radiation exposure using various analytical techniques such as Fourier-Transform Infrared spectroscopy (FTIR) and High-Performance Liquid Chromatographic (HPLC) method. The physical changes were evaluated using organoleptic evaluation. The results of the study showed that the drugs were stable to ^{56}Fe irradiation at the selected doses.

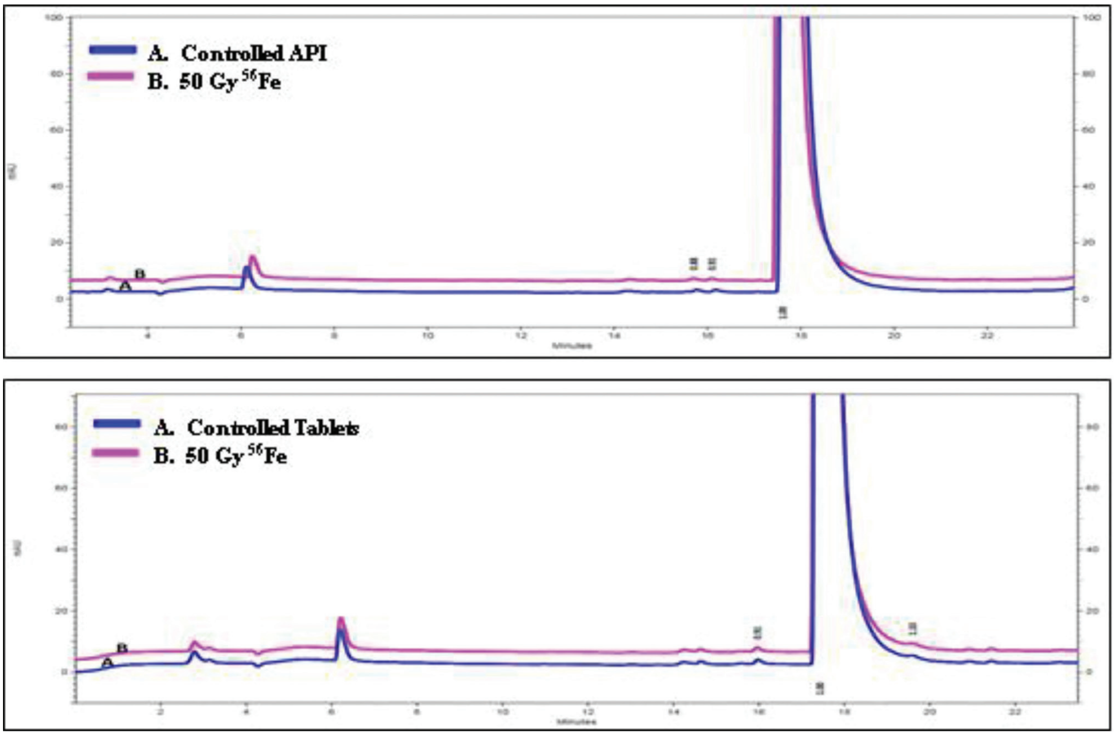

Figure 1 Stability of amlodipine API and tablets after ^{56}Fe irradiation

Experimental Details

API and tables of amlodipine were exposed to ^{56}Fe irradiation (^{56}Fe, 100 MeV with 50 cGy, 1 Gy, 10 Gy and 50 Gy doses at RT). Post radiation exposure samples were analysed for their physicochemical by organopletic evaluation, FTIR and HPLC analysis.

Results

No colour changes were observed in the ^{56}Fe irradiated API or tablet samples. No changes were observed in the recorded FTIR spectra for controlled and irradiated samples. The HPLC chromatograms of API and tablets of each drug irradiated by ^{56}Fe radiation exhibited no additional peak compare to control samples, as well as the peak areas of the peak remained unchanged. These results indicated that drugs were chemically stable to these radiations at selected doses.

We have published one article from this study in a reputed journal: ·
Bhayani, Dhara, Haladhara Naik, T. Newton Nathaniel, Saif Khan, and Priti Mehta. "Simulated space radiation: Investigating ionizing radiation effects on the stability of amlodipine besylate API and tablets." European Journal of Pharmaceutical Sciences (2019): 104982. (Impact factor: 3.5; publication house: Elsevier)

REFERENCES:
[1] Mehta, Priti, and Dhara Bhayani. J. Pharm. Biomed. Anal. 136 (2017): 111-119.
[2] B. Du, V. Daniels, Z. Vaksman, J. Boyd, C. Crady, L. Putcha. AAPS J. 13 (2011) 299–308.
[3] M.C. Chuong, D. Prasad, B. LeDuc, B. Du, L. Putcha. J. Pharm. Biomed. Anal. 55 (2011) 1197–1200.
[4] Wotring, Virginia E. AAPS J. 18(2016): 210-216.

5.2.41 Reversible phase transformation phenomenon in titanium dioxide films: evidence beyond interface-nucleation and dissolution-precipitation kinetics

Subodh K. Gautam[1,2], Jitendra Singh[1], D. K. Shukla[3], E. Pippel[4], P. Poddar[2] and Fouran Singh[1]

[1]Materials Science Group, Inter-University Accelerator Centre, Aruna Asaf Ali Marg, New Delhi, India-110 067
[2]Physical & Materials Chemistry Division, CSIR-National Chemical laboratory, Pune 411008, India.
[3]UGC-DAE Consortium for Scientific Research, University Campus, Khandwa Road, Indore 452017, India
[4]Max Planck Institute of Microstructure Physics, Weinberg 2, D-06120 Halle, Germany

Understanding of thermodynamic stability and phase control of nano-crystalline materials is more important because their device applications response and physio-chemical properties are heavily affected with the changes in crystallite size, stoichiometry and lattice parameters by impurity doping, thermal annealing and ion irradiation [1, 2]. In this study, the reversible PT in nano-crystalline TiO_2 thin films and the thermal stability of nano-sized rutile and anatase crystallites were studied at annealing temperature range from 532 K to 1323 K. The mechanism and factors affecting the phase stability and transformations are understood by the kinetics of phonon dynamics and electronic structure modification using micro-Raman and near edge X-ray absorption fine structure spectroscopy (NEXAFS), respectively. In present work, ion beam sputtered rutile TiO_2 films on silicon substrate are used. Initially, the crystalline rutile films were amorphized using the 120 MeV Ag-ions irradiation at IUAC, New Delhi. *In situ* isothermal annealing study is carried out at 523 K and shows rapid nucleation of anatase phase occurs from amorphous structure with three dimensional growths of anatase NCs. This phenomenon is well explained using Johnson–Mehl–Avrami-Kolmogorov (JMAK) model of nucleation and growth kinetics [3]. In Fig. (a), annealing at low temperature range 523 K - 673 K, shows transformation into rutile phase and follows the interface-nucleation mechanism [1]. At moderate annealing temperature from 623 K to 973 K, results show decrease in rutile weight fraction and reversible PT of nano-sized rutile TiO_2 to anatase NCs. The decrease in rutile weight fraction is related to thermodynamic un-stability of rutile NCs and lattice stress-induced dissolution of small rutile NCs into anatase phase [4]. However, annealing at higher temperature (1123 K - 1323 K) induces the growth of anatase NCs and their natural transform into rutile phase follow the well-known dissolution–precipitation mechanism. Fig. (b) shows the normalized NEXAFS spectra of Ti $L_{3,2}$-edges for the modification of local electronic structural at different annealing temperatures. Thus, overall PT kinetics at different temperature range is well understood by invoking in three step mechanism: I) early stage (523 K - 673 K), anatase-to-rutile transformation is dominated by interface-nucleation, II) then intermediate stage (673 K - 973 K), reversible rutile-to-anatase PT and, III) at later stages at high temperatures, anatase-to-rutile PT is controlled by dissolution–precipitation mechanism. Therefore, present, investigations may encourage new research in similar functional oxide materials and their potential device applications utilizing the reversible transition. For details, see the article **[Subodh K. Gautam *et al.* Acta Materialia 146 (2018) 253-264].**

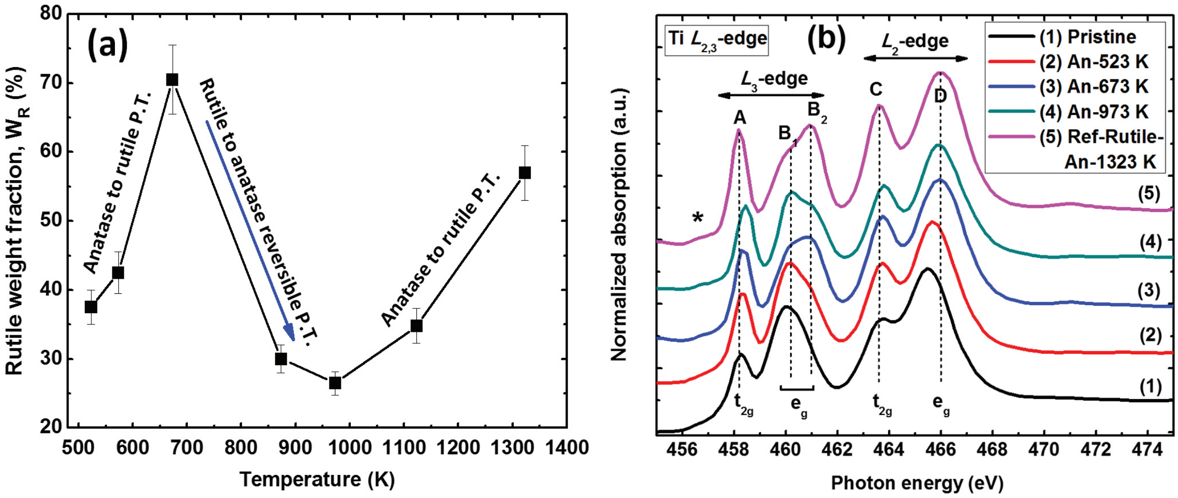

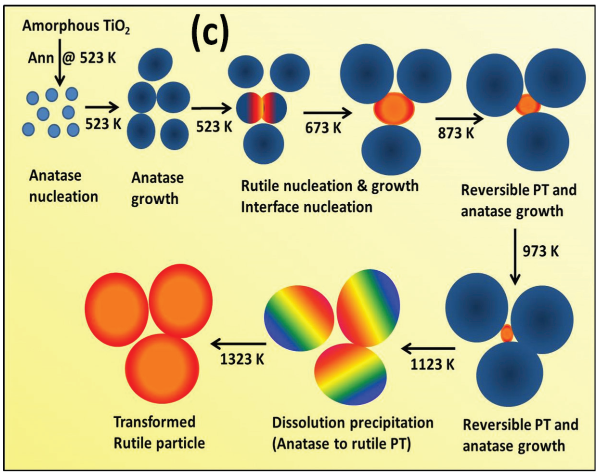

Figure: (a) Response of rutile weight fraction calculated from X-Ray diffraction data analysis and (b) normalized NEXAFS spectra of Ti $L_{3,2}$-edges for the information of local electronic structural modification during PT between anatase and rutile phases as a function of annealing temperature. (c) Schematic diagram shows the re-crystallization of amorphous to anatase phase and overall three step PT mechanisms at different annealing temperatures.

REFERENCES:

[1] H. Zhang *et al.,* Chem. Rev. **114** (2014) 9613–9644.
[2] S.K. Gautam *et al.,* J. Appl. Phys. **115** (2014) 143504
[3] M.C. Weinberg *et al.,* J. Non. Cryst. Solids. **219** (1997) 89–99
[4] K. Wu *et al.,* Appl. Phys. Lett. **91** (2007) 101903

5.2.42 Effect on Structural, Optical and Electrical Properties of Mg Doping on ZnO Nanorods Thin Films

Vishnu V. Kutwade[1], Ketan P. Gattu[2], Makrand E. Sonawane[1], Fouran Singh[3] and Ramphal Sharma[1,2*]

[1]Department of Physics, Dr. Babasaheb Ambedkar Marathwada University Aurangabad, (MS)-431004 India.
[2]Department of Nanotechnology, Dr. Babasaheb Ambedkar Marathwada University Aurangabad, (MS)-431004 India.
[3]Inter-University Accelerator Centre, New Delhi-110067, India.

Pure and (10% and 20%) Mg doped ZnO nanorods thin films have been successfully grown over glass substrate using simple cost effective chemical bath deposition method. The structural, optical and electrical properties of the synthesized materials have been studied using XRD, Raman, UV-Vis spectroscopy and I-V characteristics. The structural properties revealed the formation of MgO phase for 20% Mg doping. This formation of MgO phase had a significant effect on optical and electrical properties of the ZnO nanorods thin films, the optical band gap showed an increase of 0.46 eV with 20% Mg doping, while the electrical properties showed a decrease in resistance after Mg doping

There has been a great deal of interest in ZnO due to its potential applications in gas sensors, optical waveguides, surface acoustic devices and piezoelectric transducers. The intrinsic ZnO thin films are n-type semiconductors with high resistivity. Mg-doped ZnO is considered as the most suitable material for light emitting devices because it efficiently absorbs the near UV (330–400 nm) and emits a broad spectrum covering almost the whole visible region. In order to obtain a wider band gap, Mg doping content in ZnO thin film needs to be higher, at the same time the structure of Mg-doped ZnO thin films should retain wurtzite structure. Hence, different growth techniques are needed to synthesize Mg-doped ZnO thin films. Considering the advantages of chemical synthesis over physical methods and with an aim of mixing materials/sources atomic level so that the materials are close enough to form thermodynamic equilibrium, we have chosen chemical synthesis in our present work. The ZnMgO 1-D nanorods have been grown on the glass substrate using a single step chemical approach.

Experimental Details

Synthesis of ZnMgO 1-D nanorods and Cu2S thin films:

Fig.1. shows a schematic for the synthesis of ZnO and Mg-doped ZnO NR thin film using single-step chemical bath deposition technique on a glass slides. Initially, the glass slides were kept in chromic acid for 1.30 hr. at 80 °C and then subsequently washed with deionized water (DI) and laboline detergent. This cleaning of the substrate is important to step in the deposition process to obtain uniform thin film and achieve better adhesion and stoichiometry. The obtained films were yellowish white in color with uniform deposition over the entire surface of the substrate. The films were washed with deionised water to remove weakly bonded atoms on the surface and dried subsequently.

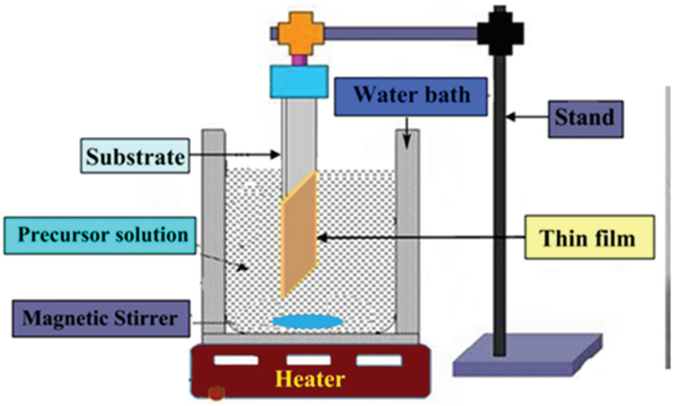

Figure.1 Schematic of a chemical bath deposition

Results and discussion:

Fig. 2a Shows the XRD patterns of ZnO: x% Mg (x= 10, 20). the intensity of the (002) peak decreases and (100) & (101) peaks intensity increases slightly, with a very low broadening at increasing Mg concentrations. This suggests that the incorporation of Mg in the ZnO structure does not substantially affect the crystallinity of the films due to the less difference in ionic radii of Mg (0.57Å) atoms and Zn (0.60 Å) atoms. Fig 2 (d1, d2) shows the SEM micrographs of Pure ZnO and Mg doped ZnO thin films which confirms the 1-D nanorods structures of ZnO thin films.

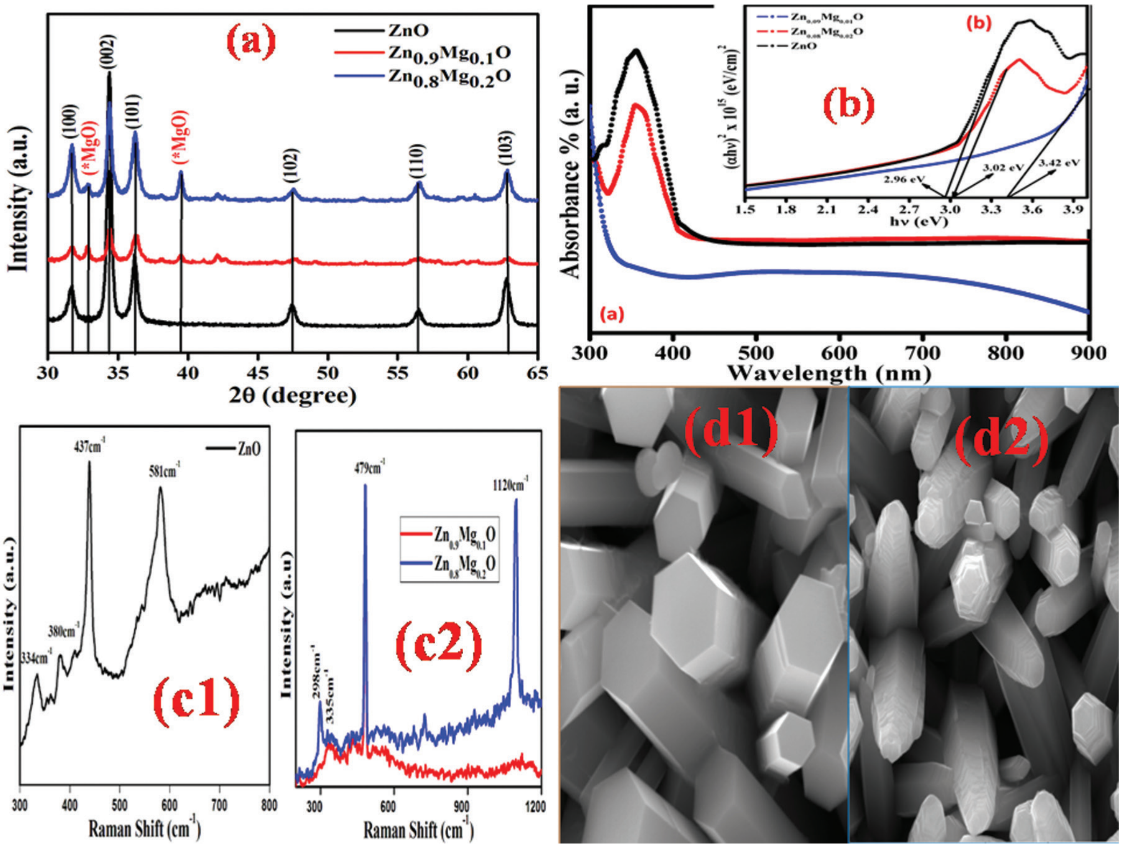

Fig 2 (a) X-ray diffraction patterns of ZnO and Mg (10% & 20%) Doped ZnO NRs thin films; (b) UV-Vis spectra of ZnO and Mg Doped ZnO NRs thin films; (c1) Raman spectra of pure ZnO and (c2) & (c3) Raman spectra of Mg-doped ZnO; (d1) Top view of SEM image of ZnO and (d2) Mg Doped ZnO NRs thin films

The UV–Vis absorption spectra obtained for ZnO and Mg-doped ZnO NRs thin film deposited on a glass substrate is shown in Fig. 2(b). The absorbance spectra show UV cut off at around 350–380 nm, due to the photoexcitation of electrons from valence to conduction band.

The bandgap of the as-grown ZnO and ZnMgO NRs thin film was calculated by extrapolating the plot of $(\alpha h\nu)^2$ vs hν using the Tauc's relation. The bandgap obtained for the ZnO and Mg (10% & 20%)-doped NRs thin films are 2.96eV and 3.02eV & 3.42eV respectively. A Raman spectrum of ZnO sample gives a sharp and dominant peak at 438 cm^{-1} assigns to the Raman active E2 (high) mode, which corresponds to hexagonal wurtzite phase of ZnO as shown in fig 2(c1). Also, three small peaks at 334cm^{-1}, 380cm-1 and 581cm^{-1} were observed. which are assigned to multiple phonon processes, A1 (TO) and E1 (LO), respectively. However, the E2 (high) mode for Mg-doped ZnO nanoparticles thin films has been blue shifted to 481cm-1 compared to ZnO thin films. Mg (10% & 20%) doping into ZnO crystal lattice, which incites the tensile strain within the wurtzite hexagonal Mg-ZnO nanorods structure. In fig 2 (c2) extra peaks at 298cm^{-1}, 335cm^{-1}, and 1120cm^{-1} observed, which shows the formation of MgO phase and the distinguished peak spectra was influenced by the 1LO band is observed at ~1120cm^{-1}. Intensity of 1LO peak increases with increase in concentration of Magnesium (Mg).

Photoluminescence spectra of pure ZnO and Mg-doped ZnO nanorods measured at room temperature with an excitation wavelength of 450 nm. Figure 4 (a) shows the spectra, three bands emission can be observed in both pure ZnO and Mg-doped ZnO thin films, one in the UV region namely near band edge (NBE) emission and another two in the visible region namely deep level (DLE) emission. The PL spectra of the prepared samples from which near-band-edge (NBE) emission band at around ~389 nm observed for all the doped and undoped samples along with the other luminescence bands. The emissions of ZnO nanostructures may consist of LO-phonon (~581 cm-1) replicas occur with a separation of the LO-phonon energy (~71 meV) from NBE. The origin of the emission band observed at around 454 nm is attributed to the presence of zinc vacancies. The broad emission band at around ~561 nm is assigned to oxygen vacancies. This broad emission is enhanced after Mg (10% & 20%) doping due to the increase in defects concentration.

We can see in PL spectra some deep level defects are observed which is due to zinc and oxygen vacancies.

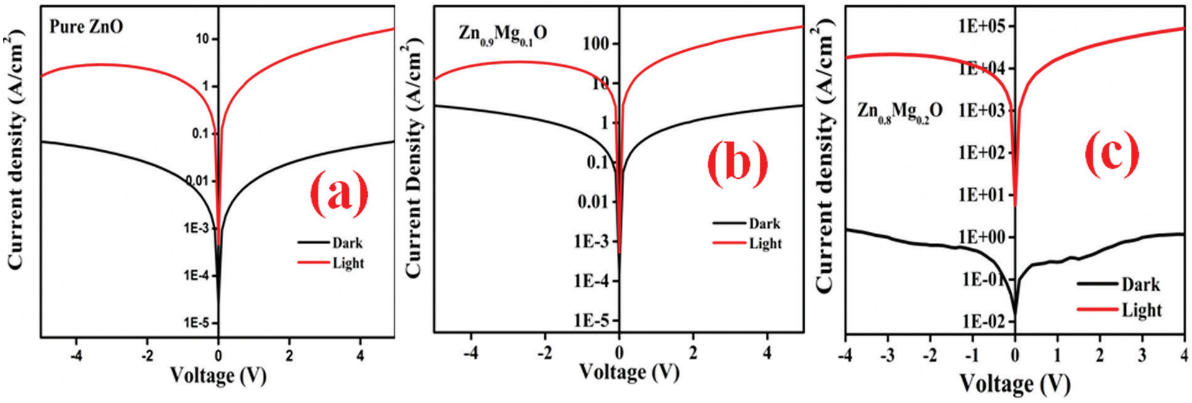

Fig. 3 J-V characteristics of (a) pure ZnO (b) $Zn_{0.9}Mg_{0.1}O$ and (c)$Zn_{0.8}Mg_{0.2}O$ thin films

From Fig. 3 we can clearly see the drastic increase in current density after illumination of light. below in Table1.

This change in resistance after light exposure demonstrates that the films are suitable for visible light photosensor. Also, from the nanorod structure has been reported to have a trapping mechanism for photoconduction. Due to the high surface-to-volume ratio the presence of a high density of hole-trap states at the nanorod surface, drastically affects the transport and photoconduction properties. In dark, a low-conductivity depletion layer is formed near the surface due to the adsorption of oxygen molecules on the oxide surface which captures the free electrons present in the n-type oxide semiconductor. Upon illumination with photon energy above Eg (bandgap energy), electron-hole pairs are photo generated; holes travel to the surface and discharge the negatively charge adsorbed oxygen ions and as a result, oxygen is desorbed from the surface. The unpaired electrons are either collected at the anode or recombine with holes generated when oxygen molecules are adsorbed and ionised at the surface. This hole-trapping mechanism through oxygen adsorption and desorption in nanorods is dominant due to the high density of trap states as a result of dangling bonds at the surface and the surface zinc vacancies enhancing the nanorod photo response.

Acknowledgment

One of the authors Vishnu V. Kutwade is thankfull to IUAC New Delhi for financial support and Dept. of Physics, Dr. B.A.M. University for providing laboratory facilities.

REFERENCES:

[1] MS Alam, U Manzoor, M Mujahid, AS Bhatti, Journal of Sensors, (2016)

[2] M Amin, NA Shah, AS Bhatti, MA Malik, Crystengcomm **16**, 6080-6088 (2014)

[3] SD Senol, C Boyraz, E Ozugurlu, A Gungor, L Arda, Crystal Research and Technology **54,** (2019)

[4] DC Agarwal, F Singh, D Kabiraj, et al., Journal of Physics D: Applied Physics **41,** 045305 (2008)

[5] N Winkler, S Edinger, W Kautek, T Dimopoulos, Journal of Materials Science **53,** 5159-5171 (2018)

[6] E Vinoth, S Gowrishankar, N Gopalakrishnan, Applied Physics a-Materials Science & Processing **124,** (2018)

[7] D-A Dive, D-N Huse, K Gattu, R Sharma, Soft Chemical Growth of Zn 0.8 Mg 0.2 S One Dimensional Nanorod Thin films for Efficient Visible Light Photosensor. (2017)

[8] PFH Inbaraj, JJ Prince, Journal of Materials Science: Materials in Electronics **29,** 935-943 (2018)

[9] ZY Jiang, KR Zhu, ZQ Lin, SW Jin, G Li, Rare Metals **37,** 881-885 (2018)

[10] E Muchuweni, TS Sathiaraj, H Nyakotyo, Heliyon **3,** e00285 (2017)

[11] M Arshad, MM Ansari, AS Ahmed, et al., Journal of Luminescence **161,** 275-280 (2015)

[12] NCS Selvam, S Narayanan, LJ Kennedy, JJ Vijaya, Journal of Environmental Sciences-China **25,** 2157-2167 (2013)

[13] L Umaralikhan, MJM Jaffar, Journal of Materials Science-Materials in Electronics **28,** 7677-7685 (2017)

[14] M Wang, J Yi, S Yang, et al., Applied Surface Science **382,** 217-224 (2016)

[15] C Soci, A Zhang, B Xiang, et al., Nano Letters **7,** 1003-1009 (2007)

[16] SK Mishra, RK Srivastava, SG Prakash, RS Yadav, AC Panday Opto-Electronics Review, (2010)

[17] YK Frodason, KM Johansen, TS Bjørheim, BG Svensson, A Alkauskas, Physical Review B **95,** 094105 (2017)

5.3 RADIATION BIOLOGY

5.3.1 Signaling pathways of activation and secretion of Matrix Metalloproteinases from human lung carcinoma cells after irradiation with carbon ion beam

Dey Payel[1], Chowdhury Priyanka[1], Ghosh Sourav[1], Sarma Asitikantha[2] and Ghosh Utpal[1*]

[1]Department Of Biochemistry & Biophysics, University of Kalyani, Kalyani, Nadia, West Bengal, PIN- 741235
[2]Inter-University Accelerator Center, New Delhi, Delhi -110067

Lung malignancy is the foremost cause of cancer-related deaths globally and most of the lung tumours are inoperable and only choice is radio or chemotherapy. Majority of death occurs due to highly metastatic nature of lung cancer [1] [2]. Matrix metalloproteinases (MMPs) are key element in metastasis and their expression is extremely high in lung tumours compared with non-malignant lung tissue [3]. MMPs are zinc-dependent proteases, involved in the degradation of extracellular matrix [4]. Low LET photon radiation, in contrast to carbon ion radiation, can enhance the metastatic nature of cancer cells by increasing the expression and activities of MMPs leading to great difficulties in radiotherapy using gamma or X-rays [5]. Signaling pathways of activation and secretion of MMPs is not clear yet. It is reported that gamma irradiation induces p38/Akt and PI3K/Akt signaling pathways which can modulate MMP-2 expression [6]. We checked EGFR/Akt/p38/ERK signaling pathways associated with activation of MMP-2 and MMP-9 in highly metastatic lung carcinoma A549 cells after irradiation with carbon ion beam in present and absence of PARP-1 inhibitor.

Results:

Cell survival assay:

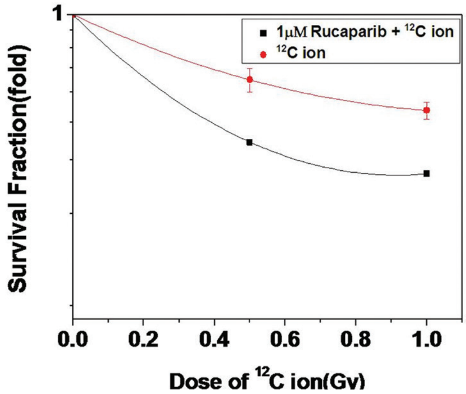

Fig1: Surviving fraction (SF) graph of A549 cell after treatment with PARP-1 inhibitor rucaparib in combination with ^{12}C ion exposure (0-1Gy). combined rucaparib and ^{12}C ion exposure synergistically reduced cell survival.

Immunofluorescence assay:

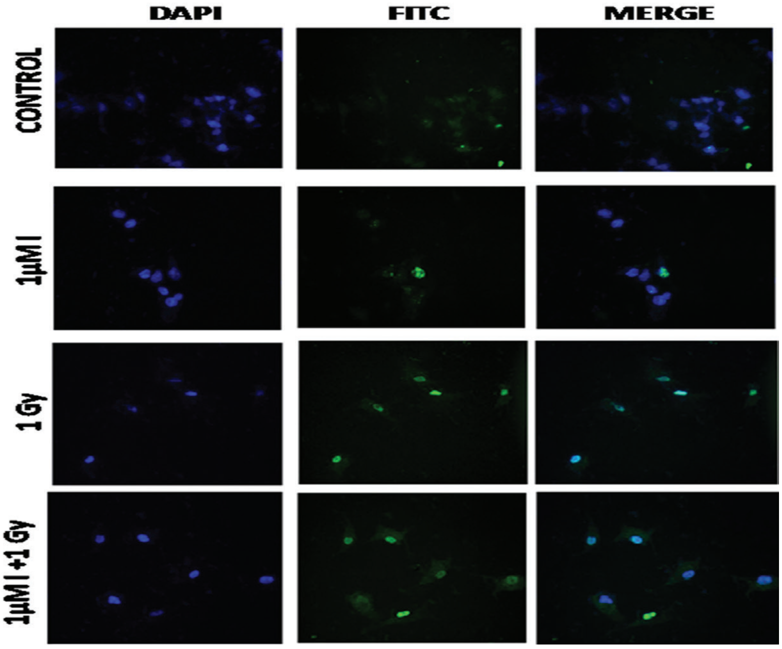

Fig2. Represents increased γ-H2AX foci formation after irradiation with ^{12}C ion in combination with PARP-1 inhibitor.

Expression of EGFR/Akt/p38/ERK involved in the transcriptional regulation of MMP-2 and MMP-9 by western blot:

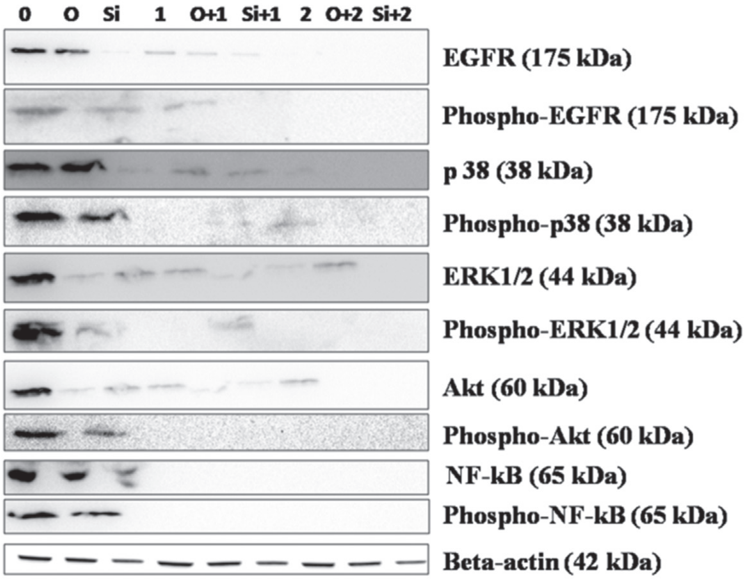

Fig 3: Expression and phosphorylation status of the signaling molecules involved in DDR pathway. Lanes from left- control, olaparib, siPARP-1, 1Gy, olaparib+1Gy, siPARP-1+1Gy, 2Gy, olaparib+2Gy, siPARP-1+2Gy. Here olaparib concentration is 2 µM. All the represented blots are part of the same gel. The number of images from the same blots are developed using anti rabbit and anti mouse secondary HRP conjugated antibodies and by stripping the same blot.

REFERENCES:

[1] Mehlen, Patrick, A. Puisieux.Nature reviews cancer 6.6 (2006): 449.
[2] Minn, A.J., *et al.* Nature 436.7050 (2005): 518.
[3] McCawley, L.J.,L.M. Matrisian. Molecular medicine today 6.4 (2000): 149-156.
[4] D. Nezza, L.A., *et al.* Cancer 94.5 (2002): 1466-1475.
[5] C. Alexander, LC Lin, S. Wen, H.Yan, and W. Hsi. Radiat Oncol. 2017 Aug 15;12(1):132.
[6] Cho, J. Hyun, *et al.* Tumor Biology 37.6 (2016): 7315-7325.
[7] A. Ghorai, N.P. Bhattacharyya, A. Sarma & U. Ghosh. Scientifica. 2014 (2014) 1-10.

5.4 ACCELERATOR MASS SPECTROMETRY

5.4.1 Cosmogenic Radio Nuclides (^{10}Be) In The Laterites of Goa: Impact On Exposure Dating

Achyuthan, H[1], Viegas, A[2], and Dessai, A.G[2].

[1]Institute for ocean Management, Anna University, Chennai 600025
[2]Department of Geology, Goa University, Panjim.

Cosmogenic Radio Nuclides (^{10}Be) In the Laterites of Goa: Impact On Exposure Dating: The project work was carried out since its commencement. Literature reviews on the laterites of Goa have been collected and studied and is updated.

a. Two field trips around Goa at different elevations from the coast were carried out since the second month of the commencement of the project work. Laterite and ferricrete profiles were litho profiled and strategic selection of sampling sites were marked both in the maps and in the filed note. Laterite samples were collected for cosmogenic radionuclide studies and ^{10}Be dating.

b. Over 70 good samples were collected during the field visits. XRF analyses of the samples and XRD analyses of the laterite samples have been carried out. Results have been obtained.

c. Samples processing for the ^{10}Be analyses have to be carried out at IUAC during June 2019.

d. ^{10}Be AMS measurements yet to be performed using accelerator mass spectrometer at IUAC, New Delhi.

Radiocarbons dating of 30 lake samples also have been carried out in February 2019 at the Inter-University Accelerator Centre, New Delhi.

5.4.2 Carbon dynamics in the Ganga basin: implications to the sources, processes and carbon reservoirs

Chinmaya Maharana[1], Pankaj Kumar[1], Rajesh Agnihotri[2], Rajveer Sharma[1], Sanjay Singh[2], J.K.Tripathi[3], Sunil Ojha[1] and Sundeep Chopra[1],

[1]Inter-University Accelerator Centre, New Delhi, India
[2]Birbal Sahni Institute of Paleosciences, Lucknow, India
[3]Jawaharlal Nehru University, New Delhi, India

Objective: The objectives of the present study are i) To elucidate the sources and processes controlling occurrence, distribution and fate of carbon in the Ganga basin ii) To determine the Δ^{14}C value and ^{14}C age (C-14 dating) of POC to elucidate the sources and age of the organic carbon reservoirs in the Ganga basin.

Methodology: Field work was carried out (March & April 2018) to collect overbank and channel sediment samples from the Ganga river including its tributaries from the Himalaya and Peninsula. Collected sediments were then dried in oven followed by grinding in agate mortar and homogenization. Total particulate carbon (TPC) in the unleached and particulate organic carbon (POC) in the leached (with 0.5M HCl) fractions were measured for the overbank and channel sediment samples by taking few milligrams of sediments in tin capsule and their subsequent analysis by an Elementar carbon analyser at IUAC. Thereafter, the particulate organic fraction was subjected to graphitization using Automated Graphitisation Equipment (AGE) followed by their measurement for ^{14}C by AMS.

Results:

pMC (percent modern carbon) and Libby age for the measured river overbank sediments (Delta 13C = -25)

River	pMC value	Libby age
Ganga river	39.463±0.518 to 86.899±0.450	7469±106 to 1128±41
Himalayan rivers	49.267±0.273 to 91.619±0.466	5686±44 to 703±40
Peninsular rivers	67.301± 0.364 to 87.300± 0.359	3180± 43 to 1091± 33

Note: The data analysis/supportive data generation is in progress.

5.4.3 AMS Dating of samples from Excavations at Uren, District Lakhisarai, Bihar (2016-18)

Bhattacharya Goutami[1] and Kumar Pankaj[2]

[1]Archaeological Survey of India, Excavation Branch III, Patna 800001, India
[2]Inter University Accelerator Centre, New Delhi 110067, India

The modern village of Uren (Urain), 25°10'3"N; 86°13'11"E, falls within Surajgarha Block of District Lakhisarai, Bihar. Excavations were carried out at the site by Excavation Branch III, Patna of the Archaeological Survey of India for two field seasons – 2016-17 and 2017-18 under the direction of the first author. Excavations at the site revealed a complete unbroken sequence of cultures starting with the proto-historic Black-and-Red Ware (henceforth BRW) using culture (around the 2nd millennium BCE) and ending with a flourishing Buddhist establishment during the Pala period (12th century CE). It was possible to visualize the growth and development of a settlement throughout the course of its history. As such Uren represented a microcosm of the ascent of human society through time and space.

It was decided to layout trenches for excavation in all the four directions of the mound and also in the central high part so that the spread of the ancient settlement through space and time could be ascertained. In total 8 trenches were laid in the specified areas and all of them were dug till the natural soil to get a complete cultural sequence at all the sites. The trench URN III laid in the Garh area of the village (highest point) proved to be the most rewarding as well as complex. It emerged as the index trench for the entire site since it revealed a complete, undisturbed and unbroken sequence from the BRW associated rural settlement to the Pala period. It was extremely rich, both in structural remains as well as in antiquities and pottery traditions. The entire cultural deposit of 14.48m above the natural soil was divided into 16 occupational layers. These 16 archaeological horizons were clubbed into 6 cultural periods. Periods I, II and III were named after their dominant pottery traditions which were the main and widely used cultural markers – Black and Red Ware (BRW) associated rural settlement; Black Slipped Ware (BSW) associated rural settlement and the Northern Black Polished Ware culure (NBPW). Periods IV, V and VI were designated after the known political dynasties of this region – Sunga-Kushana, Gupta and, Post-Gupta and Pala periods. As excavation progressed, it soon became apparent that this area of the mound saw regular and intense structural activity from the Sunga-Kushana period onwards. Majority of samples for dating were collected from this trench so that the individual cultural deposits could be dated sequentially and corroborated with those from other excavated trenches. In addition, trench URN V laid to the south of the Uren Hill gave evidence of primary iron smelting activity with no identifiable cultural markers for possible chrono-cultural affiliation. Only one sample could be had from this trench and was crucial for dating the beginning of iron working at the site.

The following table gives the list of samples along with their date range and corresponding cultural affiliation:

Sl. No.	Sample Name	Sample ID	Trench No. and Depth	Radiocarbon Age (BP)	Cal. Age (95.4% Probability) Range and Median	Cultural horizon/ Remarks
1.	URN IIIA/ 1-13.90	IUACD# 18C2181	URN III / 13.90m BS	2956 ± 32	**1261 BC - 1055 BC 1167 BC**	**All these dates correspond to layer 16 (lowermost deposit). These dates belong to Period I designated as BRW associated rural settlement**
2.	URN IIIA/ 2-13.55	IUACD# 18C2182	URN III / 13.55m BS	2901 ± 36	**1213 BC - 996 BC 1087 BC**	
3.	URN IIIA/ 3-13.25	IUACD# 18C2183	URN III / 13.25m BS	2972 ± 40	**1373 BC - 1051 BC 1189 BC**	
4.	URN IIIA/ 4-12.65	IUACD# 18C2184	URN III / 12.65m BS	2966 ± 37	**1287 BC - 1050 BC 1168 BC**	
5.	URN IIIA/ 5-12.00	IUACD# 18C2185	URN III / 12.00m BS	3039 ± 37	**1410 BC - 1135 BC 1295 BC**	
6.	URN IIIA/ 6-11.20	IUACD# 18C2186	URN III / 11.20m BS	2945 ± 43	**1269 BC - 1014 BC 1152 BC**	

7.	URN IIIA/ 8-9.60	IUACD# 18C2188	URN III / 9.60m BS	2853 ± 46	**1192 BC - 904 BC 1021 BC**	**Period II Black Slipped Ware (BSW) associated rural settlement**
8.	URN IIIA/ 9-9.15	IUACD# 18C2189	URN III / 9.15m BS	2511 ± 34	**792 BC - 540 BC 641 BC**	**Period III Northern Black Polished Ware (NBPW) cultural horizon**
9.	URN IIIA/ 10-8.75	IUACD# 18C2190	URN III / 8.75m BS	2688 ± 36	**905 BC - 801 BC 843 BC**	
10.	URN IIIA/ 11-8.50	IUACD# 18C2191	URN III / 8.50m BS	2481 ± 34	**776 BC - 431 BC 631 BC**	
11.	URN IIIA/ 12-7.00	IUACD# 18C2192	URN III / 7.00m BS	2386 ± 40	**746 BC - 387 BC 473 BC**	
12.	URN IIIA/ 13-6.75	IUACD# 18C2193	URN III / 6.75m BS	2163 ± 37	**361 BC - 99 BC 227 BC**	
13.	URN V/ 14-0.78	IUACD# 18C2194	URN V / 0.78m BS	2643 ± 31	**895 BC - 787 BC 812 BC**	**Period III Iron working site**
14.	URN IV/ 16-3.10	IUACD# 18C2196	URN IV / 3.10m BS	1914 ± 34	**6 AD - 211 AD 90 AD**	**Period IV Sunga-Kushana period**
15.	URN IIC/ 17-1.86	IUACD# 18C2197	URN II C / 1.86m BS	2187 ± 28	**360 BC - 176 BC 290 BC**	**Period III NBPW Period**
16.	URN IB/ 18-1.75	IUACD# 18C2198	URN I B / 1.75m BS	2224 ± 34	**381 BC - 203 BC 280 BC**	**Period III NBPW Period**
17.	URN IB/ 19-AAII	IUACD# 18C2199	URN I B	2159 ± 39	**361 BC - 64 BC 216 BC**	**Period IV Sunga-Kushana period**

Authors are thankful to IUAC for extending AMS facility, under Geochronology project funded by Ministry of Earth Sciences, Govt. of India

5.4.4 Brief Report on Bharati Huda Excavation, Odisha with AMS Dates

Dibishada B. Garnayak [1], S. Chopra[2], Pankaj Kumar[2] and R. Sharma[2]

[1]Archaeological Survey of India, Excavation Branch –IV, Bhubaneswar and
[2]Inter University Accelerator Center, New Delhi

The archaeological mound Bharati Huda (20º 06’47’’N 86º 05’10’’ MSL.11mt), is located in the left bank of river Prachi, 20km away from the Bay of Bengal in Jallarpur village of Niali *tehsil* in Cuttack District and at a distance of 50km from Bhubaneswar, the capital city of Odisha. The site is situated in between river Prachi and rivulet Tanala on its left and right banks respectively which is quite significant for early human settlement. Presently the site is known for its historic antiquities from Chalcolithic period to Iron Age. The region where the site is located has a remark in the map of eastern India for its cultural and religious landscape. The river Prachi gets its name from the word *prachina* meaning ancient. The existing folklore considers river to be a reincarnation of mythical river Saraswati and also references about the river found in *Markandeya Purana, Kapila Samhita, Prachi Mahatmya* and in *Odia Mahabharat.* Tradition and legend link various places of the valley with the Ramayana and the Mahabharata. The valley is studded with religious shrines, ancient forts, *mathas,* monastery and archaeological mounds. The rich and diverse cultural heritage shows that suitable climate for the growth, development, and popularity of various religious sects and culture existed in the valley from the early time.

In the year 2017-18 the excavation work was conducted at Bharati Huda site by Excavation Branch-IV of Archaeological Survey of India under the direction of the first author. During the survey Bharati Huda archaeological mound was found significant and more potential in nature in comparison to most of the sites documented in the valley.

The geology of the area is dominated by the Early Holocene sediments of alluvial origin under a deltaic environment and is one of the youngest marine horizons. The flood plain landscape has been formed out of the deposition of the alluvial sediments of the river Mahanadi around 3000-6000 BCE (Mahalik 2006). The silty clay deposits, moderate to low energy wind, flood plains became a source for agriculture, mangrove forest and biodiversity which attracted the human population to settle over it by c.1500 BCE. The surrounding soil of the archaeological site is of Alfisols (the deltaic alluvial soils) these soils are generally deficient in P2O5 and N2. The K2O are fairly adequate, and pH varies between 6 and 7 (The soil pH value of the archaeological mound varies from 6-8) and has been observed that these soils support paddy crops. This observation is true as corroborated with the present agricultural practices. The excavation also revealed plant remains of domesticated variety of rice, *kulith,* green gram, black gram, lentil and Jute. Thus, the fertile track attracted the pre-historic man for dwelling and settling in this landscape from time to time. The area around the site is highly fertile and supports *dhan/*paddy *(Oryza sativa); surjyamukhi/sun-flower (Helianthus annuus); mug/green-gram (Phaseolus mungo); sarisha/mustard (Sinapis nigra); akshu/sugarcane (Saccharum officinarum)* and other crop round the year due to the canal irrigation. Coconut *(Cocos nucffera)* and pan/betel-leaf *(Chavica betle)* plantations constitute a major economic crop of the area. The climate of the area is characterized by hot humid summers and well distributed rains of the south-west monsoon which supports the semi-evergreen types of natural vegetations. Relative humidity is generally high throughout the year and winds are fairly strong. The average annual rainfall in the area is 1448 mm (Odisha district Gazetteers: Cuttack, 2016).

The existing mound Bharati Huda measures approximately 46215 sq.mts having heights of 4mts from the surrounding landscape. The excavation at the site was carried out to know the chrono-cultural sequence of the site, to correlate the habitational deposit with other known Chalcolithic sites of Odisha in particular and that of eastern and central India in general and to see whether the site has continuous human habitation from prehistoric time to early historic period. According to the availability and suitability of land 750 sq mt area was selected for under taking excavation in 30 quadrants in three pockets within the site, out of which only three quadrants have encountered natural strata having 5mt of habitational deposits divisible into 7 to 8 layers, and divisible in to three cultural phases viz, Early Chaclolithic, Mature Chalcolithic and Iron Age from bottom to top. Among the three quadrants, Trench ZA6/III have been consider as the index trench of the site due to its location at the highest elevation and having maximum cultural deposits.

Trench ZA6/III

This trench lies on the western part of the mound and digging up to a maximum depth of 6mts below surface revealed 8 habitational layers above the natural soil. The details of the layers described below are from bottom to top.

Radiocarbon dating

The Charcoal samples have been collected from stratified layers (3), (4), (5) and (7) by taking proper procedure and were dated by using AMS radiocarbon technique at IUAC, New Delhi. Radiocarbon ages were calibrated using Oxcal software and median ages are utilized in this report.

Layer (9) is gray in colour (2.5Y 5/1 on the basis of Munsell soil colour book) having pH value 6.5, fine in texture sticky in nature, bereft of artifacts and human activity and treated as natural layer.

Layer (8) above the natural soil is dark gray in colour (2.5Y 4/1) pH value 6.5, fine in texture sticky in nature, composed of tiny potsherds of red ware, burnt clay lumps and considered as the first habitational layer dated to early phase of Chalcolithic culture. It was the period when for the first time human beings were migrated to the region and occupied the valley and continued to survive till date.

Layer (7) is grayish brown in colour (2.5Y 5/2) pH value 7, fine in texture semi-compact in nature contains charcoal sample which is dated to 1404 BCE (C^{14} sample ID- IUACD#18C2180) and ceramic assemblage of Red Ware, Red Slipped ware, Chocolate slipped/tan red ware and Grey/Black ware, cord impressed ware, perforated ware, charred bones and burnt patches along with ash.

Layer (6) is dark grayish brown in colour (10YR 4/2) pH value 6, medium to fine in texture semi compact to loose in nature contains charred and un-charred bones, a lonely piece of stone chisel, burnt clay lumps suggesting existence of wattle and daub house, ceramic assemblage of Red Ware, Red Slipped, Chocolate slipped/tan red ware, cord impressed ware, perforated ware, Grey/Black ware and in the upper level evidence of yellow colour mud structure was noticed.

Layer (5) is significant as for the first time Black and Red ware and painted pottery appeared in this layer which has been dated to 1269 BCE (C^{14} sample ID- IUACD#18C2177). It is brown in colour (10YR 5/3) pH value 6, medium to fine in texture compact to loose in nature contains charcoal, ash patches, burnt clay nodules, charred and un-charred bones, antiquities made of bone and stone and potsherds of Red ware, Red slipped ware, Chocolate slipped/Tan red ware, cord impressed ware, perforated ware, Black ware and Black-and-Red ware. In this layer a circular structure made of yellow clay was noticed. A dump in the eastern section of the quadrant containing ash, charcoal pieces, potsherds and charred bone was encountered. The evidence of domesticated rice and jute fiber was also noticed for the first time. It seems that new craft specialization emerged this time or a new ethnic group came in contact with the inhabitants.

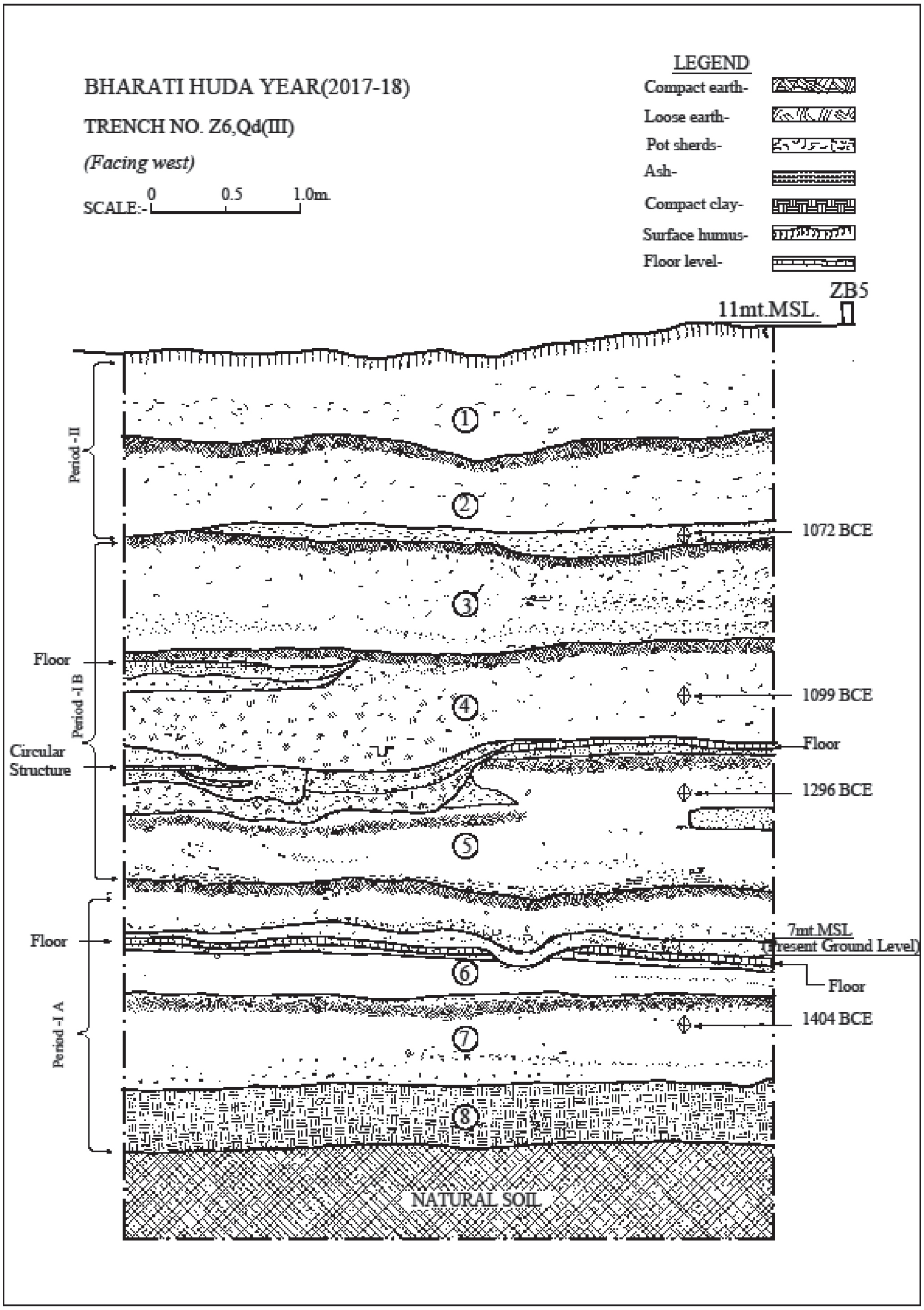

Layer (4) is light yellowish brown in colour (2.5Y 6/3) pH value 6.5 medium to fine in texture, loose in nature contains similar material culture as in layer (5), except the miniature pot in red ware which was found for the first time in this cultural level, variety of bone tools appeared in this period. The AMS date of charcoal sample collected from this layer has been dated to 1099 BCE (C^{14} sample ID- IUACD#18C2176). And within the painted pottery a lonely specimens of Sun motif in a chocolate slipped pottery found from the layer which indirectly gives light on nature worship in the valley.

Layer (3) found to be the last phase of the Chalcolithic period is gray in colour (2.5Y 5/1) pH value 6, medium texture semi compact to compact in nature contains ceramic assemblage of Red Ware in Red Slipped ware Chocolate slipped/tan red ware Grey/Black ware, cord impressed ware, perforated ware Black and Red ware and charcoal, ash patches, burnt clay nodules, charred and un-charred bones, maximum number of antiquities found from the layer assigned to 1072 BCE (C^{14} sample ID- IUACD#18C2175) are made of bone followed by stone, terracotta and a copper fish hook. The findings of toy cart wheel, shark tooth proves their acutancey in both land routes and water routs.

Layer (2) deposit is marked with the presence of iron having continuation of earlier cultural features except the occurrence of pre-firing painted pottery on dull red ware. It is light brownish gray in colour (10YR 6/2) pH value 6; medium texture compact in nature. The evidence of Iron and copper objects in this strata suggested their expanding subsistence zone during this period which can be dated to Iron Age.

Layer (1) is light brownish gray in colour (2.5Y 6/2) pH value 6.5, medium texture compact in nature contains tangible material remains in form of maximum number of Red Ware pottery in comparison to other ware like Red Slipped ware, Grey/Black ware, perforated ware and bereft of Chocolate slipped ware; burnt clay nodules, charred and un-charred bones and materials from Iron age as well as early historical inclusion is noticed in this layer.

Thus the index trench yielded 8 occupational layer, where layer 8 to 6 throw light on the incipient Chalcolithic cultural activities termed as early Chalcolithic followed by a mature phase of the culture as evidenced from the technical advancement noticed in the ceramic assemblage viz., the introduction of Black and Red ware, ochre colour painted potter on chocolate slipped ware in Layer 5 to 3. Not only in technology but also in belief system there was a change as noticed from the Sun motifs painted pottery retrieved from layer 4 which indicates about the nature worship among the inhabitants. The top 2 layers are different from the lower layers with the presence of Iron and copper. The habitation covered a long span of time as known from the 5mts habitational deposit and C^{14} dates provided by IUAC.

Acknowledgements

I am grateful to the Director General and Director (Exploration and Excavation) of Archaeological Survey of India, New Delhi for granting the permission to excavate Bharati Huda archaeological site. I am also thankful to Inter University Accelerator Center, New Delhi for extending AMS facility under Geochronology project [MoES/P.O.(Seismic)8(09)-Geochron/2012] for providing C14 dates to the site. I am also thankful to Sanjay Panda, Ashis Ranjan Sahoo, Umakanta Bhoi - Assistant Archaeologists and Suvendu Kumar Khuntia-Surveyor Gr.I, Bibhuti Bhusan Badamali-Draughtsman Gr.I, Rabindra Nath Sahoo-Photographer Gr.I, Surath Kumar Bhoi-Store keeper and other staffs for their involvement and to the villagers of Jalarpur for their cooperation and support during the excavation work.

References

[1] Mahalik, N.K. 2006. A study of the morphological features and Bore hole cuttings in understanding the evolution and geological process in Mahanadi Delta, East coast of India, *Journal Geological society of India* Vol.67:595-603 (May 2006).

5.4.5 Estimation of beryllium from Polar Regions and lake sediments - Paleo-Oceanographic implications

Nayak G. N.[1], Choudhary Shabnam[2], Chopra Sundeep[3] and Pankaj Kumar[3]

[1]CSIR Emeritus Scientist, Marine Science, School of Earth, Ocean and Atmosphere Science, Goa University, Goa 403 206, India
[2]Ministry of Earth Science, Govt. of India, New Delhi, India
[3]IUAC, New Delhi

BERYLLIUM ESTIMATION

Surface and core sediment samples were collected from lakes, fjords and bays from Arctic and Antarctic regions and stored at -20ºC. Later, sediment sample collected from lakes and bay from Antarctica was chemically processed for Be analysis at Inter University Accelerator Centre (IUAC), New Delhi. Fe-Mn oxide fraction was extracted following the sequential extraction procedure for the speciation of trace metals (Tessier et al., 1979) [1] as this method have been found efficient to extract 10Be (meteoric) as compared to other methods.

METHODOLOGY

A portion of each subsample was powdered and homogenized in an agate pestle and mortar. 1 g of sediment sample was taken in a centrifuge tube and treated with 20 ml 0.04M hydroxylamine hydrochloride ($NH_2OH.HCl$) in 25% (v/v) acetic acid (HOAc) mixture for 6 hrs at 90ºC, and run with 400 rpm with continuous agitation (Tessier et al., 1979) [1]. The supernatant was removed after centrifugation, and dried completely on the hot plate. Then, the dried extract was dissolved in 10 ml of 1N HCl (Non-Calibrated). 1 ml of this solution was removed and kept for ^{9}Be analysis by ICPMS. Remaining 9 ml of solution was spiked with (.2 ml) ^{9}Be carrier solution (NIST SRM-3105a) and dried on the hot plate. Further, the extract was dissolved in 1 ml 6N HCl and passed through Anion column and the residue was collected in Teflon beakers and dried completely. Further, it was dissolved in 0.2 M H_2SO_4 + 2% H_2O_2 and passed through cation column. This residue was collected and mixed with 5-8 drops of 8M HNO3 and dried completely and precipitated with the help of NH3. The supernatant was removed with the help of centrifugation and precipitate (BeOH) was collected in quartz vials. The quartz vials containing BeOH precipitate were kept in a furnace with step heating up to 900°C to convert precipitate BeOH to BeO. After drying, the BeO powder was loaded to the cathode tube mixed with Nb powder in a ratio of 1:3 and will be analysed for ^{10}Be/^{9}Be ratio using an Accelerator Mass Spectrometry (AMS).

DISTRIBUTION OF ^{9}Be IN SEDIMENTS

Along the Prydz Bay, in the surface sediment samples ^{9}Be content fluctuated in a range between 17.62 ppb at station P2 and 166.64 at station P6. Overall, ^{9}Be showed an increasing trend with increasing water depth (31-140 m) away from the coast (P1-P7) similar to that of silt and clay as finer grain size provides large surface area for the adsorption of authigenic ^{9}Be. In Larsemann Hills, East Antarctica ^{9}Be concentration was high (average 122.91 ppb) in core L-8 and low in core L-10 (66.97 ppb). While in Schirmacher Oasis, East Antarctica ^{9}Be concentration was high in core L-6 (average 105.74 ppb) and low in core V-1 (average 70.69 ppb). However, ^{9}Be concentration is lower in core L-8, L-10, L-12, GL-1, V-1 and L-6 as compared to the average crustal values (~2ppm). From all the six cores studied, it is observed that silt has high scavenging efficiency of ^{9}Be as compared to the clay. Clay has tendency to form aggregates which have faster sinking rates. These aggregates provide less surface area for the adsorption of ^{9}Be suggesting high scavenging efficiency of silt as compared to the clays (Simon et al., 2016)[2]. Be also showed good association with Ti supporting lithogenic source.

REFERENCES:

[1] A. Tessier, P.G. Campbell, and M. Bisson, Analytical chem. 51(7)(1979) 844-851.

[2] Q. Simon, N. Thouveny, D.L Bourles, L. Nuttin, C. Hillaire-Marcel, and G. St-Onge, Quarter. Sci. Rev. 140 (2016)142-162.

5.4.6 Beryllium concentration, clay minerals and metals in sediments in reconstruction of paleo-climate

Nayak G. N.[1*], Kangane Janhavi[1], Chopra Sundeep[2] and Pankaj Kumar[2]

[1]Marine Science, School of Earth, Ocean and Atmosphere Science, Goa University, Goa 403 206, India
[2]IUAC, New Delhi
[*]CSIR Emeritus Scientist

OBJECTIVES

To study clay minerals, selected metals, ^{10}Be and ^{9}Be concentration in sediment cores and use them to reconstruct paleoclimate
and
To understand sediment size and composition control on concentrations of 10Be and 9Be and also to understand the degree of paleo weathering using 10Be/9Be to support the climate studies.

RESEARCH WORK CARRIED OUT

Two cores, namely, GC 13 and GC 16 which were collected from Bay of Bengal (onboard SK 308) were analysed for sediment components, while the core GC 13 was further analysed for clay minerals and metals (Fe, Mn, Al, Ti, Pb and Zn) to achieve the project objectives. Sediment component profile of core GC 13 represented cyclicity in the depositional environment.

WORKSHOP ATTENDED

To understand the principle and working of Accelerator Mass Spectrometer (AMS) and also sample processing national workshop on "Isotopes in Earth, Ocean and Atmospheric Sciences" conducted by IUAC and NIO held at CSIR-National Institute of Oceanography (NIO), Goa from 18 – 20 February 2019 was attended.

5.4.7 Palaeoclimatic Reconstruction of Changme Khangpu Glacier, Upper Tista Basin, Eastern Himalaya, India

Manasi Debnath[1], Hiambok Jones Syiemlieh[1], Milap Chand Sharma[2] and Pankaj Kumar[3]

[1]Department of Geography, North-Eastern Hill University, Shillong, Meghalaya 793022, India
[2]Centre for the Study of Regional Development, School of Social Sciences, Jawaharlal Nehru University, New Delhi 110067, India
[3]AMS & Pelletron Group, Inter- University Accelerator Centre, New Delhi 110067, India

The Changme Khangpu (CK) glacier in Sikkim Himalaya has been taken to study the palaeoclimate through the proxy of glacial landforms and glacigenic sediment assemblages. The main axis of CK valley trends N-S and modern glacier restricted at an altitude between 5900 and 4810 m a.s.l. (27.9583 N, 88.6844 E). Lack of previous studies, spectacular preserved landforms and some catastrophic natural events in this valley captivated the attention and raised the importance to portrait the glacial geomorphology and reconstruct the palaeoclimate of this monsoon dominated valley.

The work related to the palaeoclimate reconstruction is supported by the geomorphology, sedimentology, geochemistry, and geochronology. Here, we have used SRTM DEM, Sentinel-2A satellite imageries, GPS, sedimentological analysis and field techniques to portrait the glacial and glacigenic sediment assemblages. The ^{14}C isotope AMS dates of glacio-fluvial and glacio-lacustrine deposition are used to place the observed phases of climate in a common chronological ground. The ^{14}C isotopic measurements of sediment samples have been done in the 500 kV Pelletron AMS. The sediment samples were acquired from the 5 different locations and landforms in the Changme Khangpu basin of North Sikkim Himalaya. Our detailed reconstructed geomorphology supports the sample bearing landforms were developed under the deglacial warmer phases. Four glacial phases have been identified by the prominent latero-frontal moraines and group of hummocky moraines during the field survey, mapping and sedimentological analysis. The deglacial sedimentation in a form of rhythmite archive has been dated back to 31.47 ± 0.15 Ka CalBP situated at 1.7 km from the present glacier snout. The younger talus scree, debris fan are the major paraglacial features are overlying the palaeo-rhythmites and enhancing the modification of primary sedimentation, and hence demarcate the deglaciation phase (Church and Ryder, 1972). This result helps to draw the relative timing of the glacial Phase I and Phase II i.e. before 31.47 ± 0.15 Ka CalBP. Sediment-chronological analysis of glacio-fluvial archive from a trench that is situated within the Phase II limit portrait the oscillating nature of palaeo-climate from 14.053 ± 0.168 to 3.447 ± 0.06 Ka CalBP. The geochemistry also supported the oscillating nature of palaeo-environment that has been identified through the analysis of major elements (SiO2, Al2O3, TiO2, Fe2O3, MnO, MgO, CaO, Na2O, K2O, and P2O5) on the same vertical profile. The elemental analysis was carried out using the XRF facility at IUAC. An inverted age of relatively modern sedimentation has been recognized through the 14C AMS dating that supports the model of the paraglacial slope processes, which is continuously modifying the primary deposited materials (Ballantyne, 2002). The rock samples from the moraines have been collected and processed for extracting the quartz mineral. Samples are ready for 10Be and 26Al dating to reconstruct the absolute age of the glacial phases.

Bibliography:

Ballantyne, C.K., 2002. Paraglacial geomorphology. Quat. Sci. Rev. 21, 1935.

Church, M., Ryder, J.M., 1972. Paraglacial sedimentation: A consideration of fluvial processes conditioned by glaciation. Bull. Geol. Soc. Am. 83, 3059–3072. https://doi.org/10.1130/0016-7606(1972)83[3059:PSACOF]

5.4.8 Investigation of Saraswati paleochannels and associated Indus Valley Civilization in context of drainage evolution and paleoclimate

Naresh Chandra Pant[1], Apoorva Alok[1], Pankaj Kumar[2] and S.Chopra[2]

[1]Department of Geology, University of Delhi, Delhi-110007
[2]Inter-University Accelerator Centre, New Delhi -110067

Introduction and background

Geographical spread of the Indus Valley civilization from NE Afganistan to Pakistan and NW India from 5000-1300 BC (Kenoyer, 1977), its evolution and demise have interesting geological implications as the archaeological remains of the settlements are spatially associated with the past and present basins of the Indus river. It being a dominantly agriculture based civilization, the twin resources of water and soil of significance in settlements and their evolution. The third major factor is that of the influence of change in the climate during Holocene epoch (last 11,700 years).

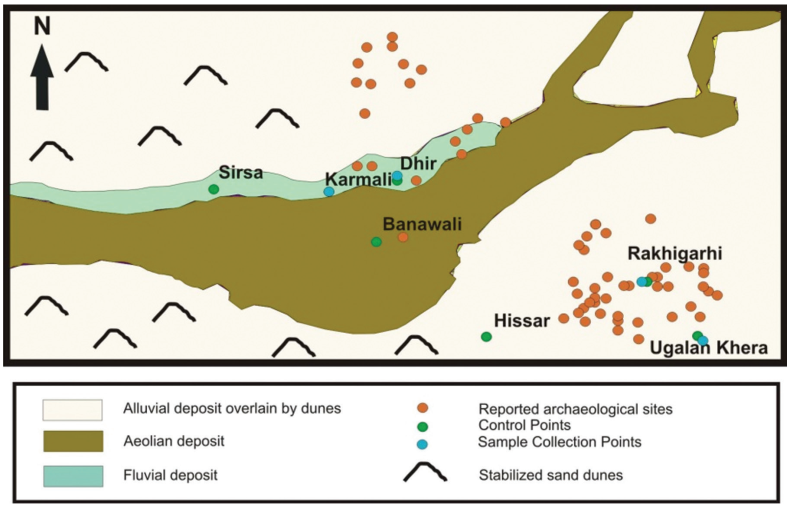

Fig. 5.4.6: Map depicting the sites from where samples were collected.

Our earlier work (Saini et al., 2005, 2009) has described the architecture of palaeochannels in the plains of Haryana and adjacent Rajasthan and had also constrained the three fluvial events starting from >30000years. A climate change in Holocene was also described leading to a reduction in precipitation in Holocene and it coincided with certain changes in the Indus valley civilizations. The ages of these events was mainly constrained by Optically Stimulated Luminescence chronology.

A study was mounted in collaboration with IUAC nearly a year ago to establish the climate change-civilization context with greater precision for Harappan settlements in the main paleochannel as well as newly described tributaries arrived at after a remote sensing and field based hydrological-geological study (Mehdi et al. 2014). In the course of this work we had also collected evidence to demonstrate the higher Himalayan (glacier water) sourcing of the paleo-river commonly referred as river Saraswati (unpublished data).

In the present work samples were collected from existing palaeochannel as well as from a well knownHarappan site at Rakhigarhi (Figure below) to understand the evolution of the mature Harappan phase and to link it to the geological processes operative at that time.

Work reported during previous report

The work carried out so far includes two field campaigns, logging of the geological and cultural mounds, sampling in Rakhigarhi (three archaeological mounds), a geological flood plain succession overlain by archeological mound at Dhir village and aeolian samples (to characterize aridity), generation of ~20 AMS radiocarbon ages, XRD analysis of ~30 samples (mainly for clay mineral content to characterize soil), SEM and sedimentological analysis.

Initial results indicate following:

1. A river (Saraswati?) flowed during Holocene in the now defunct paleochannel and it had atleast two major additional tributaries (Mehdi et al. 2014).
2. The sourcing of sediments in this continued to be from Higher Himalayas during Holocene (Zircon U-Pb unpublished data).
3. A reworking is indicated after 4100 before present (BP) and it is likely to coincide with the 4200-3800 BP rapid climate global climate change event (unpublished data).
4. The soil generally lacked the high cation exchange capacity clay minerals (CEC) thus leading to shifting cultivation and therefore continued relocation of settlements.

Work done since last report

An extensive field work was undertaken where we traversed from the base of Shivaliks to India-Pakistan border along the course of proposed river in search of crucial geological as well as archaeological samples. Samples were collected from paleochannels as well as interfluve to understand the characteristic of deposits of streams proposed by Mehdi et al. 2016. Samples were collected and are under processing.

Results and Discussion

1. The grain size analysis of the collected samples suggest variable flow regime in different layers of deposited sediment in present day channel near India-Pakistan border.
2. The sample collected from geoarchaeological mound in the paleochannel near Dhir shows the succession of clay, silty clay and sand. Floating charcoal pieces are present at several layers which were subjected to AMS radiocarbon geochronology. Sedimentological, heavy mineral and quartz microtexture studies were also carried out.As the samples are from the most prominent paleochannel which was likely to have been active till the end phase of the river, youngest ages of the fluvial activity were expected to be recovered from this site. The lower level sample of the geological component of the succession has indicated an age of C^{14} 2782 ± 43 years BP while the youngest age of 2030 ± 45yrs BP is from near the middle of the cultural succession. This is overlain by brownish silty clay from which an age of >20000 year BP has been recorded from charcoal which is not known from this area and needs to be further investigated. Since this succession is within the flood plain of the now defunct river, the older ages were interpreted to be reworking during flooding. However, this interpretation required validation and for that OSL sampling was carried out in joint traverses with the Geological Survey of India. The hypothesis was that if the river was flooded at ~2000 BP, it should be validated by younger than this OSL ages of the associated quartz grains. Two samples from the bottom of this succession gave and age range of 1.4 -1.1 ka (errors of ± 0.1 ka).
3. At Rakhigarhi, several archaeological mounds are present at this site with exposed sections of upto ~10 m. Clay, silty clay, ash and pottery rich layers constitute the major units of these mounds. AMS radiocarbon dates indicate the reign of habitation in these sites beginning during pre-Harappan time (>5250 yrs BP), flourishing during Early Harappan phase and a depleted occupation during Mature Harappan time (e.g. RGR2). Presence of a remobilized older age in mound RGR4 over a sequentially layered cultural mound may suggest reworking of older carbon material possibly during a flooding event (high precipitation).
4. Clay mineralogy of different layers suggest a relatively colder period between 5000 and 4800 BP, which is also evident by grain size parameters.
5. Absence of sand and sandy-silt deposits in other mounds of Rakhigarhi suggests the presence of a channel near the group of mounds at Rakhigarhi, proving the hypothesis proposed by Mehdi et al. and Kar et al.

Future Work:
1. A research publication is under preparation using all these inferences.
2. XRD and XRF of samples obtained from recent field campaign is to be completed.

5.4.9 Cosmogenic Radionuclide dating of glacial deposits of Thajiwas valley of Kashmir Himalaya

Omar Jaan[1], Reyaz Dar[1], Shakil Romshoo[1], Pankaj Kumar[2], Jitendar Pattanaik[3] and Soumaya Prakash Dal[2]

[1]Department of Earth Sciences, University of Kashmir, 190006
[2]Inter University Accelerator center (IUAC) New-Delhi 110067
[3]Center for Geography and Geology, Central University Punjab 151001

In the present study, glacial-geomorphic landforms of the Thajiwas glacial valley, which provide vital information about the impact of glacial advance and retreat on the geomorphology, were mapped from remote sensing data supported by extensive fieldwork. Morphology, shape and location of terminal and lateral moraine ridges were used to establish the palaeo-glacial extents, glacial volume and the number of glacial advances of the Thajiwas glacier. During the fieldwork, 15 moraine samples were collected from seven different locations to estimate the timing of the last glacial maximum. The samples of Quartz grains were processed for the ^{10}Be and ^{26}Al cosmogenic radionuclide dating.

Mapping and sampling:

The glacial geomorphic features were mapped using the high-resolution satellite data supported by the fieldwork and GPS surveys [1,2]. Vestiges of recently deposited recessional moraines of minor advances reflect the response of the glacier to the regional climate change3. The change in the glacier surface area shows that the glacier has receded from 47.4 km^2 during last glacial maximum to 3.60 km^2 at present. The greater rock excavation during glacial maximum and the concomitant head ward expansion of the glacial valley at the expense of cirque retreat has driven the drainage divide southward, thereby limiting the topographic relief. Well-preserved terminal and lateral moraines samples were collected in the Thajiwas valley, which provide evidence of the last three glacial advances[4].

Sampling Processing details

Different apparatus used for sample processing were washed with Milli-Q (deionized) water . The following steps were followed for the separation of the ^{10}Be and ^{26}Al. Quartz sample was added to the PFA wide-mouth bottle and MQ water was poured into it up to the mark of 500ml for leaching process. 5ml of Hydrofluoric acid was added to the sample and shook regularly after every 30 minutes for 72 hours. Then, the water was drained out from the sample before being transferred to oven for drying. After drying, 20-30 grams of the purified quartz were subjected to digestion process. The samples were transferred into the Teflon beakers and 20ml of HF acid (Double Distilled) was added to each sample. The beakers were put on the hotplate and heated to the temperature of ~110 to 125º C. 5-10 ml of HNO_3 was added to the sample. The samples were dried completely after the digestion. About 10ml of 1N HCl was added to each sample to dissolve it completely. The part of the sample was transferred to the 10ml bottles for the AMS studies. 0.1 ml of ^{9}Be carrier was added to the sample, the process is called spiking. The sample was thereafter transferred onto the hotplate and heated to the temp of 100-110º C. The anion and cation column separation was carried out using the Bio rad resin column. The samples of Quartz grains were processed for ^{10}Be and ^{26}Al samples and collected during the process and dried completely. The samples were then dissolved using the MQ and transferred to centrifuge tubes. Few ml of NH3 solution was added to the sample, shook and kept undisturbed for 12-15 hours to let ^{10}Be and ^{26}Al precipitate completely. The excess liquid at the surface was drained out and the sample were transferred to the quartz vials and heated in a furnace at a temp of 300º C for 12 hours.

REFERENCES

[1] Dunlop, P., Clark, C.D., 2006. The morphological characteristics of ribbed moraine. Quat. Sci. Rev. 25 (13), 1668-1691.
[2] Clark, C.D., 1997. Reconstructing the evolutionary dynamics of palaeo-ice sheets using multi-temporal evidence, remote sensing and GIS. Quat. Sci. Rev. 16 (9), 1067-1092.
[3] Porter, S.C., 1989. Some geological implications of average Quaternary glacial conditions. Quat. Res. 32 (3), 245e261.
[4] Dar, R. A., Jaan, O., Murtaza, K. O., & Romshoo, S. A. (2017). Glacial-geomorphic study of the Thajwas glacier valley, Kashmir Himalayas, India. Quaternary International, 444, 157-171

5.4.10 Radiocarbon ^{14}C dating of sub-surface sediment samples using Accelerator Mass Spectrometry (AMS)

Parveen Uzma[1], Sreekesh S[1], Pankaj Kumar[2] and S. Chopra[2]

[1]Centre for the study of Regional Development, Jawaharlal Nehru, New Delhi-110067, India.
[2]Inter-University Accelerator Centre, New Delhi-110067, India.

We have measured the absolute ages of subsurface sediments deposits along the Lower Baitarani Basin, East Coast of India using Accelerator Mass Spectrometry (AMS) facility at IUAC. The samples have been obtained from eight locations and subsurface sediment facies have been determined based on colour and textural variability. The facies with carbon content above 0.5 % have been considered for radiocarbon ^{14}C dating. The radiocarbon ages along with geochemical proxies have revealed the depositional environment and climate during the Holocene period in Lower Baitarani region.

OBJECTIVE

The major objective of this work is to analyze the chronology of sediment deposition along the lower reaches of Baitarani Basin up to the depth of 1000 cm. It is also aimed to draw inferences about the past climate based on geochemical proxies and absolute dating.

RESEARCH OUTPUT

Radiocarbon (^{14}C) ages of four samples were determined using AMS through 500 kV Pelletron' 5 accelerator (Vahila et al., 2016). The uncalibrated radiocarbon dates were converted into the calendar ages using OxCal 4.3 (Bronk and Lee, 2013) (Figure 1).

In the mixing zone active floodplain (MS1), beach ridges (MS2), paleochannels (MS3 and MS4) were recognized, and samples were collected by bore-welling at these locations (Figure 2). The samples recovered from the riverine zone could not be dated yet as permission for dating only 12 samples was granted using the AMS facility. Rest of the samples will be dated in the current session.

Samples for ^{14}C dating were collected from MS1 site at the depth of 800 cm, 350 cm and 30 cm providing age ranges (2σ date range) of 1740-1541, 1415-1296 and 961-769 cal yr BP respectively. From MS2 location, samples from 750 cm, 550 cm, and 250 cm depth were recovered giving dates of 7764-7595, 7759-7575 and 4766-4615 cal yr BP (2σ date range). From MS3 site, samples from the depth of 1000 cm, 760 cm, 600 cm, and 450 cm yielded radiocarbon ages of 7790-7610, 7634-7469, 6283-6095 and 2851-2738 cal yr BP (2σ date range). From MS4, ^{14}C samples were obtained from 1000 cm and 700 cm depth providing dates of 7792-7608 and 2441-2301 cal yr BP (2σ date range).

The chronology constructed for the landforms located in the mixing zone has shown remarkable variation in their depositional environment. The present analysis has suggested the occurrence of a relatively humid episode around 7800 cal yr BP followed by a drier phase around 6000 cal yr BP. Another episode of elevated humidity has been marked around 2700 cal yr BP. The humid and arid episodes have also been reported during the Holocene in other parts of the Indian subcontinent (Alappat et al., 2015; Narayana et al., 2017; Babeesh et al., 2019).

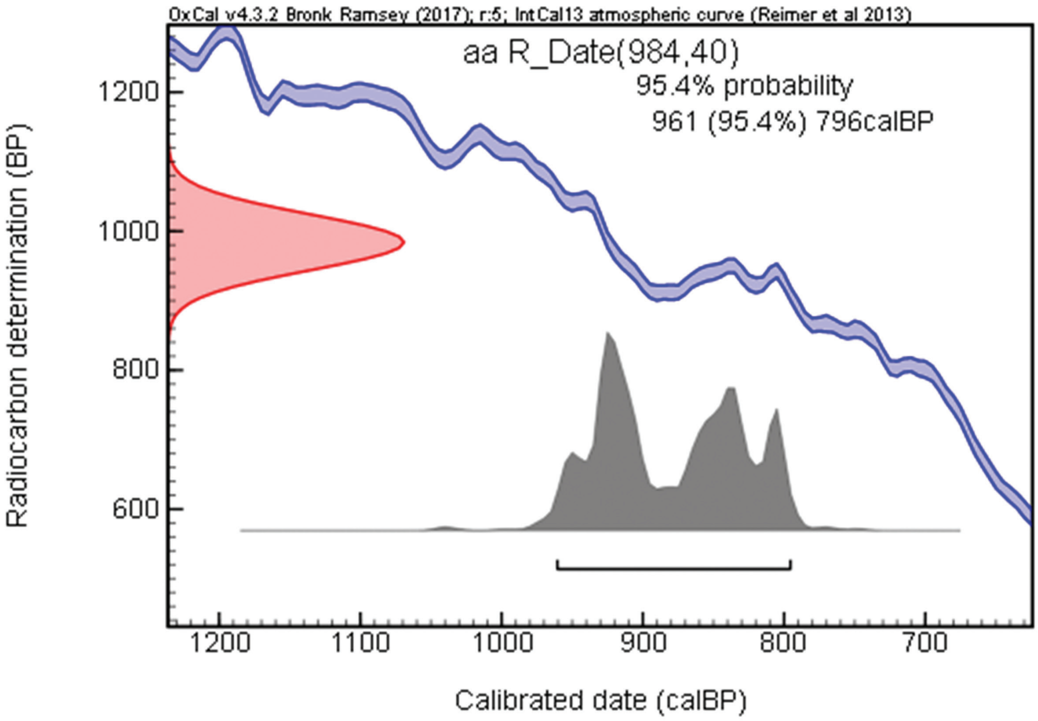

Figure 1 Calibration of radiocarbon dates using OxCal 4.3

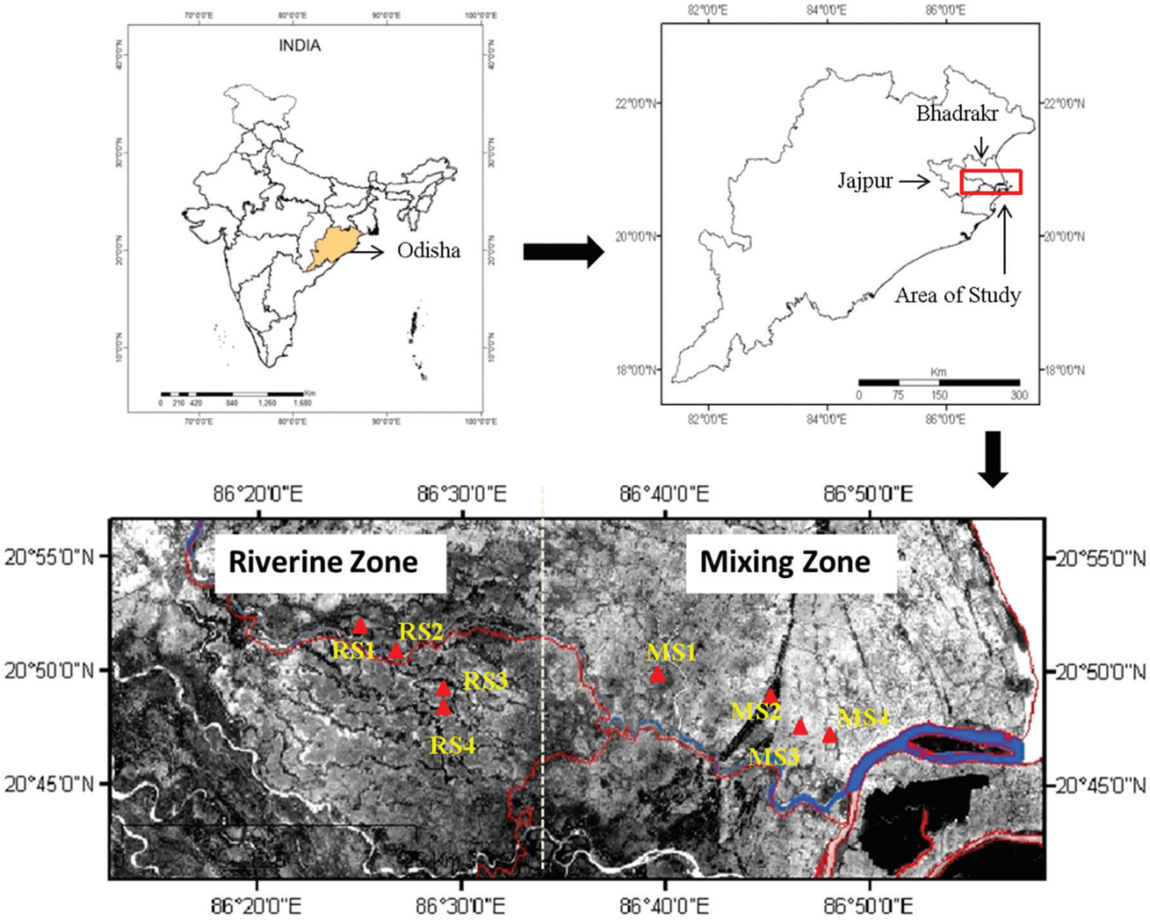

Figure 2 Area of study and sample collection sites

REFERENCES:

[1] Alappat, L., Frechen, M., Sree Kumar, S., Suresh Babu, D.S., Ravur, R., Tsukamot, S. Geomorphology, 245, 73-86 (2015).
[2] Babeesh, C., Achyuthan, H., Resmi, M.R., Nautiyal., C.M., Shah, R.A. Quaternary International, 507, 156-171 (2019).
[3] Bronk, R.C., Lee, S. Radiocarbon, 55, 720-730 (2013).
[4] Narayana A.C., Prakash V., Gautam P.K., Tripathi S. Quaternary International, 443 (3), 115-123 (2017).
[5] Vahila, M.N., Kumar, P., Bhogale, A., Chopra, S., Shinde, V., Jadhav, N., Shastri, R. Current Science, 3 (1), 27-28 (2016).

5.4.11 Radiocarbon dating of soil from Kaziranga National Park, India

Pramit Kumar Deb Burman[1]*, Supriyo Chakraborty[1], Dipankar Sarma[2], Pankaj Kumar[3] and Rajveer Sharma[3]

[1]Centre for Climate Change Research, Indian Institute of Tropical Meteorology, Pune - 411008
[2]Department of Environmental Sciences, Tezpur University, Tezpur - 784028
[3]Inter-University Accelerator Center, New Delhi, Delhi – 110067
*Corresponding author. e-mail: pramit.cat@tropmet.res.in

The terrestrial ecosystems are the largest sink of atmospheric CO_2 with a global sinking strength of 3.1 ± 0.9 GtC y-1 [1]. The soil organic matter (SOM) turnover time is an important parameter for inferring about the soil mixing and nutrient dynamics of any ecosystem that is used as an input parameter for calculating its productivity using the terrestrial biosphere models [2]. In the present proposal (btr62120) we aim to estimate the land carbon pools at the Kazirana National Park (KNP), Tezpur, Assam as part of the research objectives of the MetFlux-India project by the Ministry of Earth Sciences (MoES), the Government of India [3].

The Accelerator Mass Spectrometry (AMS) is a widely used technique for estimating the radiocarbon (C^{14}) age of different archaeological, geological, and biological samples and known for its precision [4]. The C^{14} dating of the soil samples from three different locations in KNP was carried out using the AMS facility at IUAC, Delhi. These samples were collected in April, 2017 and preserved carefully from possible degradation/contaminations. The samples were pre-processed at the wet chemistry laboratory following the standard acid-base-acid protocol [5] in March 2018 and subsequently analyzed for 14C at the IUAC AMS facility, New Delhi in June 2018.

According to the preliminary results the top soil at KNP, up to a depth of a few tens of centimeters is well mixed and has a higher percentage of modern carbon (pMC). Additionally the radiocarbon age of the soil increases with depth suggesting that the top soil is probably better-mixed than the deeply buried layers.

However, these findings are yet to be cross-checked against the supporting measurements. The carbon isotopic fractionation is an important parameter that affects the accuracy of the AMS C^{14} dating technique [6]. As recommended, we are presently in the process of measuring C^{13}/C^{12} ratio using the Isotopic Ratio Mass Spectrometer (IRMS) at IITM, Pune that can be used for an independent recalibration and recalculation of the radiocarbon dates. Additionally, various other soil parameters such as the nutrients, micronutrients, texture, bulk density etc. are being analysed for more information on the soil formation process etc. We plan to supplement our study with the similar measurements being done for the other ecosystems in the MetFlux-India network.

References

[1] C.Le Quéré R.M.Andrew J.G.Candell S.Sitch J.I.Korsbakken G.P.Peters A.C.Manning T.A.Boden P.P.Tans R.A.Houghton R.A.Keeling & others. Earth Syst. Sci. Data 8 (2016) 605-649
[2] D.B.Clark L.M.Mercado S.Sitch C.D.Jones N.Gedney M.J.Best M.Pryor G.G.Rooney R.L.H.Essery E.Blyth O.Boucher R.J.Harding C.Huntingford & P.M.Cox. Geosci. Model Dev. 4 (2011) 701-722
[3] P.K.Deb Burman D.Sarma M.Williams A.Karipot & S.Chakraborty J. Earth Syst. Sci. 126:99 (2017) 1-17
[4] L.K.Fifield Rep. Prog. Phys. 62 (1999) 1223-1274
[5] R.Sharma G.R.Umapathy P.Kumar S.Ojha S.Gargari R.J.Joshi Nuclear Inst. and Methods in Physics Research B. NA (2018) 1-7
[6] L.Calcagnile G.Quarta & M.D'Elia App. Radiat. Isot. 62 (2005) 623-629

5.4.12 Holocene Climatic changes based on multiproxy data from fluvial and lacustrine archives of eastern margin of Little Rann of Kachchh, Western India

Rachna Raj[1], Tripathi J. K[1], Sharma, A[2], Phartiyal B[2], Sridhar A[3], Pankaj Kumar[4] and Chamyal L. S[3]

[1]School of Environmental Sciences, Jawaharlal Nehru University, New Delhi-110067
[2]Birbal Sahni Institute of Palaeosciences, Lucknow-226007
[3]Department of Geology, Faculty of Science, The M. S. University of Baroda, Vadodara-390002
[4]Inter-University Accelerator Centre, New Delhi-110067

Introduction: A multiproxy studies involving palynology, phytoliths, clay mineralogy, magnetic mineralogy, carbon isotopic studies, geochemistry, granulometric analysis and the chronological studies of the lake and abandoned channels that will add meaningfully to the gap of knowledge which exists from the climatically sensitive region lying in the transitional climatic zones, semi-arid south to arid north, showing better sensitivity to even minor changes in temperature and precipitation. Being located in the northern part of the mainland Gujarat, the lakes and abandoned channels are ideal to document and assess the Holocene precipitation related changes for the regional correlation as well as to evaluate climate culture relationships.

Objective: To generate multiproxy data of the core sediments and to determine absolute ages (^{14}C) of the events identified by multi-proxy studies.

Methodology: Based on maps, satellite images and field reconnaissance coring site was identified from which Holocene climate fluctuation records was generated using multiproxy studies. Because of the semi-arid to arid climate in this region there are a limited number of archives that encompass the entire Holocene. Interpretation of data in relation to the data from in and around the study area shall be done and absolute dates shall be provided to the climatic events reflected in geochemical, mineral magnetism, palynological, sedimentological and phytolith data. Overlapping of data generated by the studies to that of regional and global events shall be undertaken to understand the Holocene palaeoclimatic changes evolution of the western India.

Data Generated:

^{14}C analysis of the samples

S. No.	Sample Name	Sample ID	pMC value	Radiocarbon Age (BP)	Median Calibrated age	Ages in BP	Depth (cm)
1.	LR_3_2	IUACD# 18C2153	81.665 ± 0.395	1627 ± 38	425 AD	**1525**	4
2.	LR_3_12	IUACD# 18C2154	70.910 ± 0.289	2761 ± 32	903BC	**2853**	24
3.	LR_3_28	IUACD# 18C2155	69.844 ± 0.284	2883 ± 32	1062 BC	**3012**	56
4.	LR_3_45	IUACD# 18C2156	62.423 ± 0.236	3785 ± 30	2215BC	**4165**	90
5.	LR_3_60	IUACD# 18C2157	56.218 ± 0.259	4626 ± 37	3456 BC	**5406**	120
6.	LR_3_106	IUACD# 18C2158	64.079 ± 0.283	3575 ± 35	1928 BC	**3878**	212
7.8.	LR_3_138	IUACD# 18C2159	55.197 ± 0.275	4773 ± 40	3568 BC	**5518**	276
9.	LR_3_173	IUACD# 18C2160	12.932 ± 0.097	16431 ± 60	17876 BC	**19826**	346
10.	LR_3_202	IUACD# 18C2161	17.767 ± 0.123	13879 ± 55	14865 BC	**16815**	404
11.	LR_3_220	IUACD# 18C2162	23.422 ± 0.133	11659 ± 45	11544 BC	**13494**	440
12.	LR_3_265	IUACD# 18C2164	13.080 ± 0.114	16339 ± 70	17776 BC	**19726**	530
13.	LR_3_270	IUACD# 18C2165	14.888 ± 0.126	15299 ± 68	16625 BC	**18575**	540
14.	LR_3_300	IUACD# 18C2166	19.594 ± 0.142	13093 ± 58	13758 BC	**15708**	600
15.	LR_3_326	IUACD# 18C2167	21.794 ± 0.149	12238 ± 55	12192 BC	**14142**	652
16.	LR_3_337	IUACD# 18C2168	11.602 ± 0.086	17303 ± 60	18916 BC	**20866**	674
17.	LR_3_351	IUACD# 18C2169	12.087 ± 0.098	16973 ± 65	18524 BC	**20474**	702
18.	LR_3_364	IUACD# 18C2170	21.463 ± 0.145	12361 ± 54	12438 BC	**14388**	728
19.	LR_3_370	IUACD# 18C2171	17.927 ± 0.126	13807 ± 56	14755 BC	**16705**	740
	LR_3_375	IUACD# 18C2172	11.758 ± 0.093	17196 ± 64	18790 BC	**20740**	750

Expected outcome: The Holocene climatic changes with absolute numbers from the arid regions of Gujarat has been done. Other proxy data is also generated, although some of the supportive data generation is under process. The detailed interpretation is under progress for a regional/global correlation of the various climatic events and to evaluate climate culture relationships.

5.4.13 Fossil fuel derived CO_2 estimation across India using radiocarbon measurement of annual crop plants

Rajveer Sharma, Pankaj Kumar, Sunil Ojha, Satinath Gargari and Sundeep Chopra

Inter University Accelerator Centre, New Delhi, India

At present, one of the most burning issues of the world is global warming. Main contributors to global warming are greenhouse gases, such as CO_2, CH_4, N_2O etc. Among all greenhouse gases, CO_2 is the largest contributor to the Earth's carbon cycle and climate change. The pre-industrial level of atmospheric CO_2, 278 ppm, reached up to a value of 403 ppm in 2017 [1]. This increase is primarily because of emissions from combustion of fossil fuels and from cement production, deforestation and other land-use changes. How much of the increased atmospheric CO_2 is derived from the combustion of fossil fuel emissions? It is an important question for the researchers and government policy makers. Radiocarbon (^{14}C, half-life of 5730 years) can be used as a tracer to answer this question because fossil fuels do not contain radiocarbon. Several such studies have been carried out in all parts of world including USA [2-3], Europe [4-6], China [7-8], Korea [9].

In present study, we have also traced fossil fuel derived CO_2 in the atmosphere across different parts of India using radiocarbon measurement of annual crop plants. Annual crop plants utilize atmospheric CO_2 for photosynthesis during their growing period. Radiocarbon measurements of these plants materials provide isotopic composition of atmospheric CO_2 utilized during their growing period. Crop plant samples (wheat, rice etc) were collected from 25 locations from different parts of India in the year 2017 and 2018. Samples were dried, grinded, pre-treated with acid and then graphitized using automated graphitization equipment (AGE) at graphitization laboratory in IUAC. AMS ^{14}C measurements of these graphitized samples were performed using XCAMS system at IUAC [10]. $\Delta^{14}C$ value for each sample was calculated from $^{14}C/^{12}C$ as described in [11]. Fossil fuel derived CO_2 mole fractions for each location were calculated using these $\Delta^{14}C$ values.

REFERENCES:

[1] WMO Greenhouse Gas Bulletine, No. 13, published on 30 October, 2017.

[2] Hsueh, D. Y., N. Y. Krakauer, J. T. Randerson, X. M. Xu, S. E. Trumbore, and J. R. Southon (2007), Regional patterns of radiocarbon and fossil fuel-derived CO_2 in surface air across North America, Geophys. Res. Lett., 34, L02816.

[3] Heather D. Graven, Thomas P. Guilderson, Ralph F. Keeling, Observations of radiocarbon in CO_2 at La Jolla, California, USA 1992-2007: Analysis of the long-term trend, Journal of Geophysical Research: Atmospheres, 2012, 117, D2302

[4] D. Bozhinova, M. Combe, S. W. L. Palstra, H. A. J. Meijer, M. C. Krol, W. Peters, The importance of crop growth modeling to interpret the Δ14CO2signature of annual plants, Global Biogeochemical Cycles, 2013, 27, 3, 792.

[5] D Bozhinova, SWL Palstra, MK van der Molen, MC Krol, HAJ Meijer, Three years of $^{14}\Delta CO_2$ observations from Maize Leaves in Netherlands and Western Europe, Radiocarbon 58, 3, 459-478.

[6] Levin, I., Kromer, B., Schmidt, M., Sartorius, H., 2003. A novel approach for independent budgeting of fossil fuel CO2over Europe by $^{14}CO_2$ observations. Geo-phys. Res. Lett. 30, 23, 2194.

[7] Zhenchuan Niu, Weijian Zhou, Xiaoshan Zhang, Sen Wang, Dongxia Zhang, Xuefeng Lu, Peng Cheng, Shugang Wu, Xiaohu Xiong, Hua Du, Yunchong Fu, The spatial distribution of fossil fuel CO_2 traced by $\Delta^{14}C$ in the leaves of gingko (Ginkgo biloba L.) in Beijing City, China, Environmental Science and Pollution Research, 2016, 23, 1, 556.

[8] Weijian Zhou, Shugang Wu, Wenwen Huo, Xiaohu Xiong, Peng Cheng, Xuefeng Lu, Zhenchuan Niu, Tracing fossil fuel CO_2 using $\Delta^{14}C$ in Xi'an City, China, Atmospheric Environment, 2014, 94, 538-545

[9] H. Park, W. Hong, X. Xu, G. Park, K.S. Sung, Kilho Sung, Jong-geol Lee, T. Nakanishi, Hyo-Seok Park, The distribution of $\Delta^{14}C$ in Korea from 2010 to 2013, Nuclear Instruments and Methods in Physics Research Section B: Beam Interactions with Materials and Atoms, 2015, 361, 609

[10] Rajveer Sharma, G.R. Umapathy, Pankaj Kumar, Sunil Ojha, Satinath Gargari, Rajan Joshi, Sundeep Chopra and Dinakar Kanjilal, AMS and upcoming geochronology facility at Inter University Accelerator Centre (IUAC), New Delhi, India, (2018) Nucl. Instr. Meth. B, 438, 124 – 130.

[11] Stuiver, M., Polach, H.A., 1977. Discussion: reporting of ^{14}C data. Radiocarbon 19, 355-363.

5.4.14 Chronology of the Iron Age Site of Ambal, Nagapattinam District, Tamil Nadu

V. Selvakumar[1], Kumar Pankaj[2], C.M. Jaseera[3] and K. Mathivanan[4]

[1]Department of Maritime History and Marine Archaeology, Tamil University, Thanjavur-613010, India.
[2]Scientist- E, AMS & Pelletron Group, Inter- University Accelerator Centre, Delhi 110067
[3]Department of Epigraphy and Archaeology, Tamil University, Thanjavur-613010, India.

The Iron Age-Historical site of Ambal (Lat.10.9482178; Long.79.7035146) located in Nagapattinam district of Tamil Nadu (Fig. 1) and excavations were undertaken in the season of 2015-16. Four organic samples were dated from the site of Ambal in Nagapattinam district of Tamil Nadu using the AMS radiocarbon facility at IUAC. The samples were selected from relatively undisturbed contexts, and to cover all the trenches excavated at the site and to understand the overall chronology of the sites.

Results of the analyses

The measured values and the radiocarbon ages are presented in Table 1.

Table 1 Radiocarbon dates of the samples from Ambal

Sample No/Trench	Context and Depth	IUAC Lab ID	pMC value	Radiocarbon Age (BP)
ABL 1	Trench I 024b, 230 cm	IUACD#18C1822	89.448± 0.322	895± 29
ABL 2 (CHARCOAL)	Trench II 019, B4 190-195	IUACD#18C1823	76.237± 0.334	2179± 35
ABL 3 (CHARCOAL)	Trench III 015, 125 cm	IUACD#18C1824	94.343± 0.349	467 ± 29
ABL 4 (JOB's TEAR SEED)	Trench II, 021, 186-205 cm	IUACD#18C1825	58.691± 0.258	4280 ± 35

Sample - ABL 2 019 B4 190-195 cm:

The sample from ABL Trench II Locus 019 from the depth of 190-195 cm has given a date of 2179± 35. This date reveals 158 cal BC for the sediment. This dating suggests that the settlement of Ambal had developed into a regular habitation by the second century BCE. The houses of this period were made of perishable material and the site witnessed agrarian activities.

Sample from ABL 1

The charcoal sample from the Trench ABL 1 revealed that Locus 024 at a depth of 024b has materials of medieval period which can be placed in the 12th and 13th century CE. This evidence is important and goes with the date of the temple and inscriptions which are found at this settlement. Currently this area is not under occupation and this date suggests that this area had residential complexes as early as 11 and 13 centuries.

Sample from ABL III

The trench ABL III revealed occupation of the site in the later medieval period around 15th century CE. The inscriptions reveal that the settlement had a *nagaram* or a commercial complex with industrial activities. Evidence of copper smelting and possibly gold working was found in this trench in the form of crucibles and fragments of gold. The excavation context matches with the date obtained from AMS. It suggests that in the pre-colonial period the settlement was brisk and there existed industrial activities. Perhaps these activities were abandoned in the colonial period, when new settlements came up on the coastal areas.

Dating of Job's Tear Seeds

A few job's tear seeds were dated sample ABL 4 (from Trench ABL II) and these seeds gave a very early date of early third millennium BCE which does not match with the dating of the context. It appears that the seeds, which were older, might have reached the sedimentary context at a later date. This cannot be ascertained without dating more such samples from the site.

Discussions

The four samples dated from the site of Ambal reveal that the site of Ambal was occupied continuously from second century BCE. These dates are in tune with the archaeological materials such as ceramics and other materials. The settlement of Ambal had established itself as an agrarian settlement as early as second century BCE. However, there is one-meter thick deposit beneath the sediment that produced the date of second century BCE and samples from the lower loci could reveal about the beginning of the Iron Age at this site. More radiocarbon dating is necessary at this site, to understand the beginning of occupation.

Acknowledgements

The authors would like to acknowledge the technical and financial support offered by Inter- University Accelerator Centre and University Grants commission for the research. Authors are thankful to IUAC for extending AMS facility, under Geochronology project funded by Ministry of Earth Sciences Govt of India. We would like to thank Dr Sundeep Chopra, Scientist-H, IUAC for the support.

REFERENCES:

[1] V. Selvakumar et al. Puratattva 46 (2016): 168-174.

[2] J. H. McGuire, D. J. Land, J. G. Brennan, and G. Basbas, Phys. Rev. A 19, 2180 (1979).

5.4.15 Holocene climatic and monsoonal variation: Benthic foraminifera records from Krishna-Godavari and Mahanadi Basins, Bay of Bengal

Mohanty Satabdi[1], Bhaumik Ajoy Kumar[1] and Pankaj Kumar[2]

[1]Department of Applied Geology, IIT (ISM) Dhanbad, Jharkhand, India
[2]Inter-University Accelerator Centre, New Delhi-110067, India.

AMS ^{14}C dating plays a significant role in paleoclimatic study as it provides the time frame to the climatic events in absolute value which is helpful in global correlation. The objective of the study is to obtain radiocarbon dates of mixed foraminifera i.e. both benthic and planktic foraminifera for the global paleoclimatic interpretation.

EXPERIMENTAL DETAILS

We have analyzed benthic and planktic foraminiferal (>125 µm) AMS ^{14}C dating using the foraminiferal calcitic test from 10 samples collected from the sediment cores 15A-1H-1 and 15A-1H-2. Total 8-10 µg of carbonate sample was weighed for the analysis of each sample. Samples were pre-treated and graphitized before radiocarbon measurement.

PRETREATMENT

Foraminiferal samples were oxidized with 15% H2O2 in an ultrasonic bath for 5–15 min and then rinsed with Milli-Q water and oven-dried. Careful handling of the sample was required in case of small samples of less than 10µg carbonate. Samples were crushed using an appropriate method to increase the surface area for chemical pre-treatment.

GRAPHITIZATION

For graphitization, automated graphitization equipment (AGE) coupled with elemental analyzer is used developed by Ionplus AG and ETH, Zurich [1]. The pre-treated foraminifera was put in 4 ml septum sealed vial and flushed with helium (100 ml/min) for 5 min by using a double-walled needle. For the decomposition of carbonate, 0.5 ml H3PO4 was added to the vial with a syringe and then heated at 75° C for at least 30 min. The purified CO2 flushed with helium (100 ml/min) via a water trap of phosphorus pentoxide to a trap containing zeolite in AGE [2]. Trapped CO2 is transferred by thermal expansion into a tube or reactor filled with iron powder. CO2 is reduced by H2 gas on the surface of iron powder at 580°C. Graphite is formed and water vapours are removed with the help of Peltier coolers. After that, the resulting graphite was pressed into cathode capsules and placed in a cathode wheel of the ion source of accelerator for radiocarbon measurements at IUAC.

Table 1: Graphitization log

Sample Name	Mass/mg	CO2/µg	COH2/mbar	T /°C	P/mbar	Time/min
19C2373	12.0	1019	1850	580	153	120
19C2374	5.33	511	938	580	119	120
19C2375	6.2	566	1044	580	144	120
19C2376	4.87	425	776	580	83	120
19C2379	5.0	441	812	580	108	120
19C2383	2.0	221	406	580	73	120
19C2385	3.38	294	554	580	101	120
19C2386	4.8	496	902	580	131	120
19C2387	3.0	224	423	580	92	120
19C2388	5.38	359	652	580	95	120

Table 2: ^{14}C AMS age (2σ) determinations of foraminifera from the Krishna-Godavari basin.

Sample ID	pMC value	Radiocarbon Age (BP)	Calibrated (BP) age ranges	Modelled age ranges (BP)
19C2373	87.688 ± 0.887	1055 ± 81	500-764	846-1058
19C2374	79.643 ± 1.005	1828 ± 102	1178-1607	970-1190
19C2375	79.990 ± 0.857	1793 ± 86	1178-1530	1021-1240
19C2376	80.158 ± 1.142	1776 ± 115	1080-1585	1087-1307
19C2379	76.753 ± 0.973	2125 ± 102	1473-1964	1850-2066
19C2383	72.017 ± 0.612	2636 ± 68	2121-2542	2181-2355
19C2385	67.824 ± 0.752	3118 ± 89	2728-3140	2421-2561
19C2386	69.669 ± 0.806	2903 ± 93	2376-2862	2498-2628
19C2387	72.931 ± 0.783	2535 ± 86	1970- 2412	2644- 2747
19C2388	66.429 ± 0.719	3285 ± 87	2882- 3342	2720- 2847

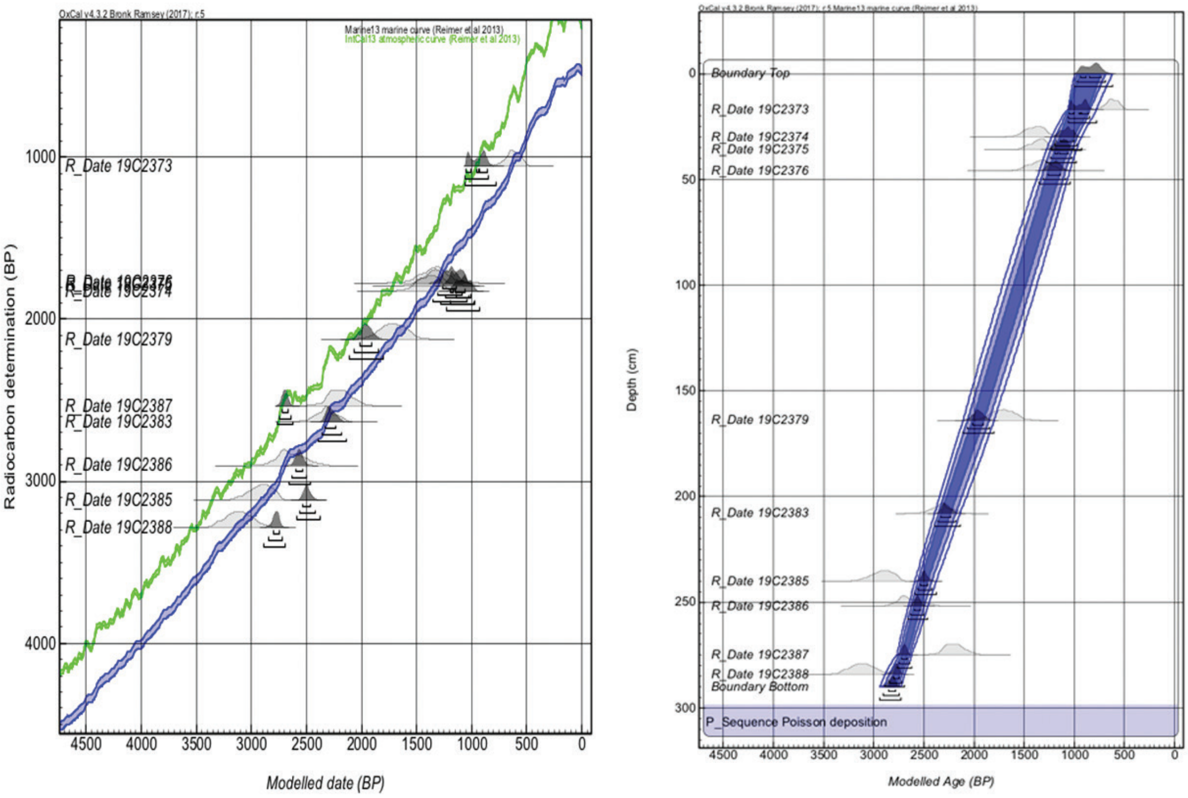

(a) (b)

Fig.1 Shows (a) Obtained ^{14}C Ages and (b) Age-Depth modelled using OxCal 4.3 (Ramsey 2017) [3]

We are still working on the data interpretation part and wait for other proxies data so that we can correlate different climatic events. Supportive data analysis and documentation is in progress that will be summarised for future publications.

REFERENCE:

[1] Wacker, L., Lippold, J., Molnár, M. and Schulz, H., 2013. Towards radiocarbon dating of single foraminifera with a gas ion source. Nuclear Instruments and Methods in Physics Research Section B: Beam Interactions with Materials and Atoms, 294, pp.307-310.

[2] Ruff, M., Szidat, S., Gäggeler, H.W., Suter, M., Synal, H.A. and Wacker, L., 2010. Gaseous radiocarbon measurements of small samples. Nuclear Instruments and Methods in Physics Research Section B: Beam Interactions with Materials and Atoms, 268(7-8), pp.790-794.

[3] Ramsey, C.B., 2017. Methods for summarizing radiocarbon datasets. Radiocarbon, 59(6), pp.1809-1833.

5.4.16 AMS Dating of bones from the Late Pleistocene fossiliferous horizons in the Manjra Valley, District Latur, Maharashtra

Sathe Vijay[1], Chakraborty Prateek[1], Kumar Pankaj[2] and Sharma Rajveer[2]

[1]Department of AIHC & Archaeology, Deccan College Postgraduate & Research Institute, Deemed University, Pune 411006, India.,
[2]Inter-University Accelerator Centre, New Delhi-110067, India.

The present work was carried out by the Department of AIHC & Archaeology, Deccan College Postgraduate & Research Institute Deemed University, Pune in conjunction with the AMS and Pelletron Group, IUAC in the first half of March 2019. The focus of this work was to establish a procedure through which reliable AMS dating of fossil bone and teeth could be carried out, using the material from sites in the Manjra Valley (dist. Latur, Maharashtra) as a case study.

The Manjra River valley is one of the richest fossil site complexes in the Indian subcontinent, and has yielded almost complete evidence of a full food chain structure from apex predator to scavengers. Establishing a clear chronology of this site is essential, since it will allow the finds to be put into a clear chronological context with respect to the appearance and disappearance of several key fauna. Moreover, accurate dating of the site will also allow a clearer analysis of the environmental and climatic data available, allowing further reconstruction of Late Pleistocene environments during the Middle Palaeolithic in Peninsular India.

Due to the low organic content in fossilized tissue, AMS dating has generally been considered inaccurate or error-prone. However, not many efforts have been made using the dental collagen powder from fossilized teeth, which are generally much more resistant to breakdown and decomposition thanks to the protection of the tooth enamel. In the present study, collagen was obtained from the molar teeth of large vertebrates, by drilling into the enamel-dentine junction.

The samples were then subjected to two different processes of AMS dating. The first batch was processed using the standard method, and did not yield measurable amounts of organic carbon. Therefore, larger amounts of sample were taken for the second batch, which were processed as per the recommendations of Cherkinsky 20091, which recommends the treatment of fossil collagen powder using acetic acid for better preservation of organic carbon.

There has been a success in processing the bone samples using method described by Alex Cherkinsky and we have graphitized samples. As explained in the Cherkinsky paper, we intend to compare it with collagen. Currently collagen extraction is in process. Once the collagen extraction is completed, we will graphite collagen and compare it. The work is in progress and hence the actual results in terms of dates are awaited.

REFERENCES.

[1] Cherkinsky, Alexander 2009. Can we get a good radiocarbon age from “bad bone”? Determining the reliability of Radiocarbon Age from Bioapatite. Radiocarbon 51 (2), 647-655.

5.5 ATOMIC PHYSICS

5.5.1 Setting up of EDXRF system using bremsstrahlung from transmission type X-ray generator

Soumya Chatterjee[1], Tapan Nandi[2] and Debasis Mitra[1]

[1]Department of Physics, University of Kalyani, West Bengal-741235, India
[2]Inter University Accelerator center, Aruna Asaf Ali Marg, NewDelhi-110067, India

In various scientific fields like geological sciences, biological sciences and environmental studies, the elemental analysis holds an important role for users. In comparison to other elemental analysis techniques like PIXE, NAA, Energy-Dispersive X-ray Fluorescence (EDXRF) [1] makes a huge impact as its use is less costly than other techniques as well assimple in handling. EDXRF system consists of an x-ray source (radioactiveor x-ray tube), x-ray detector and a data acquisition system. Two methods are available: alpha coefficient method and Fundamental Parameter method (FPM)[1]. In alpha coefficient method there is a need of only ratio (R_i) of intensity of a line for an elementpresent in the sample to that from a standard. Different standardsare required for a single sample. Making of these standards are time consuming and costlier too. For FPM, either one can use monochromatic primary radiation coming directly from radioactive source or fluorescence radiation from secondary source due to incidence of broadprimary spectrumfrom x-ray tube [2]. Sample x-rays are then detected byan x-ray detector. By using a suitable peak fitting program one can find the intensities of different diagram lines which are originating from different elements. Using those line intensities, elemental concentrations can be calculated with the help of some atomic parameters such as photo-ionization cross-section, fluorescence yields, Coster-Kronig transitions and detector efficiency. No standard is required for this technique and hence one single run is enough to determine the elemental concentrations of the sample. Now a day's very small size x-ray generatoroperated by a stable power source like a car battery is commercially available. Here we have shown how the bremsstrahlung spectrum can be used as an exciter for the sample to determine the elemental composition.We have used a small transmission type portable x-ray generator of Amptek (Mini-X), having 4W power with maximum operating voltage of 50kV. X-rays are detected by using a Silicon Pin detector. Absolute efficiency of the detector obtained at IUAC and shown in Figure 1 have been used in this experiment. Figure 2 shows the bremsstrahlung spectra from the tube for operating voltage 20kV, 25kV and 30kV and compared with the simulated one [3]. Experimentally detected bremsstrahlung spectrum matched very well with the simulated one.

For a mono-chromatic incident x-ray beam, elemental analysis can be done by using the following equation [3]

$$Ii = [(I_0\, d\omega)/ 4\pi\, \mathrm{Sin}\, (\Psi_1)]\, [\sigma_i\, \omega_i\, f_i]\, A_i\, \varepsilon_i\, C_i\, (1+H_i)$$

Where I_0 is for incident flux, ω is for solid angle subtended by detector at target, Ψ_1 denotes entrance angle, σ_i, ω_i and f_i serves the purpose for photo-ionisation cross-section for primary radiation, fluorescence yield and fraction of radiation of considered x-ray line for i^{th} element respectively. A_i is the absorption correction not only for the primary X-rays but also for the fluorescent X-rays inside the target. ε_i is the detector efficiency for fluorescent radiation, H_i is for inter-element enhancement factor and C_i is for relative concentration for i^{th} element of the sample. I_i can be found by calculating the area for K-alpha of each sample. A computer program is written to calculate the concentrations with an arbitrary initial set of values following the condition $\sum C_i=1$. After each set of calculation, the newly calculated concentrations have to be normalized. But to use this equation we have to deal with mono-chromatic x-ray beam. To convert our bremsstrahlung to mono-chromatic x-ray we have to divide our whole spectrum into large number of energy slices so that each energy slice can be treated as monochromatic source of x-ray beam. And the fluorescent lines generated for each of such energy slices can be calculated using above equation. To get the total fluorescent X-rays we have to add up all the contributions from each of these slices which is used to obtain the final result.

To demonstrate the technique, we have taken a one-rupee coin of year 2000, which is exposed to the bremsstrahlung radiation from the x-ray tube operating at 25 KeV. Typical spectrum coming from the coin is detected by the silicon PIN detector and is shown in Figure 3. The concentration calculated in this technique using theoretically generated bremsstrahlung spectra, which is perfectly matched with the experimental one, as shown in table 1 along with the earlier results [4].

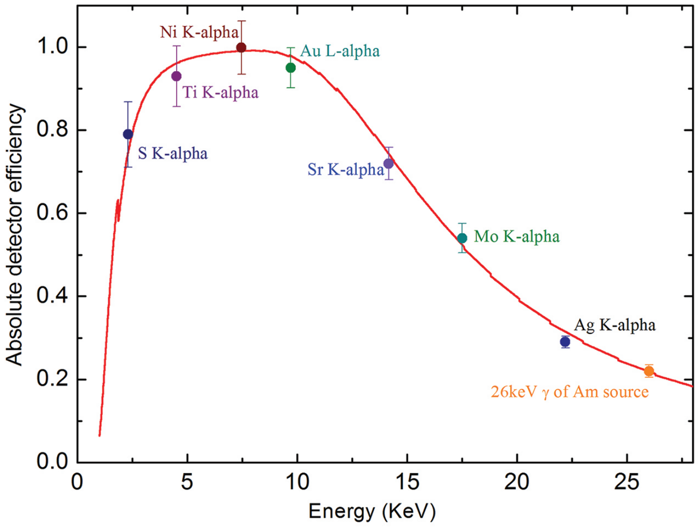

Fig. 1: Absolute efficiency of detector

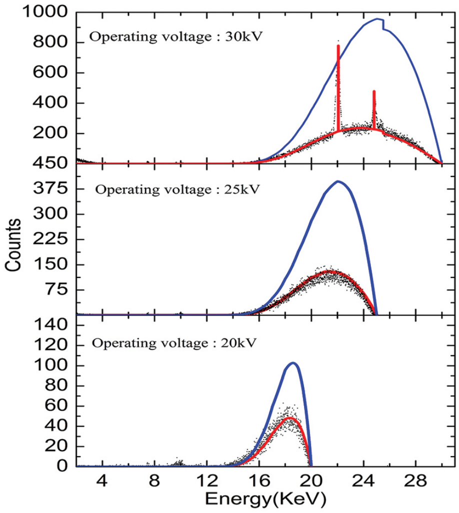

Fig. 2: Experimental (dotted), simulated coming from x-ray generator (blue line), simulated after inclusion of efficiency of x-ray detector (red line) bremsstrahlung spectrum.

REFERENCES
[1] Principles of Quantitative X-ray Fluorescence Analysis (Heyden and Son Ltd,1982).
[2] A.C. Mandal, M. Sarkar, D. Bhattacharya, Eur. Phys. J. AP17 (2002) 81.
[3] A.C. Mandal, S. Santra, D. Mitra, M. Sarkar, D. Bhattacharya, Nucl. Inst. & Meth. B **197** (2002) 179.
[4] A.C. Mandal, S. Santra, D. Mitra, M. Sarkar, D. Bhattacharya, Current Science **85** (2003) 134.

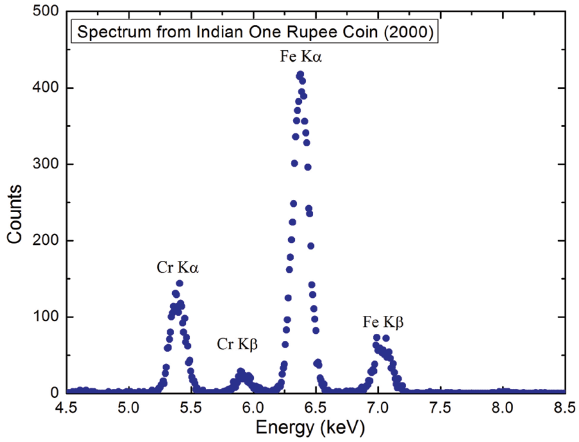

Fig. 3: X ray spectrum obtained from one-rupee coin using 25k operating voltage of the x-ray generator.

Table 1: Elemental concentration of one-rupee coin

Elements	Earlier Result [4]	Present result
Cr	16.8	17.2
Fe	83.2	82.8

5.5.2 Relativistic atomic structure calculations of helium-like ions for odd Z 3d-elements:

Gajendra Singh[1], A.K. Singh[1] and T. Nandi[2]

[1]USICT, GGSIPU, New Delhi - 110078, India.
[2]Inter University Accelerator Centre, Aruna Asaf Ali Marg, New Delhi-110067, India.

We have applied systematically enlarged Multiconfiguration Dirac-Fock (MCDF) wavefunctions [1] with the inclusion of finite nuclear size effects, Breit interactions and quantum electrodynamic corrections to evaluate relativistic atomic structure data of He-like ions for odd Z 3d-elements. Computed energy levels, transition probabilities, oscillator strength and selected x-ray wavelengths are compared with available experimental data. Special emphasis is given on forbidden transition rate, isotopic shift and hyperfine structure calculations as they are of potential interest in astrophysics. An attempt is made to report accurate hyperfine splitting constants to theoretically estimate hyperfine transitions and compared them with available experimental values.

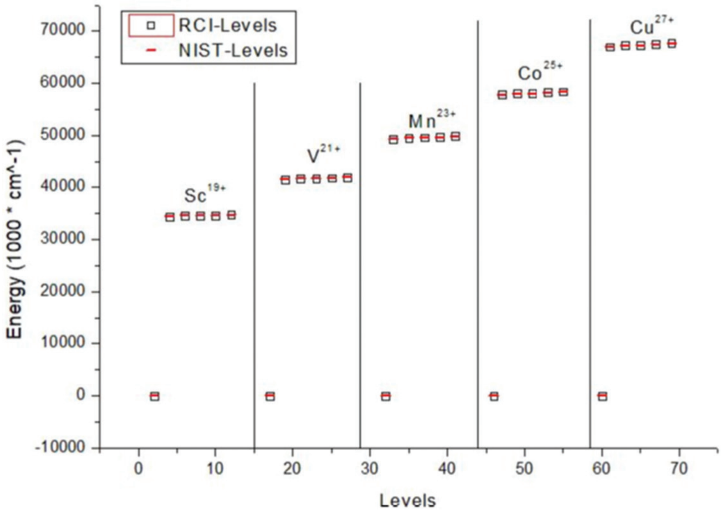

Fig.1: Comparison of the computed energy levels with the NIST energy levels of the ions under study.

Data obtained in above computations for level energies and transition rates for E1, M1 and M2 are in accordance with the NIST database as shown in Fig. 1. At present isotopic shifts and hyperfine coupling-constants are of high demand for determining nuclear quadrupole moment and hyperfine structure from experiments. Further, hyperfine data are also useful to construct fine structure levels to improve plasma diagnostics. We believe that the present work especially isotopic shift and hyperfine structure calculations will be useful to global modelling of extrasolar objects [2].

REFERENCES
[1] P. Jonsson, G. Gaigalas, J. Bieron, C.F. Fischer and I. Grant, Computer Physics Communications **184,** 2197 (2013).
[2] J.U.Ness and N.S. Brickhouse et. al. The Astrophysical Journal **598,** 1277 (2003).

5.5.3 Nuclear orbiting resonances in atomic phenomena

T. Nandi[1], Yash Kuma[2], Prashant Sharma[3], Adya P. Mishra[4], D. Mitra[5], Gajendra Singh[6], Nishchal R. Dwivedi[7], Sudhir R. Jain[7], and A.S. Kheifets[8]

[1]IUAC, JNU New Campus, Aruna Asaf Ali Marg, New Delhi 110067.
[2]Dipartimento di Fisica "Galileo Galilei", Università di Padova, I-35131 Padova, Italy.
[3]Department of Particle Physics and Astrophysics, Weizmann Institute of Science, Rehovot 76100, ISRAEL.
[4]Atomic & Molecular Physics Division, BARC, Trombay, Mumbai - 400 085.
[5]Department of Physics, Kalyani University, Kalyani, Nadia, West Bengal-741235.
[6]USICT, GGSIPU, New Delhi – 110078.
[7]Nuclear Physics Division, BARC, Trombay, Mumbai - 400 085, India.
[8]Research School of Physics, The Australian National University, Canberra, Australian Capital Territory 0200, Australia.

Nuclear orbiting resonances have been studied in the past for various nuclear reactions. However, experiments are carried out only at energies much greater than the fusion barrier energy [1]. In a recent work yet to be published [2], we demonstrate that the nuclear orbiting can occur even at the sub-barrier energies. Even though the dinuclear orbiting cross-section at these energies is an order of magnitude higher than the Coulomb excitation cross-sections, no study has been yet conducted using any nuclear techniques. The target and projectile nuclei in the dinuclear complex are so close that higher nuclear charge is felt by the orbital electrons. By incorporating this fact into a simple model, we have determined the orbiting duration for the dinuclear complex. Interestingly, these values are found to be within a factor of three larger than that of the predictions made by the nucleon exchange code HICOL [3]. Nuclear recoil induced shake off ionization explains well only the enhanced ionization [4], whereas the present mechanism of dinuclear orbiting explains both the enhanced ionization and anomalously large angle scattering. Another interesting fact is that the difference between the resonance energy and interaction barrier gives us the orbiting energy. It means the interaction barrier is revealed to be the point from where the nuclear force starts acting. Hence, interaction barrier radius can be a good measure of the range of the nuclear force. We have also tried to unravel the possible origin of the short time scale of the orbiting complex. It is the Coulomb excitation process, which diminishes the orbiting energy considerably within a few zeptoseconds so that the orbiting complex breaks into the incoming channels. We have proposed the multi photon exchange as a single virtual photon, which is responsible not only for the Coulomb excitation, but also for the atomic excitation. The excitation in a system with a vacancy in the K-shell can lead to autoionization, which does not occur instantly, rather it goes through Wigner-Smith time delay [5] of the order of a few hundreds of as. Hence, the orbiting induced ionization triggered in nuclear time scale (zs) transfers the phenomenon occurring in atomic time scale (as) so that one can measure the x-ray emissions. This process enables us to explain the longstanding discrepancy between the measured values of fission time scales by the nuclear and atomic techniques. Formation of the dinuclear orbiting complexes at sub-barrier energies thus exhibits an intriguing research area in the interface of atomic and nuclear physics.

REFERENCES
[1] Amlan Ray, Nucl. Phys. A **787,** (2007) 499.
[2] T. Nandi, Yash Kumar, Prashant Sharma, Adya P. Mishra, D. Mitra, Gajendra Singh, Nishchal R. Dwivedi, Sudhir R. Jain, and A.S. Kheifets, to be submitted soon.
[3] H. Feldmeier, Repts. Prog. Phys. **50,** (1987) 915.
[4] Prashant Sharma and T. Nandi, Phys. Rev. Lett., **119,** (2017) 203401.
[5] M. Schultze et. al., Science **328,** (2010) 1658.

5.5.4 Unusual charge exchange by swift heavy ions at solid surfaces

Tapan Nandi[1], Prashant Sharma[2] and Pravin Kumar[1]

[1]Inter University Accelerator Centre, Aruna Asaf Ali Marg, New Delhi - 110067, INDIA
[2]Department of Particle Physics and Astrophysics, Weizmann Institute of Science, Rehovot 76100, ISRAEL.

The electromagnetic methods for charge state analysis providean integral measure of the charge changing processes in the bulk and chargeexchange phenomenon at the exit surface of the foil (q^{t}_{m}) [1]. However, disentanglingthese two contributions are essential for many applications, e.g., x-ray emission of many astrophysical objects, the infrared emission bands from range of environments in the galaxies, accelerator physics, ion energy losses in solids, cancer therapy and ionization by heavy ions, and the surface modifications innanoscales. Accordingly, we have employed the x-ray spectroscopy techniqueto measure the mean charge states of swift heavy ions evolved due to the chargechanging process only in the bulk (q^b_m) if measured using Kα x-ray peak [2] and the mean charge state in the bulk plus radiative contribution if measured using radiative electron capture peak [3]. We find that the meancharge states so measured by the two methods are very different, because x-ray technique takes account of qbm, whereas q^t_m is deduced by the electromagnetic analyser; the qbm being higher than q^t_m. Theoretical predictions of q^b_m are made using a simple model if the target electrons form a Fermi-gas, withwhich the swift heavy ions interact. For a series of measurements with severalions (z = 22-35) in the energy range 1.5-3.0 MeV/u, a very good agreement isseen between the present experiments and theory [4]. The qt¬m values of the ions as measured by electromagnetic methods are also evaluated accurately by an improvedformula. The q^b_m - q^t_m is a measure of the net charge exchange contribution responsible at the exit surface of the foil. Very surprisingly, for 1 MeV/u uranium ions, up to 37 electrons per event can participate in charge exchange process at thesurface of the carbon foils [3]. In order to validate such findings in a more convincing manner, we are developing an experimental technique capable of measuring directly the charge exchange contribution at the solid surface. Further, we are in the process of establishing a method in fabricating a special type of solid foil that can avoid the charge exchange effect at the exit surface. It implies that we will get qbm from the entire foil instead of q^t_m, which means this method will give us much higher charge state from this special foil. Markedly, this technique will boost up the beam energy of the heavy ions (z>30) with existing accelerators with any budget.

REFERENCES

[1] K. Shima, T. Ishihara, T. Miyoshi, T. Mikumo, Phys. Rev, A **28**, (1983) 2162.
[2] P. Sharma and T. Nandi, Phys. Lett. A **380**, (2016) 182.
[3] P. Sharma and T. Nandi, Phys. Rev. Accl. Beams **22**, (2019) 034501.
[4] T. Nandi, P. Sharma and P. Kumar, to be submitted.

5.5.5 L-shell ionization cross sections of Ta, Pt, Th, and U by Si ions

C. Montanari[1], A. Mendez[1], D. Mitnik[1], M. Oswal[2], S. Kumar[2], U. Singh[3], G. Singh[4], K.P. Singh[2], D. Mehta[2], D. Mitra[5] and T. Nandi[6]

[1]Instituto de Astronomía y Física del Espacio, CONICET and Universidad de Buenos Aires - Buenos Aires (Argentina)
[2]Department of Physics, Panjab University, Chandigarh (India)
[3]The Marian Smoluchowski Institute of Physics, Jagiellonian University, Kraków (Poland)
[4]Department of Physics, Punjabi University, Patiala, Punjab (India)
[5]Department of Physics, University of Kalyani, West Bengal-741235, India
[6]University Accelerator Centre, Aruna Asaf Ali Marg, New Delhi-110067 (India)

Accurate determination of the x-ray production cross sections is important because of their wide use in atomic and molecular physics, and non-destructive elemental analysis of materials. Reliable values of L-shell ionization cross sections are included in the extended particle induced x-ray emission technique (PIXE) [1]. In this opportunity we will present a theoretical experimental study of the L-shell ionization of relativistic targets. The measurements of x-ray production cross sections by (84-140 MeV) Si^{+q} ions (q=8; 12), were held at the Inter-University Accelerator Centre, New Delhi. Multiple-hole fluorescence and Coster-Kronig yields were used to obtain the Li ionization cross sections (i = 1-3) from the measured x-ray production cross sections Lℓ, Lα, and Lβ, Lη, and Lγ [2]. The present experimental values are compared with full theoretical calculations by means of the shellwise local plasma approximation (SLPA) [2]. This model uses the quantum dielectric formalism to obtain the total ionization cross sections from an initial ground state. The wave functions and binding energies of the different targets were obtained by solving the fully relativistic Dirac equation using the HULLAC code package [3]. These calculations are based on first-order perturbation theory with a central field, including Breit interaction and quantum electrodynamics corrections. The new experimental data and the SLPA results for the ionization cross sections of the Li subshells are also compared with the known ECUSAR and ESPSSR [4], which are semi-empirical approximations. The agreement between the SLPA values and the experimental is rather good, also with the ECUSAR. Interestingly, the cross sections are found to be almost independent of the charge state of the Si ions, and not the outgoing charge state of the ion. This is important because the mean charge state plays a decisive role in the multiple ionization during the ion-solid collisions.

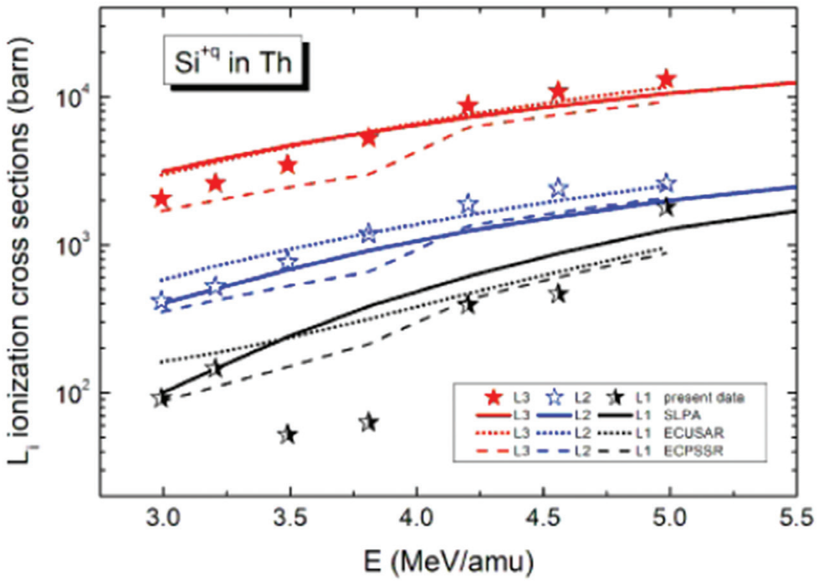

Fig 1: Measured L sub-shell ionization cross sections are compared various theoretical calculations.

REFERENCES

[1] M. Antoszewska-Moneta *et al,* Eur. Phys. J. D. **69,** (2015) 77.
[2] M. Oswal *et al,* Nucl. Instrum. Meth. Phys. Res. B **416,** (2018) 110.
[3] A. Bar-Shalom, M. Klapisch, J. Oreg, J. Quant. Spectrosc. Radiat. Transf. **71,** (2001) 169.
[4] G. Lapicki, Nucl. Instrum. Meth. Phys. Res. B **318,** (2014) 6.

5.5.6 Measurements of M X-ray relative intensities for ^{70}Yb, ^{82}Pb and ^{83}Bi induced by Low energy Carbon ions

Shehla[1], Ajay Kumar[2], Anil Kumar[1], D. K. Swami[3] and Sanjiv Puri[1]

[1]Department of Basic and Applied Sciences, Punjabi University, Patiala-147002, India
[2]Nuclear Physics Division, Bhabha Atomic Research Centre, Trombay, Mumbai - 400085, India
[3]Inter University Accelerator Center, Aruna Asaf Ali Marg, New Delhi-110067, India

In the present work, the intensity ratios, I_{MK} / I_{MN} (exp) (k = ξ, β, γ) for $_{70}$Yb, $_{82}$Pb and $_{83}$Bi induced by the C^{q+} (q = 4, 5) ions having energies in the range 800-1500 keV have been measured. These measurements were performed with the C^{q+}(q = 4, 5) ions accelerated using the Low Energy Ion Beam Facility (LEIBF) at the Inter University Accelerator Center (IUAC), New Delhi, India [1, 2].The targets mounted on a stainless steel holder (diameter 10 mm) were placed at 90° to the beam direction on a multiple target holder ladder. The pressure inside the chamber was kept at ~2×10^{-6} mbar. Targets of $_{70}$Yb, $_{82}$Pb and $_{83}$Bi having thickness ranging 36-150 μg/cm^2 prepared by vacuum evaporation on a 10 μg/cm^2 thick carbon backing have been used in the present measurements. The x-ray spectra from different targets were recorded with a Silicon Drift detector (SDD) (FWHM = 133 eV at 5.9 keV, 8μm Be window) placed at 45° angle to the incident beam direction outside the vacuum chamber. The intensity ratios, I_{MK} / I_{MN} (Exp) (k = ξ, β, γ), for a specific element induced by carbon ions have been evaluated using the relation explained elsewhere [3, 4]. These intensity ratios have been compared with those calculated using the ECPSSR model based carbon ion induced M_j (j=1-5) sub-shell ionization cross sections [5], the x-ray emission rates based on the Dirac-Fock (DF) model [6], two sets of the fluorescence and Coster-Kronig yields based on the non-relativistic Hermann-Skillman potential calculations [7] and those based on the relativistic Dirac-Hartree-Slater model [8]. Significant differences observed between the measured and calculated ratios have been attributed to multiple ionization induced effects in the investigated elements by the incident carbon ions.

REFERENCES

[1] D.Kanjilal, T.Madhu, G.Rodrigues, U.K.Rao, C.P.Safvan, A.Roy, Ind. J. Pure Appl. Phys. **39,** (2001) 25.
[2] P. Kumar, G. Rodrigues, U.K. Rao, C.P. Safvan, D. Kanjilal, A. Roy, Pramana-Journal of Physics **59,** (2002) 805
[3] Shehla, Ajay Kumar, C. Bagdia, Anil Kumar, D. Misra, Sanjiv Puri, L.C. Tribedi, Nucl. Instrum. Meth. Phys. Res. B **399,** (2017) 74.
[4] Shehla, Sanjiv Puri, Radiat. Phys. and Chem. **127,** (2016) 194.
[5] Z. Liu and S. Cipolla, Comput. Phys. Commun. **97,** (1996) 315; 176, (2007) 157; 180, (2009) 1716; 182, (2011) 243.
[6] Sanjiv Puri, At. Data Nucl. Data Tables **93,** (2007) 730 and references therein.
[7] E.J. McGuire, Phys. Rev. A **5,** (1972) 1043.
[8] Yogeshwar Chauhan, Sanjiv Puri, At. Data Nucl. Data Tables **94,** (2008) 38.

5.5.7 Exploring the accurate nuclear potential

D. K. Swami[1], Yash Kumar[2] and T. Nandi[1]

[1]Inter University Accelerator Centre, Aruna Asaf Ali Marg, New Delhi- 110067, India.
[2]Dipartimento di Fisica “Galileo Galilei”, Universit`a di Padova, I-35131 Padova, Italy

We have formulated two empirical models, one for fusion barrier and another for interaction barrier heights using the experimental values available in the literature. The present study is restricted to the fusion and interaction barriers for the reactions in the regime $8 \leq z \leq 278$ and $59 \leq z \leq 313$, respectively, where $z = \frac{(Z_p Z_t)}{A_p^{\frac{1}{3}} + A_t^{\frac{1}{3}}}$. The fusion barriers so obtained have been compared with various model predictions such as Bass potential [1,2], Christenson and Winther [3], Broglia and Winther [4], Aage Winther [5], Siwek-Wilczyńska and J.Wilczyński [6], Skyrme energy density function model [7], and the Sao Paulo optical potential [8] along with experimental results. The Broglia and Winther model is found to be the best. Further, to examine its predictability, the Broglia and Winther model parameters are used in the CCFULL code to obtain the total fusion cross sections and compared with the experimental values. The comparison shows good agreements at the energies above the fusion barriers (Fig.1), but below the barriers the predictions for some reactions show a departure from the experimental results because of the damping of quantum vibration in the reaction partners near the touching point that causes hindrance to fusion deep below the barrier (Fig. 2). A small variation of the value of radius parameter in Woods-Saxon potential turns the agreement good. Thus, this model can be useful for planning experiments, especially if one is aiming for super heavy elements. Similarly, current interaction barrier heights have also been compared with the Bass potential model [1,2] predictions and found a reasonable agreement. Nevertheless, the present model is chosen for further use as it is based on the experiments. We believe the current interaction barrier model prediction will be a good starting point for future quasi-elastic scattering experiments. Whereas both the Broglia and Winther model and our interaction barrier model will have practical implications in carrying out physics research near the Coulomb barrier [9].

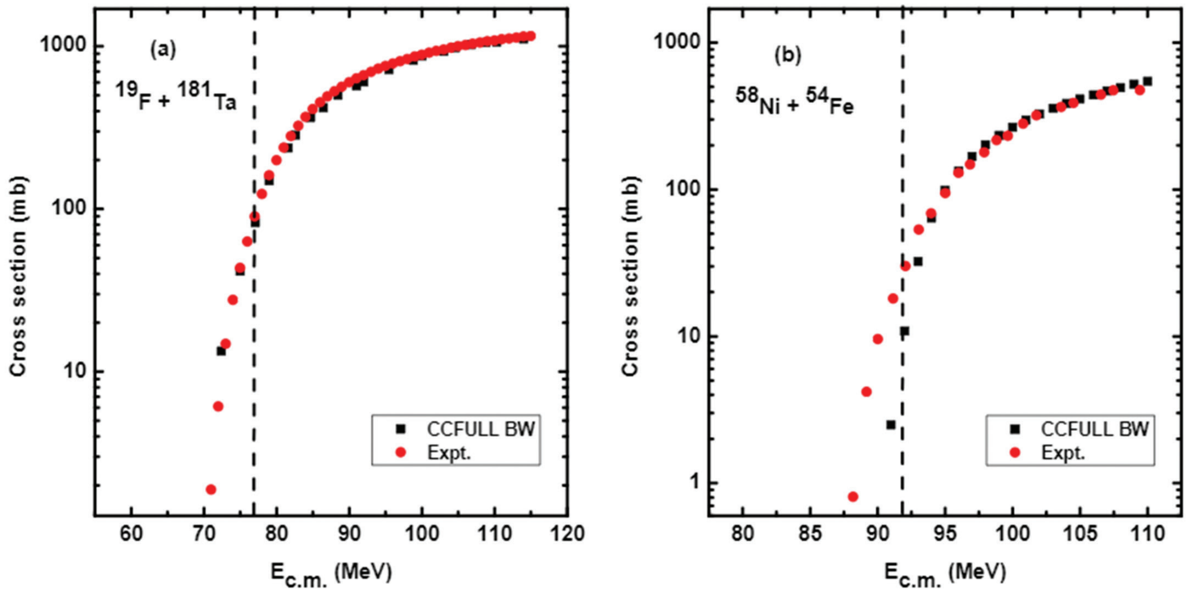

Fig 1: Comparison of total fusion cross section as a function of Ecm between the experimental and CCFULL calculation using Broglia and Winther parameters for the systems of $^{19}F+^{181}Ta$ (a) and $^{58}Ni+^{54}Fe$ (b). The dashed vertical line indicates the fusion barrier height for the corresponding reaction

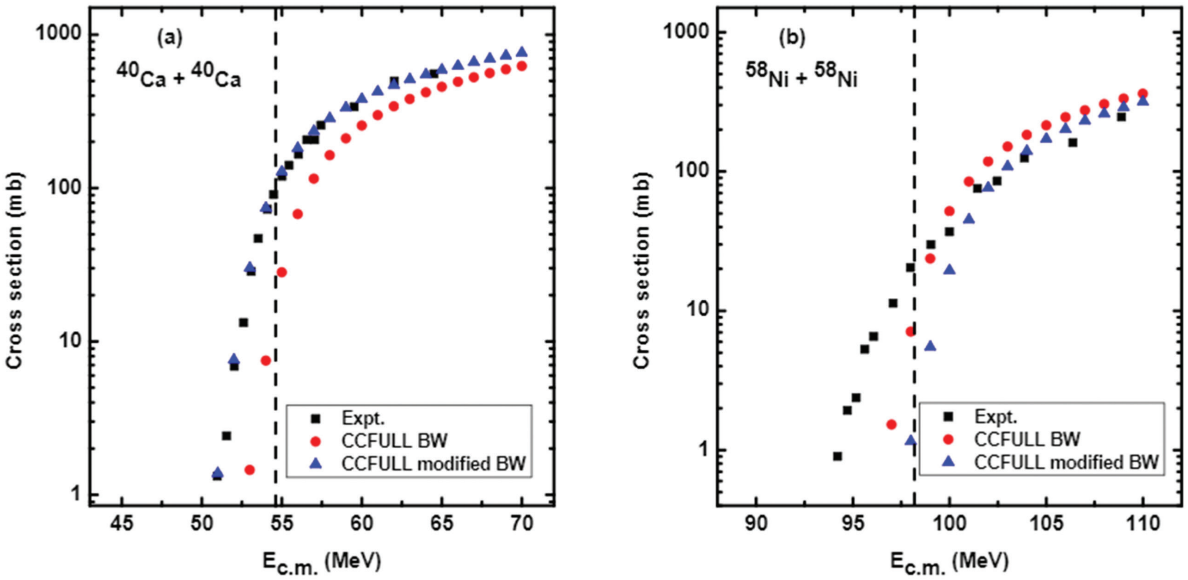

Fig. 2: Comparison of total fusion cross section (mb) as a function of Ecm between the experimental and CCFULL calculation using Broglia and Winther parameters for the systems of ^{40}Ca+^{40}Ca (a) and ^{58}Ni+^{58}Ni (b). Notice that the Broglia and Winther parameter r0 does not result in agreement with the experimental values. Good concurrence is found by changing r0 from 1.19 to 1.24 fm for ^{40}Ca+^{40}Ca and from 1.205 to 1.19 fm for ^{58}Ni+^{58}Ni. The dashed vertical line indicates the fusion barrier height for the corresponding reaction.

REFERENCES

[1] R. Bass, Nucl. Phys. A **231,** 45 (1974).
[2] R Bass, Phys. Lett. **47,** 139 (1973).
[3] P. R. Christensen and A. Winther, Phys. Lett. 65B, **19** (1976).
[4] W. Reisdorf, J.Phys. G: Nucl. Part.Phys. **20,** 1297 (1994).
[5] A. Winther, Nucl. Phys. A **594,** 203 (1995).
[6] K. Siwek-Wilczy˜nska, J. Wilczy˜nski, Phys. Rev. C **69,** 024611 (2004).
[7] V. Zanganeh, M. Mirzaei and N. Wang, Commun. Theor Phys. **64,** 177 (2015).
[8] A. S. Freitas et al., Braz J Phys **46,**120 (2016).
[9] P. Sharma and T. Nandi, Phys. Rev. Lett. **119,** 203401 (2017).

5.5.8 X-Ray spectroscopy of highly charged slow ions with solids

C. V. Ahmad[1,2,] R. Gupta[1,2], K. Chakraborty[1,2], D. K. Swami[3] and P. Verma[1*]

[1]Department of Physics, Kalindi College, East Patel Nagar, University of Delhi, New-Delhi 110008
[2]Department of Physics and Astrophysics, University of Delhi, New-Delhi 110007
[3]Inter University Accelerator Centre, Aruna Asaf Ali Marg, New Delhi-110067

The M-Shell production cross sections of heavy elements by impact of heavy ion (Xenon) of energy 3-5 MeV have been measured. Strong coulombic field of heavy ions while interacting with target atoms remove various electrons simultaneously from the target atoms. This results into the shift of position and broadening of x-ray peaks emitted from the target during collision [1]. Further, in quasi adiabatic region there is formation of molecular-orbitals between the collision partners which results in emission of non-characteristics x-rays called as Molecular Orbital X-Rays [2-4].

$_{54}$Xe^{q+} ions (q = 12,14 and 17), obtained from the 10 GHz ECR ion source of Low Energy Ion Beam Facility (LEIBF) at Inter University Accelerator Center (IUAC), New Delhi, were used to bombard solid targets of atomic number ranging between $70 \le Z_2 \le 82$ of thickness 360 μg/cm^2 as measure Rutherford back scattering method. These targets were kept in the center of the vacuum chamber mounted on target ladder at 45° with respect to beam direction. The x-rays were recorded by two silicon drift x-ray detectors mounted at 45° and 90° with respect to the incoming beam. They were kept outside the vacuum chamber by specially designed reentry cups. The x-rays before reaching the active volume of the detector passed through mylar foil, air gap and beryllium window of the detector. The detectors had resolution of 120 eV @ 5.9 keV. The ion beam current was monitored intermittently by the collection of charge on Faraday cup placed at 180°with respect to incoming beam. For accurate measurement of the current an electron suppressor was used for suppressing the secondary electrons. The suppressor was kept over the collision center by applying an optimized voltage of -300V. Another Faraday cup was also used for counting the number of outgoing projectiles.

The M X-Ray spectrum obtained in the experiment has complex structure and is not fully resolved by the detector used. Recorded (left) and fitted (right) spectra of 3 MeV Xe^{12+} on Au have been shown in Figure 1.

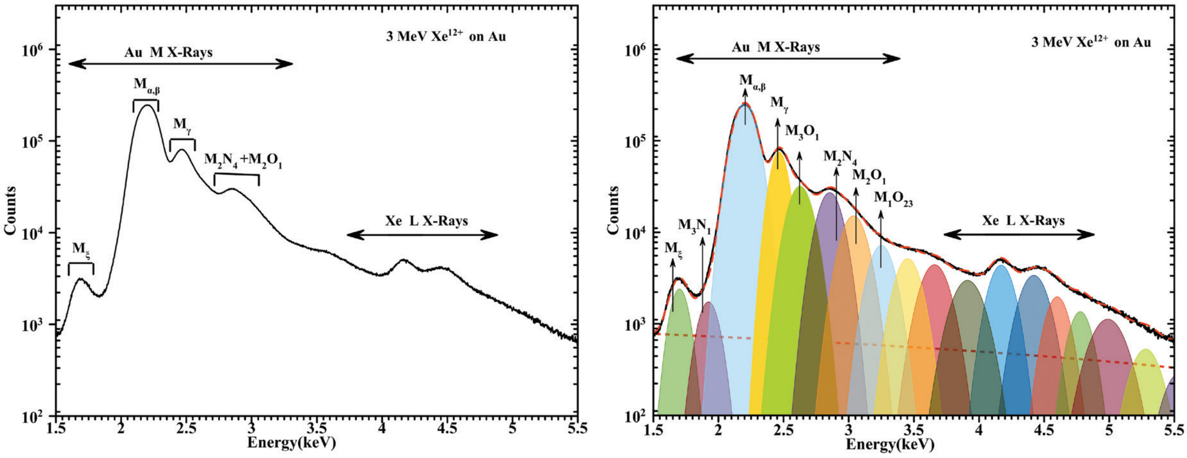

Figure 1: Measured X-Ray spectrum of Au excited by 3 MeV Xe^{12+} ion {recorded (left) and fitted (right) gaussian profiles}.

The target M x-rays showed higher intensities as compared to projectile Xe L X-Rays. This unusually high emission of target M x-rays indicates that a mechanism in addition to electron capture and Coulomb ionization is taking place during the collisions. Moreover, the target intensity ratios were also higher when compared with the theoretically calculated values. This indicates occurrence of multiple ionization of the target atoms during collisions. Measured production and ionization cross sections have been obtained. Theories have been found to underestimate the experimental cross-sections.

REFERENCES

[1] D. Banaś *et al.,* Nucl. Instrum. Meth. Phys. Res. Sect. B **195** (2002) 233.
[2] H. O. Lutz, *et al.,* J. Phys. B **9** (1976) 6.
[3] W. Lichten, J. Phys. Chem. **84** (2002) 2102.
[4] Verma P *et al.,* J. Phys. Conf. Ser. **875** (2017) 092029.

5.5.9 Inferring X-rays at small inter-atomic distances using molecular orbital approach

P Verma[1], R Gupta[1,2], C V Ahmad[1,2], K Chakraborty[1,2], A Rani[2], D. K. Swami[3], G Sharma[4], S.K. Saini[3], P Barua[3], D Mitra[5], S Mandal[2] and T Nandi[3]

[1]Department of Physics, Kalindi College, University of Delhi, East Patel Nagar, New Delhi-110008.
[2]Department of Physics and Astrophysics, University of Delhi, New Delhi-110007.
[3]Inter University Accelerator Centre, Aruna Asaf Ali Marg, New Delhi-110067.
[4]Department of Physics, Government Engineering College, Ajmer, Rajasthan-305001.
[5]Department of Physics, University of Kalyani, Kalyani, Nadia, West Bengal-741235.

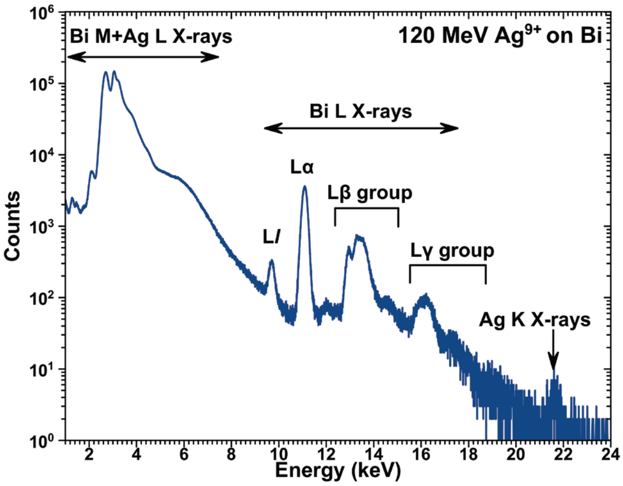

Figure 1: X-ray spectrum of 120 MeV Ag^{9+} ions on 120 μg/cm² Bi with C backing.

In close, adiabatic heavy ion-heavy atom collisions, inner - shell vacancies are produced for collision velocities smaller than the orbital velocities of the target electrons [1]. In such cases, as the inter-nuclear distance decreases, a transient quasi-molecule with a united atomic atom $Z_{UA}=Z_1+Z_2$ (subscript 1 for projectile and 2 for target) is formed. If Z_1 and Z_2 are such that $Z_{UA}\geq 100$, super heavy elements with atomic numbers beyond that of any stable element known can be investigated.

Investigation of inner shell ionization of super heavy systems with $120 \leq Z_{UA} \leq 130$ have been performed in the Atomic Physics beam line in beam hall II using the Pelletron facility at IUAC. The super heavy systems were achieved by close adiabatic collisions of 0.65-1.2 MeV/u Ag^{q+} (5 ≤

q ≤ 9) ions with target foils of $73 \le Z_2 \le 83$ of various thicknesses. The collision induced inner shell processes have been studied by measuring x-rays from both collision partners using KETEK SDD detector kept at +135º port of experimental chamber, keeping the target ladder aligned perpendicular to the beam axis (see Figure 1).

For detection of scattered particles, 3 SBD detectors were installed inside the experimental chamber at ±30° and +150°. For beam collimation to 3 mm diameter, a penetrable cylindrical Faraday cup has been designed, fabricated at IUAC workshop and installed at beam entry. The collimator along with its holder was made of SS with length and internal diameter as 60 and 30 mm, respectively. It has three circular collimators of diameter 4, 5 and 3 mm placed consecutively from beam entry side towards chambers centre. It is capable of beam current measurement. A target ladder with 3 columns which can hold 15 target positions simultaneously has been fabricated at IUAC's workshop. It is made of a 2 mm thick SS plate with dimensions 140x80 mm^2.

For correct peak identification in both x-ray and SBD spectra, calibration of the detectors was performed with radioactive sources. The x-ray detector was calibrated using Am-241, Fe-55 and Co-57 radioactive sources covering the energy range from 3 keV to 25 keV. This range pertained to both target and projectile x-rays. Similarly, the SBD detectors were calibrated using Am-241 which is also an alpha source emitting alpha particles of energy 5.5 MeV. Detailed measurements of projectile energy as well as target thickness have been performed. Preliminary analysis has yielded observations such as presence of spectator vacancies [2] giving evidence of multiple ionization of target [3]. The inner shell couplings and vacancy transfer mechanisms are being studied using correlation diagrams which require molecular orbital approach.

REFERENCES

[1] Mokler P H et al X-Ray Production in Heavy Ion-Atom Collisions. In: Sellin I.A. (eds) Structure and Collisions of Ions and Atoms. Topics in Current Physics, vol 5. Springer, Berlin, Heidelberg (1978).

[2] Verma P et al Phys. Scr. **61,** (2000) 335.

[3] Banas D et al Nucl. Instr. Meth. B **154,** (1999) 247 and J. Phys. B: At. Mol. Phys. **33,** (2000) L793.

5.5.10 Evidence of circular Rydberg states in beam-foil experiments: role of surface wake field

Gaurav Sharma[1], Nitin K. Puri[1], Pravin Kumar[2] and T. Nandi[2]

[1]Dept. of Applied Physics, Delhi Technological University, Bawana road, New Delhi 110042, India
[2]Inter University Accelerator Centre, Aruna Asaf Ali Marg, New Delhi 110067, India
[3]Department of Physics, Government Engineering College, Ajmer, Rajasthan-305001.

We have theoretically analyzed the experimental data of 125 MeV fully stripped as well as H-like sulfur ions passing through carbon foils [1] in the light of the fact that the ETACHA code represents well the charge state distribution of the projectile ions in the bulk of the target foil. Though the Rydberg states in the fast-ion foil collisions are formed in the last layers at the exit surface, the production of the projectile Rydberg states in the H-like ions exhibits a pronounce target thickness dependence because surface wake field (SWF) varies with the foil thickness [2]. Both the ions are found to contribute in the formation of circular Rydberg states (CRS) irrespective of the specific incident charge state used. The CRS formation probability (R) shows a saturation in the CRS formation after a certain thickness (Fig.1). The saturation in the value of R in the case of S^{16+} incident ion is relatively faster (about 32 $\mu g/cm^2$) than that in case of the S^{15+} ion incidence (about 55 $\mu g/cm^2$). The transfer probability of having the CRS from the high Rydberg states (HRS) depends on the magnitude of the SWF, which is smaller for the lower foil thickness and larger for higher foil thickness before the saturation. Therefore, the probability of having the CRS from the HRS is expected to be smaller for the lower foil thickness than that of the higher foil thickness. Thus, we observe the lower yield of the Ly-α x-ray for the lower foil thickness. For the low thick foil, the CRS formation is mainly due to capture in comparison to excitation, whereas, both the processes have equal contribution in the higher foil thickness. For the formation of CRS by the influence of SWF an excitation model is developed (Fig.2). The contribution arising only from the SWF is considered in developing the model. As per the present model, the low $|m|$ HRS are formed by the Stark switching process in the last layers and HRS states so formed are transformed to the CRS by the single multiphoton process while passing through the SWF. This transformation occurs with a high probability in the experiment [1] as seen by other methods [3]. The present findings provide an important connection between atomic physics and condensed matter physics. Further, an interesting role of the solid state effects [4] such as the SWF [2] on populating the CRS is evidenced. The detail explanations can be seen in our recent work [5].

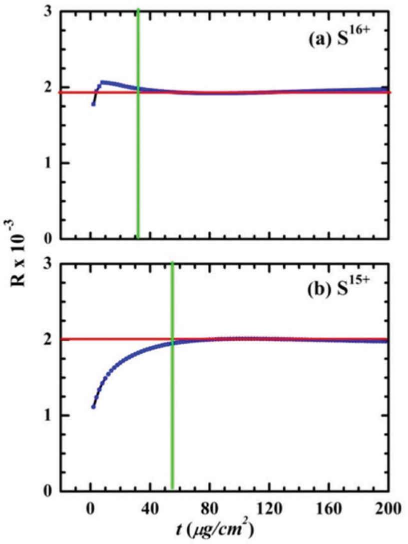

FIG. 1. Relative CRS formation probability: the ratio R, as defined in the text, is plotted as a function of carbon foil thickness (t) for incident ions (a) S^{16+} and (b) S^{15+}. Red lines represent the saturated value of R and green lines represent the thickness where the saturation is reached.

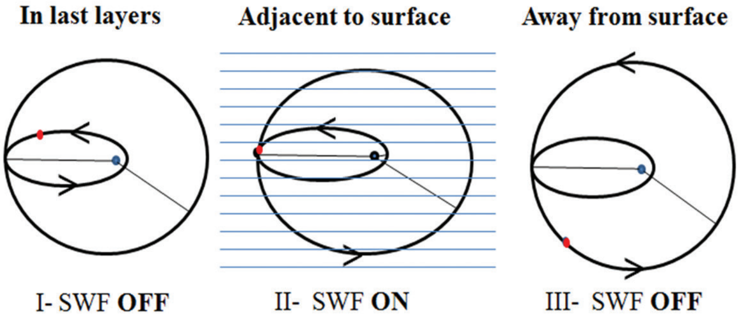

FIG. 2. Excitation model for CRS at the foil surface: I. HRS is formed at the foil surface in the absence of SWF and in the presence of BWF, II. HRS is promoted to CRS in the presence of SWF only, and III. CRS lasts as per its mean lifetime in the field-free regions. The red dot indicates orbiting electron and black dot the nucleus of the ion. The electron will remain in the circular state as the ion exits the SWF.

REFERENCES

[1] H.-D. Betz, D. Roschenthaler, and J. Rothermel, Phys. Rev. Lett. **50,** 34 (1983).
[2] T. Nandi *et. al.,* Phys. Rev. Lett. **110,** 163203 (2013).
[3] R. G. Hullet and D. Kleppner, Phys. Rev. Lett. **51,** 1430 (1983).
[4] C. O. Reinhold et al., J. Phys. B At. Mol. Phys. **33,** L111 (2000).
[5] G. Sharma, N.K. Puri, P. Kumar, and T. Nandi, Euro. Phys. Lett. **120,** 63002 (2017).